The diverse high-pressure chemistry of Y–ammonia borane and Y–paraffin oil systems

Doctoral Thesis

submitted to obtain the academic degree of Doctor of Natural Sciences

(Dr. rer. nat.)

of the Bayreuth Graduate School of Mathematical and Natural Sciences

(BayNAT)

of the University of Bayreuth

Alena Aslandukova

from *Kirov-200 (Russian Federation)*

Bayreuth, 2024

This doctoral thesis was prepared at the Bavarian Research Institute of Experimental Geochemistry and Geophysics (BGI) and the Laboratory of Crystallography (Material Physics and Technology at Extreme Conditions Group) at the University of Bayreuth from 08/2020 until 08/2024 and was supervised by Prof. Dr. Dr. h. c. Leonid Dubrovinsky and Prof. Dr. Dr. h. c. Natalia Dubrovinskaia.

This is a full reprint of the thesis submitted to obtain the academic degree of the Doctor of Natural Sciences (Dr. rer. nat.) and approved by the Bayreuth Graduate School of Mathematical and Natural Sciences (BayNAT) of the University of Bayreuth.

Form of the dissertation: cumulative thesis

Date of submission: 27.08.2024

Admission by the executive board: 12.09.2024

Date of defence: 11.02.2025

Acting director: Prof. Dr. Jürgen Köhler

Doctoral committee:

Prof. Dr. Leonid Dubrovinsky (reviewer)
Prof. Dr. Jürgen Senker (reviewer)
PD Dr. Gerd Steinle-Neumann (chair)
Prof. Dr. Sander van Smaalen

(additional reviewer: Prof. Dr. Ronald Miletich-Pawliczek)

Table of Contents

Zusammenfassung

Metallpolyhydride haben in den letzten Jahren aufgrund einer steigenden Anzahl von Vorhersagen und Messungen hoher kritischer Temperaturen (T_c) nahe der Raumtemperatur für supraleitende Übergänge unter Hochdruckbedingungen enorme Aufmerksamkeit erhalten. Üblicherweise wird die Synthese von Hydriden unter Hochdruck-Hochtemperatur-Bedingungen (HPHT) in Diamantstempelzellen (DACs) durchgeführt und T_c *in situ* gemessen. Häufig wird die Phasenzusammensetzung der untersuchten Probe durch Pulver-Röntgenbeugung (PXRD) charakterisiert, gelegentlich mit Unterstützung von *ab initio* Berechnungen. Diese Methode weist jedoch erhebliche Einschränkungen bei der Analyse von Mischungen unbekannter Reaktionsprodukte in lasererhitzten DACs (LHDACs) auf. Die Phasenzusammensetzung und die strukturellen Eigenschaften der Probe sind jedoch entscheidend für die zuverlässige Interpretation der Ergebnisse der Messung von Supraleitung. Jüngste Fortschritte in der Anwendung der Hochdruck-Synchrotron-Einkristall-Röntgenbeugung (SCXRD) zur Analyse von Mehrphasen-Multikristallproben ermöglichen die vollständige Charakterisierung von Kristallstruktur, Kristallchemie und der chemischen Zusammensetzung zahlreicher kristalliner Verbindungen in komplexen Mischungen in LHDACs.

Diese Dissertation präsentiert Ergebnisse zur Synthese mehrerer neuartiger Yttriumverbindungen in DACs durch Lasererwärmung von Yttrium mit zwei wasserstoffreichen Verbindungen – Ammoniumborid oder Paraffinöl – bei bis zu 3500 K und Drücken bis zu 170 GPa. Reaktionsprodukte wurden systematisch mittels Synchrotron-SCXRD untersucht. SCXRD-Experimente wurden überwiegend an den Strahllinien ID11, ID27 und ID15b der Europäischen Synchrotronstrahlungsquelle (ESRF) in Grenoble, Frankreich, durchgeführt. Weitere Experimente wurden am PETRA III in Hamburg und an der Advanced Photon Source in Chicago durchgeführt.

Ein wesentlicher Teil dieser Dissertation ist der Untersuchung der Kristallstrukturen neuer Yttriumhydridverbindungen gewidmet. In Experimenten wurden neben den zwei bekannten Yttriumhydriden (kubisches und tetragonales YH_3), fünf neue Yttriumhydridverbindungen (Y_3H_{11}, Y_2H_9, Y_4H_{23}, $Y_{13}H_{75}$ und Y_4H_{25}) entdeckt. Der Wasserstoffgehalt in den entdeckten Hydriden nahm mit dem Druck zu: von 1:3 in YH_3 bei 14 GPa bis zu 1:6.25 in Y_4H_{25} bei 171 GPa. Die Positionen der Nicht-Wasserstoff-Atome in den Kristallstrukturen wurden aus den SCXRD Daten bestimmt. Zur Bestimmung der Wasserstoff Positionen wurde ein eigener Ansatz entwickelt: Zuerst wird nach möglichen Anordnungen der

Wasserstoffatome für gegebene Stöchiometrien mithilfe der Endeavour©-Software gesucht, und anschließend die Strukturmodelle mittels DFT-Berechnungen verglichen. Zusätzlich ermöglichten die *ab initio* Berechnungen die Untersuchung der dynamischen Stabilität und der elektronischen Eigenschaften der synthetisierten Hydride.

Obwohl der Schwerpunkt dieser Dissertation auf der Charakterisierung der Hauptprodukte der chemischen Reaktionen in LHDACs (Hydriden) lag, wurden auch das rekristallisierte Ausgangsmaterial (Y) und Nebenprodukte analysiert, die in der Reaktionskammer gefunden wurden. Dies führte zur Entdeckung von drei neuartigen Hochdruck-Yttrium-Allotropen sowie von bisher unbekannten Carbiden, einem Carbonat und einem Borat.

Das erste Yttrium-Allotrop ist ein hexagonales *hP*3-Y-I (Raumgruppe *P*6/*mmm*), das unter Umgebungsbedingungen stabilisierbar ist. Es wurde in beiden Systemen (Y-Paraffin und Y-NH_3BH_3) über einen weiten Druckbereich gefunden. Die beiden anderen Allotrope, hexagonales *hP*3-Y-II und tetragonales *tI*8-Y, wurden nach dem Laserheizen von Yttrium in Paraffinöl bei 120 GPa beziehungsweise 138 GPa erhalten. Das *tI*8-Y-Allotrop ist von besonderem Interesse, da es eine nicht geschlossen gepackte, kanalförmige Struktur aufweist, die für ein hochdruck-synthetisiertes Material ungewöhnlich ist.

Ein neues orthorhombisches Polymorph von Yttriumcarbid, γ-Y_4C_5, wurde aus Yttrium und Paraffinöl in einer LHDAC bei 50 GPa synthetisiert. Die Struktur von γ-Y_4C_5 umfasst zwei Kohlenstoffgruppen mit ungewöhnlich hohen nicht-ganzzahligen Ladungen: $[C_2]^{5.2-}$ Dimere und nicht-lineare $[C_3]^{6.8-}$ Trimere. Ein Polymorph von Yttriumborat, *oC*20-YBO_3, wurde bei 90 und 120 GPa und Temperaturen von 3500 K synthetisiert. Die Struktur dieser Verbindung enthält BO^{4-} Tetraeder, die über gemeinsame Ecken verbunden sind und ein einzigartiges isoliertes quasi-1D-anionisches Netzwerk bilden; unendlich lange, unverzweigte Bor-Sauerstoff-Ketten in Zickzackform. Außerdem wurde das erste Orthokarbonat der Seltenen Erden, $Y_3(CO_4)_2$, unter denselben Bedingungen in denselben DACs erhalten.

Zusammenfassend zeigt die in dieser Dissertation präsentiert Arbeit, dass SCXRD von mikro-kristallinen Mehrphasenproben in LHDACs die Detektion und vollständige Charakterisierung von Phasen in komplexen Mischungen ermöglicht, die durch PXRD, selbst in Kombination mit *ab initio* Berechnungen, nicht identifiziert werden können. Unsere Ergebnisse zeigen die Komplexität der Yttrium-Paraffinöl- und Yttrium-Ammoniumboran-Systeme sowie deren Mehrphasencharakter bei hohem Druck nach Laserheizen und insbesondere die Bildung verschiedener Yttriumhydridverbindungen, Carbiden, eines Carbonats und eines Borats wurde experimentell nachgewiesen. Die zuvor vorhergesagte und

experimentell beobachtete Tendenz zur Bildung von Hydriden mit höherem Wasserstoffgehalt bei erhöhtem Druck wurde auch in dieser Dissertation bestätigt. Es wurden mehrere Yttriumhydride synthetisiert, die weder zuvor durch Simulationen vorhergesagt noch experimentell beobachtet wurden. Die Beobachtung, dass die Synthese von Hydriden in LHDACs zu komplexen Mehrphasenmischungen führt, kompliziert akkurate Messungen physikalischer Eigenschaften, insbesondere T_c, einzelner Verbindungen. Dies unterstreicht die Bedeutung der Entwicklung neuer Ansätze für die präzise Untersuchung physikalischer Eigenschaften von Mehrphasenmischungen.

Summary

Metal polyhydrides have gained enormous attention in recent years due to their claimed high critical temperature (T_c) for superconducting transitions at high pressures. Usually, hydride synthesis is carried out under high-pressure high-temperature (HPHT) conditions in diamond anvil cells (DACs), and the T_c measurements are realized *in situ*. Commonly, the phase composition of the sample under investigation is characterized using powder X-ray diffraction (PXRD), sometimes with the assistance of *ab initio* calculations. However, this approach has serious limitations when dealing with a mixture of unknown products of chemical reactions in laser-heated DACs (LHDACs). The phase composition and structural characteristics of the sample are crucial for the reliable interpretation of the results of superconductivity measurements. Recent advancements in the application of high-pressure synchrotron single-crystal X-ray diffraction (SCXRD) for the analysis of multiphase multigrain samples enable the full characterization of the crystal structures, crystal chemistry, and chemical composition of numerous crystalline compounds in complex mixtures in LHDACs.

The thesis presents results on the synthesis of several novel yttrium compounds in DACs by laser heating yttrium with two hydrogen-rich precursors — ammonia borane or paraffin oil — up to 3500 K at pressures up to 170 GPa. These compounds were systematically investigated using synchrotron SCXRD. Most of the SCXRD experiments were conducted at beamlines ID11, ID27, and ID15b of the European Synchrotron Radiation Facility (ESRF) in Grenoble, France. Additional experiments were performed at PETRA III in Hamburg and the Advanced Photon Source in Chicago.

A major part of the thesis is dedicated to the study of the crystal structures of novel yttrium hydrides. In the experiments, in addition to the two known yttrium hydrides (cubic and tetragonal YH_3), five new yttrium hydrides (Y_3H_{11}, Y_2H_9, Y_4H_{23}, $Y_{13}H_{75}$, and Y_4H_{25}) were discovered. The hydrogen content in the discovered hydrides was found to increase with pressure, from 1:3 in YH_3 at 14 GPa to 1:6.25 in Y_4H_{25} at 171 GPa. The positions of non-hydrogen atoms in the crystal structures were determined from synchrotron SCXRD data. The positions of H atoms were proposed using our original approach: first, we searched for possible arrangements of hydrogen atoms for given stoichiometries using Endeavour© software, and then the structure models were compared using DFT calculations. Additionally, the *ab initio* calculations allowed us to investigate the dynamic stability and electronic properties of the synthesized hydrides.

Although the main focus of this thesis was the characterization of the main products of the chemical reactions in LHDACs (hydrides), we also analyzed the recrystallized precursor (Y) and minor by-products found in the reaction chamber. This led to the discovery of three novel high-pressure yttrium allotropes and previously unknown carbides, a carbonate, and a borate.

The first yttrium allotrope is a hexagonal *hP*3-Y-I (space group *P*6*/mmm*), which is recoverable to ambient conditions. It was found in both systems (Y-paraffin and Y-NH_3BH_3) over a wide pressure range. The other two allotropes, hexagonal *hP*3-Y-II and tetragonal *tI*8-Y, were obtained after laser heating of yttrium in paraffin oil at 120 GPa and 138 GPa, respectively. The *tI*8-Y allotrope is of special interest as it has a non-closed-packed, channel-like structure, which is unusual for a material synthesized at high pressures.

A new orthorhombic polymorph of yttrium carbide, γ-Y_4C_5, was synthesized from yttrium and paraffin oil in a laser-heated diamond anvil cell at 50 GPa. The structure of γ-Y_4C_5 includes two carbon groups with unusually high non-integer charges: $[C_2]^{5.2-}$ dimers and non-linear $[C_3]^{6.8-}$ trimers. A polymorph of yttrium borate, *oC*20-YBO_3, was obtained at 90 and 120 GPa and temperatures of 3500 K. Its structure contains BO_4 tetrahedra connected via common vertices, forming a unique isolated quasi 1D anionic network – infinite zig-zag unbranched boron-oxygen chains. Additionally, the first rare-earth metal orthocarbonate, $Y_3(CO_4)_2$, was obtained in the same DACs under the same conditions.

In conclusion, the work performed within this dissertation demonstrates that SCXRD of microcrystalline multiphase samples in LHDACs enables the detection and full characterization of phases in complex mixtures that cannot be identified by PXRD, even when combined with *ab initio* calculations. Our results reveal the complexity of the yttrium-paraffin oil and yttrium-ammonia borane systems and their multiphase character at high pressure after laser heating – the formation of various yttrium hydrides, carbides, a carbonate, and a borate has been experimentally demonstrated. The previously predicted and experimentally observed tendency for the formation of hydrides with higher hydrogen content under increased pressure was also confirmed in this work. Several yttrium hydrides that were neither previously predicted nor observed experimentally were discovered. Since the synthesis of hydrides in laser-heated DACs leads to the formation of complex multiphase mixtures, it complicates the interpretation of measurements of physical properties, including T_c, of individual compounds, underscoring the importance of developing novel approaches for such studies.

Acknowledgments

I would like to express my deepest gratitude to my supervisor, Prof. Dr. Leonid Dubrovinsky, not only for his invaluable assistance in preparing this thesis, but also for the support throughout this challenging four-year journey. Thank you for your advice, extensive discussions and debates about the results and plans for future work. I am immensely grateful for not leaving me alone with difficult tasks, for always being ready to help me. Your patience, understanding, and wise calmness were very important to me. You have always inspired and encouraged me with your enthusiasm, and energised me with your endless optimism not only in work but also in everyday life. Thank you!

Special thanks to Prof. Dr. Natalia Dubrovinskaia for the scientific guidance and insightful discussions that greatly enriched this work. Her support extended far beyond the realm of academia, for which I am profoundly grateful.

I am very grateful to Sasha Chumakov and Elena Chumakova for their care and support, without Sasha I would not have found my place in the HP research group-family.

Deep thanks to my first supervisors Alexey Sobolev, Igor' Presniakov, and Iana Glazkova for supporting me in the initial stage of establishing myself as a "young independent scientist" during my university years. They made me fall in love with science.

I would like to express my gratitude to everyone at BGI for creating such a welcoming and warm environment, and for always being kind to me. Especially Prof. Dr. Hans Keppler, Dr. Tiziana Boffa-Ballaran, Dr. Catherine McCammon, Prof. Dr. Dan Frost, and Prof. Dr. Tomoo Katsura. I thank the administrative and technical staff of BGI Anna Dinius, Petra Buchert, Janina Potzel, Olga Gaspert, Dorothea Wiesner, Detlef Krausse, Stefan Übelhack, Sven Linhardt, Trenz Ulrike, Raphael Njul, and Alexander Rother, for all their help and support.

Moreover, I want to thank everyone at the Laboratory of Crystallography, especially Prof. Dr. Sander van Smaalen, PD Dr. Andreas Schönleber, Kerstin Kuspert, Denis Kelk-Huth.

I would like to thank my colleagues Gerd Steinle-Neumann and Liang Yuan for their help in mastering the theoretical calculations. You have patiently taught me DFT from the very beginning, and the experience you have given me is invaluable - without you I would not have been able to do the theoretical part of my work.

Many thanks to Sergey Ovsyannikov for teaching me how to use the multi-anvil press and helping me to synthesise samples.

I would like to extend my gratitude to the staff of P02.2 (Petra III), IDD-13 (APS) and ID11, ID15b, ID27, and ID14(18) (ESRF) beamlines for their invaluable support and assistance

during our experiments, especially Konstantin Glazyrin, Stella Chariton, Jonathan Wright, Michael Hanfland, Anna Pakhomova, Gaston Garbarino, Alexander Chumakov, George Aprillis, and Sergey Yaroslavtsev.

I am truly grateful to Florian Trybel for translating the summary of this thesis into German, but also for being a great colleague. Thank you for everything you taught me, the times you helped me, and the discussions we had.

Special thanks to our broad high-pressure family: Wenju Zhou, Dominique Laniel, Ilya Kupenko, Yu Wang, Maxim Bykov, Elena Bykova, Valentin Kovalev, Timofey Fedotenko, Saiana Khandarkhaeva, Egor Koemets, and Iulia Koemets, for fruitful discussions and for their emotional support when things did not go according to plan and for the pleasant atmosphere in the lab and during the experiments. Collaborating with each of them has been a continuous learning process, providing opportunities to acquire new knowledge and skills.

Special thanks to those who are not only my colleagues but also my friends—Yuqing Yin, Efim Kolesnikov, Xiang Li, Alexander Kurnosov and Anya Kurnosova, Naira Martirosyan, Dmitry Bondar, and Artem Chanyshev—for their invaluable help in work, as well as for their kindness, support, and assistance in everyday life.

A huge heartfelt thanks to my close friends who are always by my side and support me in every situation - Pashka Milkin, Ilyusha Sadilov, Anya Diukareva, Anatoly Arkhipin, and Lera Akbar.

My most sincere and affectionate gratitude goes to my family for their constant love and support. I would like to thank my mother Irina and father Alexey, my sister Nastya, and my grandparents. Most of all I would like to thank my grandmother Tanya, who raised curiosity in me from a young age and supported even my craziest desire to experiment.

No words can express my thanks to the most important person in my life - my husband Andrey Aslandukov, you are my strength and support. Thank you for your boundless love, support, understanding, and patience in every matter. We grew up together, without you I would not be me.

And infinite gratitude to my daughter Arina, who painted my life in bright colours, taught me to view life from different perspectives and find positivity in everything. Every day, I learn something new from her.

Chapter 1. Introduction.

1.1. Outlook on the evolution of superconductors.

This work is motivated by reports of high-T_c superconductivity at HP in metal-hydrogen systems [1–5], therefore, a brief overview of the development of research on superconductors is given below. Discovered in 1911 by Heike Kamerling Onnes, superconductivity in mercury at temperatures near absolute zero revolutionised the understanding of electrical conductivity. Superconductivity is a phenomenon observed in certain materials that exhibit absolutely zero electrical resistance and expel magnetic fields when cooled below a specific critical temperature (T_c). These materials enable the efficient transmission of electricity, powerful electromagnets, and advanced technologies like MRI machines and particle accelerators. Over the following decades, researchers uncovered more superconducting materials and delved into the theoretical underpinnings of the phenomenon. In 1957, John Bardeen, Leon Cooper, and Robert Schrieffer developed the BCS theory, explaining superconductivity in conventional superconductors [6]. Later, a major breakthrough in 1986 was done when Johannes Bednorz and Karl Müller discovered superconductivity in Ba−La−Cu−O ceramic materials (T_c = 35 K) [7]. The study of superconductors continues to be a vibrant field of research, with the quest for high-temperature (HT) or even room-temperature superconductivity being one of the most exciting and challenging goals in modern physics. The major advantage of high-temperature superconductors is that they can be cooled using liquid nitrogen, in contrast to the previously known superconductors that require expensive and hard-to-handle coolants, primarily liquid helium [8]. However, since the discovery of $HgBa_2CaCuO_{6+x}$ in 1993 (T_c = 130 K) [9], the search for new, more efficient higher-temperature superconductors at ambient pressure has not yet yielded promising results (Fig. 1.1).

Pressure is a key thermodynamic variable that significantly affects the properties of materials, including increasing the critical temperature of superconducting materials. Recent advances in experimental techniques have enabled the synthesis of new HT superconducting materials under high pressure (HP). Hydrogen when compressed to immense pressures of ~ 400 GPa was predicted to form a simple atomic phase with very high critical superconducting temperatures $T_c \sim 230$ K [10,11]. This theoretical insight still awaits experimental confirmation due to experimental difficulties, a variety of hydrogen-rich materials have been suggested recently to have record high T_c values. To date, all systems with high superconducting critical temperatures ($T_c > 200$ K) that have been accessed under pressure are hydrogen-rich materials (Fig. 1.1) [12–14].

Research on HT superconductors has taken a major step forward in the last decade. [13,15]. Following the discovery of HT superconductivity (T_c = 203 K at 155 GPa) in sulfur hydride (H_3S) in 2015 [14], a significant number of hydrogen-rich materials, such as metal hydrides: LaH_{10} [3,16], CaH_6 [17], BaH_{12} [18], YH_6 and YH_9 [5,19], CeH_9 [20], PrH_9 [1], ThH_{10} [21], UH_7 and UH_8 [22], were claimed to be high-T_c superconductors under HP. Nevertheless, there are still debates about the correctness of T_c measurements, data processing and interpretation of results. One of the concerns relates to T_c measurements in the absence of detailed information about the phase and chemical composition of products of chemical reactions taking place in the sample chamber of a DAC after laser heating. Reliable conclusions concerning the superconductivity, i.e., values of measured T_c, the isotopic effect, and the dependence of the superconducting transition on magnetic field, are problematic considering a variable hydrogen content in the same phase and/or the inhomogeneous products' mixture.

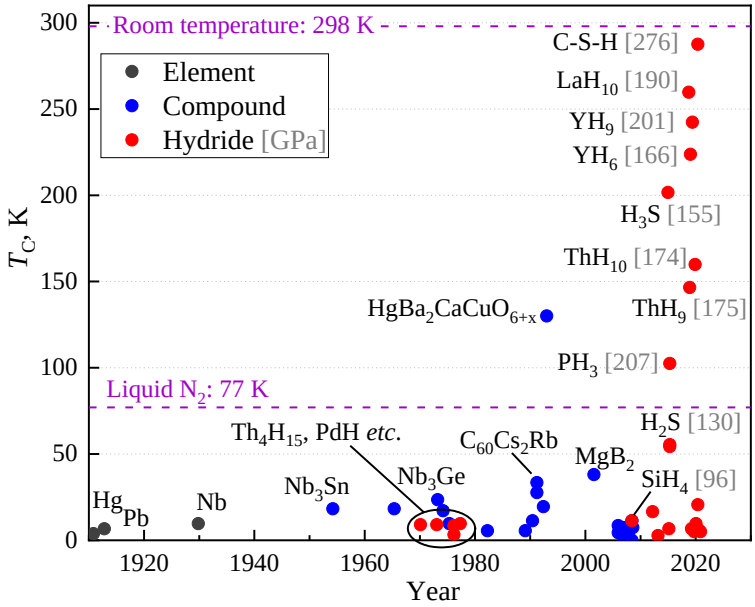

Figure 1.1. Timeline of discoveries of conventional superconductors with increasing superconducting critical temperature T_c (modified after [15]). Note: results on C-S-H room-temperature superconductor synthesis were refuted and the corresponding paper was retracted from *Nature* [23].

1.2. Yttrium hydrides.

As promising high-T_c superconductors, high-pressure yttrium hydrides have been extensively studied. Under ambient conditions, two yttrium hydrides *cF*4-YH_2 ($Fm\bar{3}m$) and *hP*2-YH_3 ($P6_3/mmc$) [24] are known (here Pearson symbols refer to the arrangement of Y atoms only; hydrogen content inferred from the chemical formulas may refer to an experimentally determined, theoretically proposed, or empirically estimated amount of hydrogen atoms). At moderately high pressures (10-25 GPa), *hP*2-YH_3 undergoes a phase

transition to *cF*4-YH_3 [25], which also can be produced by hydrogenation at ambient temperature of *cF*4-YH_2 [26]. The *cF*4-YH_3 phase was found to be stable at ambient temperature under high pressures up to 325 GPa [19]. At pressures above 200 GPa, the long treatment of YH_3 with pressurized hydrogen without heating leads to the formation of tetragonal *tI*2-YH_4 and cubic *cI*2-YH_6 [19]. Heating yttrium with hydrogen-bearing precursors at mild pressures (up to 50 GPa) results in the formation of *hP*3-YH_x (x = 1.4-3) hydrides with variable H-content along with *cF*4-YH_3 [19]. At higher pressure, above 100 GPa, the high-temperature syntheses of yttrium hydrides with a higher hydrogen content (*tI*2-YH_4 [19], *cI*2-YH_6 [19], *oI*2-YH_7 (*Imm*2) and *aP*2-YH_7 (*P*1) [5], and *hP*2-YH_9 ($P6_3/mmc$) [2,19]) were reported. Among them, based on experimental data, the *cI*2-YH_6 and *hP*2-YH_9 phases were claimed to have high superconducting transition temperatures, T_c∼224 K at 166 GPa [5] and T_c∼243 K at 201 GPa [19], respectively. Moreover, up to date several theoretical studies on the Y–H system were reported [4,5,27] and a variety of hydrides with a high hydrogen content, namely *mC*2-YH_8 [4], *cF*4-YH_9 ($F\bar{4}3m$), *cF*4-YH_{10} ($Fm\bar{3}m$) [5], and *mC*4-YH_{12} (*C*2/*c*) [4], were predicted to be stable but not yet found in experiments. It is important to note that the chemical compositions and structures of only YH_2 and YH_3 have been unambiguously determined [25,26], whereas those of all other hydrides have been based on theoretical predictions and/or empirical estimations. It is also worth mentioning that the accuracy and limitations of these predictions may vary among different studies. Therefore, there are some inconsistencies between the predictions and experiments (*i.e.* many predicted Y-H compounds have not been found so far, predicted values of T_c differ significantly from those reported based on measurements, among other discrepancies), some puzzling results, such as negative resistance for YH_6 at 183 GPa [5], and very different T_c onsets from experiment to experiment [28]. Additionally, not all of the claims are easy to justify in the absence of detailed information about the phase and chemical composition of products of chemical reactions taking place in the sample chamber of a DAC after laser heating. Some problems with the currently available experimental data interpretation may be associated with the synthesis technique: hydrides at HP are often obtained by heating metals embedded in paraffin oil or ammonia borane [3,5,19,21,29–31], and one cannot exclude that other, non-hydride phases (*e.g.*, carbon and boron compounds) may form in the system under investigation [32,33] and their properties can influence the measurements of superconductivity. Therefore, a reliable conclusions concerning the superconductivity, *i.e.* values of measured T_c, the isotopic effect, and the dependence of the superconducting transition with magnetic field, are problematic considering

a variable hydrogen content in the same phase and/or the inhomogeneous products' mixture (namely the presence of phases other than the superconducting one), which can greatly affect the resistivity [34], magnetic susceptibility [14,35], and magnetic resonance measurements [14,30]. Thus, the published values of T_c remain highly disputed [34,37–40]. Therefore, a comprehensive investigation of the reactions between yttrium and hydrogen from different initial hydrogen sources and the crystal structure determination of all individual phases after HP-HT treatment is necessary and has been carried out in the present work.

1.3. Yttrium at high pressure conditions.

Determining the crystal structure and composition of hydrides is a very complex task, since usual experimental methods, such as X-ray diffraction or optical spectroscopies, are not capable to determine the positions of hydrogen atoms. Instead, the amount of hydrogen in a metal hydride synthesized at HP is often estimated by comparing its unit cell volume with that of the metal at the same pressure. This requires information about the equation of state of the metal, and understanding of the volume changes with hydrogen content, the latter typically determined based on density functional theory (DFT) calculations.

The EoS of yttrium at pressures up to 180 GPa was published recently [41]. At ambient pressure, yttrium possesses a close-packed *hcp* structure, *hP*2-Y in Pearson's notation (space group $P6_3/mmc$), and under compression up to 100 GPa at room temperature yttrium undergoes a series of phase transitions typical for rare-earth metals, with the structures differing only in the stacking of close-packed atomic layers: *hcp* ($P6_3/mmc$, *hP*2) → *α-Sm type* (*R*-3*m*, *hR*9) → *dhcp* ($P6_3/mmc$, *hP*4) → *fcc* (*Fm*-3*m*, *cF*4) → *distorted-cF4* (*R*-3*m*, *hR*24) [41]. The sequential structural transitions are well understood with the *s-d* electronic transition model [42–44]. It should be noted that this sequence of transitions has been reported based on powder XRD data upon the compression of yttrium in the absence of a pressure transmitting medium. Interpretation of powder diffraction data is not trivial considering the coexistence of several phases due to the sluggish character of transformations at room temperature and similarities of the *hP*2, *hR*9, *hP*4, and *cF*4 structures that results in a significant overlap of diffraction peaks of different phases. The behavior of yttrium at HP-HT conditions has not been studied prior to the research described here.

1.4. By-products resulting from the synthesis of yttrium hydrides.

Complex chemical reactions, which occur upon the synthesis of hydrides at high pressures, often strongly complicate the analysis and interpretation of the results. In experiments conducted in DACs, carbon is unavoidable potential reagent/contaminant, which

can originate not only from the diamond anvils but also from hydrogen source precursors, such as paraffin oil. During laser heating, this carbon can participate in chemical reactions. In particular, it has been shown that in laser-heated DACs metal carbides appear along with metal hydrides [33,45,46]. The presence of oxygen in the reaction system is apparently related to oxygen contamination of yttrium pieces since yttrium loading was done in air, and therefore the partial oxidizing of yttrium was possible. Therefore, the observation of carbonates and other oxygen-bearing compounds is possible. In this work, several by-products were obtained, including two novel yttrium carbides, a borate, and a carbonate. Consequently, previous investigations of carbides, borates, and carbonates are briefly summarized below. The crystal chemistry of metal carbides, borates, and carbonates is of intrinsic interest and has been thoroughly investigated in this thesis.

1.4.1. Yttrium carbides.

Carbon has the capability of forming various bond states affecting the structures and properties of transition metal carbides [47]. Most metal carbides are either substitutional or interstitial solid solutions, or they form binary compounds with simple crystal structures (e.g., of a NaCl type) [48]. However, more complex carbides with covalent C-C bonds are also known.

There is a large number of metal carbides containing [C_2] dimers, for example, CaC_2, SrC_2, BaC_2, YC_2, Y_2C_3, LaC_2, La_2C_3, CeC_2, TbC_2, YbC_2, Dy_2C_3, and LuC_2 [48–53]. The C-C bond length in these carbides depends on the charge of the cation and increases proportionally with the valence of the metal [54–56]. The crystal chemistry of carbides containing triatomic [C_3] units is much more varied. The [C_3] unit is known to exist in Li_4C_3, Mg_2C_3, Me_4C_7 (*Me* = Y, Ho, Er, Tm, Lu), Sc_3C_4, and Ln_3C_4 (*Ln* = Ho - Lu) compounds [48,57–60]. The structures of Ln_3C_4 contain both [C_3] and [C_2] units, as well as isolated carbon atoms. Usually [C_3] trimers are linear $[C=C=C]^{4-}$ groups with the C-C bond length of 1.34-1.35 Å (e.g., like in Mg_2C_3), which is close to that in gaseous allene (1.335 Å) [61]. However, the [C_3] units in Sc_3C_4 and Ln_3C_4 (*Ln* = Ho – Lu) structures are not linear. Hoffmann and Meyer [62] performed a fragment molecular orbital analysis to study the bonding characteristics of the [C_3] units in Sc_3C_4 with the unusual bending (175.8°), the latter attributed to the packing arrangement. Later, more binary carbides with Me_4C_7 (*Me* = Y, Ho, Er, Tm, Lu) compositions containing similar [C_3] units, but with bending angles of 167.8° – 168.3°, were found [48,57].

High pressure alters the bonding patterns in carbides, leading to new compounds with unusual structural units and interesting properties, and as such, compression might enable

exploring the catenation of carbon. Namely, for the binary systems Mg-C [63], Ca-C [64], Y-C [65,66], and La–C [47], *ab initio* structure search predicts the formation of unusual metal carbides with exotic [C_4], [C_5] units and [C_6] rings, graphitic carbon sheets, and a number of structural transitions. Recently, the experimental observation of the CaC_2 and Ca_3C_7 with deprotonated polyacene- and *para*-poly(indenoindene)-like nanoribbons confirmed predictions of more exotic carbon polymerisation and enhanced carbon chemistry under HP-HT conditions [67]. Carbon polymerization under high pressure can drastically change the physical properties of carbides and can lead, for example, to superconductivity [68,69].

At ambient pressure, the yttrium carbides family includes a large variety of binary phases with different stoichiometry and crystal chemistry [48]: Y_2C with isolated carbon atoms; YC_2 and Y_2C_3 with [C_2] units; Y_3C_4 with [C_3] units; Y_4C_5 with both single carbon atoms and [C_2] units; Y_4C_7 with single carbon atoms and [C_3] units. For Y_4C_5, two modifications are known: low-temperature α-Y_4C_5 and high-temperature β-Y_4C_5 [70]. Whereas the crystal structure of α-Y_4C_5 was solved and refined (space group *Pbam* (#55), a = 6.5735(9) Å, b = 11.918(1) Å, c = 3.6692(5) Å) at ambient conditions [70], the structure of β-Y_4C_5 remains unknown. Under high pressure, only Y_2C_3 has been investigated [71–73]. Therefore, the carbides found as by-products of the chemical reactions in hydride synthesis were not set aside, but investigated in this work and the results become a part of this thesis.

1.4.2. Yttrium borates and carbonates.

Borates, as multifunctional optical materials, can modulate the light provided by common laser sources and have been used as nonlinear optical, and luminescent materials [74,75]. Over the past several decades, more than 4000 borates, including synthetic borates and borate minerals, have been reported [74].To date, three types of B–O units, linear [BO_2] (boron in the *sp*-hybridized state), triangular [BO_3] (boron in the sp^2-hybridized state), and tetrahedral [BO_4] (boron in the sp^3-hybridized state), have been observed in these borates [76]. While linear [BO_2] units are extremely rare [76–78], triangular [BO_3] and tetrahedral [BO_4] units are widely observed in the crystal structures of borates. The combination of corner-shared [BO_3] and [BO_4] basic units results in the rich structural chemistry of borates: isolated anionic borate clusters, or polymerization into one-dimensional chains, two-dimensional layers, or three-dimensional B-O networks [76,79–84]. The application of high pressure to borates synthesis has an immense impact on borate chemistry enriching its diversity and particularly playing an important role in the stabilization of rare borates with edge-sharing [BO_4] tetrahedra [85,86].

Currently, there are 130 known structures of anhydrous rare-earth borates in ICSD. Only for yttrium, there are a bunch of reported anhydrous borates. Besides several borates synthesized at ambient pressure, YBO_3 [87–89] and Y_3BO_6 [90] containing isolated $[B_3O_9]^{6-}$ or $[BO_3]^{3-}$ anions, several more borates $Y(BO_2)_3$ [91], α-$Y_2B_4O_9$ [92], β-$Y_2B_4O_9$ [93] and YB_7O_{12} [94] were obtained under high pressure since 2017. These high-pressure phases possess different anionic motifs: bands of BO_4 tetrahedra, as well as planar BO_3-groups in β-$Y_2B_4O_9$, ribbons of BO_4 tetrahedra in $Y(BO_2)_3$, and 3D frameworks of BO_4 tetrahedra in α-$Y_2B_4O_9$ and YB_7O_{12}.

Carbonates are important class of inorganic solids, that have been studied extensively at high pressures both from geoscience and material science perspectives [95]. The high-pressure synthesis of new carbonates enriched the list of C-O anions, including now not only the planar trigonal $[CO_3]^{2-}$ group with the sp^2-hybridized carbon, common for numerous carbonates known at ambient conditions, but also pyrocarbonate $[C_2O_5]^{4-}$ anion [96,97] and more complex sp^3-carbonates built of CO_4 tetrahedra — isolated [98–100] or connected to other tetrahedra by corner-sharing forming rings [101–103], finite [98,104] or infinite chains [105]. Rare-earth carbonates at ambient conditions are usually present as carbonate crystallohydrates, oxo- or hydroxo-carbonates. High-pressure rare-earth carbonates were previously unknown until one was discovered as a by-product in the synthesis of yttrium hydrides in the present work.

Chapter 2. Methods and instruments.

This chapter describes the main experimental methods: the generation of high pressure and temperature conditions, X-ray diffraction, and the computational approaches used in this thesis.

2.1. Generation of extreme conditions in experiments.

High-pressure high-temperature studies are of great importance for physics, chemistry, geo, and material sciences. It enables the discovery of novel materials with unexpected and previously unknown unique physical properties, as well as modelling the internal conditions of the Earth and other planetary bodies for understanding their geochemical evolution and core-mantle interactions. Pressure (P) can be expressed as $P = \frac{F}{S}$, where F is the force applied normal to the surface area and S is the area of that surface. Therefore, generating high pressures requires either decreasing the area S or increasing the force F. These concepts have been incorporated into the design of numerous high-pressure devices over the past few decades. For instance, piston-cylinder apparatuses [106] and multi-anvil presses [107] are devices primarily designed to maximize the applied force on quite large samples (~ 0.1 - 1 cm in each dimension). Conversely, reducing the area S and consequently the sample size to micrometer dimensions, as achieved with diamond anvil cell devices, has proven effective for attaining significantly higher pressures, up to 1 TPa [108,109].

2.1.1. The design and working principles of a multi-anvil press.

The standard multi-anvil apparatus can generate pressures up to ~25 GPa, while maintaining a relatively large sample (~10 mm^3 in volume). The most known design of a multi-anvil apparatus is the Kawai-type [110]. A Kawai-type multi-anvil press consists of a hydraulically driven ram that compresses two opposing guide blocks, each containing three hardened steel primary stage anvils (Fig. 2.1). These anvils are shaped to compress a cubic array of eight second-stage tungsten-carbide (WC) anvils, resulting in a so called 6-8 type multi-anvil apparatus. The interior corner of each WC cube is truncated to fit an octahedral assembly (Fig. 2.1). The smaller the size of the truncation is the higher are the pressures that one can generate. Pyrophyllite gaskets are glued along the sides of the WC-anvils truncations to enclose the high-pressure chamber where the cell assembly is placed. The sample is typically enclosed in capsules measuring a few millimeters, which are surrounded by a resistive heater made of $LaCrO_3$ or graphite cylinder furnace, surrounded by a thermally insulating ZrO_2 sleeve, and the entire assembly is placed within a MgO octahedron. The MgO octahedron serves as the pressure medium and ensures that the experiment is under hydrostatic stress. Two

disks made of either molybdenum are placed both on the top and bottom of the octahedron assembly to ensure optimal electrical connection between the resistive heater and the truncated faces of the WC cubes during the experiment.

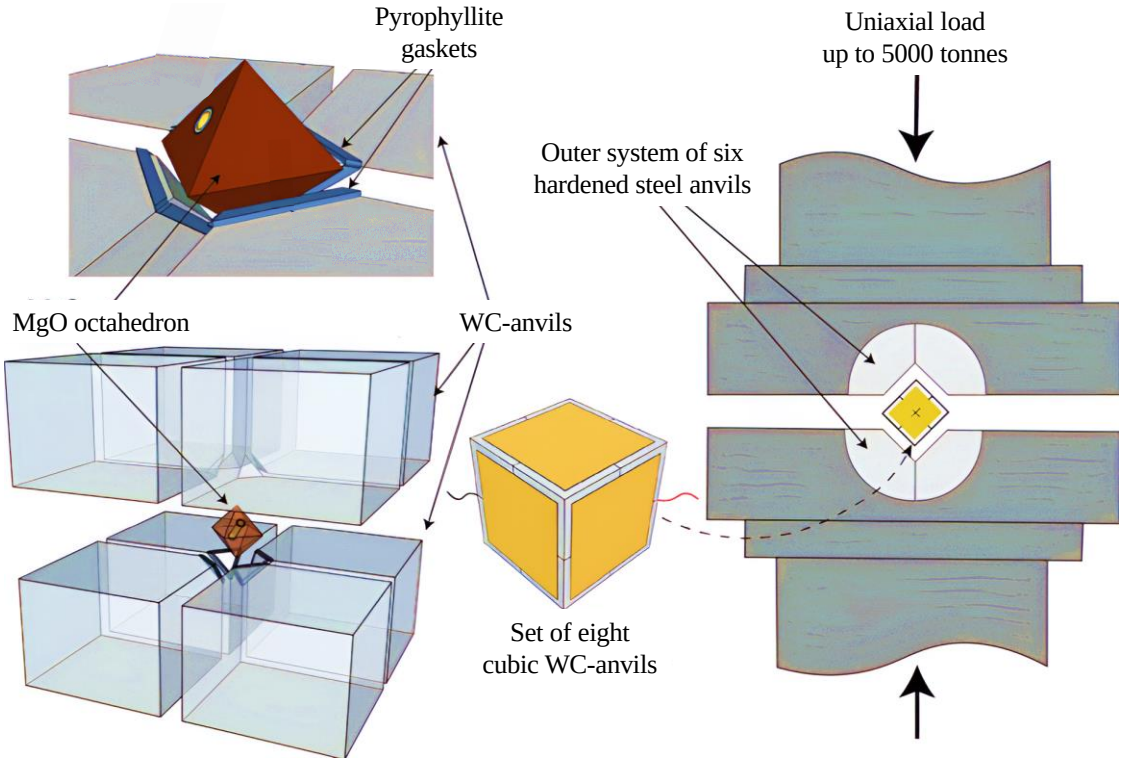

Figure 2.1. The 6-8 type multi-anvil apparatus (modified after [111]).

In this thesis, some samples were synthesized at HP-HT conditions using the multitonne multi-anvil presses at the BGI (Bayreuth, Germany) [112] at a pressure of 20 GPa and a temperature of 2000 K; synthesis times were 24 h (for more details see section 4.3). We used a standard MA assembly that included a graphite cylindrical sample capsule, a $LaCrO_3$ heater, an octahedral container, and other parts [112]. Using single-crystal XRD (SCXRD) we selected high-quality crystals from the recovered samples and used them for further investigations in diamond anvil cells.

2.1.2. The design and working principles of diamond anvil cells.

The DAC technique is the most successful method for producing high-pressure conditions. Due to the great transparency over a wide range of electromagnetic radiation and the highest thermal conductivity of diamonds among the solids known to the world, DAC is one of the most valuable tools for *in situ* studying materials under extreme conditions.

The fundamental concept of pressure generation in a diamond anvil cell involves compressing the material between the flat tips (culets) of two high-quality polished diamond anvils that are carefully driven towards each other. A typical DAC (Fig. 2.2a) consists of a metal body with a pair of hard seats, usually made of tungsten carbide. Diamond anvils are

precisely positioned on these seats, and a metallic gasket (made of chemically inert at ambient conditions metals or alloys such as rhenium, steel, or beryllium) with an indentation and a circular hole is placed between the anvils, creating a sample chamber (Fig. 2.2b-c).

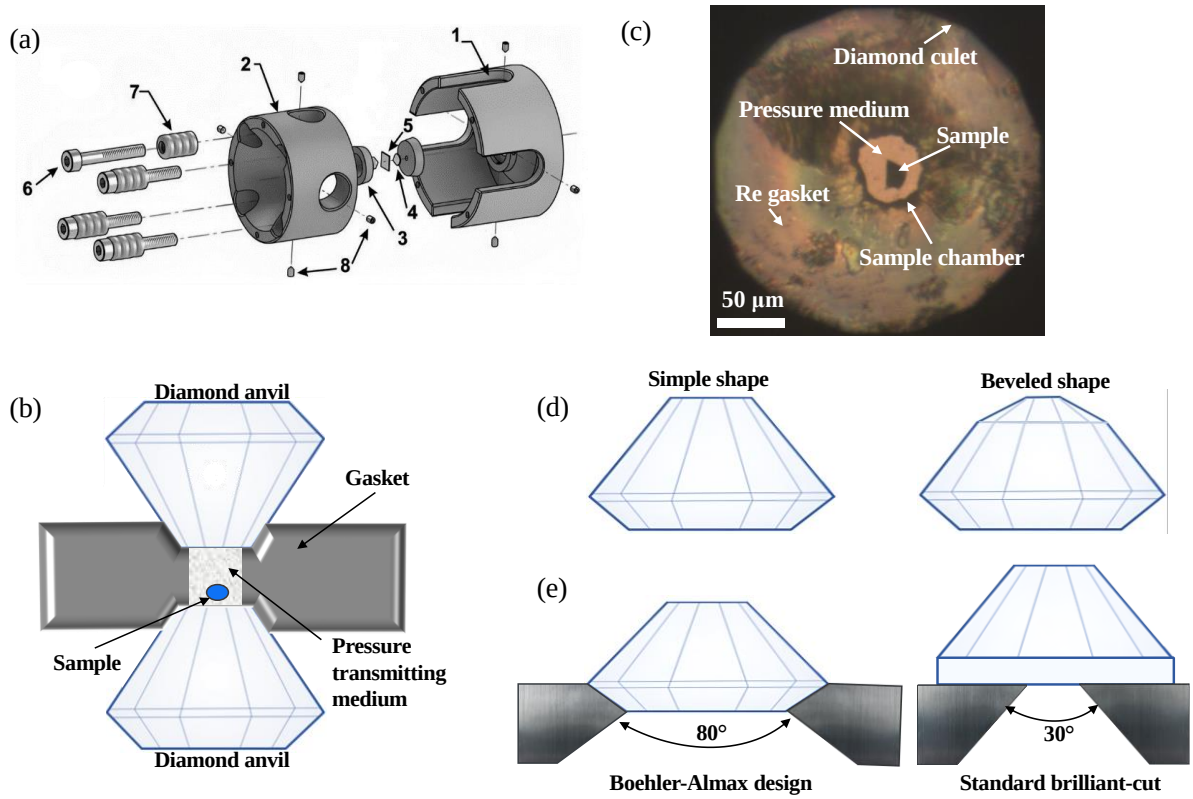

Figure 2.2. BX90-type diamond anvil cell. (a) Exploded view (modified after [113]): (1) outer cylinder part, (2) inner piston part, (3) diamond supporting plates, (4) diamond anvils, (5) metallic gasket, (6) M4 screws for generating loading force, (7) pack of conical spring washers (Belleville springs), (8) setscrews for diamond anvils alignment, (9) safety setscrews. (b) Schematic diagram of a pressure chamber. (c) A microphotograph of the DAC sample chamber was taken under an optical microscope through the diamond anvil (top view). The culet diameter is 250 µm. (d) Schematic examples of the culet shapes. Diamond anvils with culets diameter below 150 µm are usually bevelled. (e) Different types of diamond anvils and seats. Left part - standard brilliant-cut diamond and seat for spectroscopic measurements; right part - Boehler-Almax designed diamond anvil and seat for X-ray diffraction experiments.

The size of the diamond anvil culet can vary from about a millimeter to tens of micrometers (such small culets are usually beveled) (Fig. 2.2d), significantly influencing the maximum achievable pressure. However, as the culet size decreases, so does the size of the sample that can be examined. The geometric shape of the diamond cut and seat, along with the aperture of the DAC body, are critical parameters that determine the cell's suitability for specific types of experiments. For instance, in spectroscopic experiments, where the DAC remains stationary during measurements, typically standard brilliant cut anvils (Fig. 2.2e) and

flat seats are used. For experiments requiring sample rotation, such as X-ray diffraction, large aperture Boehler-Almax diamond anvils and seats are required (Fig. 2.2e).

In the current work we used specially designed BX90 cells with a large opening angle together with commercial diamonds of Boehler-Almax design [114] produced by Almax easyLab which provide the highest opening angle of 80°.

2.1.3. Pressure transmitting media.

A pressure-transmitting medium is used to isotropically transfer pressure from the compressing diamonds to the sample, providing (quasi-)hydrostatic conditions and a homogeneous pressure distribution [115]. Without this medium, a single crystal in the pressure chamber would be crushed by the contracting gasket and diamonds, since the DAC is designed for uniaxial compression. However, achieving true hydrostatic conditions above 15 GPa at ambient temperature is not possible [116], as no compounds remain in a liquid state under these conditions. To serve as proper pressure medium the solids should have low bulk and shear moduli, and tensile strength. Solid noble gases (He, Ne, Ar), and some alkali metal halides, meet these requirements. Important to note, that pressure medium not only ensure pressure distribution but also serve as pressure calibrants (e.g., Ne, Ar), or can participate in chemical reactions under extreme conditions (e.g., paraffin oil, O_2, N_2), or provide thermal insulation layers during laser heating experiments (e.g., NaCl, KCl, LiF). Gases can be loaded into the DAC sample chamber using a high-pressure gas-loading apparatus [117] or cryogenically, while solids and liquids (at atmospheric pressure) can be loaded manually.

In this work, two main pressure media were used: paraffin oil (C_nH_{2n+2}) and ammonia borane (NH_3BH_3), which also act as hydrogen-rich precursors. The use of these hydrogen sources has already been demonstrated to be an effective alternative to pure hydrogen for DAC synthesis experiments in many studies [3,5,19,21,30,31,36,46,118].

2.1.4. Pressure determination.

In diamond anvil cell experiments, accurate *in situ* pressure determination is critical. There are several common methods involving the use of various calibrants.

The first method involves using a pressure marker, a material with a well-known response to applied pressure. This marker is loaded into the DAC along with the sample and can be analyzed using various analytical techniques. For instance, one can use the pressure dependence of ruby (Cr-doped Al_2O_3) laser-induced fluorescence, measuring the positions of its particular spectral line [119,120]. As pressure increases, the intensity of the ruby fluorescence signal significantly decreases, disappearing entirely above 100 GPa. Additionally,

the presence of ruby in the DAC sample chamber may lead to chemical reactions, potentially causing contamination, especially during high-temperature experiments.

To avoid these problems one can use the pressure dependence of the first-order Raman mode of a diamond culet [121]. While less precise due to the uncertainties in laser beam focusing, this method is favored for experiments above 100 GPa or where ruby use is impractical.

The next common and most precise approach for pressure evaluation is *in situ* X-ray diffraction, where the unit cell parameters of the pressure standard are obtained. The pressure is calculated using the known equation of state (EoS) of the standard material. The EoS describes how thermodynamic variables such as volume (*V*), pressure (*P*), and temperature (*T*) are related, incorporating parameters like bulk modulus and thermal expansion. Several analytical isothermal EoS are available [122,123], with the 3rd order isothermal Birch-Murnaghan EoS [123,124] (*Equation 2.1*) being one of the most frequently used, particularly in the current thesis.

$$P = \frac{3K_0}{2}\left[\left(\frac{V_0}{V}\right)^{\frac{7}{3}} - \left(\frac{V_0}{V}\right)^{\frac{5}{3}}\right]\left\{1 - \frac{3}{4}(4 - K')\left[\left(\frac{V_0}{V}\right)^{\frac{2}{3}} - 1\right]\right\} \qquad \textit{Equation 2.1.}$$

where P is the pressure, V – volume, V0 – initial value of non-compressed compound, $K_0 = -V\left(\frac{\partial P}{\partial V}\right)_T$ – the bulk modulus, and $K' = \left(\frac{\partial K}{\partial P}\right)_T$ – its derivatives. Throughout this thesis, all EoS were established under a constant temperature of 293 K.

Typically, calibrators are chemically inert compounds with simple crystal structures and high crystal symmetry in which pressure-induced phase transitions are absent or very well known.: metals (Au, Pt, W, Mo, Re) [125–128], binary compounds (MgO, NaCl, KCl, KBr, LiF) [125,128–132], or solidified gases (Ar, Ne, He, N_2) [128,133–135].

In this study, the diamond Raman mode was employed for initial pressure estimation, while more precise determination was relied on XRD data and the EoS of Re (gasket material).

2.1.5. Generation of high temperatures through laser heating in diamond anvil cells.

Laser heating (LH) is an essential tool for *in situ* high temperature generation in DAC, enabling various studies of physical and chemical processes under extreme conditions and the synthesis of novel materials. The transparency of diamonds in a large range of energies of electromagnetic radiation and heat dissipation allows to precisely focus a high-power laser on the tiny sample, without damaging the diamond anvils. The choice of laser wavelength depends on the absorption properties of the sample. Common options include CO_2-based infrared (λ = 10.6 μm) and Nd:YAG near-infrared ($\lambda \sim 1064$ nm) lasers. The first one is suitable for heating transparent materials, whereas the second is used for non-transparent materials.

In the experiments described in this thesis a portable double-sided laser heating setup (Fig. 2.3), with the capability of in-situ temperature determination [136], was used. This setup enables heating the sample from both sides with a tightly focused Nd:YAG laser beam (5 μm at FWHM), therefore, it offers precise heating for tiny samples at very high pressure.

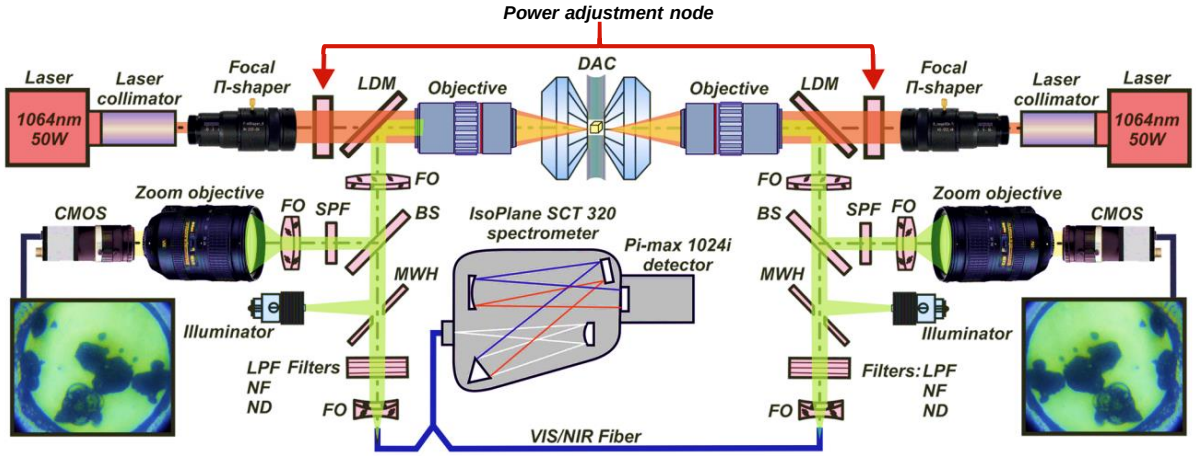

Figure 2.3. Schematic diagram of the double-sided laser heating system for diamond anvil cells. LDMs are the long-pass dichromic mirrors; FOs are the focusing optics; BSs are 50/50 beam splitters; SPFs are the short-pass filters with a cutoff at 800 nm; CMOSs are the cameras for optical observation; MWHs are the mirrors with a hole; LPFs are the long-pass filters with a cut-on wavelength of 550 nm; NFs are the notch filters at 1064 nm; and NDs are neutral density filters (modified after [136]).

2.2. X-ray diffraction.

X-ray diffraction (XRD) is a technique used to analyse the crystal structure, chemical composition, and physical properties of crystalline materials, particularly important for the study of samples in DACs.

2.2.1. Basic principles.

Atoms in a crystal form a three-dimensional lattice whose periods are comparable to the wavelength range of X-rays (0.1 – 100 Å), therefore diffraction can occur. X-ray diffraction is the interference of secondary waves in the coherent elastic scattering of X-rays, where the direction and intensity of the secondary beams depend on the wavelength and structure of the scattering. Constructive interference of rays “reflected” from two neighboring atomic planes occurs when the difference in their paths equals an integer number of the wavelength, known as the Bragg condition - $2d \cdot \sin(\theta) = n \cdot \lambda$ (Fig.2.4).

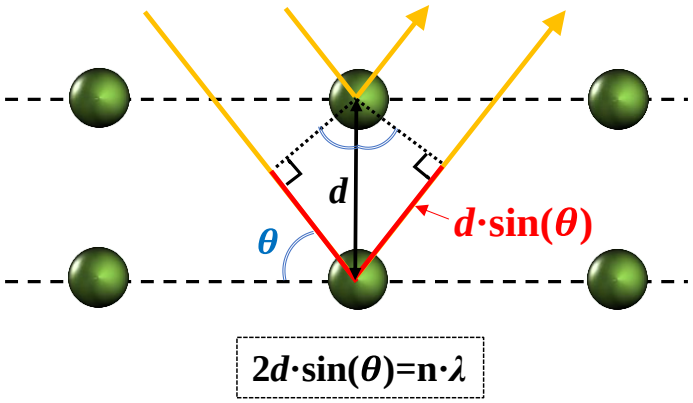

Figure 2.4. The illustration of the Bragg condition. Incident X-rays approach parallel atomic planes and diffracted X-ray beam scattered on the lower plane travels an extra length of $2d\cdot\sin(\theta)$. Constructive interference occurs when the difference in the path lengths is equal to an integer number of the wavelength. d is the spacing between diffracting crystallographic planes, θ - angle of the incident X-ray, λ - wavelength of the beam, n - integer number.

The peaks on the pattern due to constructive interference are known as Bragg reflections. The position of Bragg reflections reveals the size and shape of a unit cell. Analysing the intensities of these reflections helps reconstruct the electronic density distribution within the unit cell, which is crucial for identifying atomic positions, atom types, chemical bonds, and any crystallographic disorder.

2.2.2. Powder and single-crystal XRD.

Traditionally, X-ray diffraction (XRD) is classified into two main approaches: powder diffraction [137] and single-crystal diffraction [138]. The information that can be extracted from powder and single-crystalline samples is different.

A powder sample has many randomly oriented tiny crystallites that scatter X-rays independently. When X-rays hit a crystallite, they diffract at an angle 2θ if the Bragg condition is met. This diffraction creates a cone (an opening angle is 4θ) around the initial beam. When this cone intersects with the detector, it forms circular cross-sections known as Debye-Scherrer rings, centered on the direct beam axis (Fig. 2.5). Each ring consists of closely spaced diffraction points from individual crystallites. By determining the d-spacings of these diffraction peaks, one can identify the lattice parameters of the phase. However, this method faces challenges with new phases in the sample. In powder XRD, structure solution is nearly impossible due to the loss of intensity values of Bragg reflections.

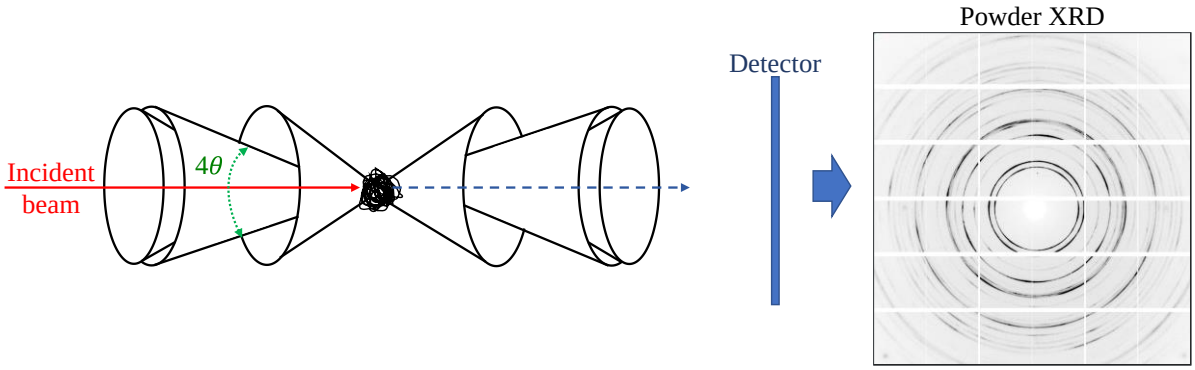

Figure 2.5. The illustration of the formation of diffraction pattern: the occurrence of Debye-Scherrer cones and an example of X-ray diffraction images produced by a powder sample (rhenium).

In contrast, single-crystal XRD is a more advanced technique for the structure solution. Single-crystal XRD patterns contain a series of diffraction spots distributed at specific positions in reciprocal space (Fig. 2.6). Since Bragg condition is satisfied only at precise θ-angles for a given d-spacing and wavelength, the crystal must be oriented in multiple directions relative to the incident beam to capture all reflections. This approach allows accurate extraction of the intensities of all measured reflections, thereby facilitating the determination of the sample's atomic structure.

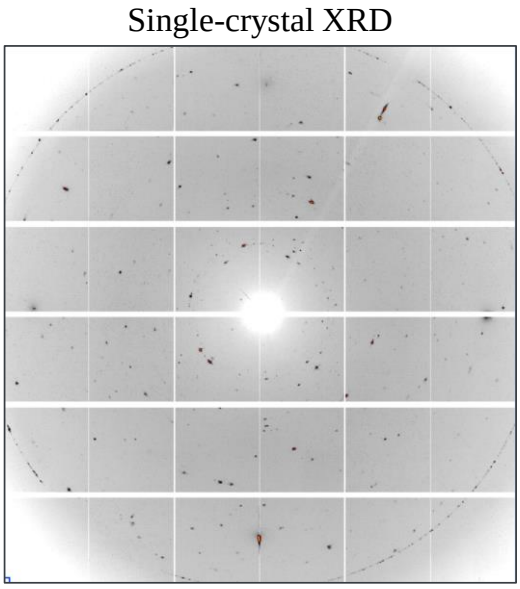

Figure 2.6. Example of X-ray diffraction images produced by a single crystal. The reflections on the pattern are the Bragg reflections from Y_4H_{25} crystal and diamond anvils.

2.3. X-ray diffraction data collection in diamond anvil cells at synchrotron facilities.

Applying XRD techniques to LH-DACs is more complex than performing routine XRD experiments under ambient conditions. Firstly, the sample environment introduces additional XRD signals: the solidified pressure-transmitting medium, the pair of diamond anvils, and the

gasket material, all of which complicate the diffraction pattern. Secondly, the metallic body of a DAC shadows over 60% of the Bragg reflections, which degrades the quality of the collected data. Thirdly, the sample size poses a challenge: for DAC experiments at pressures exceeding 50 GPa, the sample size is typically ~ 10-20 μm in each direction. Moreover, after the laser-heating procedure, the sample within the DAC may undergo decomposition and chemical reactions, potentially resulting in the formation of numerous small (even sub-micron sized) crystallites of various phases. Each of these crystallites would act as a single-crystal and give its own set of spotty Bragg's reflections. Thus, the sample in LH-DACS is usually in polycrystalline form. On the synchrotron facilities providing sufficiently small X-ray beam we can study such polycrystalline samples *in situ*, applying methods of SCXRD to individual grains of micrometer to sub-micrometer size. This, of course, demands high precision and reproducibility from the motors of the goniometer and sample stage to accurately align the sample with the X-ray beam.

The procedures of DAC's alignment, data acquisition and processing are described in the next subsections.

2.3.1. DAC alignment on a goniometer.

The sample and X-ray spot are both of an order of a few micrometres in size, requiring precise alignment based on X-ray absorption to ensure high-quality XRD data. The DAC is placed in a holder on the goniometer's sample stage, which can move the DAC in a submillimeter ranges in *y* and *z* directions perpendicular to the direction of the beam. The X-ray beam intensity through the DAC is recorded by a diode (Figure 2.7). The resulting absorption curve reflects the varying X-ray absorption of the DAC's components: tungsten carbide seats, bulk gasket, indented gasket, sample chamber, and the sample itself. If the sample has a high absorption coefficient, its position can be determined directly from the absorption curve, otherwise, the center of the sample chamber can still be aligned with the X-rays (via *y* and *z* scans) and the sample can be brought into the beam using an optical microscope.

The next critical step in SCXRD data acquisition in DACs is to align the desired sample area with the goniometer rotation axis. Since both the beam and the sample are typically a few microns in size, the sample must remain under the beam throughout the rotation during SCXRD collection. The triangulation procedure performed by scanning the sample chamber (or sample itself) along the *y*-axis at two different goniometer's angles (increasing iteratively from ±1° to ±25°) allows correcting DAC's position along the *x* direction to bring it to the rotation axis.

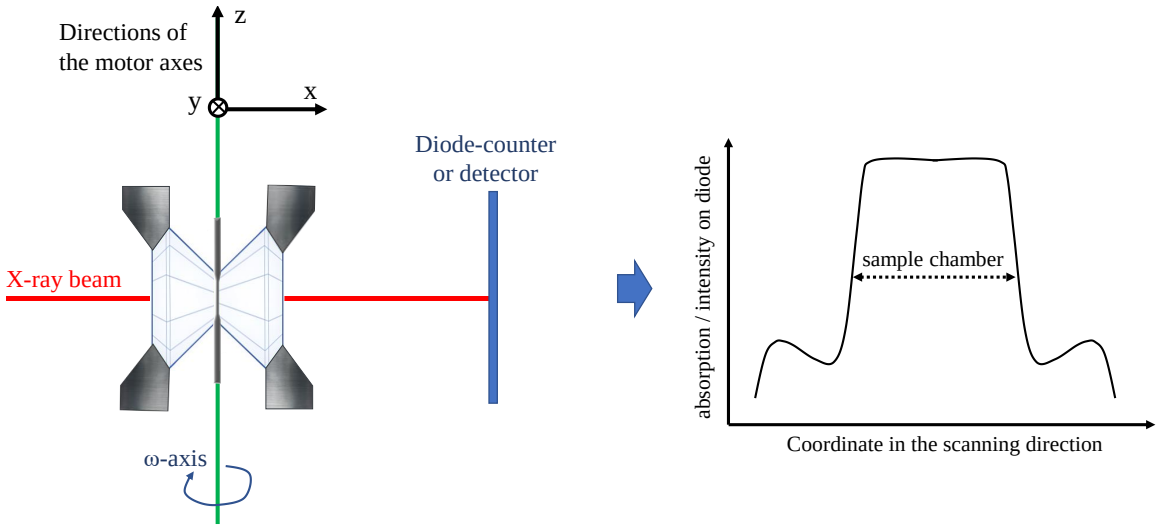

Figure 2.7. An illustration of the XRD experiment in a diamond anvil cell on synchrotron facilities: the geometry of the experiment and a schematic representation of the absorption profile acquired during the alignment procedure. Small humps on the sides of the absorption curve are caused by the deformation of diamonds and the corresponding gasket's thickness.

2.3.2. 2D X-ray maps of the DAC's sample chamber

As mentioned above, after LH of the DAC, the sample interior is often a multi-grain combination of crystallites belonging to several different phases, which may be non-homogeneously distributed within the sample chamber. In order to find the best location for the SCXRD data collection, or to obtain information on the distribution of different phases, 2D XRD maps can be collected. In this procedure, XRD images (with or without ω rotation) are collected stepwise as the DAC moves in the *y* and *z* directions with a step equal to the beam size. The number of steps should be sufficient to cover the entire sample chamber or the desired sample area. This set of images can be manually analyzed using the DIOPTAS program [139] or imported into XDI software [140], which creates contrast maps based on the intensity of selected *d*-spacing (one needs to find the unique non-overlapping peaks for each phase) and therefore allows to observe a phase distribution in the sample. Figure 2.8. shows an example of a D XRD map for a sample in the chamber of ~120 μm in diameter with diamond culet size of 250 μm. The map is built upon 3721 frames (61x61 points separated by Δ = 2 μm in each direction). The map enables also to pinpoint the location of grains (domains) of the best crystallinity for a particular phase, those giving the richest spotty pattern, thus most appropriate for SCXRD measurements.

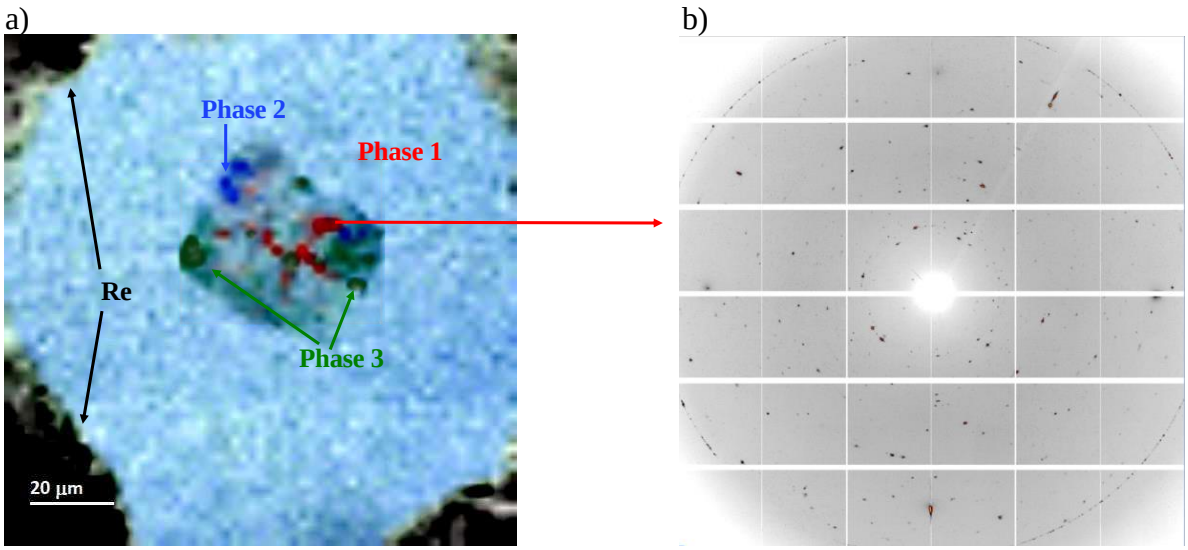

Figure 2.8. Illustration of the 2D X-ray map showing the localization of the phase distribution in the sample chamber. (a) A 2D XRD map (61x61, Δ=2 μm) of the sample chamber showing the distribution of three phases (coloured in green, red, and blue) in the DAC. (b) One frame from the SCXRD dataset taken at ω = 0° at the area of Phase 1.

2.3.3. Data processing.

Since the majority of this thesis relies on single-crystal XRD, with powder XRD serving as a supplementary method, this section will primarily focus on the data processing procedures for single-crystal XRD datasets.

Prior to any data collection powder and single-crystal calibration files must be created. The calibration file contains valuable information for the correct data processing. This information usually is the X-ray wavelength, the sample to detector distance, the x-y position of the primary beam, the pixel size of the detector, the beam polarization, as well as, corrections for the tilting of the detector. To create a calibration file for SCXRD data processing one has to collect SCXRD of a material with very well-known unit cell parameters (i.e. a standard). In this thesis, a single crystal of $(Mg_{1.93},Fe_{0.06})(Si_{1.93},Al_{0.06})O_6$ orthoenstatite (*Pbca*, *a* = 18.2391(3), *b* = 8.8117(2), *c* = 5.18320(10) Å), was used to calibrate the instrument model of the CrysAlisPro software [141]. Once the calibration is complete, the experiments with the desired samples can be started.

The SCXRD is then measured in the selected from mapping points while the DAC is rotated around the vertical goniometer axis ω with the frames being collected from ω = -36° to ω = 36° with a step of Δω = 0.5°. After the collection of the dataset for the selected point, it is analyzed in the CrysAlis^{Pro} software to identify phases and their crystal structures and chemical composition. The general procedure of the multigrain dataset analysis contains the following steps:

- **Step 1.** Perform the peak search using CrysAlis^{Pro} package.

Peak hunting involves extracting peak intensities and coordinates from the experimental diffraction frames. The software then reconstructs the positions of the peaks in reciprocal space. Figure 2.9a. shows the reciprocal space representing all reflections of the dataset for the example under consideration. These can be the reflections from reaction products, initial reagents, pressure-transmitting medium, diamonds, and gasket material.

- **Step 2.** Apply 'advanced filtering' in CrysAlis^{Pro} to get rid of diamond or other parasitic peaks and artifacts.
- **Step 3.** Find all single-crystal domains in the dataset.

Finding the initial peaks to determine the unit cell is typically challenging, particularly with laser-heated samples that contain numerous crystallites. The recently developed DAFi program [142] allows automatic the separation of SCXRD from the individual crystallites of polycrystalline samples (Figure 2.9b).

- **Step 4.** Find the lattice parameters of all domains in the dataset using the indexing procedure implemented in CrysAlis^{Pro} [141].

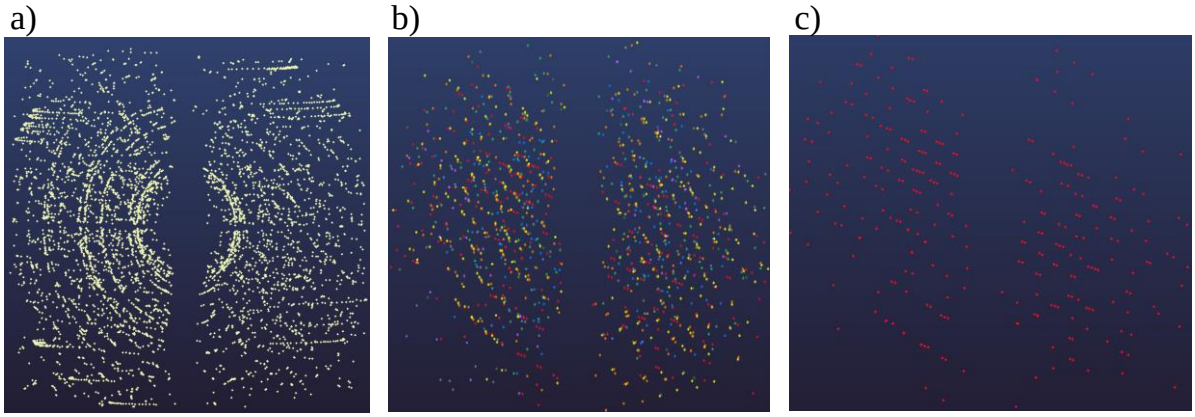

Figure 2.9. Illustration of the data analysis of the SCXRD. (a) All collected reflections of a full dataset displayed in the reciprocal space. (b) Eighteen sets of reflections from different domains found in the dataset using DAFi software. (c) Reflections of the strongest domain of the desired phase, which was chosen for integration and structure solution.

- **Step 5.** Select the most strongly diffracting domain for each found phase (Figure 2.9c.), perform integration, and extract the *.hkl* file.

For the given single-crystal domain the CrysAlis^{Pro} predicts the positions of the reflections and integrates their intensities, taking into account the reflection's shape and the background level. The software proposes a space group based on systematic absences, while the user evaluates data quality using metrics such as the frame scaling curve and confidence values provided by the program: R_σ and $F_{obs}^2/\sigma_{int}(F_{obs}^2)$ and the quality of merged intensities of symmetry-equivalent reflections represented by R_{int}. These values can be expressed as follows:

$$R_\sigma = \frac{\sum[\sigma_{int}(F^2_{obs})]}{\sum[F^2_{obs}]}$$ *Equation 2.2.*

$$\sigma_{int}(F^2_{obs}) = \sqrt{\frac{\sum[F^2_{obs} - \langle F^2_{obs}\rangle]^2}{n}}$$ *Equation 2.3.*

$$R_{int} = \frac{\sum|F^2_{obs} - \langle F^2_{obs}\rangle|}{\sum|F^2_{obs}|}$$ *Equation 2.4.*

where the sums are taken over all input reflections for which more than one symmetry equivalent is averaged, F^2_{obs} is intensity corrected for Lorentz-polarization and $\langle F^2_{obs}\rangle$ is its mean value over all measured equivalents, n is the number of redundant reflections.

If the integration quality is not satisfactory, the process can be re-run by adjusting various variables that affect the processing of detector images, such as background correction, reflection masking, integration range, and others. At the end, the software generates a file containing all *hkl* reflections with their intensities, which can then be used to solve the structure.

- **<u>Step 6.</u>** Solve and refine the crystal structure of each of the different phases found using Olex2 software [143].

The files generated in the previous step further are imported into structure solution software, in this thesis it was Olex2. During the structure solution process, the atomic positions, atom types, and thermal parameters are calculated from the intensities of collected reflections. The diffracted X-rays carry information on both the reciprocal vectors and the electronic density distribution within the sample's unit cell.

The intensities *I* of Bragg reflections are proportional to the square of the structure factor $I \sim |F_q|^2$, which is a Fourier transform of the electron density ρ of the crystal. However, the exact distribution of electron density in a crystal is unknown, so the electron density in a crystal is represented as the sum of the electron densities of atoms ρ_a. Therefore, the structure factor *F* is described as the sum of atomic scattering factors f_a, which are very well studied (Equation 2.5.). In the case of X-ray diffraction, the atomic scattering factor f_a depends on the atomic number of the element Z and scattering angle ($\sin(\theta)/\lambda$): at zero angle it is equal to Z, and as the angle increases it decreases sharply. According to the Bragg law, the vector *q* can be written as $\vec{q} = h\overrightarrow{a^*} + k\overrightarrow{b^*} + l\overrightarrow{c^*}$ (the *a**, *b**, and *c** - are the unit cell vectors in reciprocal space: (*aa**) = (*bb**) = (*cc**) = 1, (*ab**) = (*ac**) = (*ba**) = (*bc**) = (*ca**) = (*cb**) = 0. Thus, the structural factor can be expressed as:

$$F_{hkl} = \sum_j e^{-2\pi i \vec{q}\overrightarrow{r_j}} \int_V \rho_a^j(\vec{r}_a) e^{-2\pi i \vec{q}\overrightarrow{r_a}}\, d\vec{r} = \sum_j e^{-2\pi i \vec{q}\overrightarrow{r_j}} f_{a_j} = \sum_j e^{-2\pi i (hx_j + ky_j + lz_j)} f_{a_j}$$

Equation 2.5.

where the summing is carried out for the all atoms in the unit cell; *hkl* – Miller indices of a given Bragg reflection; x_j, y_j, z_j – coordinates of the *j* atom.

However, for a real crystal it is necessary to take into account corrections for the population of the position of each atom a_j and its thermal displacements t_j ($t_j = e^{-2\pi^2 U q^2} = e^{-8\pi^2 U \frac{sin^2\theta}{\lambda^2}} = e^{-B\frac{sin^2\theta}{\lambda^2}}$). Therefore, the structural factor F reflections can be written as:

$$F_{hkl} = \sum_{j=1}^{N} a_j f_{aj} e^{-B_n\left(\frac{sin\theta}{\lambda}\right)^2} e^{2\pi i(hx_j+ky_j+lz_j)} \quad \textit{Equation 2.6.}$$

where $B=8\pi^2 U$ [Å^2] is a B-factor directly related to the mean square isotropic displacement of the j^{th} atom U. It is important to note, that thermal motion is always anisotropic, because motion along an atomic bond with a change in its length is significantly less likely than motion across it. Thus, the anisotropic form of thermal oscillations can be represented by ellipsoids with six parameters: $t_{hkl} = e^{-2\pi^2(U_{11}h^2a^{*^2}+U_{22}k^2b^{*^2}+U_{33}l^2c^{*^2}+2U_{12}hka^*b^*+2U_{13}hla^*c^*+2U_{23}klb^*c^*)}$

It is important to note that the structure factor F expresses in electronic units the wave field scattered by all the atoms in the cell, so as expected for a travelling wave, it should have not only an amplitude component but also a phase component: $F = |F(q)|\cdot\exp(i\psi(q))$. Due to the high frequency of X-ray radiation the existing today detectors can only measure the time-averaged value of the energy flux (intensity I) carried by the wave, which is proportional to the amplitude. Therefore, the phase can be extracted from experiments that creates a "phase problem" [144], the main issue of the structure solution process. A process of elaboration of phases is nowadays automated; there are a number of techniques implemented in different structure solution programs: direct methods, Patterson synthesis, heavy-atom method, charge flipping, etc [145–147]. However, incomplete high-pressure datasets can decrease chances of the structure solution especially for low-symmetry structures (triclinic and monoclinic).

After evaluation of the structural factor, the electronic density distribution can be established (within the inverse Fourier transform (FT): $\rho = FT^{-1}(F_{hkl})$), completing the initial structural model. The next step involves refining the structural model against the experimental dataset using least-squares minimization. This process adjusts parameters such as atomic coordinates, occupancies, and anisotropic thermal displacement parameters.

Agreement between the model and experimental data is defined by residual R-factors, which represent the quality of the structural model:

$$R_1 = \frac{\sum||F_{obs}|-|F_{calc}||}{\sum|F_{obs}|} \quad \textit{Equation 2.7.}$$

$$wR_2 = \left[\frac{\sum w|F_{obs}^2-F_{calc}^2|}{\sum wF_{obs}^2}\right]^{\frac{1}{2}} \quad \textit{Equation 2.8.}$$

where F_{obs} – the observed structure factor amplitude, F_{calc} – the calculated structure factor amplitude based on the model; and w – weighting factor derived for each measured reflection based on its standard uncertainty.

2.4. Computational approaches. Density functional theory in solid state chemistry and physics.

Density functional theory (DFT) is a powerful computational method in modern theoretical physics, chemistry, and materials science. In the context of computational materials science, DFT calculations allow the prediction and calculation of material behavior. Due to the limitations of direct measurement of sample properties in high-pressure experiments in DACs, DFT calculations are especially important for high-pressure research because of their ability to predict and explain the properties of materials under extreme conditions. Moreover, DFT aids in solving crystal structures under high pressure, compensating for the uncertainties of high-pressure experiments and improving the reliability of structural analysis results, especially for the hydride structures where hydrogen atoms cannot be located from SCXRD data.

2.4.1. Basics of DFT approaches.

DFT is grounded in the quantum mechanical description of many-electron systems. In many-body electronic structure calculations, according to the Born–Oppenheimer approximation the nuclei can be fixed [148], generating a static external potential V_{ext}, in which the electrons are moving. The starting point for any quantum mechanical system is the time-independent Schrödinger equation for many electrons [149]:

$$\widehat{H}\Psi = \left[\hat{T} + \hat{V} + \widehat{U}\right]\Psi = \left[\sum_{i=1}^{N}\left(-\frac{\hbar^2}{2m_i}\nabla_i^2\right) + \sum_{i=1}^{N} V(r_i) + \sum_{i<j}^{N}\frac{e^2}{|r_i - r_j|}\right]\Psi = \mathrm{E}\Psi, \qquad \textit{Equation 2.9.}$$

where the first term $\hat{T}$ is the kinetic energy, $\hat{V}$ is the potential energy from the external field due to the positively charged nuclei, and $\widehat{U}$ is the electron-electron Coulomb interaction energy.

For periodic systems, Bloch's theorem [150] simplifies the treatment of electrons in a crystal lattice. It states that the wavefunctions can be expressed as:

$$\Psi_{nk}(r) = e^{ikr}u_{nk}(r), \qquad \textit{Equation 2.10.}$$

where $u_{nk}(r)$ is a function with the periodicity of the lattice, e^{ikr} is a plane wave, k is the wavevector, and n is the band index.

This form reduces the problem to solving for the periodic part $u_{nk}(r)$ within a single unit cell within the plane-wave representation of the electronic wavefunctions, greatly simplifying the calculations. The Projector-Augmented-Wave (PAW) method [151,152] is commonly used to expand the electronic wave function in plane waves.

The next step to simplify the computational complexity and the core idea of DFT is to use the electron density $\rho(r)$ rather than the many-electron wavefunction to determine the properties of a system. The electron density is a function of three spatial coordinates, whereas the wavefunction is a function of $3N$ coordinates for a system with N electrons. This

simplification is due to the Hohenberg-Kohn theorems [153], which state that the ground-state properties of a many-electron system are uniquely determined by its electron density $\rho(r)$.

Based on these theorems, Kohn and Sham developed an approach to simplify the complex many-body problem with a one-body problem within an effective potential [154]. This potential accounts for electron-electron interactions via the exchange correlation functional, ensuring that it has the same ground state density as the interacting system. Kohn-Sham equation can be written as:

$$\left[-\frac{\hbar^2}{2m_i}\nabla_i^2 + V_{\text{eff}}(r)\right]\psi_i(r) = \varepsilon_i\psi_i(r), \qquad \textit{Equation 2.11.}$$

where ε_i is the orbital energy of the corresponding Kohn–Sham orbital ψ_i, therefore, the density for an N-particle system can be written as:

$$\rho(r) = \sum_i^N |\psi_i(r)|^2, \qquad \textit{Equation 2.12.}$$

The V_{eff} is the effective potential:

$$V_{\text{eff}}(r) = V_{\text{ext}}(r) + \int \frac{\rho(r')}{|r-r'|}dr' + V_{xc}(\rho(r)), \qquad \textit{Equation 2.13.}$$

The first term in Equation 2.13. equation is the external potential due to the nuclei, the second describes the electron-electron interaction, and the third is the exchange-correlation potential.

The iterative Self-Consistent Field (SCF) method [155] is used to find the ground state and energy of a system. The SCF procedure can be described following way: (1) initial guess for the electron density $\rho(r)$ → (2) construct effective potential V_{eff} (Equation 2.13.) → (3) solve the Kohn-Sham equations to obtain the Kohn-Sham orbitals ψ_i and eigenvalues ε_i (Equation 2.11.) → (4) calculate the new electron density from the Kohn-Sham orbitals (Equation 2.12.) → (5) check if the change in density (or energy) is below a predefined convergence criteria. If the convergence is not sufficient, repeat the procedure with the updated value of $\rho(r)$.

Exchange-Correlation Functional

The exact form of the exchange-correlation functional $V_{xc}[\rho(r)]$ is unknown and must be approximated. The accuracy of energy predictions depends significantly on the choice of exchange-correlation functional. Several main approximations are known:

1. *Local Density Approximation (LDA).*

LDA [154] assumes the exchange-correlation energy per electron at an exact point depends only on the density $\rho(r)$ of a homogeneous electron gas at that point. Works well for systems with slowly varying electron density but can be less accurate for strongly correlated systems or those with rapidly varying densities. LDA often overestimates total and binding energies (resulting in shorter predicted bond lengths), and underestimates band gaps.

2. *Generalized Gradient Approximation (GGA).*

GGA [156] improves upon LDA by incorporating the gradient of the electron density, therefore, the energy is a function of both the density $\rho(\mathrm{r})$ and its gradient $\nabla\rho(\mathrm{r})$. Generally, GGA is more accurate than LDA, but can still overestimate exchange-correlation energy, and underestimate total energy (overestimate band gaps) of systems, especially those involving weak interactions such as van der Waals forces. Popular GGA functionals are PBE [157] and BLYP [158] functionals.

3. Meta-GGA.

By considering additional terms in the functional - by including higher derivatives of the density – and considering the Kohn-Sham kinetic energy it provides a more accurate description of total energy and band gaps for semiconductors. Popular meta-GGA functionals include TPSS and SCAN [159].

4. Hybrid Functionals.

Further improvement in accuracy by considering the combination of the exact Hartree-Fock exchange with GGA or LDA exchange-correlation functionals. Typically provide better accuracy for band gaps and overall energies, but can sometimes underestimate reaction energies. Examples: B3LYP [160] and HSE [161].

More complex and accurate Meta-GGA and Hybrid functionals are more time-consuming and require more computational resources than LDA and GGA. GGA strikes a good balance between accuracy and computational efficiency, making it suitable for large systems and extensive simulations. Therefore, the GGA PBE functional, proposed by Perdew–Burke–Ernzerhof [162], is the most commonly used in solid-state physics

Several DFT programs support LDA, GGA, hybrid functionals, and more advanced methods, namely Vienna Ab initio Simulation Package (VASP) [163], Quantum ESPRESSO [164], ABINIT [165], WIEN2k [166] – are widely used for materials science and solid-state physics research.

Once the ground state has been found, it is possible to calculate various physical properties, such as elastic, magnetic and optical properties, phonon and electronic band structures, densities (total DOS and partial PDOS) of states, charge density distribution, energy surface in reciprocal space (Fermi energy surface), electron localisation function (ELF), chemical reactivity and more.

2.4.2. Evaluation of physical properties using DFT calculations.

Lattice vibrational and dynamic properties.

Lattice vibrations are the oscillations of atoms around their equilibrium positions within a crystal lattice. These vibrations can be quantized into collective excitations known as phonons. Phonons significantly influence various physical properties of materials. Therefore, DFT phonon calculations provide crucial insights into the dynamic behavior of materials, which is essential for understanding and predicting material properties and stability under various conditions. The phonon band structure can be obtained through the calculation of the force constants which describe how the force on one atom changes due to the displacement of another atom. Typically, it is done using the finite displacement method or density functional perturbation theory (DFPT) [167]. In the first approach, small displacements are applied to atoms, and the resulting forces are calculated to derive the force constants. The second is a more efficient and accurate approach that calculates the response of the system to small perturbations directly within the DFT framework, but it is more time-consuming and can hardly be used for complex systems with a large number of atoms in the unit cell.

Electronic Properties Calculation

Band structure and DOS. The electronic band structure of a material describes the relationship between the energy of electrons and their wave vectors in solids. It provides critical information about the electronic properties of the material, such as its conductivity or band gap. After charge density and the potential are calculated self-consistently (SCF calculations), the electronic band structure along high-symmetry paths in the Brillouin zone can be calculated using Non-Self-Consistent Field calculation. For the DOS and PDOS calculations, an accurate integration over the whole Brillouin zone is crucial (e.g. for accurate band gap evaluation). The tetrahedron method [168] is often used to integrate the Brillouin zone. In this method, the Brillouin zone is divided into a large number of small tetrahedra, usually using a *k*-point grid, then the integrals within each tetrahedron are calculated, and the integration over the Brillouin zone is approximated by summing the contributions from each tetrahedron.

Electron Localization Function. The ELF [169] is a tool to quantify the degree and the regions of electron localization, therefore, it provides insight into chemical bonding. From the obtained Kohn-Sham orbitals, one can calculate the probability of finding an electron in a given position relative to its homogeneously distributed counterpart (homogeneous electron gas):

$$\mathrm{ELF(r)} = \left(1 + \left(\frac{D(\mathrm{r})}{D_{hom}(\mathrm{r})}\right)^2\right)^{-1} \qquad \textit{Equation 2.14.}$$

where D(r) – is the total electron localisation and D_{hom}(r) – for a homogeneous electron gas. Thus, ELF values range from 0 (delocalized electrons) to 1 (localized electrons), with 0.5 representing electron gas-like behavior. Visualization through contour plots or isosurfaces can be used for understanding bonding patterns or lone pairs.

Fermi Surface Calculation. The Fermi surface is the surface in reciprocal space that separates occupied from unoccupied electron states. The geometrical characteristics of the Fermi surfaces, such as the shape, curvature, and cross-sectional area, are related to the physical properties of metals such as electronic transport (including predictions of the superconductivity), specific heat, magnetic susceptibility, optical absorption. It can be obtained from the electronic structure calculation – one can identify the points in the Brillouin zone where the energy equals to the calculated Fermi energy (the energy difference between the highest and lowest occupied single-particle states in a quantum system). The most common software packages for visualizing Fermi surfaces, allowing analysis of its topology, are XCrySDen [170] and FermiSurfer [171].

Bader's analysis: charge and critical points calculations. Using the Bader's Quantum Theory of Atoms in Molecules [172], one can analyse the critical points of the electron density ρ (the points where $\nabla\rho = 0$) and the Bader charges for each atom [172]. This provides a framework for a better understanding of the nature of bonding interactions between atoms. The total electronic charge density, obtained from DOS DFT calculations, is partitioned into regions corresponding to individual atoms using Bader's method [172,173], which identifies critical points in the charge density gradient. Charges associated with each atom are obtained by integrating the charge density around the critical points within the atomic basins.

Thus, the DFT is a powerful and versatile tool in solid-state chemistry and physics, allowing researchers to model and predict the properties of materials from first principles. Although it has limitations, ongoing developments in functionals and computational methods continue to improve its accuracy and applicability.

In this study, the first-principles calculations were done using the framework of density functional theory as implemented in the VASP [174]. To expand the electronic wave function in plane waves we used PAW method [151,152]. The GGA PBE functional [162] was used for calculating the exchange-correlation energies. Convergence tests for energy and forces per atom were conducted for each understudied system to find the proper Monkhorst-Pack [175] *k*-point grid and an energy cutoff for the plane wave expansion. The phonon frequencies and phonon band structure calculations were performed in the harmonic approximation with non-analytical term correction (Born's correction [176,177] for semiconductor cases) with the help of PHONOPY software [178] using the finite displacement method and DFPT for proper supercell. The tetrahedron method [168] was used for Brillouin zone integration. Fermi surface visualization was made with the XCrySDen software [170]. The analysis of the critical points of the electron density ρ and Bader charges was done with the assistance of the Critic2

software [179], and the special code from Henkelman Group© [173,180], respectively, both codes are compatible with DFT output files. In our static calculations, the effect of zero-point motion and temperature was neglected. More details on the DFT calculations used in this thesis can be found in Sections 4.1 - 4.4.

Chapter 3. Thesis synopsis.

This chapter provides a short overview of the results presented in Chapter 4, that have been published or will be submitted to peer-reviewed journals. All sections are focused on the diverse high-pressure chemistry found in Y-paraffin oil and Y-NH_3BH_3 systems at different pressure ranges.

Section 4.1 is dedicated to the detailed study of the Y-paraffin oil and Y-NH_3BH_3 systems at pressures up to 50 GPa and temperatures up to 3000 K. A novel *hP*3 yttrium allotrope and its hydride with variable hydrogen content were synthesized. The synopsis of Section 4.1 is presented below in Section 3.1.

In Section 4.2 the crystal chemistry of the products of the reactions between Y and paraffin oil or Y-NH_3BH_3 in a pressure range of 87-171 GPa is discussed. It includes a description of two novel yttrium allotropes, five hydrides - Y_3H_{11}, Y_2H_9, Y_4H_{23}, $Y_{13}H_{75}$, and Y_4H_{25}, and one carbide – YC_2. The synopsis of Section 4.2 is presented below in Section 3.2.

In Section 4.3, the synthesis and structure characterization of a novel orthorhombic polymorph of yttrium carbide, γ-Y_4C_5, at pressures of ~16-50 GPa are presented. Section 4.4 focused on more complex by-products of hydride synthesis - yttrium orthocarbonate Y_3CO_4 and borate YBO_3 - obtained in the Y-NH_3BH_3 system at two pressures of 90 and 120 GPa and a temperature of 3500 K. The synopses of Sections 4.3 and 4.4 are presented in Section 3.3.

3.1. The Y-paraffin oil and Y-ammonia borane systems at pressures up to 50 GPa and temperatures up to 3000 K.

As was explained in the Introduction Chapter, for complete understanding of behavior of Y-H system above 150 GPa, where superconductive phases are expected, the systematic study of the system at moderate pressure range is mandatory. Moreover, the structure determination of the metal hydrides requires information about the equation of state of the metal, and an understanding of the volume changes with hydrogen content. In this part of the thesis, we report the results of HP-HT study of the Y-paraffin oil and Y-NH_3BH_3 at pressures up to ~50 GPa. In both investigated systems, synchrotron SCXRD reveals the formation of novel *hP*3 yttrium allotrope with the $CaHg_2$–type structure and its hydride. Additional experiments with Gd and Nd have shown that this structural type is common for rare-earth hydrides.

A novel high-pressure yttrium allotrope, *hP*3-Y (space group *P*6*/mmm*), was synthesized in a multi-anvil press at 20 GPa and 2000 K which is recoverable to ambient conditions. The SCXRD data from recovered material prove the formation of the hexagonal *hP*3-Y phase. The existence of a novel Y phase with non-close-packed structure is unexpected finding and to confirm such a result, its relative stability and electronic properties were investigated using *ab initio* calculations. The enthalpy calculations demonstrated, that *hP*3-Y allotrope is metastable at ambient conditions, but became thermodynamically preferable above 28 GPa in comparison to other yttrium allotropes. With a detailed analysis of the electronic structure of the new yttrium allotrope from DFT calculations, the stabilization of *hP*3-Y can be rationalized in terms of electronic $s \rightarrow d$ transfer, a mechanism common for lanthanides.

We have further shown that at HP-HT conditions *hP*3-Y can dissolve a significant amount of hydrogen (up to 3 hydrogen atoms per one yttrium atom) through a direct reaction of yttrium with different hydrogen-rich precursors, this may play an important role in the synthesis of potential high-T_c superconducting yttrium hydrides under higher pressures. Hydrogen content was estimated based on the difference in volume per yttrium atom in the obtained YH_x phase and yttrium metal under the same conditions. We showed that *hP*3-YH_x hydrides feature a variable hydrogen content (x = 1.4-3) depending on pressure.

To extend this study, we perform similar HP-HT experiments with Nd and Gd metals in paraffin oil. Isostructural *hP*3-(RE)H_x hydrides (RE= Nd and Gd) were obtained, which suggests that *hP*3-Y structure type may be common for other rare-earth elements. Thus, the presented results enrich the Y phase diagram and suggest that it is important to further investigations of the structural phase transitions in other RE metals and their hydrides.

3.2. The Y-paraffin oil and Y-ammonia borane systems at pressure of 87-171 GPa and temperatures up to 3500 K.

The yttrium-hydrogen system at higher pressures (above 50 GPa) has gained a special attention due to reported near-ambient temperature superconductivity in yttrium hydrides at such pressure regime. We conducted a study using synchrotron single-crystal X-ray diffraction (SCXRD) at 87-171 GPa, resulting in the discovery of known (two YH_3 phases) and five new yttrium hydrides (Fig. 3.1). These were synthesized in diamond anvil cells by laser heating yttrium with hydrogen-rich precursors — ammonia borane or paraffin oil. The arrangements of yttrium atoms in the crystal structures of new phases were determined based on SCXRD, and the hydrogen content estimations based on empirical relations and *ab initio* calculations revealed the following compounds: Y_3H_{11}, Y_2H_9, Y_4H_{23}, $Y_{13}H_{75}$, and Y_4H_{25}. The study also uncovered a carbide (YC_2) and two yttrium allotropes (see Sections 4.3 and 4.4).

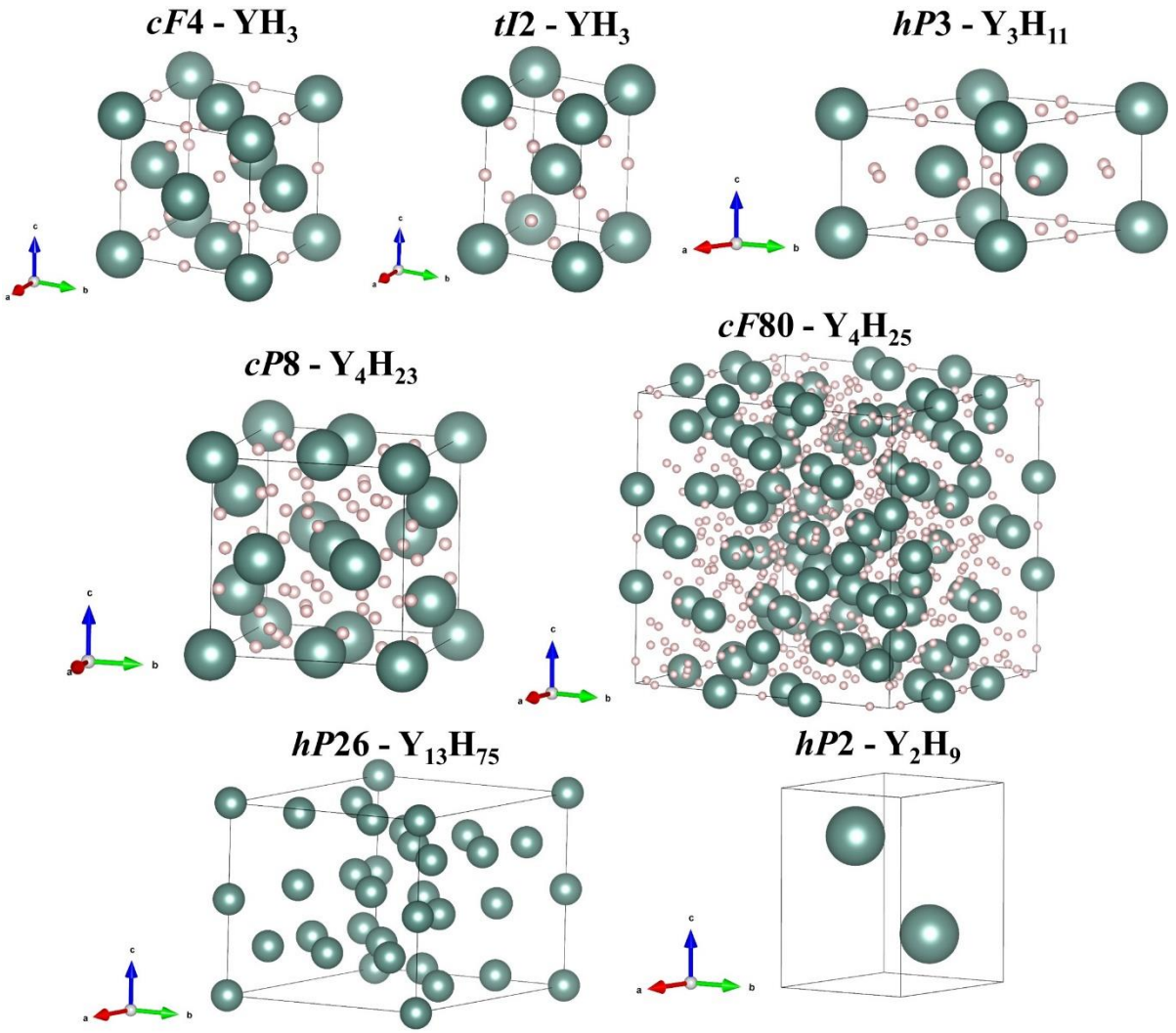

Figure 3.1. The crystal structures of the yttrium hydrides synthesized in this work [45]. Yttrium and hydrogen atoms are shown in green and light pink, respectively. For Y_2H_9 and $Y_{13}H_{75}$, only the Y metal framework is shown.

Novel yttrium allotropes, hexagonal *hP*3-Y-II ($P\bar{6}m2$) and tetragonal *tI*2-Y (*I*4/*mcm*), were obtained at 120 GPa and 138 GPa after laser heating Y in paraffin oil, respectively. The crystal structure of *tI*8-Y is quite unusual, especially for material synthesized at very high pressures, it is isostructural to the host sublattice of the incommensurate Bi-III phase. Moreover, such an arrangement of Y atoms was predicted for the host sublattice of a hypothetical host-guest structure of yttrium.

The previously known cubic *cF*4-YH_3 and tetragonal *tI*2-YH_3 yttrium hydrides were obtained simultaneously after sample laser-heating, regardless of the hydrogen precursor – paraffin oil or NH_3BH_3, at five different pressures: 87, 90, 100, 116, and 120 GPa. The *tI*2 phase obtained from ammonia borane has a larger atomic volume and is thus expected to have the $YH_{3+\delta}$ composition.

Five novel Y-H phases with a so far unknown arrangement of yttrium atoms were revealed by SCXRD data analysis. To search for possible hydrogen positions in hydride structures, we have proposed our original approach involving the use of Endeavour™ software and DFT calculations. Below a summary of the phases' composition and synthesis conditions is given:

- *hP*3-Y-I based hydride (which was discussed above in Section 3.1) were synthesized by the reaction between Y and paraffin oil at 87 GPa and between Y and ammonia borane at both 90 GPa and 120 GPa. In this study, the estimated stoichiometry at all experimental pressures is Y_3H_{11} = $YH_{3.77}$ (Fig. 3.1), which differs from previously published results at lower pressures.
- The *hP*2-Y_2H_9 solid was observed at 120 GPa in the cell with Y in NH_3BH_3. The same *hcp* yttrium framework was reported in *hP*2-YH_9 synthesized above 180 GPa, however, according to Retger's law approximation, in our experiment the volume per atom suggested half as less hydrogen content.
- Two $Y_{13}H_{75}$ and Y_4H_{23} compounds were found after LH yttrium in paraffin oil at 138 GPa (Fig. 3.1). For $Y_{13}H_{75}$ we weren't able to propose a reliable model for the H atoms' location in the structure. Y_4H_{23} hydride adopts the Na_4Si_{23}-type, which has previously been experimentally seen and/or theoretically predicted for the three metal hydrides M_4H_{23}, where *M* = Ba, La, Eu.
- The Y_4H_{25} compound was synthesized upon laser-heating Y and paraffin oil at 171 GPa (Fig. 3.1).

Furthermore, along with hydride phases, in our experiments at 87 and 120 GPa with paraffin oil we found a previously unknown yttrium carbide, YC_2.

This work demonstrates the complexity of the chemical processes in the Y–NH_3BH_3 and the Y–paraffin oil systems at high pressures and high temperatures. In total, seven yttrium hydrides YH_x (x=3-6.25), two novel yttrium allotropes, and one carbide YC_2 were detected and characterized using synchrotron SCXRD. The hydrogen content in the discovered hydrides was found to increase with pressure, *i.e.* from YH_3 at 87 GPa to $YH_{6.25}$ at 171 GPa. The presence of phases other than yttrium hydrides, especially compounds with metallic conductivity, can lead to a sharp drop in the electrical resistance of a sample upon low-temperature measurements and the misinterpretation of the results. Therefore, knowledge of the phase composition, crystal structures, and transport properties of individual phases is needed for unambiguous judgment on the electronic properties of complex hydride systems. Our results point out significant difficulties in producing monophase samples using paraffin oil and NH_3BH_3 precursors, which are necessary for a reliable assessment of the physical properties of materials, including superconductivity, and promote the use of SCXRD on polycrystalline samples as an essential tool for hydrides' characterization.

3.3. Hydrogen-free minor by-products found in the reaction chamber.

The carbon, originating from the diamond anvils, are capable of acting as a carbon source and participate in chemical reactions. Therefore, the formation of the carbides during synthesis in DACs cannot be excluded. Due to the possible partial oxidizing of metal pieces, the presence of oxygen in the reacting mixture is also possible. Apart from hydrogen, paraffin oil and ammonia borane also contain carbon, nitrogen, and boron, which can react with yttrium, resulting in the formation of various yttrium compounds beyond yttrium allotropes and yttrium hydrides. These unexpected byproducts may also feature a unique crystal chemistry. In this section we describe γ-Y_4C_5, which was obtained in Y-paraffin oil system at mild pressures, and ternary *oC*20-YBO_3 and $Y_3(CO_4)_2$ compounds, formed in Y-NH_3BH_3 system at higher pressure.

3.3.1. Yttrium carbide γ-Y_4C_5.

The chemical reaction of yttrium and paraffin oil at pressures of ~ 44 and 51 GPa and temperatures of ~2500°C led to the synthesis of a previously unknown polymorph of yttrium carbide, orthorhombic γ-Y_4C_5. It was characterized by synchrotron SCXRD. On decompression, diffraction lines of HP-Y_4C_5 were traced down to at least 16(2) GPa.

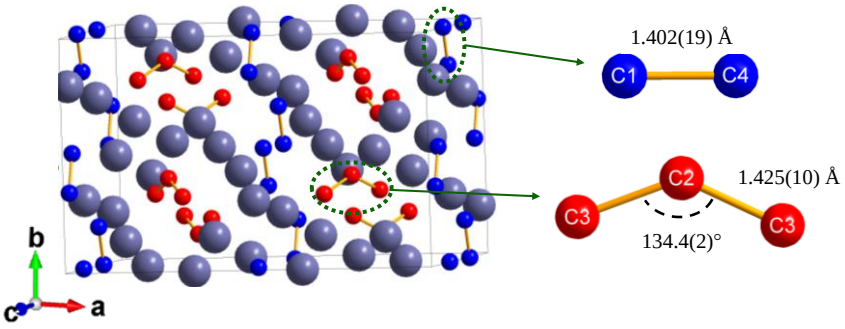

Figure 3.2. Crystal structure of Y_4C_5 at 44 GPa [33]. The grey, blue and red spheres represent yttrium and carbon atoms in dimers and trimers, respectively. The $[C_2]^{5.24-}$ and $[C_3]^{6.76-}$ species with their bond lengths and angles are indicated on the right side.

The carbon atoms in the γ-Y_4C_5 crystal structure form $[C_2]$ dumbbells and nonlinear $[C_3]$ trimers with a bending angle of 134.4(1)° (Fig. 3.2). Usually, $[C_3]$ units in known carbides are linear or almost linear with a bending angle 170-180° and which is in consistence with organic analog—allene, therefore bending angle of 134.4(1)° in γ-Y_4C_5 is indeed unique. While the first coordination sphere Y-C distances (2.24-2.69 Å) are typical for yttrium carbides—accounting for high-pressure conditions—C-C distances in the $[C_2]$ dimers (~1.40(2) Å) and the $[C_3]$ trimers (~1.43(1) Å) are unusual: they are significantly larger than expected for double-bonded carbon atoms (~1.33 Å) and much shorter than for single-bonded (~1.54 Å). Density functional theory-based charge distribution analysis revealed non-integer charges of carbon units, $[C_2]^{5.24-}$ and $[C_3]^{6.76-}$, which can be explained by the delocalization of the electrons donated by Y on the partially filled antibonding π* molecular orbitals of the $[C_2]$ and $[C_3]$ units. This specific charge distribution results in unusual C-C bond orders of 1.38 and 1.31, respectively, and a considerable previously never observed bending of the $[C_3]$ units. Density functional theory-based calculations demonstrate the metallic nature of γ-Y_4C_5. Thus, carbon polymerization under high pressure can drastically change the common arrangement of carbon atoms in metal carbides and their physical properties. In this work we have demonstrated that covalently bonded carbon species can accommodate very large non-integer formal charges. Our results extend the list of possible carbon states at extreme conditions.

3.3.2. Yttrium orthocarbonate hR39-$Y_3(CO_4)_2$.

The novel high-pressure yttrium orthocarbonate *hR*39-$Y_3(CO_4)_2$ was obtained as a minor byproduct during the high-pressure synthesis of the yttrium hydrides in one out of five laser-heated DACs reported in Section 3.2. This DAC was loaded with the yttrium (Y) pieces in between two layers of ammonia borane (NH_3BH_3), which was used as a hydrogen-rich source, as well as a pressure-transmitting media. The presence of oxygen in $Y_3(CO_4)_2$ is

apparently related to oxygen contamination of yttrium pieces since yttrium loading was done in air. $Y_3(CO_4)_2$ was observed at ~ 120 GPa and 90 GPa after laser-heating to ~ 3500 K. In the structure of $Y_3(CO_4)_2$, yttrium atoms occupy two 3*a* (Y1) and 6*c* (Y2) Wyckoff positions, oxygen atoms are located at 6*c* and 18*h* sites, while carbon atoms are located at one 6*c* Wyckoff site, similarly to Ca, O, and P atoms, respectively, in the γ-form of the $Ca_3(PO_4)_2$ structure [181]. An anionic subsystem can be considered as layers of isolated orthocarbonate CO_4 tetrahedral units. The $Y1O_{12}$ and $Y2O_{10}$ polyhedra share common faces and form a sandwich-like stacking of $Y2O_{10}$ - $Y1O_{12}$ - $Y2O_{10}$, which ends with a corner coordinated CO_4 polyhedron (Fig. 3.3a), spaced by empty octahedral sites – "voids" (marked via green circle at Fig. 3.3b). This is a first representative of rare-earth orthocarbonates.

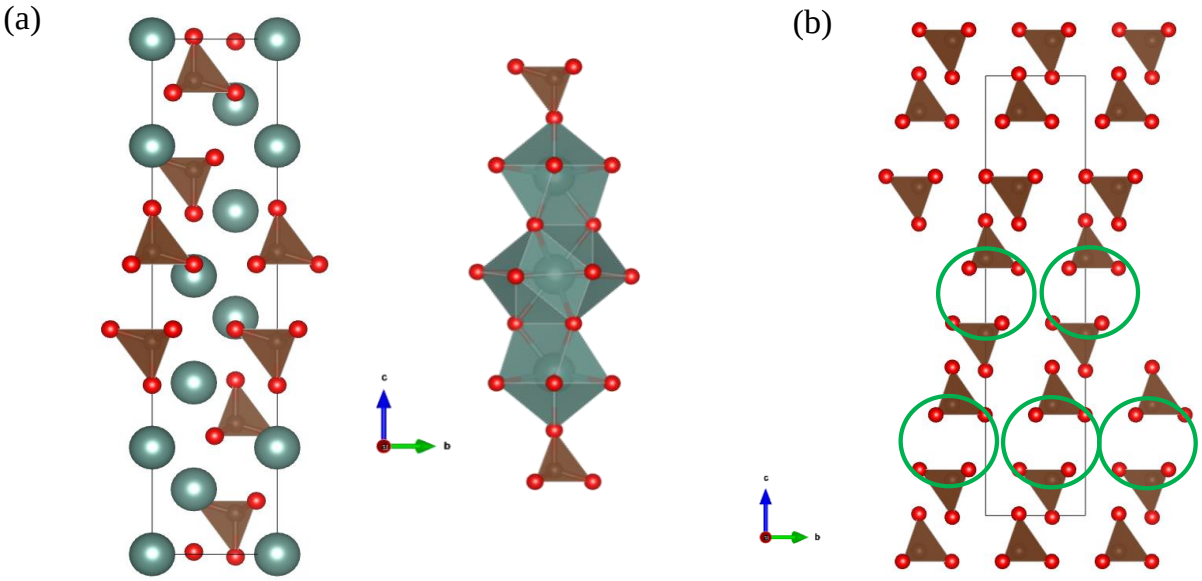

Figure 3.3. Crystal structure of $Y_3(CO_4)_2$ (a) A unit cell of the structure with the Y, C, and O atoms shown as green, brown, and red balls, respectively, along *a* direction with the illustration of the linkage scheme of polyhedral cations and surrounded oxygen atoms. (b) A unit cell along *a* direction, showing the CO_4 polyhedron and "voids" – yttrium atoms are not shown.

3.3.3. Yttrium borate oC20-YBO_3.

The high-pressure polymorph of YBO_3, *oC*20-YBO_3, was obtained in the same DAC along with discussed above *hR*39-$Y_3(CO_4)_2$ at ~ 120 GPa and 90 GPa after laser-heating to ~ 3500 K through a chemical reaction of yttrium (probably contaminated by oxygen) with ammonia borane. The *in-situ* synchrotron SCXRD enabled the crystal structure solution and refinement. In this structure (Fig. 3.4a), BO_4 tetrahedra connected via common vertices, form a complex quasi 1D anionic network – infinite zig-zag unbranched boron-oxygen chains $[-O-B(O_2)-]^{3-}$ along the *c* axis (Fig. 3.4b).

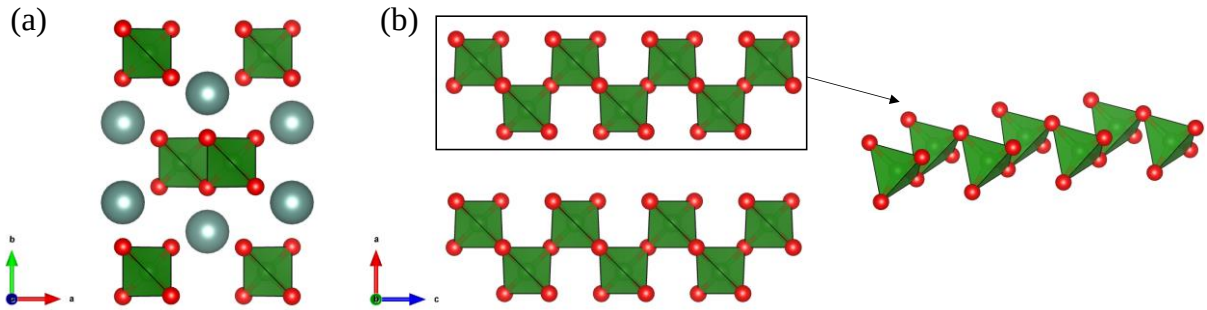

Figure 3.4. Crystal structures of *oC*20-YBO_3. (a) A unit cell of the structure with the Y, B, and O atoms shown as gray, green, and red balls, respectively, along *c* direction and (b) along *b* direction with the illustration of the unique zig-zag unbranched boron-oxygen chains (yttrium atoms are not shown).

The structure motif of unbranched chains, solely built up by one BO_4 tetrahedron as a fundamental building block, is known to borate chemistry but very scarce. Hitherto, there are no known anhydrous borates featuring 1D anionic $[BO_3]_\infty$ chains. Among oxo-hydroxoborates, there is the only one known mineral vimsite, $Ca[B_2O_2(OH)_4]$, which consists of highly protonated BO_4 chains. In $Ca[B_2O_2(OH)_4]$, the chains form sheets, which are connected by H-bonds, and Ca^{2+} cations only reside between these layers, whereas the chains in here-discovered *oC*20-YBO_3 are not linked and are surrounded by Y^{3+} cations. Therefore, anionic unbranched $[BO_3]_\infty$ chains of corner-sharing $[BO_4]$ tetrahedra found in *oC*20-YBO_3 is a unique structure motif that enrich the state-of-art borate chemistry.

To conclude, presented studies enrich chemistry of carbides, orthocarbonates, and borates. These results highlight the chemical richness and heterogeneity of reaction products in the two most common systems used for yttrium hydride synthesis, namely Y–NH_3BH_3 and the Y–paraffin oil and therefore difficulties in the targeted synthesis of high-T_c hydride phases.

3.4. List of manuscripts and statement of authors' contribution.

1) A. Aslandukova (AlA), A. Aslandukov (AnA), D. Laniel (DL), S. Khandarkhaeva (SK), G. Steinle-Neumann (GSN), T. Fedotenko (TF), S. Ovsyannikov (SO), Y. Yin (YY), F. I. Akbar (FA), K. Glazyrin (KG), M. Hanfland (MH), N. Dubrovinskaia (ND), L. Dubrovinsky (LD). High-pressure *hP*3 yttrium allotrope with $CaHg_2$-type structure as a prototype of the *hP*3 rare-earth hydride series, ***Phys. Rev. B*** **107**, 014103(8) (2023).
DOI: 10.1103/PhysRevB.107.014103.

AlA, LD, and ND designed the work. Sample and DACs preparation were done by AlA. Multi-anvil experiments were done by AlA and SO. AlA, AnA, DL, SK, TF, KG, YY, FA, GG, and MH performed the synchrotron XRD experiments. AlA and LD processed the synchrotron XRD data. AlA and GSN performed the theoretical calculations. AlA, LD, and ND contextualized the data interpretation. AlA, LD, and ND prepared the manuscript with contributions from all co-authors.

2) A. Aslandukova (AlA), A. Aslandukov (AnA), D. Laniel (DL), Y. Yin (YY), F. I. Akbar (FA), M. Bykov (MB), T. Fedotenko (TF), K. Glazyrin (KG), A. Pakhomova (AP), G. Garbarino (GG), E. L. Bright (EB), J. Wright (JW), M. Hanfland (MH), S. Chariton (SC), V. Prakapenka (VP), N. Dubrovinskaia (ND), L. Dubrovinsky (LD). Diverse high-pressure chemistry in Y–NH_3BH_3 and Y–paraffin oil systems, ***Science Advances*** **10**, 1-8 (2024).
DOI: 10.1126/sciadv.adl5416.

AlA, LD, and ND designed the work. Sample and DACs preparation were done by AlA. AlA, AnA, DL, YY, FA, MB, TF, KG, AP, GG, EB, JW, MH, SC, and VP performed the synchrotron XRD experiments. AlA and LD processed the synchrotron XRD data. AlA performed the theoretical calculations. AlA, AnA, LD, and ND contextualized the data interpretation. AlA, AnA, LD, and ND prepared the manuscript with contributions from all co-authors.

3) A. Aslandukova (AlA), A. Aslandukov (AnA), L. Yuan (LY), D. Laniel (DL), S. Khandarkhaeva (SK), T. Fedotenko (TF), G. Steinle-Neumann (GSN), K. Glazyrin (KG), N. Dubrovinskaia (ND), L. Dubrovinsky (LD). Novel High-Pressure Yttrium Carbide γ-Y_4C_5 Containing [C_2] and Nonlinear [C_3] Units with Unusually Large Formal Charges, ***Phys Rev Lett*** **127**, 135501(6) (2021).
DOI: 10.1103/PhysRevLett.127.135501

AlA, LD, and ND designed the work. Sample and DACs preparation were done by AlA and LD. AlA, AnA, DL, SK, TF, KG, and GG performed the synchrotron XRD experiments. AlA, DL, and LD processed the synchrotron XRD data. AlA, LY, and GSN performed the theoretical calculations. AlA, LD, and ND contextualized the data interpretation. AlA, LD, and ND prepared the manuscript with contributions from all co-authors.

4) A. Aslandukova (AlA), A. Aslandukov (AnA), Y. Yin (YY), M. Bykov (MB), A. Pakhomova (AP), N. Dubrovinskaia (ND), L. Dubrovinsky (LD). High-pressure yttrium borate *oC*20-YBO_3 and orthocarbonate $Y_3(CO_4)_2$ synthesized at megabar pressure range. To be submitted to Angewandte Chemie.

AlA, LD, and ND designed the work. Sample and DACs preparation were done by AlA. AlA, AnA, YY, MB, and AP performed the synchrotron XRD experiments. AlA and LD processed the synchrotron XRD data. AlA performed the theoretical calculations. AlA, LD, and ND contextualized the data interpretation. AlA, LD, and ND prepared the manuscript with contributions from all co-authors.

References

[1] D. Zhou, D. V. Semenok, D. Duan, H. Xie, W. Chen, X. Huang, X. Li, B. Liu, A. R. Oganov, and T. Cui, *Superconducting Praseodymium Superhydrides,* Sci Adv **6**, 6849 (2020).

[2] E. Snider, N. Dasenbrock-Gammon, R. McBride, X. Wang, N. Meyers, K. V. Lawler, E. Zurek, A. Salamat, and R. P. Dias, *Synthesis of Yttrium Superhydride Superconductor with a Transition Temperature up to 262 K by Catalytic Hydrogenation at High Pressures*, Phys Rev Lett **126**, 117003 (2021).

[3] M. Somayazulu, M. Ahart, A. K. Mishra, Z. M. Geballe, M. Baldini, Y. Meng, V. V. Struzhkin, and R. J. Hemley, *Evidence for Superconductivity above 260 K in Lanthanum Superhydride at Megabar Pressures*, Phys Rev Lett **122**, 27001 (2019).

[4] H. Liu, I. I. Naumov, R. Hoffmann, N. W. Ashcroft, and R. J. Hemley, *Potential High-T_c Superconducting Lanthanum and Yttrium Hydrides at High Pressure*, Proc Natl Acad Sci U S A **114**, 6990 (2017).

[5] I. A. Troyan et al., *Anomalous High-Temperature Superconductivity in YH_6*, Advanced Materials **33**, 2006832 (2021).

[6] J. Bardeen, L. N. Cooper, and J. R. Schrieffer, *Theory of Superconductivity*, Physical Review **108**, 1175 (1957).

[7] J. G. Bednorz and K. A. Muller, *Possible High T_c Superconductivity in the Ba-La-Cu-O System*, Zeitschrift Fur Physik B Condensed Matter **64**, 189 (1986).

[8] P. J. Ford and G. A. Saunders, *The Rise of the Superconductors* (CRC Press, 2004).

[9] A. Schilling, M. Cantoni, J. D. Guo, and H. R. Ott, *Superconductivity above 130 K in the Hg–Ba–Ca–Cu–O System*, Nature **363**, 56 (1993).

[10] T. W. Barbee, A. García, and M. L. Cohen, *First-Principles Prediction of High-Temperature Superconductivity in Metallic Hydrogen*, Nature **340**, 369 (1989).

[11] N. W. Ashcroft, *Metallic Hydrogen: A High-Temperature Superconductor?*, Phys Rev Lett **21**, 1748 (1968).

[12] J. A. Flores-Livas, L. Boeri, A. Sanna, G. Profeta, R. Arita, and M. Eremets, *A Perspective on Conventional High-Temperature Superconductors at High Pressure: Methods and Materials*, Phys Rep **856**, 1 (2020).

[13] I. A. Troyan, D. V. Semenok, A. G. Ivanova, A. G. Kvashnin, D. Zhou, A. V. Sadakov, O. A. Sobolevsky, V. M. Pudalov, I. S. Lyubutin, and A. R. Oganov, *High-Temperature Superconductivity in Hydrides*, Physics-Uspekhi **65**, 748 (2022).

[14] A. P. Drozdov, M. I. Eremets, I. A. Troyan, V. Ksenofontov, and S. I. Shylin, *Conventional Superconductivity at 203 Kelvin at High Pressures in the Sulfur Hydride System*, Nature **525**, 73 (2015).

[15] J. Lv, Y. Sun, H. Liu, and Y. Ma, *Theory-Orientated Discovery of High-Temperature Superconductors in Superhydrides Stabilized under High Pressure*, Matter and Radiation at Extremes **5**, (2020).

[16] A. P. Drozdov et al., *Superconductivity at 250 K in Lanthanum Hydride under High Pressures*, Nature **569**, 528 (2019).

[17] L. Ma et al., *High-Temperature Superconducting Phase in Clathrate Calcium Hydride CaH_6 up to 215 K at a Pressure of 172 GPa*, Phys Rev Lett **128**, 167001 (2022).

[18] W. Chen et al., *Synthesis of Molecular Metallic Barium Superhydride: Pseudocubic BaH_{12}*, Nat Commun **12**, 273 (2021).

[19] P. Kong et al., *Superconductivity up to 243 K in the Yttrium-Hydrogen System under High Pressure*, Nat Commun **12**, 5075 (2021).

[20] N. P. Salke et al., *Synthesis of Clathrate Cerium Superhydride CeH_9 at 80-100 GPa with Atomic Hydrogen Sublattice*, Nat Commun **10**, 4453 (2019).

[21] D. V. Semenok, A. G. Kvashnin, A. G. Ivanova, V. Svitlyk, V. Y. Fominski, A. V. Sadakov, O. A. Sobolevskiy, V. M. Pudalov, I. A. Troyan, and A. R. Oganov, *Superconductivity at 161 K in Thorium Hydride ThH_{10}: Synthesis and Properties*, Materials Today **33**, 36 (2020).
[22] I. A. Kruglov, A. G. Kvashnin, A. F. Goncharov, A. R. Oganov, S. S. Lobanov, N. Holtgrewe, S. Jiang, V. B. Prakapenka, E. Greenberg, and A. V. Yanilkin, *Uranium Polyhydrides at Moderate Pressures: Prediction, Synthesis, and Expected Superconductivity*, Sci Adv **4**, 1 (2018).
[23] N. Dasenbrock-Gammon et al., *RETRACTED ARTICLE: Evidence of near-Ambient Superconductivity in a N-Doped Lutetium Hydride*, Nature **615**, 244 (2023).
[24] D. Khatamian and F. D. Manchester, *The H−Y (Hydrogen-Yttrium) System*, Bulletin of Alloy Phase Diagrams **9**, 252 (1988).
[25] A. Machida, A. Ohmura, T. Watanuki, K. Aoki, and K. Takemura, *Long-Period Stacking Structures in Yttrium Trihydride at High Pressure*, Phys Rev B **76**, 12 (2007).
[26] A. Machida, A. Ohmura, T. Watanuki, T. Ikeda, K. Aoki, S. Nakano, and K. Takemura, *X-Ray Diffraction Investigation of the Hexagonal-Fcc Structural Transition in Yttrium Trihydride under Hydrostatic Pressure*, Solid State Commun **138**, 436 (2006).
[27] Y. Li, J. Hao, H. Liu, J. S. Tse, Y. Wang, and Y. Ma, *Pressure-Stabilized Superconductive Yttrium Hydrides*, Sci Rep **5**, 9948 (2015).
[28] D. Wang, Y. Ding, and H.-K. Mao, *Future Study of Dense Superconducting Hydrides at High Pressure*, Materials **14**, 7563 (2021).
[29] T. Meier et al., *Pressure-Induced Hydrogen-Hydrogen Interaction in Metallic FeH Revealed by NMR*, Phys Rev X **9**, 31008 (2019).
[30] T. Meier et al., *Proton Mobility in Metallic Copper Hydride from High-Pressure Nuclear Magnetic Resonance*, Phys Rev B **102**, 165109 (2020).
[31] T. Meier, A. Aslandukova, F. Trybel, D. Laniel, T. Ishii, S. Khandarkhaeva, N. Dubrovinskaia, and L. Dubrovinsky, *In Situ High-Pressure Nuclear Magnetic Resonance Crystallography in One and Two Dimensions*, Matter and Radiation at Extremes **6**, 068402 (2021).
[32] A. F. Goncharov, E. Bykova, M. Bykov, X. Zhang, Y. Wang, S. Chariton, V. B. Prakapenka, and J. S. Smith, *Synthesis and Structure of Carbon-Doped H_3S Compounds at High Pressure*, J Appl Phys **131**, 025902 (2022).
[33] A. Aslandukova, A. Aslandukov, L. Yuan, D. Laniel, S. Khandarkhaeva, T. Fedotenko, G. Steinle-Neumann, K. Glazyrin, N. Dubrovinskaia, and L. Dubrovinsky, *Novel High-Pressure Yttrium Carbide Γ−Y_4C_5 Containing $[C_2]$ and Nonlinear $[C_3]$ Units with Unusually Large Formal Charges*, Phys Rev Lett **127**, 135501 (2021).
[34] J. E. Hirsch and F. Marsiglio, *Unusual Width of the Superconducting Transition in a Hydride*, Nature **596**, E9 (2021).
[35] X. Huang et al., *High-Temperature Superconductivity in Sulfur Hydride Evidenced by Alternating-Current Magnetic Susceptibility*, Natl Sci Rev **6**, 713 (2019).
[36] T. Meier, F. Trybel, S. Khandarkhaeva, D. Laniel, T. Ishii, A. Aslandukova, N. Dubrovinskaia, L. Dubrovinsky, L. *Structural independence of hydrogen-bond symmetrisation dynamics at extreme pressure conditions*. Nat Commun **13**(1), 3042 (2022).
[37] J. E. Hirsch and F. Marsiglio, *Absence of Magnetic Evidence for Superconductivity in Hydrides under High Pressure*, Physica C: Superconductivity and Its Applications **584**, 1353866 (2021).
[38] J. E. Hirsch and F. Marsiglio, *Nonstandard Superconductivity or No Superconductivity in Hydrides under High Pressure*, Phys Rev B **103**, 134505 (2021).
[39] J. E. Hirsch and F. Marsiglio, *Clear Evidence against Superconductivity in Hydrides under High Pressure*, Matter and Radiation at Extremes **7**, 058401 (2021).

[40] N. Dasenbrock-Gammon et al., *Evidence of Near-Ambient Superconductivity in a N-Doped Lutetium Hydride*, Nature **615**, 244 (2023).
[41] E. J. Pace, S. E. Finnegan, C. V. Storm, M. Stevenson, M. I. McMahon, S. G. MacLeod, E. Plekhanov, N. Bonini, and C. Weber, *Structural Phase Transitions in Yttrium up to 183 GPa*, Phys Rev B **102**, 094104 (2020).
[42] J. C. Duthie and D. G. Pettifor, *Correlation between D-Band Occupancy and Crystal Structure in the Rare Earths*, Phys Rev Lett **38**, 564 (1977).
[43] P. P. Singh, *Electronic Structure and Electron-Phonon Interaction in Hexagonal Yttrium by Density Functional Calculations*, Phys Rev B Condens Matter Mater Phys **75**, 125101 (2007).
[44] H. Olijnyk, *Lattice Vibrations and Electronic Transitions in the Rare-Earth Metals: Yttrium, Gadolinium and Lutetium*, Journal of Physics Condensed Matter **17**, 43 (2005).
[45] A. Aslandukova et al., *Diverse High-Pressure Chemistry in Y-NH_3BH_3 and Y–Paraffin Oil Systems*, Sci Adv **10**, (2024).
[46] D. Laniel et al., *High-Pressure Synthesis of Seven Lanthanum Hydrides with a Significant Variability of Hydrogen Content*, Nat Commun **13**, 6987 (2022).
[47] C. Su, J. Zhang, G. Liu, X. Wang, H. Wang, and Y. Ma, *Catenation of Carbon in LaC_2 Predicted under High Pressure*, Physical Chemistry Chemical Physics **18**, 14286 (2016).
[48] V. Babizhetskyy, B. Kotur, V. Levytskyy, and H. Michor, *Handbook on the Physics and Chemistry of Rare Earths*, 1st ed., Vol. 52 (Elsevier B.V., 2017).
[49] Louis E. Toth, *Transition Metal Carbides and Nitrides* (1971).
[50] F. H. Spedding, K. Gschneidner, and A. H. Daane, *The Crystal Structures of Some of the Rare Earth Carbides*, J Am Chem Soc **80**, 4499 (1958).
[51] T. Sakai, G. Y. Adachi, T. Yoshida, and J. Shiokawa, *Magnetic and Electrical Properties of LaC_2, CeC_2, PrC_2, NdC_2, and SmC_2*, J Chem Phys **75**, 3027 (1981).
[52] R. E. Rundle, N. C. Baenziger, A. S. Wilson, and R. A. McDonald, *The Structures of the Carbides, Nitrides and Oxides of Uranium*, J Am Chem Soc **70**, 99 (1948).
[53] F. I. Akbar et al., *High-Pressure Synthesis of Dysprosium Carbides*, Front Chem **11**, (2023).
[54] M. Atoji, K. Gschneidner, A. H. Daane, R. E. Rundle, and F. H. Spedding, *The Structures of Lanthanum Dicarbide and Sesquicarbide by X-Ray and Neutron Diffraction*, J Am Chem Soc **80**, 1804 (1958).
[55] M. Atoji and R. C. Medrud, *Structures of Calcium Dicarbide and Uranium Dicarbide by Neutron Diffraction*, J Chem Phys **31**, 332 (1959).
[56] M. Atoji, *Neutron Diffraction Studies of CaC_2, YC_2, LaC_2, CeC_2, TbC_2, YbC_2, LuC_2, and UC_2*, J Chem Phys **35**, 1950 (1961).
[57] H. Mattausch, T. Gulden, R. K. Kremer, J. Horakh, and A. Simon, *Carbide Mit C_3^{4-}- Und C^{4-}-Ionen*, 1439 (1994).
[58] R. West, I. A. Carney, and I. C. Mineo, *The Tetralithium Derivative of Propyne and Its Use in Synthesis of Polysilicon Compounds*, J. Am. Chem. Soc. **87**, 3788 (1965).
[59] H. Fjellvág and P. Karen, *Crystal Structure of Magnesium Sesquicarbide*, Inorg Chem **31**, 3260 (1992).
[60] R. Pöttgen and W. Jeitschko, *Sc_3C_4, a Carbide with C_3 Units Derived from Propadiene*, Inorg Chem **30**, 427 (1991).
[61] M. Almenningen, A. Bastiansen, O. Trætteberg, *An Electron Diffraction Investigation of the Molecular Structure of Allene*, Acta Chem. Scand. **13**, 1699 (1959).
[62] R. Hoffmann and H. Meyer, *The Electronic Structure of Two Novel Carbides, $Ca_3Cl_2C_3$ and Sc_3C_4, Containing C_3 Units*, ZAAC - Journal of Inorganic and General Chemistry **607**, 57 (1992).

[63] T. A. Strobel, O. O. Kurakevych, D. Y. Kim, Y. Le Godec, W. Crichton, J. Guignard, N. Guignot, G. D. Cody, and A. R. Oganov, *Synthesis of β-Mg_2C_3: A Monoclinic High-Pressure Polymorph of Magnesium Sesquicarbide*, Inorg Chem **53**, 7020 (2014).
[64] Y. L. Li, S. N. Wang, A. R. Oganov, H. Gou, J. S. Smith, and T. A. Strobel, *Investigation of Exotic Stable Calcium Carbides Using Theory and Experiment*, Nat Commun **6**, 1 (2015).
[65] S. Roszak and K. Balasubramanian, *Theoretical Study of Structural and Thermodynamic Properties of Yttrium Carbides, YC_n (n = 2-6)*, Journal of Physical Chemistry **100**, 8254 (1996).
[66] X. Gao, Y. Jiang, R. Zhou, and J. Feng, *Stability and Elastic Properties of Y-C Binary Compounds Investigated by First Principles Calculations*, J Alloys Compd **587**, 819 (2014).
[67] S. Khandarkhaeva et al., *Extending Carbon Chemistry at High-Pressure by Synthesis of CaC_2 and Ca_3C_7 with Deprotonated Polyacene- and Para-Poly(Indenoindene)-like Nanoribbons*, Nat Commun **15**, 2855 (2024).
[68] M. C. Krupka, A. L. Giorgi, N. H. Krikorian, and E. G. Szklarz, *High Pressure Synthesis and Superconducting Properties of Yttrium Sesquicarbide*, Journal of The Less-Common Metals **17**, 91 (1969).
[69] C. P. Poople, *Handbook of Superconductivity* (2020).
[70] R. Czekalla, T. Hüfken, W. Jeitschko, R. D. Hoffmann, and R. Pöttgen, *The Rare Earth Carbides R_4C_5 with R=Y, Gd, Tb, Dy, and Ho*, J Solid State Chem **132**, 294 (1997).
[71] G. Amano, S. Akutagawa, T. Muranaka, Y. Zenitani, and J. Akimitsu, *Superconductivity at 18 K in Yttrium Sesquicarbide System, Y_2C_3*, J Physical Soc Japan **73**, 530 (2004).
[72] S. Akutagawa and J. Akimitsu, *Superconductivity in Y_2C_3 with Medium T_c*, Sci Technol Adv Mater **7**, 2 (2006).
[73] T. Nakane, T. Naka, H. Kito, T. Wada, A. Matsushita, H. Kumakura, and T. Mochiku, *The Effect of Pressure on the T_c Value of Y_2C_3 Compounds*, Physica C **426–431**, 492 (2005).
[74] M. Mutailipu, K. R. Poeppelmeier, and S. Pan, *Borates: A Rich Source for Optical Materials*, Chem Rev **121**, 1130 (2021).
[75] C. Chen et al., *Nonlinear Optical Borate Crystals* (Wiley, 2012).
[76] J. B. Farmer, *Metal Borates*, in (1982), pp. 187–237.
[77] C. Huang, M. Mutailipu, F. Zhang, K. J. Griffith, C. Hu, Z. Yang, J. M. Griffin, K. R. Poeppelmeier, and S. Pan, *Expanding the Chemistry of Borates with Functional $[BO_2]^-$ Anions*, Nat Commun **12**, 2597 (2021).
[78] Y. Zhang, F. Li, R. Yang, Y. Yang, F. Zhang, Z. Yang, and S. Pan, *$Rb_5Ba_2(B_{10}O_{17})_2(BO_2)$: The Formation of Unusual Functional $[BO_2]^-$ in Borates with Deep-Ultraviolet Transmission Window*, Sci China Chem **65**, 719 (2022).
[79] E.-R. Wang, J.-H. Huang, S.-J. Yu, Y.-Z. Lan, J.-W. Cheng, and G.-Y. Yang, *An Ultraviolet Nonlinear Optic Borate with 13-Ring Channels Constructed from Different Building Units*, Inorg Chem **56**, 6780 (2017).
[80] X.-Y. Li and G.-Y. Yang, *$LiB_9O_{15}·H_2O$: A Cotemplated Acentric Layer-Pillared Borate Built by Mixed Oxoboron Clusters*, Inorg Chem **60**, 16085 (2021).
[81] L. C. Pasqualini and H. Huppertz, *Expanding Transition Metal Borate Chemistry to Include Main Group Elements: High-Pressure Synthesis and Structural Relation of* β *-MgB_4O_7*, Zeitschrift Für Naturforschung B **78**, 285 (2023).
[82] D. Vitzthum, L. Bayarjargal, B. Winkler, and H. Huppertz, *Synthesis and Crystal Structure of the Acentric Indium Borate $InB_6O_9(OH)_3$*, Inorg Chem **57**, 5554 (2018).

[83] S. Guo, W. Zhang, R. Yang, M. Zhang, Z. Yang, and S. Pan, *$Pb_{2.28}Ba_{1.72}B_{10}O_{19}$ Featuring a Three-Dimensional B–O Anionic Network with Edge-Sharing [BO_4] Obtained under Ambient Pressure*, Inorg Chem Front **8**, 3716 (2021).
[84] J.-J. Li, W.-F. Chen, Y.-Z. Lan, and J.-W. Cheng, *Recent Progress in Crystalline Borates with Edge-Sharing BO_4 Tetrahedra*, Molecules **28**, 5068 (2023).
[85] H. Huppertz and B. von der Eltz, *Multianvil High-Pressure Synthesis of $Dy_4B_6O_{15}$: The First Oxoborate with Edge-Sharing BO_4 Tetrahedra*, J Am Chem Soc **124**, 9376 (2002).
[86] H. Emme and H. Huppertz, *High-Pressure Preparation, Crystal Structure, and Properties of $\alpha(RE)_2B_4O_9$ (RE=Eu, Gd, Tb, Dy): Oxoborates Displaying a New Type of Structure with Edge-Sharing BO_4 Tetrahedra*, Chemistry – A European Journal **9**, 3623 (2003).
[87] K. C. Mishra, B. G. Deboer, P. C. Schmidt, I. Osterloh, M. Stephan, V. Eyert, and K. H. Johnson, *Electronic Structures and Nature of Host Excitation in Borates*, Berichte Der Bunsengesellschaft Für Physikalische Chemie **102**, 1772 (1998).
[88] J. Lin, D. Sheptyakov, Y. Wang, and P. Allenspach, *Structures and Phase Transition of Vaterite-Type Rare Earth Orthoborates: A Neutron Diffraction Study*, Chemistry of Materials **16**, 2418 (2004).
[89] R. Turnbull, D. Errandonea, J. Á. Sans, V. P. Cuenca-Gotor, R. I. Vilaplana, J. Ibáñez, C. Popescu, A. Szczeszak, S. Lis, and F. J. Manjón, *$GdBO_3$ and YBO_3 Crystals under Compression*, J Alloys Compd **866**, 158962 (2021).
[90] J. H. Lin, S. Zhou, L. Q. Yang, G. Q. Yao, M. Z. Su, and L. P. You, *Structure and Luminescent Properties of $Y_{17.33}(BO_3)_4(B_2O_5)_2O_{16}$*, J Solid State Chem **134**, 158 (1997).
[91] M. K. Schmitt and H. Huppertz, *β-$Y(BO_2)_3$–a New Member of the β - $Ln(BO_2)_3$(Ln=Nd, Sm, Gd–Lu) Structure Family*, Zeitschrift Für Naturforschung B **72**, 983 (2017).
[92] M. K. Schmitt and H. Huppertz, *High-Pressure Synthesis and Crystal Structure of α - $Y_2B_4O_9$*, Zeitschrift Für Naturforschung B **72**, 977 (2017).
[93] Fuchs, Schröder, Heymann, Jüstel, and Huppertz, *High-Pressure Synthesis, Crystal Structure, and Photoluminescence Properties of β-$Y_2B_4O_9$:Eu^{3+}*, Inorganics (Basel) **7**, 136 (2019).
[94] B. Fuchs, M. K. Schmitt, K. Wurst, and H. Huppertz, *High-Pressure Synthesis and Crystal Structure of the Highly Condensed Yttrium Borate YB_7O_{12}*, Eur J Inorg Chem **2019**, 271 (2019).
[95] B. N. Orcutt, I. Daniel, and R. Dasgupta, *Deep Carbon* (Cambridge University Press, 2019).
[96] D. Spahr, J. König, L. Bayarjargal, V. Milman, A. Perlov, H.-P. Liermann, and B. Winkler, *$Sr[C_2O_5]$ Is an Inorganic Pyrocarbonate Salt with $[C_2O_5]^{2-}$ Complex Anions*, J Am Chem Soc **144**, 2899 (2022).
[97] D. Spahr, J. König, L. Bayarjargal, R. Luchitskaia, V. Milman, A. Perlov, H.-P. Liermann, and B. Winkler, *Synthesis and Structure of $Pb[C_2O_5]$: An Inorganic Pyrocarbonate Salt*, Inorg Chem **61**, 9855 (2022).
[98] V. Cerantola et al., *Stability of Iron-Bearing Carbonates in the Deep Earth's Interior*, Nat Commun **8**, 15960 (2017).
[99] D. Laniel et al., *Synthesis, Crystal Structure and Structure–Property Relations of Strontium Orthocarbonate, Sr_2CO_4*, Acta Crystallogr B Struct Sci Cryst Eng Mater **77**, 131 (2021).
[100] J. Binck et al., *Synthesis of Calcium Orthocarbonate, Ca_2CO^{4-} Pnma at P-T Conditions of Earth's Transition Zone and Lower Mantle*, American Mineralogist **107**, 336 (2022).
[101] J. Binck et al., *Phase Stabilities of $MgCO_3$ and $MgCO_3$-II Studied by Raman Spectroscopy, x-Ray Diffraction, and Density Functional Theory Calculations*, Phys Rev Mater **4**, 055001 (2020).

[102] S. Chariton et al., *The Crystal Structures of Fe-Bearing $MgCO_3$ Sp^2 and Sp^3 Carbonates at 98 GPa from Single-Crystal X-Ray Diffraction Using Synchrotron Radiation*, Acta Crystallogr E Crystallogr Commun **76**, 715 (2020).
[103] M. Merlini, V. Cerantola, G. D. Gatta, M. Gemmi, M. Hanfland, I. Kupenko, P. Lotti, H. Müller, and L. Zhang, *Dolomite-IV: Candidate Structure for a Carbonate in the Earth's Lower Mantle*, American Mineralogist **102**, 1763 (2017).
[104] M. Merlini, M. Hanfland, A. Salamat, S. Petitgirard, and H. Müller, *The Crystal Structures of $Mg_2Fe_2C_4O_{13}$, with Tetrahedrally Coordinated Carbon, and $Fe_{13}O_{19}$, Synthesized at Deep Mantle Conditions*, American Mineralogist **100**, 2001 (2015).
[105] S. S. Lobanov et al., *Raman Spectroscopy and X-Ray Diffraction of Sp^3 CaC_3 at Lower Mantle Pressures*, Phys Rev B **96**, 104101 (2017).
[106] F. R. Boyd and J. L. England, *Apparatus for Phase-Equilibrium Measurements at Pressures up to 50 Kilobars and Temperatures up to 1750°C*, J Geophys Res **65**, 741 (1960).
[107] N. Kawai and S. Endo, *The Generation of Ultrahigh Hydrostatic Pressures by a Split Sphere Apparatus*, Review of Scientific Instruments **41**, 1178 (1970).
[108] N. Dubrovinskaia et al., *Terapascal Static Pressure Generation with Ultrahigh Yield Strength Nanodiamond*, Sci Adv **2**, (2016).
[109] L. Dubrovinsky et al., *Materials Synthesis at Terapascal Static Pressures*, Nature **605**, 274 (2022).
[110] N. Kawai and S. Endo, *The Generation of Ultrahigh Hydrostatic Pressures by a Split Sphere Apparatus*, Review of Scientific Instruments **41**, 1178 (1970).
[111] D. C. Rubie, *Characterising the Sample Environment in Multianvil High-Pressure Experiments*, Phase Transitions **68**, 431 (1999).
[112] D. J. Frost, B. T. Poe, R. G. Trønnes, C. Liebske, A. Duba, and D. C. Rubie, *A New Large-Volume Multianvil System*, Physics of the Earth and Planetary Interiors **143**, 507 (2004).
[113] I. Kantor, V. Prakapenka, A. Kantor, P. Dera, A. Kurnosov, S. Sinogeikin, N. Dubrovinskaia, and L. Dubrovinsky, *BX90: A New Diamond Anvil Cell Design for X-Ray Diffraction and Optical Measurements*, Review of Scientific Instruments **83**, 125102 (2012).
[114] R. Boehler and K. De Hantsetters, *New Anvil Designs in Diamond-Cells*, High Press Res **24**, 391 (2004).
[115] R. Miletich, D. R. Allan, and W. F. Kuhs, *High-Pressure Single-Crystal Techniques*, Rev Mineral Geochem **41**, 445 (2000).
[116] A. Jayaraman, *Diamond Anvil Cell and High-Pressure Physical Investigations*, Rev Mod Phys **55**, 65 (1983).
[117] A. Kurnosov, I. Kantor, T. Boffa-Ballaran, S. Lindhardt, L. Dubrovinsky, A. Kuznetsov, and B. H. Zehnder, *A Novel Gas-Loading System for Mechanically Closing of Various Types of Diamond Anvil Cells*, Review of Scientific Instruments **79**, (2008).
[118] A. Aslandukova et al., *High-Pressure hP3 Yttrium Allotrope with $CaHg_2$-Type Structure as a Prototype of the hP3 Rare-Earth Hydride Series*, Phys Rev B **107**, 014103 (2023).
[119] H. K. Mao, J. Xu, and P. M. Bell, *Calibration of the Ruby Pressure Gauge to 800 Kbar under Quasi-hydrostatic Conditions*, J Geophys Res Solid Earth **91**, 4673 (1986).
[120] K. Syassen, *Ruby under Pressure*, High Press Res **28**, 75 (2008).
[121] Y. Akahama and H. Kawamura, *Pressure Calibration of Diamond Anvil Raman Gauge to 410 GPa*, J Phys Conf Ser **215**, 012195 (2010).
[122] P. Vinet, J. Ferrante, J. H. Rose, and J. R. Smith, *Compressibility of Solids*, J Geophys Res Solid Earth **92**, 9319 (1987).
[123] F. Birch, *Finite Elastic Strain of Cubic Crystals*, Physical Review **71**, 809 (1947).

[124] F. D. Murnaghan, *The Compressibility of Media under Extreme Pressures*, Proceedings of the National Academy of Sciences **30**, 244 (1944).
[125] P. I. Dorogokupets and A. Dewaele, *Equations of State of MgO, Au, Pt, NaCl-B1, and NaCl-B2: Internally Consistent High-Temperature Pressure Scales*, High Press Res **27**, 431 (2007).
[126] A. Dewaele, M. Torrent, P. Loubeyre, and M. Mezouar, *Compression Curves of Transition Metals in the Mbar Range: Experiments and Projector Augmented-Wave Calculations*, Phys Rev B **78**, 104102 (2008).
[127] Y. Fei, A. Ricolleau, M. Frank, K. Mibe, G. Shen, and V. Prakapenka, *Toward an Internally Consistent Pressure Scale*, Proceedings of the National Academy of Sciences **104**, 9182 (2007).
[128] S. M. Dorfman, V. B. Prakapenka, Y. Meng, and T. S. Duffy, *Intercomparison of Pressure Standards (Au, Pt, Mo, MgO, NaCl and Ne) to 2.5 Mbar*, J Geophys Res Solid Earth **117**, (2012).
[129] A. Dewaele, *Equations of State of Simple Solids (Including Pb, NaCl and LiF) Compressed in Helium or Neon in the Mbar Range*, Minerals **9**, 684 (2019).
[130] S. Tateno, T. Komabayashi, K. Hirose, N. Hirao, and Y. Ohishi, *Static Compression of B2 KCl to 230 GPa and Its P-V-T Equation of State*, American Mineralogist **104**, 718 (2019).
[131] T. Sakai, E. Ohtani, N. Hirao, and Y. Ohishi, *Equation of State of the NaCl-B2 Phase up to 304 GPa*, J Appl Phys **109**, (2011).
[132] A. Dewaele, A. B. Belonoshko, G. Garbarino, F. Occelli, P. Bouvier, M. Hanfland, and M. Mezouar, *High-Pressure–High-Temperature Equation of State of KCl and KBr*, Phys Rev B **85**, 214105 (2012).
[133] Y. Ye, S.-H. Shim, V. Prakapenka, and Y. Meng, *Equation of State of Solid Ne Inter-Calibrated with the MgO, Au, Pt, NaCl-B2, and Ruby Pressure Scales up to 130 GPa*, High Press Res **38**, 377 (2018).
[134] M. Ross, H. K. Mao, P. M. Bell, and J. A. Xu, *The Equation of State of Dense Argon: A Comparison of Shock and Static Studies*, J Chem Phys **85**, 1028 (1986).
[135] A. Dewaele, F. Datchi, P. Loubeyre, and M. Mezouar, *High Pressure–High Temperature Equations of State of Neon and Diamond*, Phys Rev B **77**, 094106 (2008).
[136] T. Fedotenko et al., *Laser Heating Setup for Diamond Anvil Cells for in Situ Synchrotron and in House High and Ultra-High Pressure Studies*, Review of Scientific Instruments **90**, 104501 (2019).
[137] R. E. Dinnebier and S. L. Billinge, *Powder Diffraction: Theory and Practice* (Royal Society of Chemistry, Cambridge, 2008).
[138] G. Fetisov, *Synchrotron Radiation. Methods for Substance Structure Investigation*, Moscow, FIZMATLIT (2007).
[139] C. Prescher and V. B. Prakapenka, *DIOPTAS: A Program for Reduction of Two-Dimensional X-Ray Diffraction Data and Data Exploration*, High Press Res **35**, 223 (2015).
[140] R. Hrubiak, J. S. Smith, and G. Shen, *Multimode Scanning X-Ray Diffraction Microscopy for Diamond Anvil Cell Experiments*, Review of Scientific Instruments **90**, (2019).
[141] CrysAlisPRO. Rigaku Oxford Diffraction. Agilent Technologies UK Ltd, Yarnton, England. *https://www.rigaku.com/products/ crystallography/crysalis* (2015).
[142] A. Aslandukov, M. Aslandukov, N. Dubrovinskaia, and L. Dubrovinsky, *Domain Auto Finder(DAFi) Program: The Analysis of Single-Crystal X-Ray Diffraction Data from Polycrystalline Samples*, J Appl Crystallogr **55**, 1383 (2022).

[143] O. V. Dolomanov, L. J. Bourhis, R. J. Gildea, J. A. K. Howard, and H. Puschmann, *OLEX2: A Complete Structure Solution, Refinement and Analysis Program*, J Appl Crystallogr **42**, 339 (2009).
[144] G. Taylor, *The Phase Problem*, Acta Crystallogr D Biol Crystallogr **59**, 1881 (2003).
[145] G. M. Sheldrick, *SHELXT – Integrated Space-Group and Crystal-Structure Determination*, Acta Crystallogr A Found Adv **71**, 3 (2015).
[146] G. M. Sheldrick, *Crystal Structure Refinement with SHELXL*, Acta Crystallogr C Struct Chem **71**, 3 (2015).
[147] K. Cowtan, *Phase Problem in X-ray Crystallography, and Its Solution*, in *Encyclopedia of Life Sciences* (Wiley, 2003).
[148] M. Born and R. Oppenheimer, *Zur Quantentheorie Der Molekeln*, Ann Phys **389**, 457 (1927).
[149] E. Schrödinger, *An Undulatory Theory of the Mechanics of Atoms and Molecules*, Physical Review **28**, 1049 (1926).
[150] F. Bloch, *Ber Die Quantenmechanik Der Elektronen in Kristallgittern*, Zeitschrift Fur Physik **52**, 555 (1929).
[151] P. E. Blöchl, *Projector Augmented-Wave Method*, Phys Rev B **50**, 17953 (1994).
[152] G. Kresse and D. Joubert, *From Ultrasoft Pseudopotentials to the Projector Augmented-Wave Method*, Phys Rev B **59**, 1758 (1999).
[153] P. Hohenberg and W. Kohn, *Inhomogeneous Electron Gas*, Physical Review **136**, B864 (1964).
[154] W. Kohn and L. J. Sham, *Self-Consistent Equations Including Exchange and Correlation Effects*, Physical Review **140**, A1133 (1965).
[155] F. Finocchi, *Density Functional Theory for Beginners Basic Principles and Practical Approaches* (2011).
[156] D. C. Langreth and M. J. Mehl, *Beyond the Local-Density Approximation in Calculations of Ground-State Electronic Properties*, Phys Rev B **28**, 1809 (1983).
[157] J. P. Perdew, K. Burke, and M. Ernzerhof, *Generalized Gradient Approximation Made Simple*, Phys Rev Lett **77**, 3865 (1996).
[158] A. D. Becke, *Density-Functional Thermochemistry. III. The Role of Exact Exchange*, J Chem Phys **98**, 5648 (1993).
[159] J. Tao, J. P. Perdew, V. N. Staroverov, and G. E. Scuseria, *Climbing the Density Functional Ladder: Nonempirical Meta–Generalized Gradient Approximation Designed for Molecules and Solids*, Phys Rev Lett **91**, 146401 (2003).
[160] A. D. Becke, *Density-Functional Exchange-Energy Approximation with Correct Asymptotic Behavior*, Phys Rev A **38**, 3098 (1988).
[161] J. Heyd, G. E. Scuseria, and M. Ernzerhof, *Hybrid Functionals Based on a Screened Coulomb Potential*, J Chem Phys **118**, 8207 (2003).
[162] J. P. Perdew, K. Burke, and M. Ernzerhof, *Generalized Gradient Approximation Made Simple*, Phys Rev Lett **77**, 3865 (1996).
[163] G. Kresse and J. Hafner, *Ab Initio Molecular Dynamics for Liquid Metals*, Phys Rev B **47**, 558 (1993).
[164] P. Giannozzi et al., *QUANTUM ESPRESSO: A Modular and Open-Source Software Project for Quantum Simulations of Materials*, Journal of Physics: Condensed Matter **21**, 395502 (2009).
[165] X. Gonze et al., *First-Principles Computation of Material Properties: The ABINIT Software Project*, Comput Mater Sci **25**, 478 (2002).
[166] P. Blaha, K. Schwarz, F. Tran, R. Laskowski, G. K. H. Madsen, and L. D. Marks, *WIEN2k: An APW+lo Program for Calculating the Properties of Solids*, J Chem Phys **152**, (2020).

[167] A. Togo and I. Tanaka, *First Principles Phonon Calculations in Materials Science*, Scr Mater **108**, 1 (2015).
[168] P. E. Blöchl, O. Jepsen, and O. K. Andersen, *Improved Tetrahedron Method for Brillouin-Zone Integrations*, Phys Rev B **49**, 16223 (1994).
[169] A. D. Becke and K. E. Edgecombe, *A Simple Measure of Electron Localization in Atomic and Molecular Systems*, J Chem Phys **92**, 5397 (1990).
[170] A. Kokalj, *XCrySDen-a New Program for Displaying Crystalline Structures and Electron Densities*, J Mol Graph Model **17**, 176 (1999).
[171] M. Kawamura, *FermiSurfer: Fermi-Surface Viewer Providing Multiple Representation Schemes*, Comput Phys Commun **239**, 197 (2019).
[172] Bader R. F. W., *Atoms in Molecules: A Quantum Theory*, Vol. 22 (Oxford University Press 1990).
[173] M. Yu and D. R. Trinkle, *Accurate and Efficient Algorithm for Bader Charge Integration*, J Chem Phys **134**, (2011).
[174] G. Kresse and J. Furthmüller, *Efficiency of Ab-Initio Total Energy Calculations for Metals and Semiconductors Using a Plane-Wave Basis Set*, Comput Mater Sci **6**, 15 (1996).
[175] Hendrik J. Monkhorst and James D. Pack, *Special Points for Brillonin-Zone Integrations*, Phys Rev B **13**, 5188 (1976).
[176] R. M. Pick, M. H. Cohen, and R. M. Martin, *Microscopic Theory of Force Constants in the Adiabatic Approximation*, Phys Rev B **1**, 910 (1970).
[177] M. Born and K. Huang, *Dynamical Theory of Crystal Lattices* (1954).
[178] A. Togo and I. Tanaka, *First Principles Phonon Calculations in Materials Science*, Scr Mater **108**, 1 (2015).
[179] A. Otero-de-la-Roza, E. R. Johnson, and V. Luaña, *Critic2: A Program for Real-Space Analysis of Quantum Chemical Interactions in Solids*, Comput Phys Commun **185**, 1007 (2014).
[180] W. Tang, E. Sanville, and G. Henkelman, *A Grid-Based Bader Analysis Algorithm without Lattice Bias*, Journal of Physics: Condensed Matter **21**, 084204 (2009).
[181] R. M. Thompson, X. Xie, S. Zhai, R. T. Downs, and H. Yang, *A Comparison of the $Ca_3(PO_4)_2$ and $CaSiO_3$ Systems, with a New Structure Refinement of Tuite Synthesized at 15 GPa and 1300 C*, American Mineralogist **98**, 1585 (2013).

Chapter 4. Manuscripts of the thesis.

4.1. High-pressure *hP*3 yttrium allotrope with $CaHg_2$-type structure as a prototype of the *hP*3 rare-earth hydride series.

This section contains the following manuscript and the related supplementary material:

"High-pressure *hP*3 yttrium allotrope with $CaHg_2$-type structure as a prototype of the *hP*3 rare-earth hydride series"

A. Aslandukova, A. Aslandukov, D. Laniel, S. Khandarkhaeva, G. Steinle-Neumann, T. Fedotenko, S.V. Ovsyannikov, Y. Yin, F.I. Akbar, K. Glazyrin, M. Hanfland, N. Dubrovinskaia & L. Dubrovinsky

Status: published in *Physical Review B*, 107, 014103 (2023)

High-pressure *hP*3 yttrium allotrope with $CaHg_2$-type structure as a prototype of the *hP*3 rare-earth hydride series

Alena Aslandukova,[1,*] Andrey Aslandukov,[1,2] Dominique Laniel,[3] Saiana Khandarkhaeva,[2] Gerd Steinle-Neumann,[1] Timofey Fedotenko,[4] Sergey V. Ovsyannikov,[1] Yuqing Yin,[2,5] Fariia Iasmin Akbar,[1] Konstantin Glazyrin,[4] Michael Hanfland,[6] Leonid Dubrovinsky,[1] and Natalia Dubrovinskaia[2,7]

[1]*Bavarian Research Institute of Experimental Geochemistry and Geophysics (BGI), University of Bayreuth, Universitaetsstrasse 30, 95440 Bayreuth, Germany*

[2]*Material Physics and Technology at Extreme Conditions, Laboratory of Crystallography, University of Bayreuth, 95440 Bayreuth, Germany*

[3]*Centre for Science at Extreme Conditions and School of Physics and Astronomy, University of Edinburgh, Edinburgh EH93FD, United Kingdom*

[4]*Deutsches Elektronen-Synchrotron DESY, Notkestr. 85, 22607 Hamburg, Germany*

[5]*State Key Laboratory of Crystal Materials, Shandong University, Jinan 250100, China*

[6]*European Synchrotron Radiation Facility (ESRF), BP 220, 38043 Grenoble Cedex, France*

[7]*Department of Physics, Chemistry and Biology (IFM), Linköping University, SE-581 83 Linköping, Sweden*

(Received 28 September 2022; revised 7 December 2022; accepted 9 December 2022; published 9 January 2023)

A high-pressure (HP) yttrium allotrope, *hP*3-Y (space group $P6/mmm$), was synthesized in a multi-anvil press at 20 GPa and 2000 K which is recoverable to ambient conditions. Its relative stability and electronic properties were investigated using density functional theory calculations. A *hP*3-Y derivative hydride, *hP*3-YHx, with a variable hydrogen content ($x = 2.8$, 3, 2.4), was synthesized in diamond anvil cells by the direct reaction of yttrium with paraffin oil, hydrogen gas, and ammonia borane upon laser heating to ∼3000 K at 51, 45 and 38 GPa, respectively. Room-temperature decompression leads to gradual reduction and eventually the complete loss of hydrogen at ambient conditions. Isostructural *hP*3-NdHx and *hP*3-GdHx hydrides were synthesized from Nd and Gd metals and paraffin oil, suggesting that the *hP*3-Y structure type may be common for rare-earth elements. Our results expand the list of allotropes of trivalent lanthanides and their hydrides and suggest that they should be considered in the context of studies of HP behavior and properties of this broad class of materials.

DOI: 10.1103/PhysRevB.107.014103

I. INTRODUCTION

The study of rare-earth (RE) metal hydrides is one of the most interesting research topics in current solid-state physics due to the search for high-T_C superconductivity, as key advances in experimental techniques lead to the synthesis of hydrides at high pressure (HP) that were then reported to become high-T_C superconductors [1]. Recent publications on record high-T_C superconductivity in LaH_{10} at 250–260 K [2,3] and HP–high-temperature (HT) synthesis of CeH_9 [4], UH_7, UH_8 [5], ThH_{10} [6], as well as a series of yttrium hydrides (YH_9, YH_6, YH_4) [7–9] motivated us to study the Y-H system at HP. The reason is that there are still many open questions regarding, for example, the origin of the superconducting effect and the structure (or chemical composition) of the materials for which the phenomenon is described [10–12]. Some problems with the currently available experimental data interpretation may be associated with the synthesis technique: hydrides at HP are often obtained by heating metals embedded in paraffin oil or ammonia borane [3,6–8,13–15], and one cannot exclude that other nonhydride phases (e.g., carbon and boron compounds) may form in the system under investigation [16,17], and their properties can influence the measurements of superconductivity.

Determining the crystal structure and composition of hydrides is a very complex task since usual experimental methods such as x-ray diffraction (XRD) are not capable of determining the positions of hydrogen atoms. Instead, the amount of hydrogen in a metal hydride synthesized at HP is often estimated by comparing its unit cell volume with that of the metal at the same pressure. This requires information about the equation of state (EoS) of the metal and an understanding of the volume changes with hydrogen content, the latter typically determined by using density functional theory (DFT) calculations.

The EoS of yttrium at pressures up to 180 GPa was published recently [18]. At ambient pressure, yttrium possesses a hexagonal close-packed (hcp) structure, *hP*2-Y in Pearson's notation (space group $P6_3/mmc$). Under compression up to 100 GPa at room temperature, yttrium undergoes a series of phase transitions typical for RE metals, with the structures differing only in the stacking of close-packed atomic layers: hcp ($P6_3/mmc$, *hP*2) → α-Sm type ($R\text{-}3m$, *hR*9) → double hcp (dhcp; $P6_3/mmc$, *hP*4) → face-centered cubic (fcc; $Fm\text{-}3m$, *cF*4) → distorted-*cF*4 ($R\text{-}3m$, *hR*24) [18]. The sequential

*alena.aslandukova@uni-bayreuth.de

structural transitions are well understood with the *s-d* electronic transition model [19–21]. It should be noted that this sequence of transitions has been reported based on powder XRD data upon the compression of yttrium in the absence of a pressure-transmitting medium. Interpretation of powder diffraction data is not trivial, considering the coexistence of several phases due to the sluggish character of transformations at room temperature and similarities of the *hP*2, *hR*9, *hP*4, and *cF*4 structures, which results in a significant overlap of diffraction peaks of different phases. Research on the behavior of yttrium at HP-HT conditions is lacking.

While at pressures >150 GPa the synthesis of a number of yttrium hydrides YH_4 YH_6, YH_7, and YH_9 [7,8] was reported, at lower pressures (up to 90 GPa), only hcp YH_3 and fcc YH_x ($x = 2$–3) are known [22–24]. It was suggested that yttrium hydride YH_x has a continuous hcp-to-fcc structure phase transition at pressures from 12.5 to 22 GPa with an intermediate yet uncharacterized structure state in between [24]. Notably, all reported high-T_C yttrium hydrides were synthesized by heating of Y in H_2 gas or in ammonia borane at pressures $>\sim$ 90 GPa; at lower pressures, HT experiments in the Y-H system have not been carried out.

Here, we report on the synthesis and characterization of a HP yttrium allotrope, *hP*3-Y, formed upon heating of Y to ∼2000 K at 20 GPa in a multi-anvil (MA) apparatus. Derivative hydrides, *hP*3-YH_x, were obtained from Y and various hydrogen precursors in diamond anvil cells (DACs) laser heated to ∼3000 K at 38, 45, and 51 GPa. On decompression to 14 GPa, these hydrides were observed to gradually lose hydrogen. We have extended our study by synthesizing Nd and Gd hydrides isostructural to *hP*3-YH_x, allowing us to generalize our conclusions.

II. EXPERIMENTAL METHODS

A. Sample preparation

1. MA synthesis

Samples of the *hP*3 yttrium allotrope were synthesized at HP-HT conditions using the multiton MA presses at the BGI (Bayreuth, Germany) [25] at a pressure of 20 GPa and a temperature of 2000 K; synthesis times were 24 h. We used a standard MA assembly that included a graphite cylindrical sample capsule, a $LaCrO_3$ heater, an octahedral container, and other parts [25]. Using single-crystal XRD (SCXRD), we selected high-quality crystals from the recovered samples and used them for further investigations.

2. Synthesis in DAC

The BX90-type large x-ray aperture DAC equipped with Boehler-Almax-type diamonds (culet diameter is 250 mm) was used for SCXRD studies [26,27]. Rhenium foil preindented to a thickness of ∼20 μm and a hole of ∼100 μm in diameter drilled in the center of the indentation served as a sample chamber. A piece of yttrium (or Nd/Gd) was placed in the sample chamber filled with paraffin oil (DAC1, DAC4, and DAC5) or ammonia borane (DAC2). The sample chamber of DAC3 was loaded with hydrogen gas using the HP gas loading system at Petra III (DESY, Hamburg, Germany). The pressure was determined using the EoS of Re [28,29] (for all DACs except DAC3) and additionally monitored by the Raman signal from the diamond anvils [30]. Samples were compressed up to 51 GPa (DAC1), 38 GPa (DAC2), 42 GPa (DAC3), 40 GPa (DAC4), and 45 GPa (DAC5) and laser heated to ∼3000(200) K. Laser heating of the samples was performed using an in-house setup [31] equipped with two YAG lasers (1064 nm central wavelength).

B. XRD measurements and data analysis procedure

XRD measurements for DAC1, DAC2, and DAC3 were performed at beamline P02.2 of Petra III (DESY, Hamburg, Germany) with the x-ray beam ($\lambda = 0.2891$ Å) focused down to $1.8\times2\,\mu m^2$ by a Kirkpatrick-Baez mirror system, and diffraction patterns were collected on a PerkinElmer 1621 XRD flat-panel detector. XRD measurements for DAC3, DAC4, and samples from MA1 and MA2 were performed at the ID15B beamline (ESRF, Grenoble, France) with an x-ray beam ($\lambda = 0.4103$ Å) focused to a size of $8\times8\,\mu m^2$, and the XRD patterns were collected on an Eiger2X CdTe 9M hybrid photon-counting pixel detector. For SCXRD measurements, samples were rotated around a vertical ω axis in a range of ±35°. The XRD images were collected with an angular step $\Delta\omega = 0.5°$. The CRYSALISPRO software package [32] was used for the analysis of the SCXRD data (indexing, data integration, frame scaling, and absorption correction). A single crystal of $(Mg_{1.93}, Fe_{0.06})(Si_{1.93}, Al_{0.06})O_6$ orthoenstatite [*Pbca*, $a = 18.2391(3)$, $b = 8.8117(2)$, and $c = 5.18320(10)$ Å] was used to calibrate the instrument model of the CRYSALISPRO software. The DAFI program [33] was used for the search of reflection groups belonging to the individual single-crystal domains. Using the OLEX2 software package [34], the structures were solved with the SHELXT structure solution program [35] using intrinsic phasing and refined with the SHELXL [36] refinement package using least-squares minimization. Crystal structure visualizations were made with VESTA software [37]. The experimental EoSs of the synthesized materials were obtained by fitting the pressure-volume data using the EoSFit7-GUI [38].

III. COMPUTATIONAL DETAILS

The properties of the systems were determined via first-principles calculations using Kohn-Sham DFT with the generalized gradient approximation by Perdew-Burke-Ernzerhof [39] for the exchange-correlation energy implemented within the projector augmented-wave method [40] for describing the interaction between the core and the valence electrons ($4s4p5s4d$) in the Vienna *Ab initio* Simulation Package (VASP) [41]. We used the Monkhorst-Pack scheme with $8\times8\times14$ *k*-points for Brillouin zone sampling and an energy cutoff for the plane-wave expansion of 600 eV, with which total energies are converged to better than 2 meV/atom. EoS and static enthalpy calculations were performed via variable-cell structural relaxations for 11 volumes that cover the pressure range of 0–50 GPa. The phonon calculations were performed in the harmonic approximation with the help of PHONOPY software using density functional perturbation theory for a $2\times2\times2$ supercell with respectively adjusted *k*-points [42]. In our calculations, temperature, configurational entropy, and the

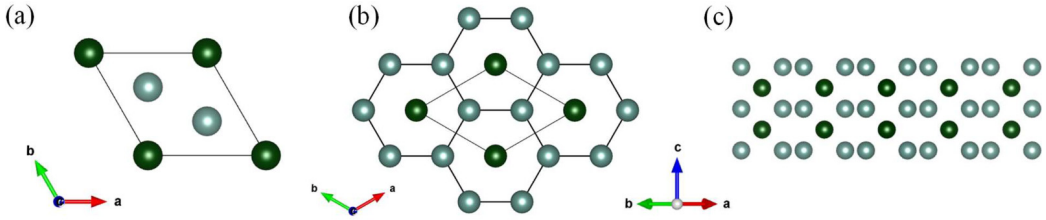

FIG. 1. Crystal structure of the *hP*3 yttrium allotrope. (a) Unit cell, (b) graphenelike nets of Y2 atoms alternating with nets of Y1 atoms along the *c* direction, and (c) a view along the [110] direction showing the stacking of nets of yttrium atoms (oriented perpendicular to the page) along the *c* direction. Yttrium atoms, Y1 and Y2, are shown in dark green and light green, respectively.

entropy contribution due to lattice vibrations were neglected. Fermi surface visualization was made with XCRYSDEN software [43].

IV. RESULTS AND DISCUSSION

The *hP*3 yttrium allotrope was synthesized in HP-HT experiments in a MA press (Table S1 in the Supplemental Material [44]): a piece of yttrium metal was compressed to 20 GPa and heated to 2000 K for 24 h (MA1 and MA2), with two independent MA experiments at the same conditions yielding the same result. The *hP*3 yttrium allotrope, along with two known carbides [45], cubic NaCl-type YC_x and Y_2C_3 (products of yttrium interaction with the graphite capsule, Table S1 in the Supplemental Material [44]), was characterized by in-house and synchrotron powder and SCXRD from products of both MA experiments. The details of the sample preparation, data collection, structure determination, and refinement are described in the Supplemental Material [44].

The yttrium allotrope has a hexagonal *hP*3 structure (space group $P6/mmm$, $Z = 3$) with unit cell parameters $a = 5.7809(10)$ Å, $c = 3.3453(5)$ Å, and $V = 96.82(4)$ Å^3 at 1 bar. Yttrium atoms occupy two crystallographically independent positions: Y1 at the 1*a* (0, 0, 0) site and Y2 at the 2*d* ($\frac{1}{3}$, $\frac{2}{3}$, $\frac{1}{2}$) site [Fig. 1(a)], like Ca and Hg atoms, respectively, in the $CaHg_2$ structure (58901-ICSD). The structure can be described as an alternation of graphenelike nets of Y2 atoms with nets of Y1 atoms along the *c* direction [Figs. 1(b)–1(c)]. All distances between Y1 and Y2 are equal to 3.7333(5) Å, which is significantly longer than the distances between Y1 and Y1 or Y2 and Y2, 3.3453(5) Å and 3.3376(6) Å, respectively. Interestingly, the Y1-Y1 and Y2-Y2 distances are shorter than the Y-Y distance in hcp yttrium, *hP*2-Y [$d_{Y-Y} = 3.5559(5)$ Å, data from 660002-ICSD]. Titanium also has an *hP*2 allotrope, α-Ti, and an *hP*3-Ti allotrope, ω-Ti (space group $P6/mmm$), both isostructural to *hP*2-Y and *hP*3-Y, respectively, with Ti2-Ti2 distances in *hP*3-Ti also shorter than Ti-Ti in *hP*2-Ti [46,47]. The densities of *hP*3-Y and *hP*2-Y (4.57 and 4.47 g/cm^3 at 1 bar, respectively) differ by ~1.7%, similar to titanium (4.61 g/cm^3 for ω-Ti and 4.51 g/cm^3 for α-Ti at 1 bar, data from 52521- and 253841-ICSD, respectively).

To gain deeper insight into the stability and pressure-volume behavior of *hP*3-Y, we performed calculations on the full relaxation of the structural model of *hP*3-Y at 1 bar using DFT, which results in unit cell parameters and atomic coordinates that perfectly agree with the experimental data at ambient conditions (Table S2 in the Supplemental Material [44]). To assess the dynamical stability of *hP*3-Y, harmonic phonon dispersion calculations along the high-symmetry directions of the Brillouin zone were made, showing that hexagonal *hP*3-Y is dynamically stable at 1 bar [Fig. 2(a)]. Static enthalpy calculations up to 50 GPa reproduced the experimentally known sequence of yttrium phase transitions, hcp ($P6_3/mmc$, *hP*2) → α-Sm type (R-3m, *hR*9) → dhcp ($P6_3/mmc$, *hP*4), but with a little shift of transition pressure values. Over the whole pressure range considered, the *hP*3-Y allotrope is thermodynamically unfavorable [Fig. 2(b)]. The observed formation of *hP*3-Y instead of other yttrium allotropes is expected to be due to the applications of HT (i.e., k_BT equaling 0.172 eV at 2000 K, less than the calculated enthalpy difference at 20 GPa) during HP synthesis and stabilization of the metastable phase by rapid quenching down to room temperature.

The pressure dependence of the volume per yttrium atom (V_0/atom) for *hP*3-Y in comparison with that for previously known allotropes [18] is shown in Figs. 3 and S1 in the Supplemental Material [44]. As mentioned above, the structures of known yttrium allotropes, *hP*2, *hR*9, *hP*4, and *cF*4, differ only in the stacking of close-packed atomic layers, and their pressure-volume relations can be described by a single third-order Birch-Murnaghan (BM3) EoS with the following parameters: bulk modulus $K_0 = 29(1)$ GPa, V_0/atom = 34.5(4) Å^3, the pressure derivative of the bulk modulus $K_0' = 3.54(5)$ (Fig. S1 in the Supplemental Material [44]). Interestingly, although the allotrope *hP*3-Y has a different structure, the parameters of its BM3 EoS (based on the pressure-volume relation from DFT calculations for *hP*3-Y) are similar: $K_0 = 36(1)$ GPa, V_0/atom = 32.7(1) Å^3, $K_0' = 3.54(1)$. which is in good agreement with the BM3 fit of the data from Ref. [18] (Fig. S1 in the Supplemental Material [44]).

Previously, it has been shown that pressure induces $s \rightarrow d$ electron transfer that can play an important role in phase stabilization. Therefore, the phase transitions observed under pressure in many lanthanides and yttrium are common [19–21]. For a deeper understanding of the electronic properties of *hP*3-Y, we calculated the electronic band structure, the electronic density of states (eDOS), and Fermi surfaces of the two allotropes, *hP*2-Y (hcp) and *hP*3-Y, that exist at ambient conditions. Figures 4(a)–4(c) show the calculated total and partial eDOS at 1 bar. Both yttrium allotropes exhibit metallic properties, and the main contribution at the Fermi level for both phases comes from the *d* states, while *p* and *s* states make quite small contributions. A detailed inspection of the difference in the contribution of the *s* and *d* states to the total eDOS [insert in Fig. 4(c)] reveals that, during the transition

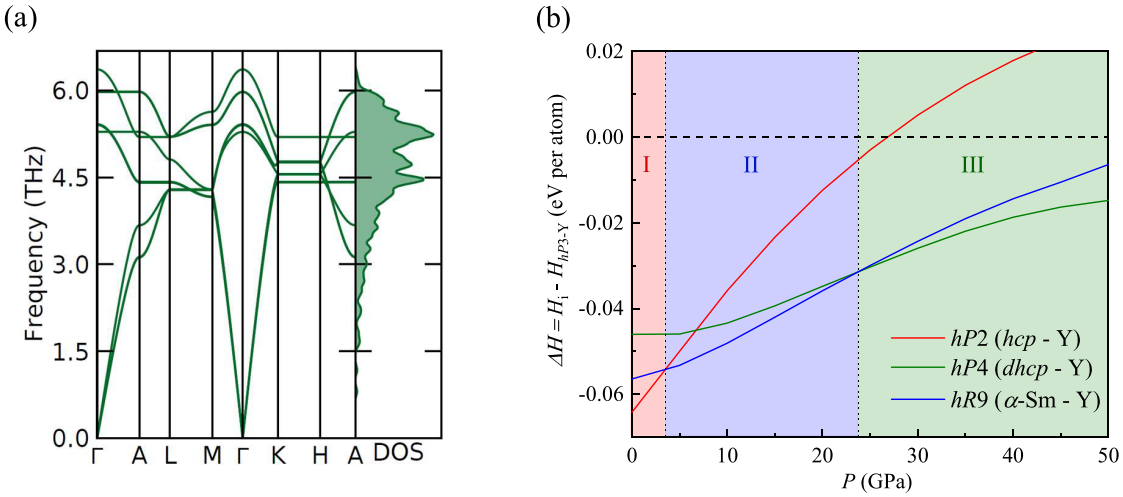

FIG. 2. Results of density functional theory (DFT) calculations. (a) Phonon dispersion curves for *hP*3-Y ($P6/mmm$) calculated at 1 bar along high-symmetry directions in the Brillouin zone and resulting phonon density of states. (b) Calculated enthalpy difference between known yttrium allotropes (hcp, α-Sm type, and dhcp) and *hP*3-Y: $\Delta H = H_i - H_{hP3-Y}$.

from *hP*2-Y to *hP*3-Y, the relative contribution of the *d* states to the density of states near the Fermi level increases from ~25% for *hP*2-Y to 75% for *hP*3-Y. Moreover, Fig. 4(a) shows a higher total eDOS at the Fermi level for *hP*3-Y than for *hP*2-Y. Usually, an increase in the eDOS at the Fermi energy strengthens the electron-phonon coupling, and as the range of phonon frequencies for *hP*3-Y [Fig. 2(a)] and *hP*2-Y [20] is very similar, one can assume a higher phonon-electron coupling constant for *hP*3-Y (i.e., potential superconductivity with enhanced T_C).

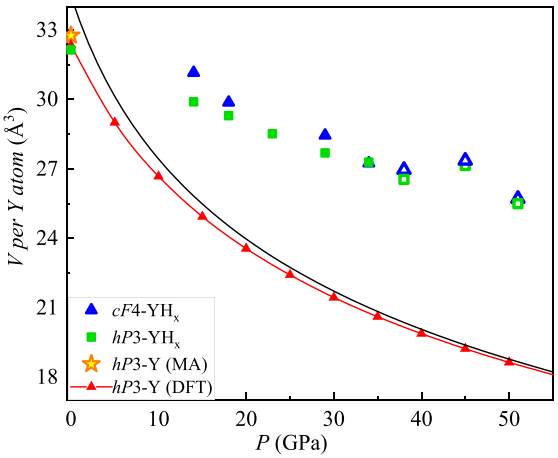

FIG. 3. Pressure dependence of the volume per yttrium atom for *hP*3-Y and yttrium hydrides, *hP*3-YH_x and *cF*4-YH_x, determined in this paper. The literature data for previously known yttrium allotropes, fitted by a single Birch-Murnaghan (BM3) equation of state (EoS; black line), are given for comparison. All blue symbols represent experimental values for *cF*4-YH_x, green symbols for *hP*3-YH_x. Open and filled symbols represent data obtained at high-pressure–high-temperature (HP-HT) conditions and on decompression, respectively. The density functional theory (DFT)-calculated pressures for given volume for *hP*3-Y are shown by red triangles and solid line.

For a comparison of the properties of two yttrium allotropes, *hP*3-Y and *hP*2-Y, Fermi surfaces were calculated.

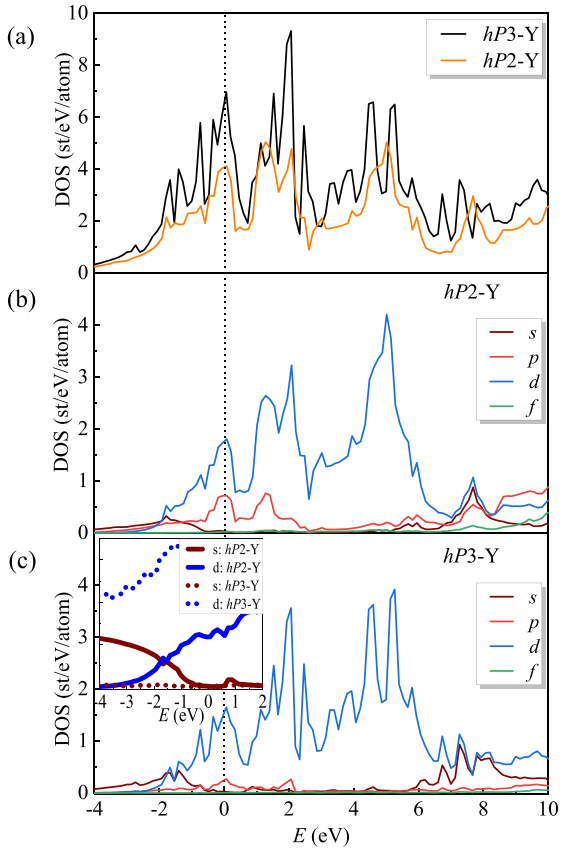

FIG. 4. Electronic density of states (eDOS) calculations at 1 bar. (a) Total eDOS for *hP*2-Y and *hP*3-Y. Partial eDOS for (b) *hP*2-Y and (c) *hP*3-Y. The inset in (c) shows relative contributions to the total eDOS of the *s* and *d* states for *hP*3-Y (dashed brown line = *s* states, dashed blue line = *d* states) and for *hP*2-Y (solid brown line = *s* states, solid blue line = *d* states). The vertical dashed line indicates the Fermi energy.

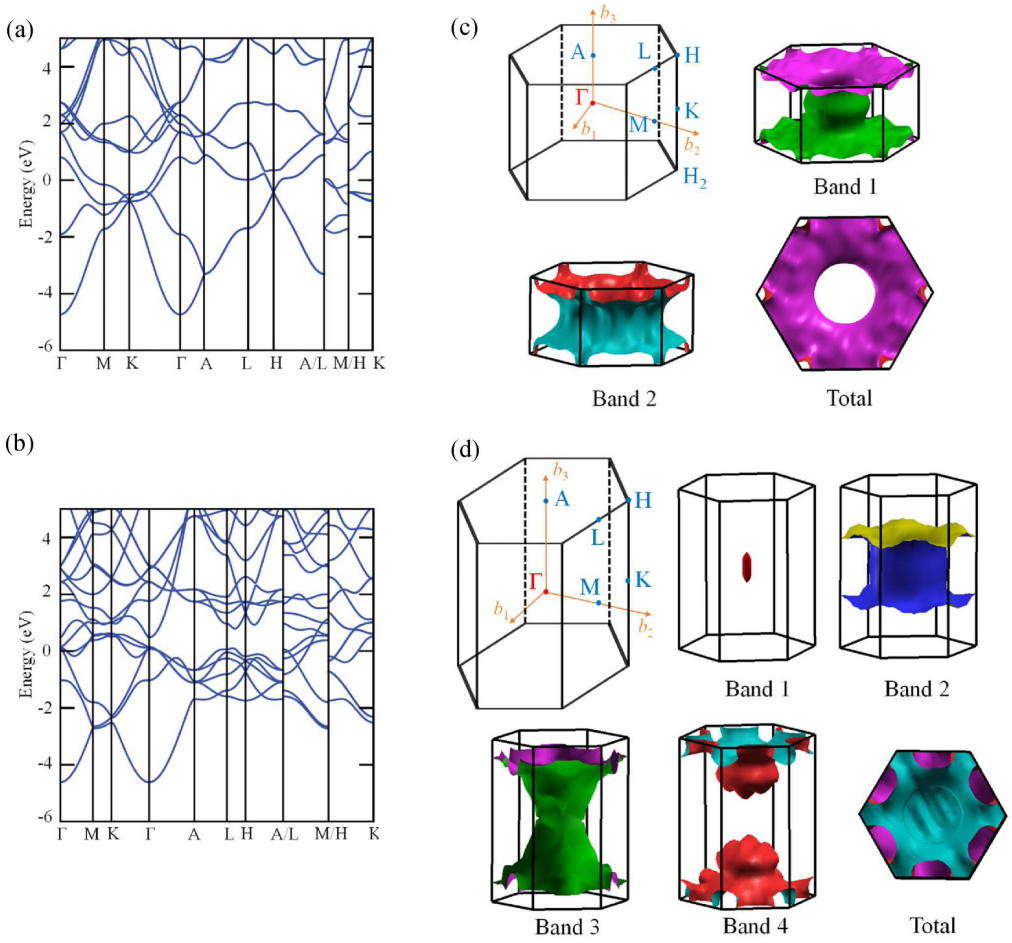

FIG. 5. Electronic band structure along high-symmetry directions in the hexagonal Brillouin zones of (a) *hP*2-Y and (b) *hP*3-Y at 1 bar. Brillouin zone and density functional theory (DFT)-calculated Fermi surfaces of (c) *hP*2-Y and (d) *hP*3-Y at 1 bar.

Figure 5 shows calculated band structures along high-symmetry directions in the hexagonal Brillouin zones *hP*3-Y and *hP*2-Y at ambient pressure. In the case of *hP*2-Y, two bands cross the Fermi energy; for *hP*3-Y, multiple electronic bands. As a result, the yttrium allotrope has a more complicated Fermi surface with a higher amount of contributing Fermi subsurfaces than *hP*2-Y (Fig. 5). The geometrical characteristics of the Fermi surfaces, such as the shape, curvature, and cross-sectional area, are related to the physical properties of metals such as electronic transport, specific heat, magnetic susceptibility, and optical absorption [48,49].

In *hP*2-Y, both bands cross the Fermi level, giving rise to two open distorted cylindricallike tubes with different radii along the Γ-*A* direction in the Brillouin zone, together forming a honeycomblike structure with hexagonal symmetry [Fig. 5(c)]. By contrast, the Fermi surface of *hP*3-Y consists not only of open surfaces with irregular shapes but also contains a closed surface and Fermi pockets that are restricted within the first Brillouin zone [Band 1 around the Γ point and Band 4 around the *A* point at the Brillouin zone boundary in Fig. 5(d)]. For some systems, it has been shown that the presence of coexisting Fermi pockets and Fermi surface nesting can indicate a strong electron-phonon coupling and hence potentially interesting electronic properties including superconductivity [50–52]. For titanium, which has a similar $hP2 \rightarrow hP3$ transition, it was shown that the holelike or electronlike Fermi pockets and nesting features that appear at the Fermi surface during pressure-induced phase transitions $\alpha(P6_3/mmc) \rightarrow \omega(P6/mmm) \rightarrow \gamma(Cmcm) \rightarrow \delta(Cmcm)$ [53] (Fig. S2 in the Supplemental Material [44]) substantially enhance the electron-phonon coupling and result in an increase of T_C (from 0.5 K at 1 bar for α-Ti to 2.3 K at 40.9 GPa for ω-Ti, with the maximum $T_C = 23.6$ K at 145 GPa for δ-Ti) [53,54]. Yttrium metal at ambient pressure has T_C of 6 mK [55]; however, it drastically increases with pressure (1.3 K at 11 GPa [56] and 19.5 K at 115 GPa [57]). The value of dT_C/dP for pressures < 50 GPa for yttrium is higher than for Ti [53]; therefore, one can expect enhanced superconductivity for *hP*3-Y.

The synthesis of a yttrium allotrope at HP-HT conditions indicates that yet unknown hydrides may exist at the same conditions. To check this, we studied chemical reactions between yttrium and three different hydrogen-rich precursors—hydrogen gas, paraffin oil, and ammonia borane—in the pressure range between 38 and 51 GPa upon heating up to ∼3400 K (Tables S1 and S3 in the Supplemental Material [44]). Regardless of the hydrogen source, two kinds of yttrium hydrides YH_x were synthesized: Y frameworks were either in the cubic (*Fm*-3*m*) or hexagonal (*P*6/*mmm*) structures, hereafter named *cF*4-YH_x and *hP*3-YH_x phases,

respectively. For example, at the highest pressure reached in this paper (51 GPa), a reaction between Y and paraffin oil led to the formation of both $hP3$-YH_x [$a = 5.299(1)$ Å, $c = 3.145(7)$ Å, and $V = 76.48(17)$ Å^3] and $cF4$-YH_x [$a = 4.685(1)$ Å and $V = 102.81(5)$ Å^3] with yttrium atoms on the nodes of the fcc lattice (Table S3 in the Supplemental Material [44]). Additionally, in the experiment with paraffin oil as a hydrogen precursor, we obtained two previously unknown yttrium carbides (Table S1 in the Supplemental Material [44]), which we have already described in Ref. [12].

The positions of yttrium atoms in hydrides were determined from SCXRD. The positions of the light hydrogen atoms could not be found from XRD data, and therefore, only the hydrogen content was estimated based on the difference in volume per yttrium atom between hydrides YH_x and yttrium metal at the same pressure [18], using a previously established pressure dependence of the volume per atomic H [58]. The evaluated stoichiometries for yttrium hydrides at each pressure point are given in Table S3 in the Supplemental Material [44]. Due to the systematic theoretical errors of the atomic hydrogen pressure-volume dependence model [58], the uncertainties of the hydrogen content in yttrium hydrides are difficult to estimate and therefore are not given.

During decompression (Table S3 in the Supplemental Material [44], Fig. 3) both hexagonal and cubic hydrides, $hP3$-YH_x and $cF4$-YH_x, gradually lost hydrogen (from $x = 2.9$ at 51 GPa to $x = 1.4$ at 14 GPa). At ambient conditions, hydrogen was fully released, and only $hP3$-Y was recovered. The volume per Y atom of the $hP3$-Y decompressed in DAC2 [$V = 32.32(2)$ Å^3] is consistent with that of the $hP3$-Y sample obtained from MA experiments [$V = 32.76(4)$ Å^3] and of $hP2$-Y [$V = 33.01(6)$ Å^3] [18]. Thus, the YH_x phases (both cubic and hexagonal) behave like metal-hydrogen solid solutions. The pressure-volume relation observed for hydrides synthesized from paraffin oil and ammonia borane as a hydrogen reservoir (DAC1 and DAC2) are similar (Fig. 3), but the cubic hydride contains a little bit more hydrogen than the hexagonal one at the same pressure (Fig. 3 and Table S3 in the Supplemental Material [44]).

The discovery of a Y allotrope, $hP3$-Y, and its derivative YH_x hydrides significantly extends the Y and Y-H phase diagrams at moderate pressures (up to 51 GPa). Since RE metals and their known hydrides usually behave similarly at HP-HT conditions, it is important to examine if other RE metals also form $hP3$-RE hydrides. We tested this on Nd and Gd metals that we laser heated to ~3000 K in paraffin oil at 40 and 45 GPa, leading to the synthesis of $hP3$-NdH_4 and $hP3$-$GdH_{3.5}$ (see information for DAC4 and DAC5 in Table S1 in the Supplemental Material [44]). In addition, at 40 GPa, a cubic $cF4$-$NdH_{4.1}$ (with fcc metal lattice) was observed with the same (within uncertainty) volume per Nd atom as in $hP3$-NdH_4, i.e., with the same hydrogen content. Upon decompression of DAC4, NdH_x hydrides (both cubic and hexagonal) lost hydrogen (at 24 GPa, $x = 3$; at 4 GPa, $x = 0.7$; Table S4 in the Supplemental Material [44]), showing a behavior like that of yttrium hydrides discussed above. This suggests that $hP3$-$(RE)H_x$ hydrides may be common for RE metals, and their existence and properties should be considered in a broad context of studies on different aspects of the HP behavior of RE hydrides, particularly with respect to superconductivity.

V. CONCLUSIONS

To summarize, the HP-HT approach allowed us to synthesize a yttrium allotrope, hexagonal $hP3$-Y, recoverable to ambient conditions. DFT-based phonons calculations confirm its dynamic stability at 1 bar. The enthalpy calculations showed that $hP3$-Y is metastable up to 50 GPa but may be synthesized at HP-HT conditions and stabilized by rapid quenching. With a detailed analysis of the electronic structure of the yttrium allotrope from DFT calculations, the stabilization of $hP3$-Y can be rationalized in terms of electronic $s \rightarrow d$ transfer, a mechanism common for lanthanides. We have further shown that, at HP-HT conditions, $hP3$-Y can dissolve a significant amount of hydrogen (up to 3 hydrogen atoms per 1 yttrium atom) through a direct reaction of yttrium with different hydrogen-rich precursors. Decompression experiments revealed the release of hydrogen with decreasing pressure, leading to the formation of hydrides with variable hydrogen content. Isostructural $hP3$-$(RE)H_x$ hydrides (RE = Nd and Gd) were obtained, which suggests that the structure type may be common for RE elements. Thus, our results enrich the Y phase diagram and suggest that it is important to further study the structural phase transitions in other RE metals and their hydrides.

ACKNOWLEDGMENTS

The authors acknowledge the DESY, PETRA III for the provision of beamtime at the P02.2 and the ESRF for the provision of beamtime at the ID15b beamline. D.L. thanks the UKRI Future Leaders Fellowship (No. MR/V025724/1) for financial support. N.D. and L.D. thank the Federal Ministry of Education and Research, Germany (Grant No. 05K19WC1) and the Deutsche Forschungsgemeinschaft (DFG Projects No. DU 954–11/1, No. DU 393–9/2, and No. DU 393–13/1) for financial support. N.D. also thanks the Swedish Government Strategic Research Area in Materials Science on Functional Materials at Linköping University (Faculty Grant SFO-Mat-LiU No. 2009 00971). G.S.N. acknowledges financial support by DFG through Project No. STE1105/13-2 in the Research Unit FOR2440.

[1] J. A. Flores-Livas, L. Boeri, A. Sanna, G. Profeta, R. Arita, and M. Eremets, Phys. Rep. **856**, 1 (2020).

[2] A. P. Drozdov, P. P. Kong, V. S. Minkov, S. P. Besedin, M. A. Kuzovnikov, S. Mozaffari, L. Balicas, F. F. Balakirev, D. E. Graf, V. B. Prakapenka *et al.*, Nature (London) **569**, 528 (2019).

[3] M. Somayazulu, M. Ahart, A. K. Mishra, Z. M. Geballe, M. Baldini, Y. Meng, V. V. Struzhkin, and R. J. Hemley, Phys. Rev. Lett. **122**, 027001 (2019).

[4] N. P. Salke, M. M. Davari Esfahani, Y. Zhang, I. A. Kruglov, J. Zhou, Y. Wang, E. Greenberg, V. B. Prakapenka, J. Liu, A. R. Oganov *et al.*, Nat. Commun. **10**, 4453 (2019).

[5] I. A. Kruglov, A. G. Kvashnin, A. F. Goncharov, A. R. Oganov, S. S. Lobanov, N. Holtgrewe, S. Jiang, V. B. Prakapenka, E. Greenberg, and A. V. Yanilkin, Sci. Adv. **4**, eaat9776 (2018).

[6] D. V. Semenok, A. G. Kvashnin, A. G. Ivanova, V. Svitlyk, V. Y. Fominski, A. V. Sadakov, O. A. Sobolevskiy, V. M. Pudalov, I. A. Troyan, and A. R. Oganov, Mater. Today **33**, 36 (2020).

[7] P. Kong, V. S. Minkov, M. A. Kuzovnikov, A. P. Drozdov, S. P. Besedin, S. Mozaffari, L. Balicas, F. F. Balakirev, V. B. Prakapenka, S. Chariton *et al.*, Nat. Commun. **12**, 5075 (2021).

[8] I. A. Troyan, D. V. Semenok, A. G. Kvashnin, A. V. Sadakov, O. A. Sobolevskiy, V. M. Pudalov, A. G. Ivanova, V. B. Prakapenka, E. Greenberg, A. G. Gavriliuk *et al.*, Adv. Mater. **33**, 2006832 (2021).

[9] E. Snider, N. Dasenbrock-Gammon, R. McBride, X. Wang, N. Meyers, K. V. Lawler, E. Zurek, A. Salamat, and R. P. Dias, Phys. Rev. Lett. **126**, 117003 (2021).

[10] J. E. Hirsch and F. Marsiglio, Matter Radiat. Extrem. **7**, 058401 (2022).

[11] J. E. Hirsch and F. Marsiglio, Phys. Rev. B **103**, 134505 (2021).

[12] D. Laniel, B. Winkler, E. Bykova, T. Fedotenko, S. Chariton, V. Milman, M. Bykov, V. Prakapenka, L. Dubrovinsky, and N. Dubrovinskaia, Phys. Rev. B **102**, 134109 (2020).

[13] T. Meier, F. Trybel, S. Khandarkhaeva, G. Steinle-Neumann, S. Chariton, T. Fedotenko, S. Petitgirard, M. Hanfland, K. Glazyrin, N. Dubrovinskaia *et al.*, Phys. Rev. X **9**, 031008 (2019).

[14] T. Meier, F. Trybel, G. Criniti, D. Laniel, S. Khandarkhaeva, E. Koemets, T. Fedotenko, K. Glazyrin, M. Hanfland, M. Bykov *et al.*, Phys. Rev. B **102**, 165109 (2020).

[15] T. Meier, A. Aslandukova, F. Trybel, D. Laniel, T. Ishii, S. Khandarkhaeva, N. Dubrovinskaia, and L. Dubrovinsky, Matter Radiat. Extrem. **6**, 068402 (2021).

[16] A. Aslandukova, A. Aslandukov, L. Yuan, D. Laniel, S. Khandarkhaeva, T. Fedotenko, G. Steinle-Neumann, K. Glazyrin, N. Dubrovinskaia, and L. Dubrovinsky, Phys. Rev. Lett. **127**, 135501 (2021).

[17] A. F. Goncharov, E. Bykova, M. Bykov, X. Zhang, Y. Wang, S. Chariton, V. B. Prakapenka, and J. S. Smith, J. Appl. Phys. **131**, 025902 (2022).

[18] E. J. Pace, S. E. Finnegan, C. V. Storm, M. Stevenson, M. I. McMahon, S. G. MacLeod, E. Plekhanov, N. Bonini, and C. Weber, Phys. Rev. B **102**, 094104 (2020).

[19] J. C. Duthie and D. G. Pettifor, Phys. Rev. Lett. **38**, 564 (1977).

[20] P. P. Singh, Phys. Rev. B **75**, 125101 (2007).

[21] H. Olijnyk, J. Phys. Condens. Matter **17**, 43 (2005).

[22] R. J. Wijngaarden, J. N. Huiberts, D. Nagengast, J. H. Rector, R. Griessen, M. Hanfland, and F. Zontone, J. Alloys Compd. **308**, 44 (2000).

[23] A. Machida, A. Ohmura, T. Watanuki, K. Aoki, and K. Takemura, Phys. Rev. B **76**, 052101 (2007).

[24] A. Machida, A. Ohmura, T. Watanuki, T. Ikeda, K. Aoki, S. Nakano, and K. Takemura, Solid State Commun. **138**, 436 (2006).

[25] D. J. Frost, B. T. Poe, R. G. Trønnes, C. Liebske, A. Duba, and D. C. Rubie, Phys. Earth Planet. Inter. **143**, 507 (2004).

[26] I. Kantor, V. Prakapenka, A. Kantor, P. Dera, A. Kurnosov, S. Sinogeikin, N. Dubrovinskaia, and L. Dubrovinsky, Rev. Sci. Instrum. **83**, 125102 (2012).

[27] Rigaku Oxford Diffraction, CRYSALISPRO Software system (2015).

[28] C. S. Zha, W. A. Bassett, and S. H. Shim, Rev. Sci. Instrum. **75**, 2409 (2004).

[29] S. Anzellini, A. Dewaele, F. Occelli, P. Loubeyre, and M. Mezouar, J. Appl. Phys. **115**, 043511 (2014).

[30] Y. Akahama and H. Kawamura, J. Appl. Phys. **100**, 043516 (2006).

[31] T. Fedotenko, L. Dubrovinsky, G. Aprilis, E. Koemets, A. Snigirev, I. Snigireva, A. Barannikov, P. Ershov, F. Cova, M. Hanfland *et al.*, Rev. Sci. Instrum. **90**, 104501 (2019).

[32] CRYSALISPRO Data Collection and Processing Software for Agilent X-ray Diffractometers.

[33] A. Aslandukov, M. Aslandukov, N. Dubrovinskaia, and L. Dubrovinsky, J. Appl. Cryst. **55**, 1383 (2022).

[34] O. V. Dolomanov, L. J. Bourhis, R. J. Gildea, J. A. K. Howard, and H. Puschmann, J. Appl. Cryst. **42**, 339 (2009).

[35] V. Petrícek, M. Dušek, and L. Palatinus, Z. Kristallogr. Cryst. Mater. **229**, 345 (2014).

[36] G. M. Sheldrick, Acta Cryst. C **71**, 3 (2015).

[37] K. Momma and F. Izumi, J. Appl. Cryst. **44**, 1272 (2011).

[38] J. Gonzalez-Platas, M. Alvaro, F. Nestola, and R. Angel, J. Appl. Cryst. **49**, 1377 (2016).

[39] J. P. Perdew, K. Burke, and M. Ernzerhof, Phys. Rev. Lett. **77**, 3865 (1996).

[40] G. Kresse and D. Joubert, Phys. Rev. B **59**, 1758 (1999).

[41] G. Kresse and J. Furthmüller, Phys. Rev. B **54**, 11169 (1996).

[42] A. Togo and I. Tanaka, Scr. Mater. **108**, 1 (2015).

[43] A. Kokalj, J. Mol. Graph. Model. **17**, 176 (1999).

[44] See Supplemental Material at http://link.aps.org/supplemental/10.1103/PhysRevB.107.014103 for the full description of the sample preparation, the full crystallographic details on the structures solved by SCXRD, as well as complementary figures.

[45] V. Babizhetskyy, B. Kotur, V. Levytskyy, and H. Michor, in *Handbook on the Physics and Chemistry of Rare Earths*, edited by J.-C. G. Bünzli and V. K. Pecharsky (Elsevier, Amsterdam, 2017), Vol. 52, pp. 1–263.

[46] E. S. Chebotareva and S. G. Nuzhdina, Phys. Metals Metallogr. **36**, 200 (1973).

[47] M. Sabeena, S. Murugesan, P. Anees, E. Mohandas, and M. Vijayalakshmi, J. Alloys Compd. **705**, 769 (2017).

[48] W. A. Harrison and R. W. Schmitt, Phys. Today **14**, 20 (1961).

[49] B. Zimmermann, P. Mavropoulos, N. H. Long, C. R. Gerhorst, S. Blügel, and Y. Mokrousov, Phys. Rev. B **93**, 144403 (2016).

[50] C. M. Hao, Y. Li, H. M. Huang, Y. Li, and Y. L. Li, Inorg. Chem. **59**, 484 (2020).

[51] S. Lebègue, Phys. Rev. B **75**, 035110 (2007).

[52] D. Kasinathan, J. Kuneš, A. Lazicki, H. Rosner, C. S. Yoo, R. T. Scalettar, and W. E. Pickett, Phys. Rev. Lett. **96**, 047004 (2006).

[53] X. Liu, P. Jiang, Y. Wang, M. Li, N. Li, Q. Zhang, Y. Wang, Y.-L. Li, and W. Yang, Phys. Rev. B **105**, 224511 (2022).

[54] I. O. Bashkin, V. G. Tissen, M. V. Nefedova, and E. G. Ponyatovsky, Phys. C Supercond. Appl. **453**, 12 (2007).

[55] C. Probst and J. Wittig, in *Handbook on the Physics and Chemistry of Rare Earths* (Elsevier, Amsterdam, 1978), Vol. 1, pp. 749–795.

[56] J. Wittig, Phys. Rev. Lett. **24**, 812 (1970).

[57] J. J. Hamlin, V. G. Tissen, and J. S. Schilling, Phys. C Supercond. Appl. **451**, 82 (2007).

[58] B. Guigue, A. Marizy, and P. Loubeyre, Phys. Rev. B **102**, 014107 (2020).

Supplementary Materials

High-pressure *hP*3 yttrium allotrope with the $CaHg_2$–type structure as a prototype of *hP*3 rare-earth hydrides series

Alena Aslandukova[1], Andrey Aslandukov[1,2], Dominique Laniel[3], Saiana Khandarkhaeva[2], Gerd Steinle-Neumann[1], Timofey Fedotenko[4], Sergey V. Ovsyannikov[1], Yuqing Yin[2,5], Fariia Iasmin Akbar[1], Konstantin Glazyrin[4], Michael Hanfland[6], Leonid Dubrovinsky[1], Natalia Dubrovinskaia[2,7]

[1] Bavarian Research Institute of Experimental Geochemistry and Geophysics (BGI), University of Bayreuth, Universitaetsstrasse 30, 95440 Bayreuth, Germany

[2] Material Physics and Technology at Extreme Conditions, Laboratory of Crystallography, University of Bayreuth, 95440 Bayreuth, Germany

[3] Centre for Science at Extreme Conditions and School of Physics and Astronomy, University of Edinburgh, Edinburgh EH93FD, United Kingdom

[4] Photon Science, Deutsches Elektronen-Synchrotron, Notkestrasse 85, 22607 Hamburg, Germany

[5] State Key Laboratory of Crystal Materials, Shandong University, Jinan 250100, China

[6] European Synchrotron Radiation Facility, BP 220, 38043 Grenoble Cedex, France

[7] Department of Physics, Chemistry and Biology (IFM), Linköping University, SE-581 83, Linköping, Sweden

Tables.

Table S1: DAC and multi-anvil (MA) experiments and the lists of obtained phases.

	Reagents	Synthesis conditions		Pressure range on decompression (GPa)	Products of reaction at synthesis conditions
		P (GPa)	*T* (K)		
MA1	Y	20(2)	2000(100)	-	*hP*3-Y, YC_x, Y_2C_3
MA2	Y	20(2)	1900(100)	-	*hP*3-Y, YC_x, Y_2C_3
DAC1	Y in paraffin oil	51(1)	3000(200)	18(1) – 51(1)	Y_2C_3, Y_4C_5, *cF*4-$YH_{2.9}$, *hP*3-$YH_{2.8}$
DAC2	Y in NH_3BH_3	38(1)	3000(200)	1bar – 38(1)	*cF*4-$YH_{2.5}$, *hP*3-$YH_{2.4}$
DAC3	Y in H_2	45(1)	3400(200)	-	*cF*4-YH_3, *hP*3-YH_3
DAC4	Nd in paraffin oil	40(1)	3000(200)	4(1) – 40(1)	*hP*3-NdH_3, *cF*4-$NdH_{3.1}$
DAC5	Gd in paraffin oil	45(1)	3000(200)	-	*hP*3-$GdH_{3.5}$

Table S2: Experimentally determined crystallographic data for a new yttrium allotrope at 1bar in comparison to the corresponding DFT-relaxed structure. The full crystallographic dataset was deposited to the CCDC under the deposition number 2202826.

Crystal phase			*hP*3-Y (experiment)	*hP*3-Y (theory)
Space group, *Z*			*P*6/*mmm*, 3	*P*6/*mmm*, 3
a (Å)			5.781(4)	5.6282
c (Å)			3.345(2)	3.5293
V (Å^3)			96.82(4)	96.818
Wyckoff site and fractional atomic coordinates (*x*; *y*; *z*):	Y1	*1a*	0; 0; 0	0; 0; 0
	Y2	*2d*	1/3; 2/3; 0.5	1/3; 2/3; 0.5
Number of measured/independent reflections ($I \geq 3\sigma$)			178/ 75 (52)	-
R_{int}			0.0833	-
Final R indexes ($I \geq 3\sigma$)			R_1 = 0.0723; wR_2 = 0.0817	-
Final R indexes (all data)			R_1 = 0.0842; wR_2 = 0.0834	-
Number of refined parameters			5	-

Table S3: Lattice parameters and unit cell volumes for yttrium hydrides, *hP*3-YH_x and *cF*4-YH_x, synthesized in DACs, as determined from the analysis of SCXRD data.

Phase, space group	*a* (Å)	*b* (Å)	*c* (Å)	*V* (Å^3)	*V* (Å^3) / atom Y
DAC1, *P* = 51(1) GPa, after LH at *T* = 3000(200) K					
$YH_{2.9}$, *Fm*-3*m*	4.685(1)	-	-	102.81(5)	25.71
$YH_{2.8}$, *P*6/*mmm*	5.299(1)	-	3.145(7)	76.48(17)	25.49
DAC3, *P* = 45(1) GPa, after LH at *T* = 3400(200) K					
YH_3, *Fm*-3*m*	4.7706(11)	-	-	108.57(4)	27.14
YH_3, *P*6/*mmm*	5.4456(14)	-	3.1953(12)	82.06(4)	27.35
DAC2, *P* = 38(1) GPa, after LH at *T* = 3000(200) K					
$YH_{2.5}$, *Fm*-3*m*	4.7596(2)	-	-	107.82(8)	26.96
$YH_{2.4}$, *P*6/*mmm*	5.389(4)	-	3.166(3)	79.63(13)	26.54
DAC1, *P* = 34(1) GPa, decompression					
$YH_{2.4}$, *Fm*-3*m*	4.7764(13)	-	-	108.97(5)	27.24
$YH_{2.4}$, *P*6/*mmm*	5.4383(16)	-	3.1959(7)	81.86(4)	27.29
DAC2, *P* = 29(1) GPa, decompression					
$YH_{2.4}$, *Fm*-3*m*	4.8459(10)	-	-	113.79(2)	28.45
$YH_{2.1}$, *P*6/*mmm*	5.472(5)	-	3.203(4)	83.06(6)	27.69
DAC1, *P* = 23(1) GPa, decompression					
$YH_{1.9}$, *P*6/*mmm*	5.5300(12)	-	3.2296(2)	85.55(2)	28.51
DAC1, *P* = 18(1) GPa, decompression					
$YH_{1.8}$, *Fm*-3*m*	4.9255(9)	-	-	119.49(1)	29.87
$YH_{1.6}$, *P*6/*mmm*	5.5780(10)	-	3.2614(1)	87.89(2)	29.29
DAC2, *P* = 14(1) GPa, decompression					
$YH_{1.7}$, *Fm*-3*m*	4.9951(5)	-	-	124.63(2)	31.16
$YH_{1.4}$, *P*6/*mmm*	5.6238(13)	-	3.2742(11)	89.68(8)	29.89
DAC2, *P* = 1 bar, decompression					
Y, *P*6/*mmm*	5.791(8)	-	3.338(6)	96.95(8)	32.32

Table S4: Lattice parameters and unit cell volumes for Nd and Gd hydride phases obtained from analysis of SCXRD data from DAC4 and DAC5.

Phase, space group	*a* (Å)	*b* (Å)	*c* (Å)	*V* (Å^3)	*V* (Å^3) / atom Y
DAC4, *P* = 40(1) GPa, after LH at *T* = 3000(200) K					
$NdH_{4.1}$, *Fm*-3*m*	4.8878(9)	-	-	116.77(4)	29.19
NdH_4, *P*6/*mmm*	5.483(2)	-	3.3325(12)	86.76(6)	28.92
DAC4, *P* = 24(1) GPa, decompression					
$NdH_{3.1}$, *Fm*-3*m*	4.9371(12)	-	-	120.34(5)	30.09
NdH_3, *P*6/*mmm*	5.536(2)	-	3.3609(8)	89.21(5)	29.74
DAC4, *P* = 4(2) GPa, decompression					
$NdH_{0.7}$, *P*6/*mmm*	6.0210(16)	-	3.5147(13)	110.35(3)	36.78
DAC5, *P* = 45(1) GPa, after LH at *T* = 3000(200) K					
$GdH_{3.5}$, *P*6/*mmm*	5.4108(11)	-	3.2773(16)	83.09(8)	27.69

Figures.

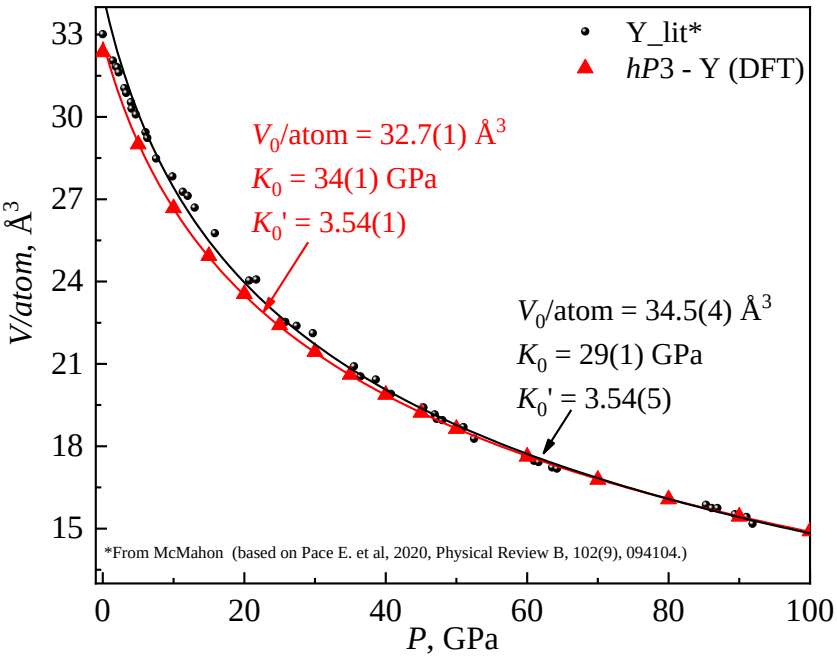

Fig. S1. The experimental pressure dependence of the volume per yttrium atom for known yttrium allotropes (*hcp* (*hP*2), *α-Sm type* (*hR*9), *dhcp* (*hP*4), *fcc* (*cF*4), *distorted-cF4*) (black dots), and the DFT-calculated values for *hP*3-Y (red dots). Solid lines represent the fit of values with a third-order Birch-Murnaghan equation-of-state.

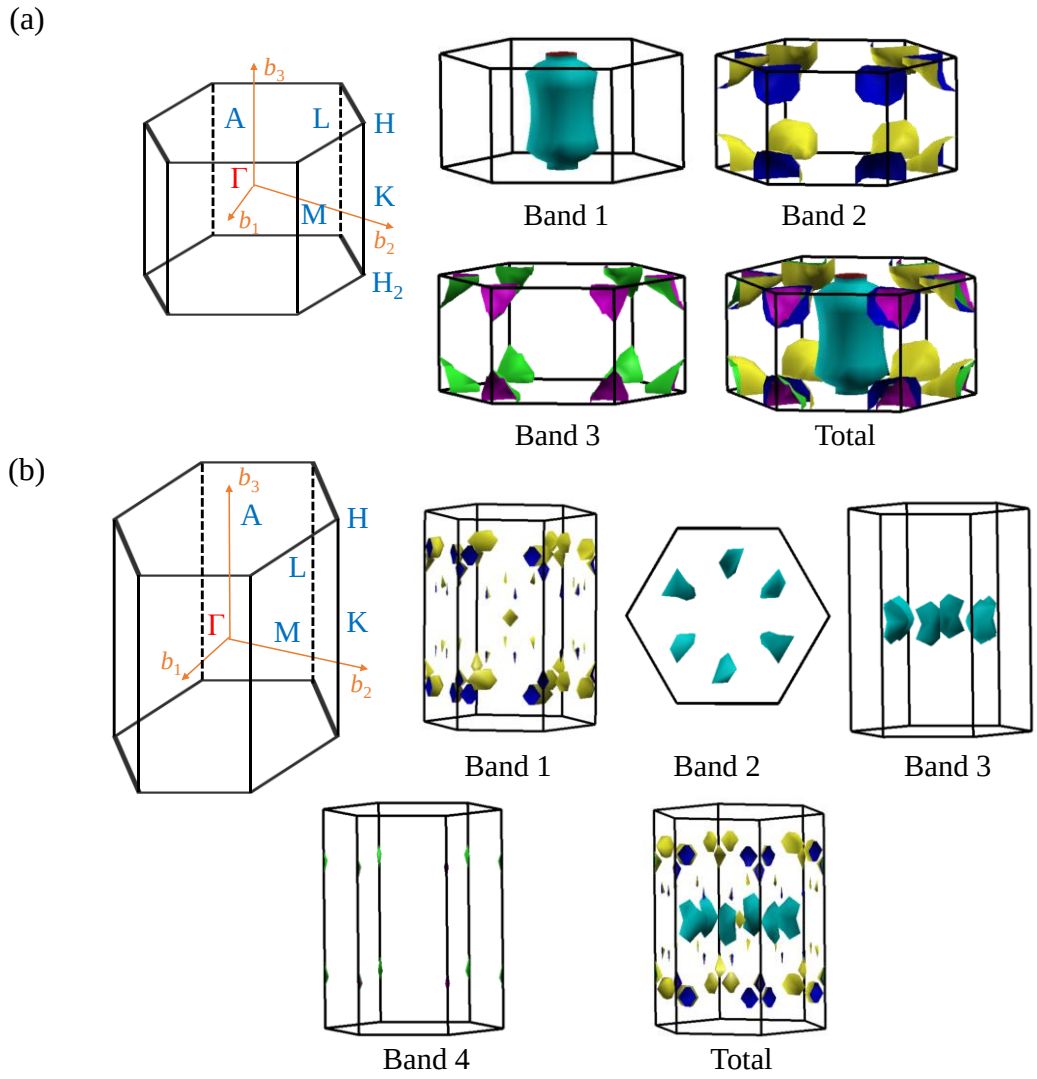

Fig. S2. Brillouin zone and DFT calculated Fermi surfaces of (a) α –Ti and (b) ω – Ti at 1bar.

4.2. Diverse high-pressure chemistry in Y–NH_3BH_3 and Y–paraffin oil systems.

This section contains the following manuscript and the related supplementary material:

"Diverse high-pressure chemistry in Y–NH_3BH_3 and Y–paraffin oil systems"

A. Aslandukova, A. Aslandukov, D. Laniel, Y. Yin, F. I. Akbar, M. Bykov, T. Fedotenko, K. Glazyrin, A. Pakhomova, G. Garbarino, E. L. Bright, J. Wright, M. Hanfland, S. Chariton, V. Prakapenka, N. Dubrovinskaia & L. Dubrovinsky

Status: published in *Science Advances*, 10, 1

(2024)

CHEMISTRY

Diverse high-pressure chemistry in Y-NH_3BH_3 and Y–paraffin oil systems

Alena Aslandukova[1]*, Andrey Aslandukov[1,2], Dominique Laniel[3], Yuqing Yin[2,4,5], Fariia Iasmin Akbar[1], Maxim Bykov[6], Timofey Fedotenko[7], Konstantin Glazyrin[7], Anna Pakhomova[8], Gaston Garbarino[8], Eleanor Lawrence Bright[8], Jonathan Wright[8], Michael Hanfland[8], Stella Chariton[9], Vitali Prakapenka[9], Natalia Dubrovinskaia[2,5], Leonid Dubrovinsky[1]

The yttrium-hydrogen system has gained attention because of near-ambient temperature superconductivity reports in yttrium hydrides at high pressures. We conducted a study using synchrotron single-crystal x-ray diffraction (SCXRD) at 87 to 171 GPa, resulting in the discovery of known (two YH_3 phases) and five previously unknown yttrium hydrides. These were synthesized in diamond anvil cells by laser heating yttrium with hydrogen-rich precursors—ammonia borane or paraffin oil. The arrangements of yttrium atoms in the crystal structures of new phases were determined on the basis of SCXRD, and the hydrogen content estimations based on empirical relations and ab initio calculations revealed the following compounds: Y_3H_{11}, Y_2H_9, Y_4H_{23}, $Y_{13}H_{75}$, and Y_4H_{25}. The study also uncovered a carbide (YC_2) and two yttrium allotropes. Complex phase diversity, variable hydrogen content in yttrium hydrides, and their metallic nature, as revealed by ab initio calculations, underline the challenges in identifying superconducting phases and understanding electronic transitions in high-pressure synthesized materials.

INTRODUCTION

Near–room temperature superconductors can drastically affect many areas of technology (*1*–*3*). Because of recent advances in experimental techniques, namely, due to the improvements of the diamond anvil cells (DACs), it became possible to synthesize novel materials, including polyhydride phases, through a combination of high temperature and high pressure. Many hydrogen-rich materials [such as metal hydrides LaH_{10} (*4*), CaH_6 (*5*), BaH_{12} (*6*), YH_6 and YH_9 (*7*, *8*), CeH_9 (*9*), PrH_9 (*10*), ThH_{10} (*11*), UH_7 and UH_8 (*12*)] and covalent polyhydrides [H_3S (*3*)] were claimed to be high temperature (high-T_C) superconductors under high pressure. However, not all of the claims are easy to justify in the absence of detailed information about the phase and chemical composition of products of chemical reactions taking place in the sample chamber of a DAC after laser heating (LH). Reliable conclusions concerning the superconductivity, i.e., values of measured T_C, the isotopic effect, and the dependence of the superconducting transition with magnetic field, are problematic considering a variable hydrogen content in the same phase and/or the inhomogeneous products' mixture (namely, the presence of phases other than the superconducting one), which can greatly affect the resistivity (*13*), magnetic susceptibility (*3*, *14*), and magnetic resonance measurements (*3*, *15*, *16*). Therefore, the results of the published T_C are still heavily disputed (*13*, *17*–*20*).

As promising high-T_C superconductors, high-pressure yttrium hydrides have been extensively studied. Under ambient conditions, two yttrium hydrides *cF*4-YH_2 ($Fm\bar{3}m$) and *hP*2-YH_3 ($P6_3/mmc$) (*21*) are known (in this work, we use Pearson symbols, which refer to the arrangement of Y atoms only; hydrogen content inferred from the chemical formulas may refer to an experimentally determined, theoretically proposed, or empirically estimated amount of hydrogen atoms). At low pressures (10 to 25 GPa), *hP*2-YH_3 undergoes a phase transition to *cF*4-YH_3 (*22*), which also can be produced by cold hydrogenation of *cF*4-YH_2 (*23*). The *cF*4-YH_3 phase was found to be stable at ambient temperature under high pressures up to 325 GPa (*7*). At pressures above 200 GPa, the long treatment of YH_3 with pressurized hydrogen without heating leads to the formation of tetragonal *tI*2-YH_4 and cubic *cI*2-YH_6 (*7*). Heating yttrium with hydrogen precursors at mild pressures (up to 50 GPa) results in the formation of *hP*3-YH_x (x = 1.4 to 3) hydrides with variable H-content along with *cF*4-YH_3 (*7*). At higher pressure, above 100 GPa, the high-temperature syntheses of yttrium hydrides with a higher hydrogen content [*tI*2-YH_4 (*7*), *cI*2-YH_6 (*7*), *oI*2-YH_7 (*Imm*2) and *aP*2-YH_7 (*P*1) (*8*), and *hP*2-YH_9 ($P6_3/mmc$) (*7*, *24*)] were reported and obtained from different precursors. Among them, based on experimental data, the *cI*2-YH_6 and *hP*2-YH_9 phases were determined to have high superconducting transition temperatures, $T_C \sim 224$ K at 166 GPa (*8*) and $T_C \sim 243$ K at 201 GPa (*7*), respectively. Moreover, up to date, several theoretical studies on the Y-H system were reported (*8*, *25*, *26*) and a variety of hydrides with a high hydrogen content, namely, *mC*2-YH_8 (*25*), *cF*4-YH_9 ($F\bar{4}3m$), *cF*4-YH_{10} ($Fm\bar{3}m$) (*8*), and *mC*4-YH_{12} (*C*2/*c*) (*25*), were predicted to be stable but not yet found in experiments. It is important to note that the chemical compositions and structures of only YH_2 and YH_3 have been unambiguously determined (*22*, *23*), whereas those of all other hydrides have been based on theoretical predictions and/or empirical estimations. It is also worth mentioning that the accuracy and limitations of these predictions may vary among different studies. Therefore, there are some inconsistencies between the predictions

[1]Bavarian Research Institute of Experimental Geochemistry and Geophysics (BGI), University of Bayreuth, Universitaetsstrasse 30, 95440 Bayreuth, Germany. [2]Material Physics and Technology at Extreme Conditions, Laboratory of Crystallography, University of Bayreuth, 95440 Bayreuth, Germany. [3]Centre for Science at Extreme Conditions and School of Physics and Astronomy, University of Edinburgh, Edinburgh EH9 3FD, UK. [4]State Key Laboratory of Crystal Materials, Shandong University, Jinan 250100, China. [5]Department of Physics, Chemistry and Biology (IFM), Linköping University, SE-581 83 Linköping, Sweden. [6]Institute of Inorganic Chemistry, University of Cologne, Greinstrasse 6, 50939 Cologne, Germany. [7]Deutsches Elektronen-Synchrotron DESY, Notkestr. 85, 22607 Hamburg, Germany. [8]European Synchrotron Radiation Facility, BP 220, 38043 Grenoble Cedex, France. [9]Center for Advanced Radiation Sources, University of Chicago, Chicago, IL 60637, USA.
*Corresponding author. Email: alena.aslandukova@uni-bayreuth.de

and experiments (i.e., many predicted Y-H compounds have not been found so far, predicted T_C notably different from reported ones, etc.), some puzzling results, such as negative resistance for YH_6 at 183 GPa (*8*), and very different T_C onsets from experiment to experiment (*27*).

Complex chemical reactions, which occur upon the synthesis of hydrides at high pressures, often strongly complicate the analysis and interpretation of the results. In experiments conducted in DACs, carbon is unavoidable and upon LH can participate in the chemical reactions. In particular, it has been shown that in laser-heated DACs yttrium carbides appear along with yttrium hydrides (*28*). So far, structures of high-pressure yttrium hydrides mentioned above have been determined from powder x-ray diffraction (XRD) data with the assistance of computations based on various structure search algorithms. Powder XRD patterns of the reaction products obtained by LH yttrium in hydrogen-containing precursors (NH_3BH_3 or paraffin oil) (*7*, *8*, *11*, *29*, *30*) are often complex due to overlapping reflections from many compounds, which make phase identification and structural analysis difficult and ambiguous. Moreover, there are reports on still unknown phases whose structures could not be solved from powder XRD data (*7*, *8*).

Here, we present the results of the first single-crystal XRD (SCXRD) studies of the Y-NH_3BH_3 and Y–paraffin oil systems in the laser-heated DACs under high-pressure, high-temperature conditions up to ~170 GPa and ~3000 K. The extremely rich chemistry of the synthesized high-pressure yttrium compounds (hydrides and carbides) was observed. Besides two known solids (*cF*4-YH_3 and *tI*2-YH_3), five previously unknown yttrium hydrides (*hP*3-Y_3H_{11}, *hP*2-Y_2H_9, *cP*8-Y_4H_{23}, *hP*26-$Y_{13}H_{75}$, and *cF*80-Y_4H_{25}), two previously unknown yttrium allotropes (*hP*3-Y-II and *tI*8-Y), and an yttrium carbide (YC_2) have been found. They were all characterized experimentally and through density functional theory (DFT) calculations. Our results demonstrate the broad compositional and structural variety of possible phases in Y-NH_3BH_3 and Y–paraffin oil systems.

RESULTS

The details of the sample preparation, data collection, structure determination, and refinement are described in the Supplementary Materials (see Supplementary Text, fig. S1, and table S1). The hydrides were obtained in DACs via LH up to ~3000 K the starting material, i.e., yttrium, loaded along with one of two kinds of hydrogen-rich precursors—ammonia borane (NH_3BH_3) or paraffin oil (C_nH_{2n+2})—which also act as pressure transmitting media. The use of these hydrogen sources has already been demonstrated to be an effective alternative to pure hydrogen for DAC synthesis experiments in many studies (*7*, *8*, *11*, *15*, *16*, *29*–*32*). Concerning the potential contamination of the system with carbon from paraffin oil, the use of pure H_2 in experiments in laser-heated DACs does not bring a substantial advantage, as carbon from diamond anvils is always present in the system. Each sample was pressurized to the target pressure, laser-heated, and then characterized by in situ synchrotron SCXRD. The details of all DAC experiments and a list of obtained phases are provided in table S1. The positions of nonhydrogen atoms in the crystal structures of yttrium hydrides synthesized in this work were determined from synchrotron SCXRD data; the positions of H atoms could not be constrained from the SCXRD data, and therefore, hydrogen content was estimated from the volume per yttrium atom (see Methods). The possible models of hydrogen arrangement in yet unknown hydrides were analyzed with the help of the Endeavour software (*33*) and then refined by DFT calculations when possible (for more details, see Supplementary Text and fig. S2 in the Supplementary Materials).

Yttrium allotropes

Structural transformations of yttrium upon compression to more than 180 GPa at room temperature are well described in the literature (*34*). A recent study of the high-pressure (up to ~50 GPa) behavior of Y and Y-H systems under high temperatures (*32*) showed that LH affects the experimental results and revealed the *hP*3-Y yttrium allotrope (hereafter, this phase will be referred to as *hP*3-Y-I) and its hydride. In this work, after LH of yttrium at pressures of 120 and 138 GPa (tables S2 and S3 and fig. S3), two novel yttrium allotropes (*hP*3-Y-II and *tI*8-Y) were found. The volume per yttrium atom for both novel allotropes perfectly agrees with previously published data on the yttrium's equation of state (EoS) (fig. S4) (*34*). SCXRD data unambiguously exclude any other nonhydrogen atoms apart from Y in the structures of these two new phases, and the presence of a detectable amount of hydrogen in these materials is excluded based on density considerations.

The Y allotrope found at 120 GPa has a hexagonal symmetry (space group $P\bar{6}m2$). Its unit cell contains three Y atoms distributed over two Wyckoff positions (table S2). As the Pearson symbol of this phase is the same as of the previously known hexagonal yttrium allotrope (*hP*3-Y-I), we designate it as *hP*3-Y-II. The structure consists of tightly packed layers of Y atoms stacked in a "..AAB.." block-sequence manner along the *c* direction (fig. S3A). Distances between yttrium atoms vary from 2.679 to 2.788 Å at 120 GPa.

The yttrium allotrope found at 138 GPa has a tetragonal symmetry (space group *I*4/*mcm*). The Y atoms are located at the 8*h* Wyckoff site (Pearson symbol *tI*8-Y; table S3) and form channels along the *c* direction (fig. S3B; interatomic distances vary from ~2.49 to ~2.84 Å at 138 GPa). While the crystal structure of *tI*8-Y is quite unusual, especially for material synthesized at very high pressures, it is isostructural to the host sublattice of the incommensurate Bi-III phase (*35*). Moreover, such an arrangement of Y atoms was predicted for the host sublattice of a hypothetical host-guest structure of yttrium (*36*). The analysis of our SCXRD data does not reveal any detectable residual electron density in the channels.

The full structural relaxations with fixed (experimental) volume for both Y allotropes reveal a substantial difference between the calculated pressure value and the experimental one (table S2 and fig. S4). Nevertheless, when considering DFT relaxations above 70 GPa for all Y allotropes known in the literature at these pressures [*oF*16 and *hR*24 (*34*)], they exhibit the same inconsistency (fig. S4). This further supports our interpretation that these yttrium phases obtained in our experiments are pure.

As mentioned above, yttrium undergoes several phase transitions upon compression at ambient temperature (*34*). For the pressure range relevant to our study, DFT enthalpy calculations reproduce the well-known *hR*24-Y → *oF*16-Y phase transition at 106 GPa (fig. S5) (*34*). The previously unknown *hP*3-Y-II and *tI*8-Y yttrium allotropes are not thermodynamically stable with respect to the competing phases. Considering that at ~120 GPa the enthalpy difference of the previously unknown *hP*3-Y-II and *tI*8-Y yttrium allotropes with the known *oF*16-Y phase is significant (~0.20 and ~0.32 eV/atom, correspondingly; fig. S5) and cannot be

explained only by the temperature contribution (k_BT is equal to 0.259 eV at 3000 K), the reason for the formation of the two phases, *hP*3-Y-II and *tI*8-Y, remains unclear.

The improvement of modern synchrotron x-ray sources and the recently developed methodology of diffraction analysis of polycrystalline samples allowed us to find two known and five previously unknown yttrium hydrides apart of the yttrium allotropes described above (table S1 and Fig. 1). They could form due to temperature gradients during LH and due to possible differences in hydrogen diffusion into the depth of the metal in different samples. A detailed description of these compounds is given below.

Previously known yttrium hydrides: YH_3 and YH_4

The previously known cubic yttrium hydride *cF*4-YH_3 (Fig. 1 and table S4) was obtained after sample LH, regardless of the hydrogen precursor, at five different pressures: 87, 90, 100, 116, and 120 GPa. The crystallographic data and refinement parameters at all pressures are summarized in table S4. Phonon dispersion calculations in the harmonic approximation showed the dynamical stability of this phase in the whole studied pressure range (fig. S6A). The pressure dependence of the unit cell volume is shown in fig. S7 and is in a good agreement with the DFT calculations. The mutual agreement of experimental and theoretical results allows us to conclude that the structural model of *cF*4-YH_3 (i.e., the location of hydrogen atoms) and the used Vienna Ab initio Simulation Package (VASP) potentials are correct (see Methods for computational details).

Tetragonal yttrium hydride (*I*4/*mmm*, *tI*2-YH_3; Fig. 1) was found at five different pressures: 87, 90, 100, 116, and 120 GPa (table S5). Yttrium atoms occupy the 2*a* Wyckoff position (0; 0; 0) in the nodes of the body-centered tetragonal lattice. Two phases with different stoichiometries, *tI*2-YH_3 (*8*, *37*) and *tI*2-YH_4 (*7*, *8*), were reported to have similar Y atom arrangement in structures with different *a*/*c* ratios: 0.6819 and 0.5303 at 150 GPa, respectively. The experimentally determined pressure dependence of the unit cell volume of the hydrides is shown in fig. S7. For experiments in which paraffin was used as a hydrogen source, there is a good agreement with the DFT results for the *tI*2-YH_3 model, whereas, for the experiment with ammonia borane, the DFT calculated unit cell volume is much closer to

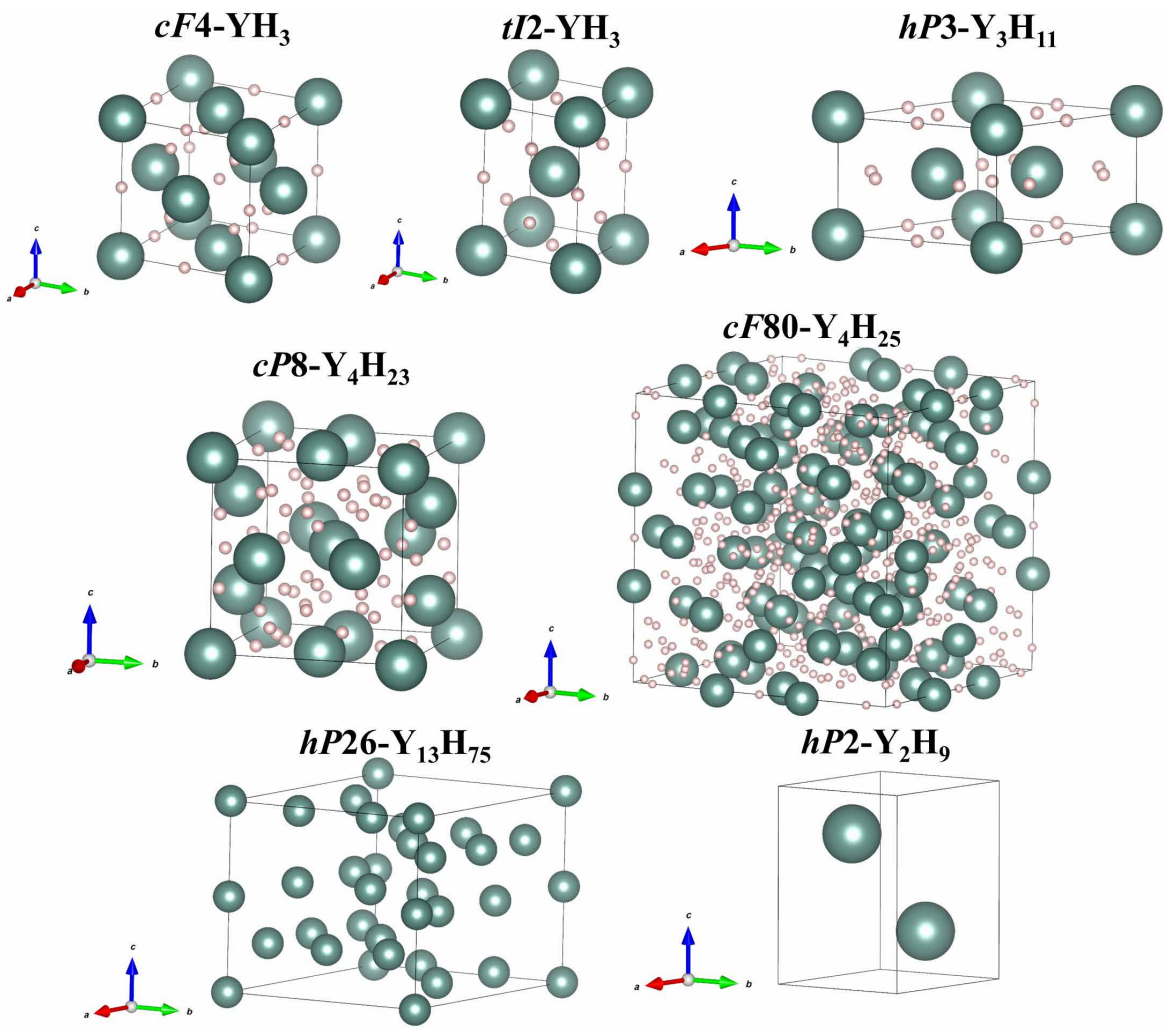

Fig. 1. The crystal structures of the yttrium hydrides synthesized in this work. Yttrium and hydrogen atoms are shown in green and light pink, respectively. For Y_2H_9 and $Y_{13}H_{75}$, only the Y metal framework is shown.

that corresponding to the YH_4 composition. However, the *a*/*c* ratios for all experimental *tI*2 phases are similar within the experimental uncertainties and differ a lot from values reported for the YH_4 phase (*7*, *8*). Thus, the differences in the volume per yttrium atom among *tI*2 yttrium hydrides (fig. S7) could be explained by the variable hydrogen content depending on hydrogen precursors. The cubic phase synthesized in the DACs with paraffin oil has a volume per Y atom systematically smaller than the tetragonal one (fig. S7) that suggests a lower hydrogen content, which can be reflected in the chemical formula as $YH_{3-\delta}$. The *tI*2 phase obtained from ammonia borane has a larger atomic volume and is thus expected to have the $YH_{3+\delta}$ composition. For an ideal YH_3 stoichiometry, theoretical calculations show no difference in volume and enthalpy between the *cF*4 and *tI*2 phases. Phonon calculations demonstrate that hydrides with the YH_3 composition are dynamically stable at all experimental pressures (fig. S6, A and B), while YH_4 can be stabilized only at 140 GPa (fig. S6, C and D), which is in good agreement with previously published experimental results, in which this phase was seen above 135 GPa (*7*, *8*).

Previously unknown yttrium hydrides synthesized in this work

The analysis of SCXRD data revealed five phases with a so far unknown arrangement of yttrium atoms. The shortest Y-Y distances in each of the five previously unknown yttrium-based compounds are remarkably larger than those in pure yttrium metal under the same conditions (table S6). Neither boron, carbon, nor nitrogen was detected by SCXRD data analysis in these structures, which allows classifying the novel phases as hydrides.

For these yttrium hydrides, the hydrogen contents were estimated using the "Retger's law" approximation, which is based on the empirical linear relationship between composition and the unit cell volume (fig. S8; for more details, see the Supplementary Materials). The obtained hydrides' stoichiometries were then used for proposing structural models. For this purpose, we applied our original approach involving the application of Endeavour software and DFT calculations: Possible arrangements of hydrogen atoms for given stoichiometries were proposed by Endeavour, and the following validation of the structure models was done by DFT. The details of this approach are described explicitly in Supplementary Text.

The reaction between Y and paraffin oil at 87 GPa and between Y and ammonia borane at both 90 and 120 GPa led to the formation of the *hP*3-Y-I (*32*)–based hydride (space group *P*6/*mmm*; Fig. 1 and table S7). At 120 GPa, it has a lattice parameter of $a = 4.978(3)$ Å and $c = 3.0784(15)$ Å [$V = 66.06(9)$ Å^3]. The *hP*3-YH_x hydrides with variable stoichiometry ($x = 2.4..3$) have been reported, but the arrangement of hydrogen atoms has not been proposed yet (*32*). In this study, the estimated stoichiometry at all experimental pressures is $Y_3H_{11} = YH_{3.77}$ (fig. S8, B and C), which differs from previously published results at lower pressures (*32*). A possible structural model for the Y_3H_{11} hydride is shown in Fig. 1 and fig. S9, and the corresponding crystallographic data are summarized in table S8.

There are a few yttrium hydrides, which we observed only at a single pressure point (table S9). The $YH_{4.5}$ hydride, whose stoichiometry in integer numbers is Y_2H_9, was obtained at 120 GPa (Fig. 1 and table S9). Yttrium atoms have the hexagonal close-packed (*hcp*) arrangement (*P*6$_3$/*mmc*, *hP*2). The lattice parameters at 120 GPa are $a = 3.162(3)$ Å and $c = 4.958(2)$ Å [$V = 42.94(9)$ Å^3]. The same *hcp* yttrium framework was reported in *hP*2-YH_9 synthesized above 180 GPa (*7*); however, according to Retger's law approximation, in our experiment, the volume per atom suggested half as less hydrogen content. It is impossible to find a reliable DFT-verified crystal structure of Y_2H_9, because the lattice symmetry does not allow placing an odd number of hydrogen atoms with full chemical occupancy in the unit cell, so one can assume either partial occupancy of some hydrogen positions or a symmetry reduction due to the hydrogen sublattice.

At 138 GPa, after LH yttrium in paraffin oil, two previously unknown yttrium hydrides were found: $YH_{5.77}$ ($Y_{13}H_{75}$, the closest stoichiometry in integer numbers) and $YH_{5.75}$ (Y_4H_{23}) (Fig. 1 and table S9). The structure formed by the Y atoms in $Y_{13}H_{75}$ has a hexagonal symmetry (space group *P*6$_3$/*mmc*, *hP*26). At 138 GPa, it has the lattice parameters of $a = 8.9730(13)$ Å and $c = 8.9085(8)$ Å [$V = 621.17(19)$ Å^3]. The DFT structure relaxation of several of the created structural models of the hydride with the $Y_{13}H_{75}$ composition resulted in a high disagreement with experimental data and showed dynamical instability of all of them. Thus, there is no reliable model for the H atoms' location in the structure of $Y_{13}H_{75}$ yet.

According to our calculations, the Y_4H_{23} hydride adopts the Na_4Si_{23}-type structure (*Pm*$\bar{3}$*n*, *cP*8) (Fig. 1 and table S9), which has previously been experimentally seen and/or theoretically predicted for the three metal hydrides M_4H_{23}, where *M* = Ba (*38*), La (*31*), and Eu (*39*, *40*). The DFT structure relaxation shows a very good agreement with the experimental data (table S10), and *cP*8-Y_4H_{23} was found to be dynamically stable at the experimentally produced pressure of 138 GPa (Fig. 2C). This compound has two isolated H atoms (H1 and H3) and hydrogen dimers H2-H2 with an intramolecular bond length of 0.95 Å; therefore, one can suggest that the electronic state of these two kinds of hydrogen atoms has to be very different. For a deeper understanding of the electronic properties of Y_4H_{23}, we calculated the electronic band structure and the electronic density of states (eDOS) at the synthesis pressure of 138 GPa. It was found that this compound exhibits metallic properties and the main contribution at the Fermi level comes from the Y *d*-states, while hydrogen makes quite small contributions (fig. S10A). Previously, it was shown that strong Y-H hybridization could be responsible for the superconductivity in *cF*4-YH_3 and *cI*2-YH_6 (*26*). For Y_4H_{23}, there is a negligible overlap of Y- and H-eDOS (no strong Y-H hybridization), and therefore, this compound is not expected to be a high-temperature superconductor (*26*).

The Y_4H_{25} (= $YH_{6.25}$) compound was synthesized upon laser-heating yttrium and paraffin oil at 171 GPa (Fig. 1 and table S11). Yttrium atoms form a cubic structure (space group *F*$\bar{4}$3*m*, *cF*80) with a large unit cell [$a = 12.4201(14)$ Å, $V = 1915.9(4)$ Å^3]. The full relaxation of the obtained hydride shows perfect agreement with the experimental data (table S11). Hydrogen triatomic units found in this compound have an intramolecular bond length of 0.93 Å, which is shorter than the H-H distance of the dimers constituting Y_4H_{23}. The calculations of eDOS at the synthesis pressure of 171 GPa showed the metallic nature of *cF*80-Y_4H_{25}, with the ratio of hydrogen/yttrium's partial density of states at the Fermi level being higher than that in *cP*8-Y_4H_{23} (fig. S10B).

The yttrium hydride *cI*2-YH_6 (*Im*$\bar{3}$*m*), widely discussed in the literature (*7*, *8*, *24*–*26*), was not observed in this work. As reported in (*7*), YH_6 was obtained by keeping YH_3 in a hydrogen pressure medium at room temperature and pressures of over 100 GPa for a dozen hours. Calculated convex hulls of the Y-H system (*8*) showed

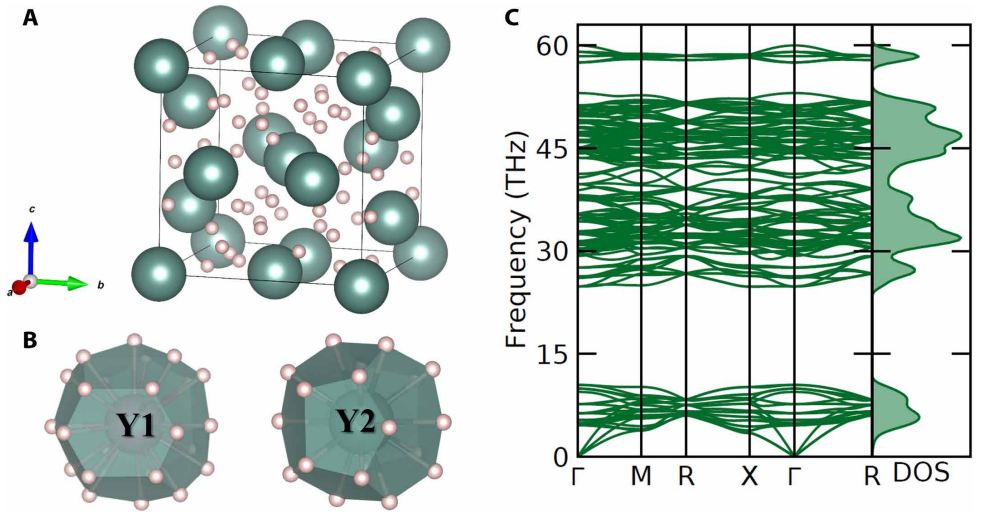

Fig. 2. Crystal structure and the results of DFT phonon calculations for the *cP*8-Y_4H_{23} yttrium hydride. (**A**) Compound's unit cell, with the Y atoms shown as green and hydrogen atoms as light pink balls. (**B**) Coordination environment of the Y1 and Y2 atoms in Y_4H_{23}. (**C**) Phonon dispersion curves along high-symmetry directions in the Brillouin zone and phonon density of states for Y_4H_{23} calculated at 138 GPa.

that *cI*2-YH_6 is metastable even at 150 GPa and lays 30 meV per atom above the convex hull. This may mean that yttrium hexahydride was observed in the experiments below 150 GPa (*7*, *24*) only due to the temperature factor. Our calculations of the convex hull for phases with available structural models at 90, 120, 138, and 171 GPa showed that Y_3H_{11}, Y_4H_{23}, and Y_4H_{25} lay slightly above the convex hull (fig. S11). Among them, Y_4H_{23} is preferable at all pressures. At 150 GPa, the hydrides with a higher hydrogen content, *aP*2-YH_7, *cF*4-YH_9, and *hP*2-YH_9, were predicted to be stable (*8*). The hydride synthesized in this work with the highest hydrogen content, *cF*80-Y_4H_{25}, was the only phase found at 171 GPa, and the calculated convex hull suggests that it is thermodynamically not preferable. The temperature contribution to the energy, k_BT equal to 0.259 eV at 3000 K, could play an important role in the hydride's formation, and rapid quenching down to room temperature could stabilize the metastable phase.

The idea that with increasing pressure the H:Y ratio should increase is common in the literature (*8*, *31*). Our results support this idea: The hydrogen content per yttrium atom increases from 3 at 87 GPa (YH_3, both *cF*4 and *tI*2) to 6.25 at 171 GPa (*cF*80-Y_4H_{25}) (Fig. 3).

Yttrium carbide

Apart from hydrogen, paraffin oil and ammonia borane also contain carbon, nitrogen, and boron, which can react with yttrium, resulting in the formation of various yttrium compounds. In our experiments at 87 and 120 GPa with paraffin oil, we found a previously unknown yttrium carbide, YC_2.

In the structure of YC_2 ($P6_3/mmc$, *hP*2), the yttrium atoms occupy the 2*c* Wyckoff position (1/3; 2/3; 3/4) forming a hexagonal close packing. The carbon atoms C1 and C2 are located at the 2*a* (0; 0; 0) and 2*d* (1/3; 2/3; 1/4) Wykoff positions, respectively (fig. S12A). The lattice parameters at 120 GPa are a = 3.600(17) Å and c = 4.439(8) Å [V = 49.82(13) Å^3]. A similar metal-carbon framework was reported for $LaCH_2$ synthesized at 96 GPa (*31*); however, our detailed analysis showed that the high remaining electronic density at the 2*d* position can be better described as an additional carbon atom C2, instead of H_2 units. Y is surrounded by 11 carbon atoms (6·C1 and 5·C2), with an average Y—C bond length of 2.25 Å (fig. S12B). The unit cell parameters, atomic coordinates, and pressure obtained from DFT structure relaxation agree with the experimental data (table S12).

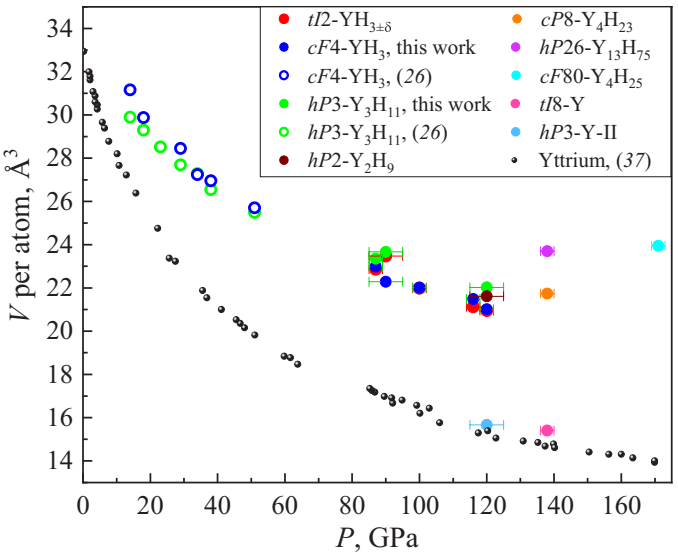

Fig. 3. The pressure dependence of the volume per Y atom in the range of 1 bar to 170 GPa for the Y allotropes and the hydrides as determined from the experimental data. The data for the hexagonal *hP*3-Y-II and tetragonal *tI*8-Y allotropes, for *tI*2-$YH_{3\pm\delta}$, *cF*4-YH_3, *hP*3-Y_3H_{11}, *hP*2-Y_2H_9, *cP*8-Y_4H_{23}, *cF*80-Y_4H_{25}, and *hP*26-$Y_{13}H_{75}$, which were obtained in this work, are shown in red, blue, green, brown, orange, cyan, and violet circles, respectively. The experimental pressure dependence of the volume per Y atom for yttrium allotropes published in (*34*) is shown in small black circles; the experimental values for *cF*4-YH_3 and *hP*3-Y_3H_{11} from (*32*) are shown as open blue and green symbols, respectively. Pearson symbols refer to the arrangement and content of Y atoms only.

DISCUSSION

To summarize, in this work, the complexity of the chemical processes in the Y-NH_3BH_3 and the Y–paraffin oil systems at high pressures and high temperatures was proven due to the analysis of products of chemical reactions in DACs after LH, which revealed inhomogeneous mixtures of various phases at a pressure range of 87 to 171 GPa. Seven yttrium hydrides YH_x (x = 3 to 6.25), two previously unknown yttrium allotropes, and one carbide YC_2 were detected and characterized using synchrotron SCXRD. The hydrogen content in the discovered hydrides was found to increase with pressure, i.e., from YH_3 at 87 GPa to $YH_{6.25}$ at 171 GPa.

Theory is not yet able to predict all possible hydride and nonhydride phases, and powder XRD is prone to missing some reaction products in laser-heated DACs. The presence of phases other than yttrium hydrides, especially compounds with metallic conductivity, can lead to a sharp drop in the electrical resistance of a sample upon low-temperature measurements and the misinterpretation of the results. Therefore, knowledge of the phase composition, crystal structures, and transport properties of individual phases is needed for unambiguous judgment on the electronic properties of complex hydride systems. Our results point out substantial difficulties in producing monophase samples using paraffin oil and NH_3BH_3 precursors, which are necessary for a reliable assessment of the physical properties of materials, including superconductivity, and promote the use of SCXRD on polycrystalline samples as an essential tool for hydrides' characterization.

METHODS

Sample preparation

The BX90-type large x-ray aperture DAC equipped with Boehler-Almax–type diamonds (culet diameter of DAC1, DAC2, DAC3, and DAC5 is 120 μm, while that of DAC4 is 80 μm) was used for SCXRD studies (*41*, *42*). Rhenium foil preindented to a thickness of ~20 or ~13 μm and a hole of ~60 or ~40 μm in diameter drilled in the center of the indentation served as a sample chamber, for 120- and 80-μm culets, respectively. A piece of yttrium was placed in the sample chamber filled with paraffin oil (DAC1 to DAC4) or NH_3BH_3 (DAC5). Pressure was determined using the EoS of Re (*43*, *44*) and additionally monitored by the Raman signal from the diamond anvils (*45*). Samples were compressed up to their target pressure and laser-heated to ~3000(200) K. LH of the samples was performed using an in-house LH setup (*46*), equipped with two yttrium-aluminum-garnet (YAG) lasers (1064 nm central wavelength) and an IsoPlane SCT 320 spectrometer with a 1024 × 2560 PI-MAX 4 camera for collection of thermal emission spectra from the heated spot. Temperatures were estimated by fitting of thermal emission spectra of the sample to the gray body approximation of Planck's radiation function over a given λ range (570 to 830 nm).

XRD measurements

XRD measurements for DAC1 (at 87 GPa) and DAC4 (at 138 GPa) were performed at the ID11 beamline of the European Synchrotron Radiation Facility (ESRF; Grenoble, France) with the x-ray beam (λ = 0.2844 Å) focused down to 0.75 μm × 0.75 μm, and data were collected with the Eiger2X CdTe 4M hybrid photon-counting pixel detector. XRD measurements for DAC5 (at 90 GPa) and DAC4 (at 171 GPa) were performed at the ID27 beamline of the ESRF with the x-ray beam (λ = 0.3738 Å) focused down to 1.5 μm × 1.5 μm. DAC5 (at 120 GPa) was measured at the ID15B beamline (ESRF) with an x-ray beam (λ = 0.4103 Å) focused to a size of 4 μm × 4 μm. At ID27 and ID15B, the XRD patterns were collected on an Eiger2X CdTe 9M hybrid photon-counting pixel detector. XRD measurements for DAC2 and DAC3 were done at the GSECARS 13IDD beamline of the Advanced Photon Source (APS; Lemont, USA; λ = 0.2952 Å, 2 μm × 2 μm), and data were collected with Pilatus 1M detector. The data for DAC1 (at 116 GPa) were collected at the P02.2 beamline of Petra III [Deutsches Elektronen-Synchrotron (DESY), Hamburg, Germany] with the x-ray beam (λ = 0.2882 Å) focused down to 1.8 μm × 2 μm by a Kirkpatrick-Baez mirror system, and diffraction patterns were collected on a PerkinElmer 1621 XRD flat-panel detector.

For SCXRD measurements, samples were rotated around the vertical ω axis in a range of ±36°. The XRD images were collected with an angular step Δω = 0.5°. The CrysAlisPro software package was used for the analysis of the SCXRD data (indexing, data integration, frame scaling, and absorption correction) (*47*). A single crystal of $(Mg_{1.93},Fe_{0.06})(Si_{1.93},Al_{0.06})O_6$ orthoenstatite [*Pbca*, a = 18.2391(3), b = 8.8117(2), c = 5.18320(10) Å] was used to calibrate the instrument model of the CrysAlisPro software (sample-to-detector distance, the detector's origin, offsets of the goniometer angles, and rotation of the x-ray beam and the detector around the instrument axis). The DAFi program (*48*) was used for the search of reflections' groups belonging to individual single-crystal domains. Using the OLEX2 software package (*49*), the structures were solved with the ShelXT structure solution program (*50*) using intrinsic phasing and refined with the ShelXL (*51*) refinement package using least-squares minimization. The procedure of the analysis of the SCXRD data is described explicitly in Supplementary Text in the Supplementary Materials. Crystal structure visualizations were made with the VESTA software (*52*). The experimental EoSs were obtained by fitting the pressure-volume data using the EoSFit7-GUI (*53*).

Computational details

The first-principles calculations were done using the framework of DFT as implemented in the VASP (*54*). To expand the electronic wave function in plane waves, we used the projector-augmented-wave (PAW) method (*55*, *56*). The generalized gradient approximation (GGA) functional was used for calculating the exchange-correlation energies, as proposed by Perdew-Burke-Ernzerhof (PBE) (*57*). The PAW potentials with following valence electrons of 4*s*4*p*5*s*4*d* for Y, 1*s* for H (the potential "H_h"-harder than the standard potential), and 2*s*2*p* for C were used. The Monkhorst-Pack (*58*) k-point grid and an energy cutoff for the plane wave expansion were selected on the basis of convergence tests with a threshold of 2 meV per atom for energy and 1 meV/Å per atom for forces. The phonon frequencies and phonon band structure calculations were performed in the harmonic approximation with the help of the PHONOPY software (*59*) using the density-functional-perturbation theory (DFPT) for yttrium hydrides. The tetrahedron method was used for Brillouin zone integrations (*60*). EoS and static enthalpy calculations were performed via variable-cell structural relaxations between 70 and 170 GPa. In our calculations, temperature, configurational entropy, and the entropy contribution due to lattice vibrations were neglected.

Supplementary Materials

This PDF file includes:

Supplementary Text
Figs. S1 to S12
Tables S1 to S12
Legends for data S1 to S8

Other Supplementary Material for this manuscript includes the following:

Data S1 to S8

REFERENCES AND NOTES

1. A. Schilling, M. Cantoni, J. Guo, H. R. Ott, Superconductivity above 130 K in the Hg–Ba–Ca–Cu–O system. *Nature* **363**, 56–58 (1993).
2. J. Nagamatsu, N. Nakagawa, T. Muranaka, Y. Zenitani, J. Akimitsu, Superconductivity at 39 K in magnesium diboride. *Nature* **410**, 63–64 (2001).
3. A. P. Drozdov, M. I. Eremets, I. A. Troyan, V. Ksenofontov, S. I. Shylin, Conventional superconductivity at 203 kelvin at high pressures in the sulfur hydride system. *Nature* **525**, 73–76 (2015).
4. A. P. Drozdov, P. P. Kong, V. S. Minkov, S. P. Besedin, M. A. Kuzovnikov, S. Mozaffari, L. Balicas, F. F. Balakirev, D. E. Graf, V. B. Prakapenka, E. Greenberg, D. A. Knyazev, M. Tkacz, M. I. Eremets, Superconductivity at 250 K in lanthanum hydride under high pressures. *Nature* **569**, 528–531 (2019).
5. L. Ma, K. Wang, Y. Xie, X. Yang, Y. Wang, M. Zhou, H. Liu, X. Yu, Y. Zhao, H. Wang, G. Liu, Y. Ma, High-temperature superconducting phase in clathrate calcium hydride CaH_6 up to 215 K at a Pressure of 172 GPa. *Phys. Rev. Lett.* **128**, 167001 (2022).
6. W. Chen, D. V. Semenok, A. G. Kvashnin, X. Huang, I. A. Kruglov, M. Galasso, H. Song, D. Duan, A. F. Goncharov, V. B. Prakapenka, A. R. Oganov, T. Cui, Synthesis of molecular metallic barium superhydride: Pseudocubic BaH_{12}. *Nat. Commun.* **12**, 273 (2021).
7. P. Kong, V. S. Minkov, M. A. Kuzovnikov, A. P. Drozdov, S. P. Besedin, S. Mozaffari, L. Balicas, F. F. Balakirev, V. B. Prakapenka, S. Chariton, D. A. Knyazev, E. Greenberg, M. I. Eremets, Superconductivity up to 243 K in the yttrium-hydrogen system under high pressure. *Nat. Commun.* **12**, 5075 (2021).
8. I. A. Troyan, D. V. Semenok, A. G. Kvashnin, A. V. Sadakov, O. A. Sobolevskiy, V. M. Pudalov, A. G. Ivanova, V. B. Prakapenka, E. Greenberg, A. G. Gavriliuk, I. S. Lyubutin, V. V. Struzhkin, A. Bergara, I. Errea, R. Bianco, M. Calandra, F. Mauri, L. Monacelli, R. Akashi, A. R. Oganov, Anomalous high-temperature superconductivity in YH_6. *Adv. Mater.* **33**, 2006832 (2021).
9. N. P. Salke, M. M. Davari Esfahani, Y. Zhang, I. A. Kruglov, J. Zhou, Y. Wang, E. Greenberg, V. B. Prakapenka, J. Liu, A. R. Oganov, J.-F. Lin, Synthesis of clathrate cerium superhydride CeH_9 at 80–100 GPa with atomic hydrogen sublattice. *Nat. Commun.* **10**, 4453 (2019).
10. D. Zhou, D. V. Semenok, D. Duan, H. Xie, W. Chen, X. Huang, X. Li, B. Liu, A. R. Oganov, T. Cui, Superconducting praseodymium superhydrides. *Sci. Adv.* **6**, 6849–6877 (2020).
11. D. V. Semenok, A. G. Kvashnin, A. G. Ivanova, V. Svitlyk, V. Y. Fominski, A. V. Sadakov, O. A. Sobolevskiy, V. M. Pudalov, I. A. Troyan, A. R. Oganov, Superconductivity at 161 K in thorium hydride ThH_{10}: Synthesis and properties. *Mater. Today* **33**, 36–44 (2020).
12. I. A. Kruglov, A. G. Kvashnin, A. F. Goncharov, A. R. Oganov, S. S. Lobanov, N. Holtgrewe, S. Jiang, V. B. Prakapenka, E. Greenberg, A. V. Yanilkin, Uranium polyhydrides at moderate pressures: Prediction, synthesis, and expected superconductivity. *Sci. Adv.* **4**, eaat9776 (2018).
13. J. E. Hirsch, F. Marsiglio, Unusual width of the superconducting transition in a hydride. *Nature* **596**, E9–E10 (2021).
14. X. Huang, X. Wang, D. Duan, B. Sundqvist, X. Li, Y. Huang, H. Yu, F. Li, Q. Zhou, B. Liu, T. Cui, High-temperature superconductivity in sulfur hydride evidenced by alternating-current magnetic susceptibility. *Natl. Sci. Rev.* **6**, 713–718 (2019).
15. T. Meier, F. Trybel, S. Khandarkhaeva, G. Steinle-Neumann, S. Chariton, T. Fedotenko, S. Petitgirard, M. Hanfland, K. Glazyrin, N. Dubrovinskaia, L. Dubrovinsky, Pressure-induced hydrogen-hydrogen interaction in metallic FeH revealed by NMR. *Phys. Rev. X* **9**, 031008 (2019).
16. T. Meier, F. Trybel, G. Criniti, D. Laniel, S. Khandarkhaeva, E. Koemets, T. Fedotenko, K. Glazyrin, M. Hanfland, M. Bykov, G. Steinle-Neumann, N. Dubrovinskaia, L. Dubrovinsky, Proton mobility in metallic copper hydride from high-pressure nuclear magnetic resonance. *Phys. Rev. B* **102**, 165109 (2020).
17. J. E. Hirsch, F. Marsiglio, Absence of magnetic evidence for superconductivity in hydrides under high pressure. *Phys. C Supercond. Appl.* **584**, 1353866 (2021).
18. J. E. Hirsch, F. Marsiglio, Nonstandard superconductivity or no superconductivity in hydrides under high pressure. *Phys. Rev. B* **103**, 134505 (2021).
19. J. E. Hirsch, F. Marsiglio, Clear evidence against superconductivity in hydrides under high pressure. *Matter Radiat. Extrem.* **7**, 058401 (2021).
20. N. Dasenbrock-Gammon, E. Snider, R. McBride, H. Pasan, D. Durkee, N. Khalvashi-Sutter, S. Munasinghe, S. E. Dissanayake, K. V. Lawler, A. Salamat, R. P. Dias, Evidence of near-ambient superconductivity in a N-doped lutetium hydride. *Nature* **615**, 244–250 (2023).
21. D. Khatamian, F. D. Manchester, The H—Y (hydrogen-yttrium) system. *Bull. Alloy Phase Diagr.* **9**, 252–260 (1988).
22. A. Machida, A. Ohmura, T. Watanuki, K. Aoki, K. Takemura, Long-period stacking structures in yttrium trihydride at high pressure. *Phys. Rev. B* **76**, 052101 (2007).
23. A. Machida, A. Ohmura, T. Watanuki, T. Ikeda, K. Aoki, S. Nakano, K. Takemura, X-ray diffraction investigation of the hexagonal-fcc structural transition in yttrium trihydride under hydrostatic pressure. *Solid State Commun.* **138**, 436–440 (2006).
24. E. Snider, N. Dasenbrock-Gammon, R. McBride, X. Wang, N. Meyers, K. V. Lawler, E. Zurek, A. Salamat, R. P. Dias, Synthesis of yttrium superhydride superconductor with a transition temperature up to 262 K by catalytic hydrogenation at high pressures. *Phys. Rev. Lett.* **126**, 117003 (2021).
25. H. Liu, I. I. Naumov, R. Hoffmann, N. W. Ashcroft, R. J. Hemley, Potential high-T_c superconducting lanthanum and yttrium hydrides at high pressure. *Proc. Natl. Acad. Sci. U.S.A.* **114**, 6990–6995 (2017).
26. Y. Li, J. Hao, H. Liu, J. S. Tse, Y. Wang, Y. Ma, Pressure-stabilized superconductive yttrium hydrides. *Sci. Rep.* **5**, 9948 (2015).
27. D. Wang, Y. Ding, H.-K. Mao, Future study of dense superconducting hydrides at high pressure. *Materials* **14**, 7563 (2021).
28. A. Aslandukova, A. Aslandukov, L. Yuan, D. Laniel, S. Khandarkhaeva, T. Fedotenko, G. Steinle-Neumann, K. Glazyrin, N. Dubrovinskaia, L. Dubrovinsky, Novel high-pressure yttrium carbide γ–Y_4C_5 containing $[C_2]$ and nonlinear $[C_3]$ units with unusually large formal charges. *Phys. Rev. Lett.* **127**, 135501 (2021).
29. M. Somayazulu, M. Ahart, A. K. Mishra, Z. M. Geballe, M. Baldini, Y. Meng, V. V. Struzhkin, R. J. Hemley, Evidence for superconductivity above 260 K in lanthanum superhydride at megabar pressures. *Phys. Rev. Lett.* **122**, 027001 (2019).
30. T. Meier, A. Aslandukova, F. Trybel, D. Laniel, T. Ishii, S. Khandarkhaeva, N. Dubrovinskaia, L. Dubrovinsky, In situ high-pressure nuclear magnetic resonance crystallography in one and two dimensions. *Matter Radiat. Extrem.* **6**, 068402 (2021).
31. D. Laniel, F. Trybel, B. Winkler, F. Knoop, T. Fedotenko, S. Khandarkhaeva, A. Aslandukova, T. Meier, S. Chariton, K. Glazyrin, V. Milman, V. Prakapenka, I. A. Abrikosov, L. Dubrovinsky, N. Dubrovinskaia, High-pressure synthesis of seven lanthanum hydrides with a significant variability of hydrogen content. *Nat. Commun.* **13**, 6987 (2022).
32. A. Aslandukova, A. Aslandukov, D. Laniel, S. Khandarkhaeva, G. Steinle-Neumann, T. Fedotenko, S. V. Ovsyannikov, Y. Yin, F. I. Akbar, K. Glazyrin, M. Hanfland, L. Dubrovinsky, N. Dubrovinskaia, High-pressure *hP3* yttrium allotrope with $CaHg_2$-type structure as a prototype of the *hP3* rare-earth hydride series. *Phys. Rev. B* **107**, 014103 (2023).
33. H. Putz, J. C. Schön, M. Jansen, Combined method for *ab initio* structure solution from powder diffraction data. *J. Appl. Cryst.* **32**, 864–870 (1999).
34. E. J. Pace, S. E. Finnegan, C. V. Storm, M. Stevenson, M. I. McMahon, S. G. MacLeod, E. Plekhanov, N. Bonini, C. Weber, Structural phase transitions in yttrium up to 183 GPa. *Phys. Rev. B* **102**, 094104 (2020).
35. D. Kartoon, G. Makov, Structural and electronic properties of the incommensurate host-guest Bi-III phase. *Phys. Rev. B* **100**, 014104 (2019).
36. P. Tsuppayakorn-aek, T. Bovornratanaraks, R. Ahuja, T. Bovornratanaraks, W. Luo, Existence of yttrium allotrope with incommensurate host–guest structure at moderate pressure: First evidence from computational approach. *Comput. Mater. Sci.* **213**, 111652 (2022).
37. L.-L. Liu, H.-J. Sun, C. Z. Wang, W.-C. Lu, High-pressure structures of yttrium hydrides. *J. Phys. Condens. Matter* **29**, 325401 (2017).
38. W. Jung, H. Kessens, A. Ormeci, W. Schnelle, U. Burkhardt, H. Borrmann, H. D. Nguyen, M. Baitinger, Y. Grin, Synthesis, crystal structure and physical properties of the clathrate-I phase $Ba_8Rh_xSi_{46-x-y}$. *Dalton Trans.* **41**, 13960 (2012).
39. L. Ma, M. Zhou, Y. Wang, S. Kawaguchi, Y. Ohishi, F. Peng, H. Liu, G. Liu, H. Wang, Y. Ma, Experimental clathrate superhydrides EuH_6 and EuH_9 at extreme pressure conditions. *Phys. Rev. Res.* **3**, 043107 (2021).
40. D. V. Semenok, D. Zhou, A. G. Kvashnin, X. Huang, M. Galasso, I. A. Kruglov, A. G. Ivanova, A. G. Gavriliuk, W. Chen, N. V. Tkachenko, A. I. Boldyrev, I. Troyan, A. R. Oganov, T. Cui, Novel strongly correlated europium superhydrides. *J. Phys. Chem. Lett.* **12**, 32–40 (2021).
41. I. Kantor, V. Prakapenka, A. Kantor, P. Dera, A. Kurnosov, S. Sinogeikin, N. Dubrovinskaia, L. Dubrovinsky, BX90: A new diamond anvil cell design for x-ray diffraction and optical measurements. *Rev. Sci. Instrum.* **83**, 125102 (2012).
42. R. Boehler, New diamond cell for single-crystal x-ray diffraction. *Rev. Sci. Instrum.* **77**, 115103 (2006).
43. C. S. Zha, W. A. Bassett, S. H. Shim, Rhenium, an in situ pressure calibrant for internally heated diamond anvil cells. *Rev. Sci. Instrum.* **75**, 2409–2418 (2004).
44. S. Anzellini, A. Dewaele, F. Occelli, P. Loubeyre, M. Mezouar, Equation of state of rhenium and application for ultra high pressure calibration. *J. Appl. Phys.* **115**, 043511 (2014).
45. Y. Akahama, H. Kawamura, Pressure calibration of diamond anvil Raman gauge to 310GPa. *J. Appl. Phys.* **100**, 043516 (2006).
46. T. Fedotenko, L. Dubrovinsky, G. Aprilis, E. Koemets, A. Snigirev, I. Snigireva, A. Barannikov, P. Ershov, F. Cova, M. Hanfland, N. Dubrovinskaia, Laser heating setup for diamond anvil cells for in situ synchrotron and in house high and ultra-high pressure studies. *Rev. Sci. Instrum.* **90**, 104501 (2019).

47. CrysAlisPRO. Rigaku Oxford Diffraction. Agilent Technologies UK Ltd., Yarnton, England (2015). https://www.rigaku.com/products/crystallography/crysalis.
48. A. Aslandukov, M. Aslandukov, N. Dubrovinskaia, L. Dubrovinsky, Domain Auto Finder (DAFi) program: The analysis of single-crystal x-ray diffraction data from polycrystalline samples. *J. Appl. Cryst.* **55**, 1383–1391 (2022).
49. O. V. Dolomanov, L. J. Bourhis, R. J. Gildea, J. A. K. Howard, H. Puschmann, OLEX2: A complete structure solution, refinement and analysis program. *J. Appl. Cryst.* **42**, 339–341 (2009).
50. G. M. Sheldrick, SHELXT - Integrated space-group and crystal-structure determination. *Acta Crystallogr. Sect. A Found Crystallogr.* **71**, 3–8 (2015).
51. G. M. Sheldrick, Crystal structure refinement with *SHELXL*. *Acta Crystallogr. C. Struct. Chem.* **71**, 3–8 (2015).
52. K. Momma, F. Izumi, *VESTA 3* for three-dimensional visualization of crystal, volumetric and morphology data. *J. Appl. Cryst.* **44**, 1272–1276 (2011).
53. J. Gonzalez-Platas, M. Alvaro, F. Nestola, R. Angel, *EosFit7-GUI*: A new graphical user interface for equation of state calculations, analyses and teaching. *J. Appl. Cryst.* **49**, 1377–1382 (2016).
54. G. Kresse, J. Furthmüller, Efficiency of ab-initio total energy calculations for metals and semiconductors using a plane-wave basis set. *Comput. Mater. Sci.* **6**, 15–50 (1996).
55. P. E. Blöchl, Projector augmented-wave method. *Phys. Rev. B* **50**, 17953 (1994).
56. G. Kresse, D. Joubert, From ultrasoft pseudopotentials to the projector augmented-wave method. *Phys. Rev. B* **59**, 1758 (1999).
57. J. P. Perdew, K. Burke, M. Ernzerhof, Generalized gradient approximation made simple. *Phys. Rev. Lett.* **77**, 3865–3868 (1996).
58. H. J. Monkhorst, J. D. Pack, Special points for Brillonin-zone integrations. *Phys. Rev. B* **13**, 5188 (1976).
59. A. Togo, I. Tanaka, First principles phonon calculations in materials science. *Scr. Mater.* **108**, 1–5 (2015).
60. P. E. Blöchl, O. Jepsen, O. K. Andersen, Improved tetrahedron method for Brillouin-zone integrations. *Phys. Rev. B* **49**, 16223 (1994).

Acknowledgments: We acknowledge the DESY (PETRA III) for the provision of beamtime at the P02.2 beamline and the ESRF for the provision of beamtime at the ID15b, ID27, and ID11 beamlines. A portion of this work was performed at GeoSoilEnviroCARS (The University of Chicago, Sector 13), APS (13ID-D beamline), and Argonne National Laboratory. Computations were performed at the Leibniz Supercomputing Center of the Bavarian Academy of Sciences and the Humanities and the research center for scientific computing at the University of Bayreuth. **Funding:** M.B. acknowledges the support of Deutsche Forschungsgemeinschaft (DFG Emmy-Noether project BY112/2-1). D.L. thanks the UKRI Future Leaders Fellowship (MR/V025724/1) for financial support. N.D. and L.D. thank the Deutsche Forschungsgemeinschaft (DFG projects DU 954-11/1, DU 393-9/2, DU 393-13/1, and DU 945/15-1) for financial support. N.D. also thanks the Swedish Government Strategic Research Area in Materials Science on Functional Materials at Linköping University (Faculty Grant SFO-Mat-LiU no. 2009 00971). GeoSoilEnviroCARS was supported by the NSF–Earth Sciences (EAR-1634415). This research used resources of the Advanced Photon Source, a US Department of Energy (DOE) Office of Science User Facility operated for the DOE Office of Science by Argonne National Laboratory under contract no. DE-AC02-06CH11357. This work was funded by the Open Access Publishing Fund of the University of Bayreuth. **Author contributions:** A. Aslandukova, L.D., and N.D. designed the work. A. Aslandukova and L.D. prepared the high-pressure experiments. A. Aslandukova, A. Aslandukov, D.L., Y.Y., F.I.A., M.B., T.F., A.P., K.G., G.G., E.L.B., J.W., M.H., S.C., and V.P. performed the synchrotron XRD experiments. A. Aslandukova and L.D. processed the synchrotron XRD data. A. Aslandukova performed the theoretical calculations. A. Aslandukova, A. Aslandukov, and L.D. contextualized the data interpretation. A. Aslandukova, A. Aslandukov, L.D., and N.D. prepared the first draft of the manuscript with contributions from all other authors. **Competing interests:** The authors declare that they have no competing interests. **Data and materials availability:** The details of the crystal structure investigations may be obtained from FIZ Karlsruhe (76344 Eggenstein-Leopoldshafen, Germany) by quoting the deposition numbers CSD 2295619, 2295636, 2295638, 2295639, 2295644, 2295626, 2295645, and 2295620. These data will be available on https://www.ccdc.cam.ac.uk/structures/ after the embargo period, i.e., after 18 July 2024. All CIF files and other information can be found in the main text or in the Supplementary Materials.

Submitted 24 October 2023
Accepted 9 February 2024
Published 13 March 2024
10.1126/sciadv.adl5416

Science Advances
AAAS

Supplementary Materials for

Diverse high-pressure chemistry in Y-NH_3BH_3 and Y–paraffin oil systems

Alena Aslandukova *et al.*

Corresponding author: Alena Aslandukova, alena.aslandukova@uni-bayreuth.de

Sci. Adv. **10**, eadl5416 (2024)
DOI: 10.1126/sciadv.adl5416

The PDF file includes:

Other Supplementary Material for this manuscript includes the following:

Supplementary Text

Discussion 1. Details of the data acquisition and processing for synchrotron single-crystal X-ray diffraction in DACs from laser-heated polycrystalline samples

The high-pressure high-temperature reactions in DACs usually result in multigrain and often multiphase samples. On the synchrotron facilities providing sufficiently small X-ray beam we can study such polycrystalline samples *in situ*, applying methods of SCXRD to individual grains of micrometer to sub-micrometer size. The procedure is briefly described below.

First, we conduct an XRD mapping of the sample chamber to locate various phases within the laser-heated spot. The phases are assigned based on single-crystal XRD and are shown in the resulting 2D XRD map in different colors. In this procedure, XRD is collected stepwise with a step (Δ) equal to the beam size. The number of steps should be sufficient to cover the entire sample chamber.

Figure S1a shows an example of a 2D XRD map for a sample in the chamber of ~30 μm in diameter with a diamond culet size of 80 μm. The map is built upon 961 frames (31x31 points separated by Δ = 1 μm in each direction). The map enables also to pinpoint the location of grains (domains) of the best crystallinity for a particular phase, those giving the richest spotty pattern, thus most appropriate for SCXRD measurements.

The SCXRD is then measured in the selected points while the DAC is rotated around the vertical goniometer axis ω with the frames being collected from ω = -36° to ω = 36° with a step of $\Delta\omega$ = 0.5°. A single frame from the SCXRD dataset at ω = 0° is shown in Fig. S1b. After the collection of the dataset for the selected point, it is analyzed in the CrysAlis^{Pro} software to identify phases and their crystal structures and chemical composition. The general procedure of the multigrain dataset analysis contains the following steps:

- Step 1. Perform the peak search using CrysAlis^{Pro} package. Figure S1c shows the reciprocal space representing all reflections of the dataset for the example under consideration. These can be the reflections from reaction products, initial reagents, pressure-transmitting medium, diamonds, and gasket material.
- Step 2. Apply 'advanced filtering' to get rid of diamond peaks and artifacts.
- Step 3. Find all single-crystal domains in the dataset using DAFi software (Fig. S1d).
- Step 4. Find the lattice parameters of all domains in the dataset using the indexing procedure implemented in CrysAlis^{Pro}.

- Step 5. Select the most strongly diffracting domain for each found phase (Fig. S1e), perform integration, and extract the *.hkl* file.
- Step 6. Solve and refine the crystal structure of each of the different phases found using Olex2 software.

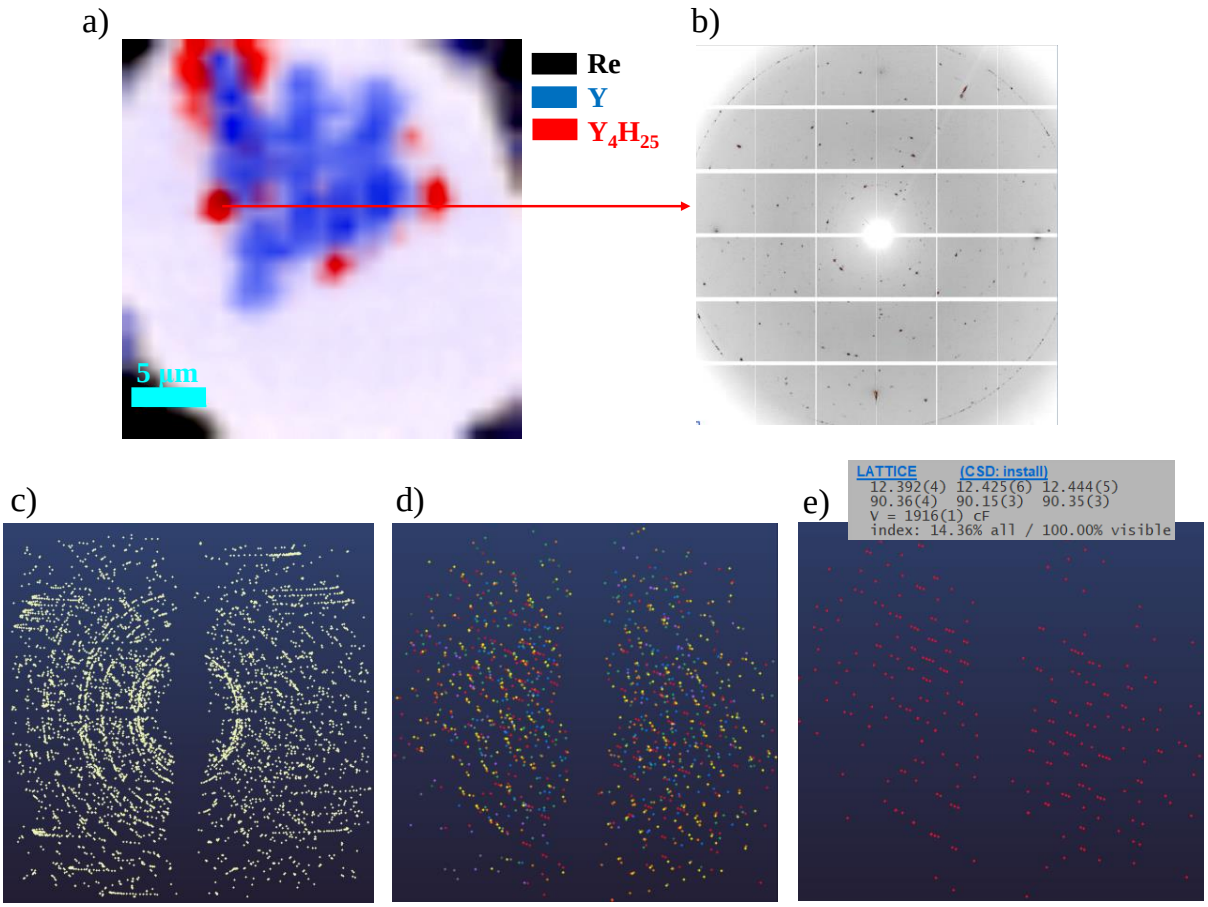

Fig. S1. Illustration of the procedure of the SCXRD data collection from a polycrystalline sample and the data analysis on example of *cF*80-Y_4H_{25} found in a DAC at 171 GPa. a) A 2D XRD map (31x31, Δ=1 μm) of the sample chamber showing the distribution of three phases (coloured in black, red, and blue) in the DAC. Phases assignment is based on single-crystal XRD. b) One frame from the SCXRD dataset taken at ω = 0°. c) All collected reflections of a full dataset displayed in the reciprocal space. d) Eighteen sets of reflections from different domains (marked with different colours) found in this dataset using DAFi software. e) Reflections of the strongest *cF*80-Y_4H_{25} domain found by the DAFi program, for which integration and structure solution were done.

Structural description of novel yttrium allotropes

The hexagonal *hP*3-Y-II ($P\bar{6}m2$) was obtained at 120 GPa after laser heating Y in paraffin oil. At 120 GPa, the unit cell parameters are a = 2.773(4) Å and c = 7.06(2) Å (V = 47.0(2) Å^3). Yttrium atoms occupy two Wyckoff positions: Y1 at 1*a* (0; 0; 0) and Y2 at 2*i* (2/3; 1/3; 0.3043) (Table S2). Y-Y distances vary from 2.679 Å to 2.788 Å.

Tetragonal *tI*2-Y (*I*4/*mcm*) was found at 138 GPa, the unit cell parameters a = 5.3001(10) Å and c = 4.391(3) Å (V = 123.35(8) Å^3) (Table S3). Y atoms are located at 8*h* Wyckoff site (0.17029; 0.67029;0.5).

Structural description of yttrium hydrides

In the cubic *cF*4-YH_3 (space group $Fm\bar{3}m$, Pearson symbol *cF*4 refers to the structure formed by Y atoms), the yttrium atoms occupy the 4*a* Wyckoff position (0; 0; 0) forming the *fcc* lattice. Hydrogen atoms were placed to all octahedral (4*b* Wyckoff position (0.5; 0.5; 0.5)) and tetrahedral voids (8*c* Wyckoff position (0.25; 0.25; 0.25)) according to literature data (*23*).

In tetragonal yttrium hydride (*I*4/*mmm*, Pearson symbol *tI*2 refers to the structure formed by Y atoms) yttrium atoms occupy the 2*a* Wyckoff position (0; 0; 0). This tetragonal structure was reported to have two stoichiometries YH_3 (*8, 37*) and YH_4 (*7, 8*), with different *a*/*c* ratio. In the YH_3 hydrogen atoms occupy 4*d* (0; 0.5; 0.25) and 2*b* (0; 0; 0.5) Wyckoff positions, while in the YH_4 hydrogens are located at 4*e* (0; 0; 0.371) and 4*d* (0; 0.5; 0.25) Wyckoff positions.

The structural models of five novel yttrium hydrides were obtained using an original procedure involving the application of Endeavour™ software and DFT calculations (for more details see discussion 2). They may be not unique, but these models allow us to describe experimental and theoretical results in the best way.

The *hP*3-Y_3H_{11} hydride (space group of Y lattice is *P*6/*mmm*, *hP*3) was observed at 87, 90, and 120 GPa. Yttrium atoms occupy two Wyckoff positions: 1*a* (0; 0; 0) and 2*d* (1/3; 2/3; 1/2). In our proposed structural model, the hydrogen atoms are located at the 2*c* (0.5; 0; 0), 3*f* (2/3; 1/3; 0), and 6*k* (0.24; 0; 0.5) Wyckoff positions. The full structural relaxation perfectly reproduces experimental observations (Table S8). In the structure of *hP*3-Y_3H_{11} yttrium atoms Y1 are surrounded by 8 hydrogen atoms, while Y2 atoms have 18 hydrogen atoms in their first coordination sphere (Fig. S9). This compound has only isolated H atoms because the shortest H-H distance of ~1.13 Å at 120 GPa, that is too long for hydrogen H_2 molecule.

The *hP*2-Y_2H_9 was observed at 120 GPa. Yttrium atoms occupy the 2*c* Wyckoff position (1/3; 2/3; 1/4) forming the *hcp* lattice ($P6_3/mmc$, *hP*2). The lattice parameters at 120 GPa are a = 3.162(3) Å and c = 4.958(2) Å (V = 42.94(9) Å^3). The structural model of hydride with the Y_2H_9 composition was not suggested.

The lattice formed by yttrium in the structure of *hP*26-$Y_{13}H_{75}$ has hexagonal symmetry (space group $P6_3/mmc$, *hP*26). At 138 GPa, it has the unit cell parameters of a = 8.9730(13) Å and c = 8.9085(7) Å (V = 621.17(19) Å^3). Yttrium atoms occupy four crystallographically independent positions: 2*a* (0; 0; 0), 12*k* (0.2041; 0.4083; 0.5629), 6*h* (0.1186; 0.2373; 0.25), and 6*h* (0.4558; 0.9116; 0.25). The analysis of the data from the ICSD showed that this arrangement of metal atoms is known in Hf_9Mo_4B structure type (ICSD 23788) – Y occupies the positions of both Hf and Mo. The structural model of hydride with the $Y_{13}H_{75}$ composition was not suggested.

The *cP*8-Y_4H_{23}, which was obtained at 138 GPa, has a cubic structure ($Pm\bar{3}n$, *cP*8) made of two types of Y atoms: Y1 at 6*d* (0.25; 0.5; 0) and Y2 at 2*a* (0; 0; 0) Wyckoff positions. Y2 atoms form a *bcc* lattice and have twelve Y1 neighbors, each located at the same distance of 3.12043(12) Å at 138 GPa (Table S10). The shortest metal-metal distance is $d_{Y1\text{-}Y1}$ = 2.791 Å. Hydrogen atoms in a suggested structure occupy three different Wyckoff positions: 6*c* (0.25; 0; 0.5), 16*i* (0.201; 0.201; 0.201), and 24*k* (0; 0.3103; 0.1492). The Y2 – H polyhedron is almost a perfect dodecahedron consisting of twelve H_5 pentagons with two types of Y-H distances: $d_{Y2\text{-}H2}$ = 1.921 Å –and $d_{Y2\text{-}H3}$ = 1.943 Å (Fig. 2b). The Y1 atoms surrounded by 24 hydrogen atoms, with Y-H distances ranging between 1.939 and 2.029 Å (Fig. 2b). This compound has isolated H atoms (H1 and H3) as well as hydrogen dimers H2-H2 with an intramolecular bond length of 0.95 Å.

The *cF*80-Y_4H_{25} was found at 171 GPa. Yttrium atoms form a cubic lattice ($F\bar{4}3m$, *cF*80) with a big unit cell (a = 12.4184(11) Å, V = 1915.1(5) Å^3) (Table S11). Y located at four Wyckoff positions: 24*f* (0.3130; 0; 0), 16*e* (0.3368; 0.3368; 0.3368), 24*g* (0.5616; 0.25; 0.25), and 16*e* (0.0943; 0.0943; 0.0943). The framework of yttrium atoms resembles the inverted sublattices of Dy and Co in the Dy_4CoCd structure type (ICSD 417044). We were able to locate hydrogen atoms in this cell at eleven different Wyckoff positions: 4*b* (0.5, 0; 0), 16*e* (0.7018; 0.2018; 0.2018), 24*g* (0.25; 0.0952; 0.25), 24*f* (0.0765; 0; 0), 48*h* (0.6255; 0.1255; 0.2969), 48*h* (0.6054; 0.1054; 0.2232), 48*h* (0.6425; 0.1425; 0.0404), 48*h* (0.86997; 0.1303; 0.0395), 48*h* (0.5374; 0.0374; 0.3702), 96*i* (0.6312; 0.0391; 0.7562), and 96*i* (0.7984; 0.0093; 0.0837) (TableS11). The shortest

metal-metal distance is $d_{Y2\text{-}Y4}$ = 2.799 Å, which agrees well with discussed above Y_4H_{23} hydride. The Y – H distances in the first coordination sphere of Y are varied from 1.833 Å to 2.079 Å. This compound has hydrogen triatomic units H7-H10-H7 with an intramolecular bond length of 0.9317 Å, which is shorter than the H-H distance in dimers in Y_4H_{23}.

Discussion 2. The procedure of finding possible positions of the hydrogen atoms in the structures of yttrium hydrides

The starting point for search of hydrogen positions in structures of the novel hydrides was the assumption that the symmetry of the hydride phase would be the same as the symmetry of the yttrium lattice. The hydrogen content of each phase was estimated using a linear relationship between the volume per metal atom in hydrides and their stoichiometry (*i.e.* "Retger's law" approximation, Fig. S8). The search of possible hydrogen atoms position(s) was realized with help of the Endeavour™ software. The composition of the compound is considered as fixed, and positions of yttrium atoms are fixed based on the experimental data. In the Endeavour™ software, we employ a two-body Lennard-Jones potential in the form of $V_{LJ}(r) = 4\varepsilon \cdot \left[\left(\frac{\sigma}{r}\right)^{12} - \left(\frac{\sigma}{r}\right)^{6}\right]$, where r is the distance between two interacting particles, ε is the depth of the potential well, and σ is the distance at which the particle-particle potential energy V is zero. The program searches for the position of the hydrogen atoms by minimizing "cost function" that is the sum of the potential defined above. The output of the Endeavour™ program may contain more than one model for the location of hydrogen atoms. Once the structural search in Endeavour™ is completed, the predicted models are validated using DFT calculations, which involve structural relaxation, verifying their dynamical stability, and the position of the phases on the convex hull in the Y-H binary system. This approach was validated by testing known *cF*4-YH_3 yttrium hydride, and the obtained results were consistent with the literature

The procedure is illustrated below using the novel hydride *cF*80-Y_4H_{25} as an example. The first step of the preparation of the structure solution/search involved defining the cell parameter (a = 12.4201 Å) and the space group ($F\bar{4}3m$) (Fig. S2a), followed by specifying the composition and positions of the yttrium atoms (Fig. S2b-c, Table S11). Then, we state that no "diffraction data" would be used, and the search would be conducted solely through "energy" minimization (Fig. S2d). In the subsequent step, the appropriate potential was selected (Fig. S2e). As a result, the program generated a list of the best structural candidates, all of which were validated through DFT calculations. The optimal structure of the phase should meet the following criteria: the difference

in the calculated by DFT unit cell parameters, atomic coordinates, and the calculated pressure should be minimal compared to the experimental values (the numerical criteria for agreement of different characteristics of calculated and experimental data are not strict, and choice of the best or acceptable models in this work is subjective). Fig. S2g illustrates the DFT-relaxed structure for the chosen model from Endeavour, which exhibited a good agreement between theory and experiment (Table S11): for a fixed unit cell volume, the difference between the experimental (171 GPa) and the calculated (168.6 GPa) pressures is ~1.4%; the smallest and the average Y-Y distance in the initial (2.881 Å and 3.208 Å) and in DFT-relaxed (2.811 Å and 3.241 Å) models are very close.

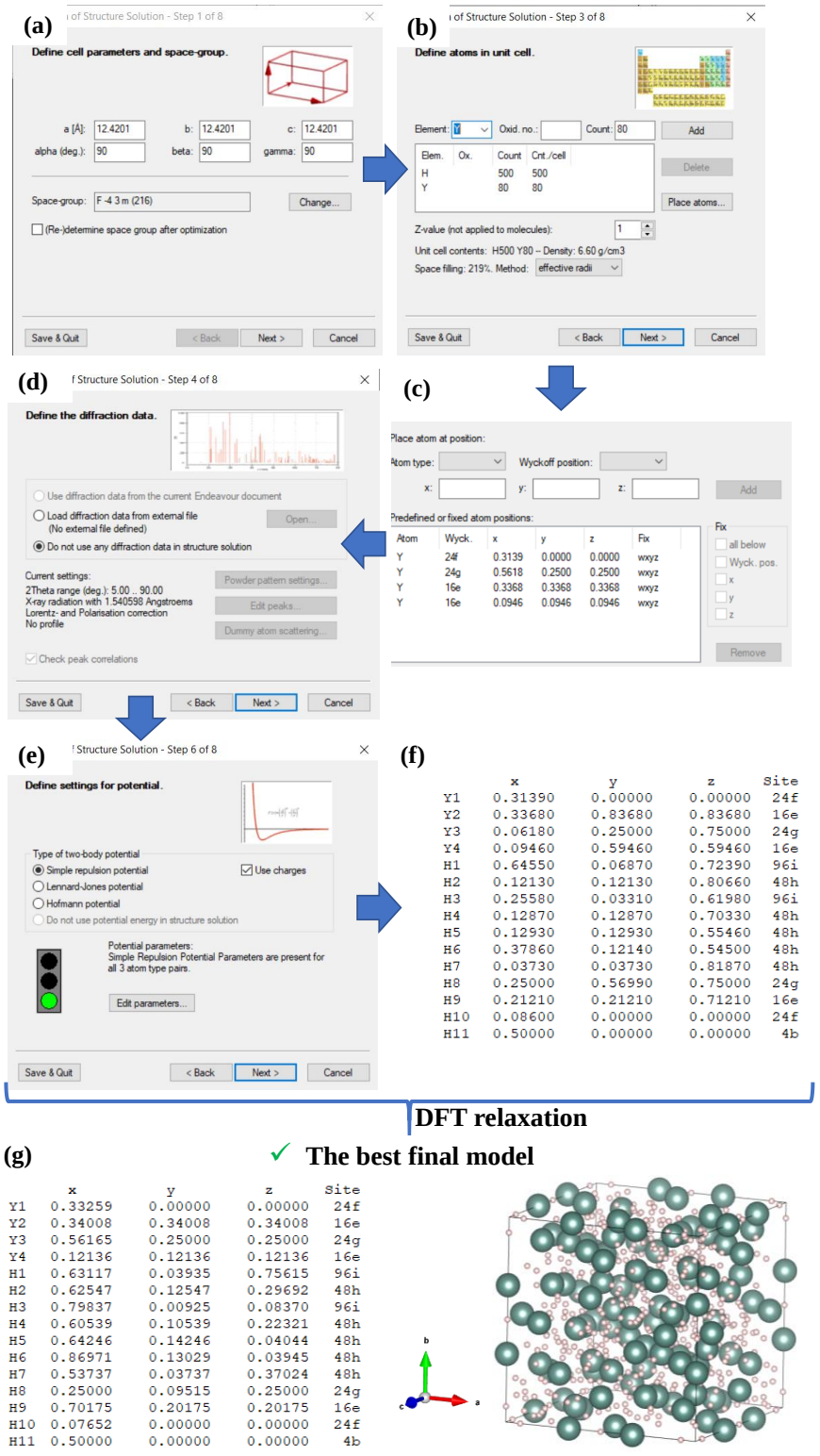

Fig. S2. Schematic step-by-step illustration of the procedure of finding the models of the arrangement of the hydrogen atoms in the structures of novel hydrides

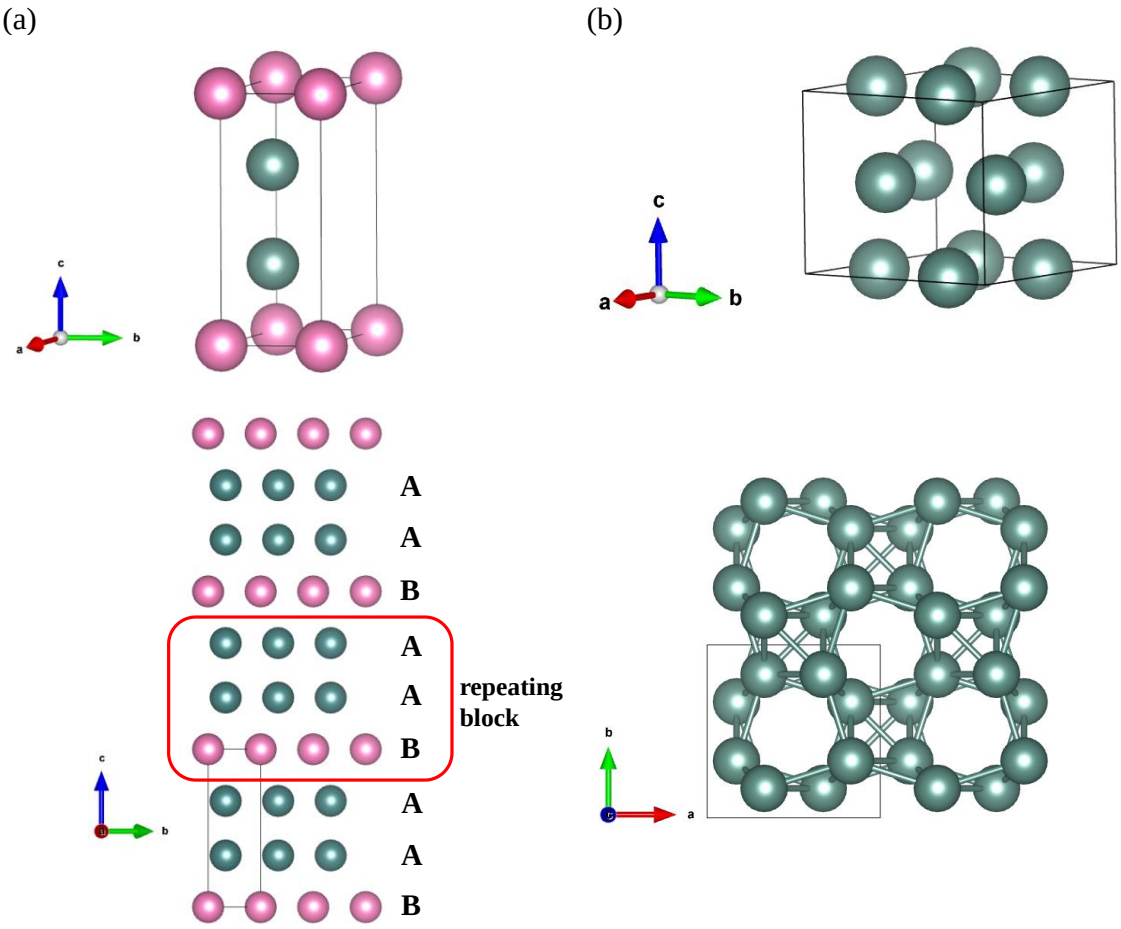

Fig. S3. Crystal structure of the hexagonal *hP*3-Y-II and tetragonal *tI*8-Y yttrium allotropes. (a) Top: the unit cell of *hP*3 Y-II; Y1 and Y2 atoms are marked as pink and green balls, respectively. Bottom: A view of the structure of *hP*3-Y-II along the *a* direction, showing the layer stacking in a '..AAB..' block-sequence pattern along the *c* direction. (b) Top: a unit cell of *tI*8-Y. Yttrium atoms are marked as green balls. Bottom: A view of the structure of *tI*8-Y along the *c* direction, highlighting the channels.

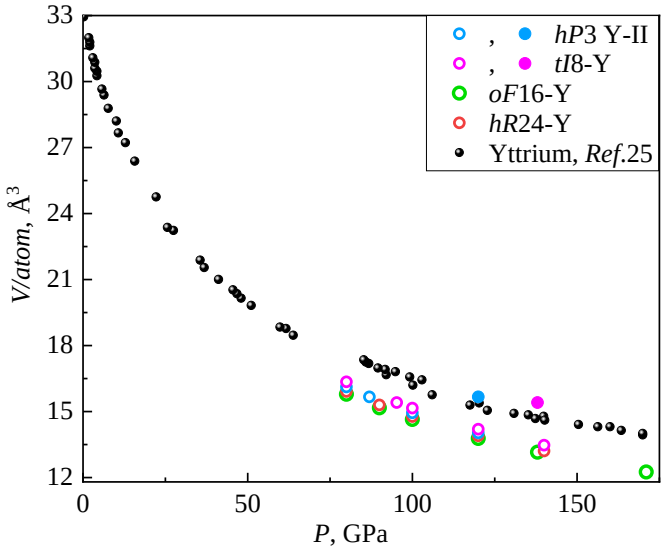

Fig. S4. The experimental and DFT-calculated pressure dependence of the volume per Y atom (*V/atom)* for Y allotropes in a pressure range of 1 bar to 170 GPa. The data for the new hexagonal *hP*3-Y-II and tetragonal *tI*8-Y allotropes as well as for the known *oF*16-Y and *hR*24-Y phases, are shown in blue, pink, green, and red circles, respectively. The pressure dependence of the volume per Y atom for yttrium allotropes, published in *Ref. (34)*, is shown in black circles. The experimental values are shown as solid symbols, while open symbols represent the DFT-calculated values.

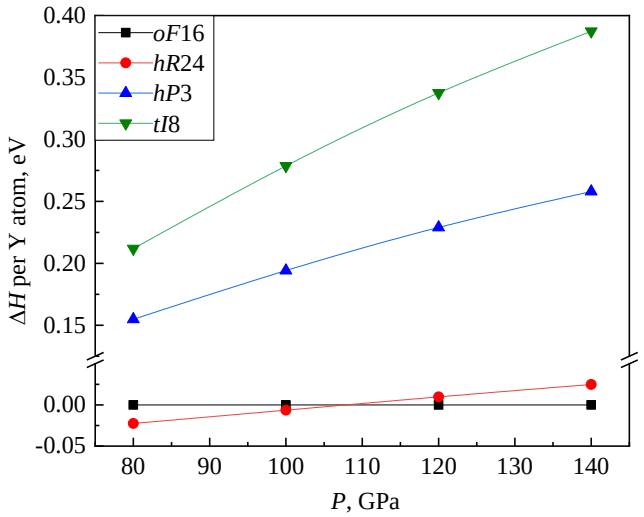

Fig. S5. Results of DFT calculated enthalpy difference between a previously known yttrium allotrope *hR*24-Y, synthesized in this work novel *hP*3-Y-II and *tI*8-Y yttrium allotropes, and previously known *oF*16-Y as a function of pressure: $\Delta H = H_i - H_{oF16\text{-}Y}$.

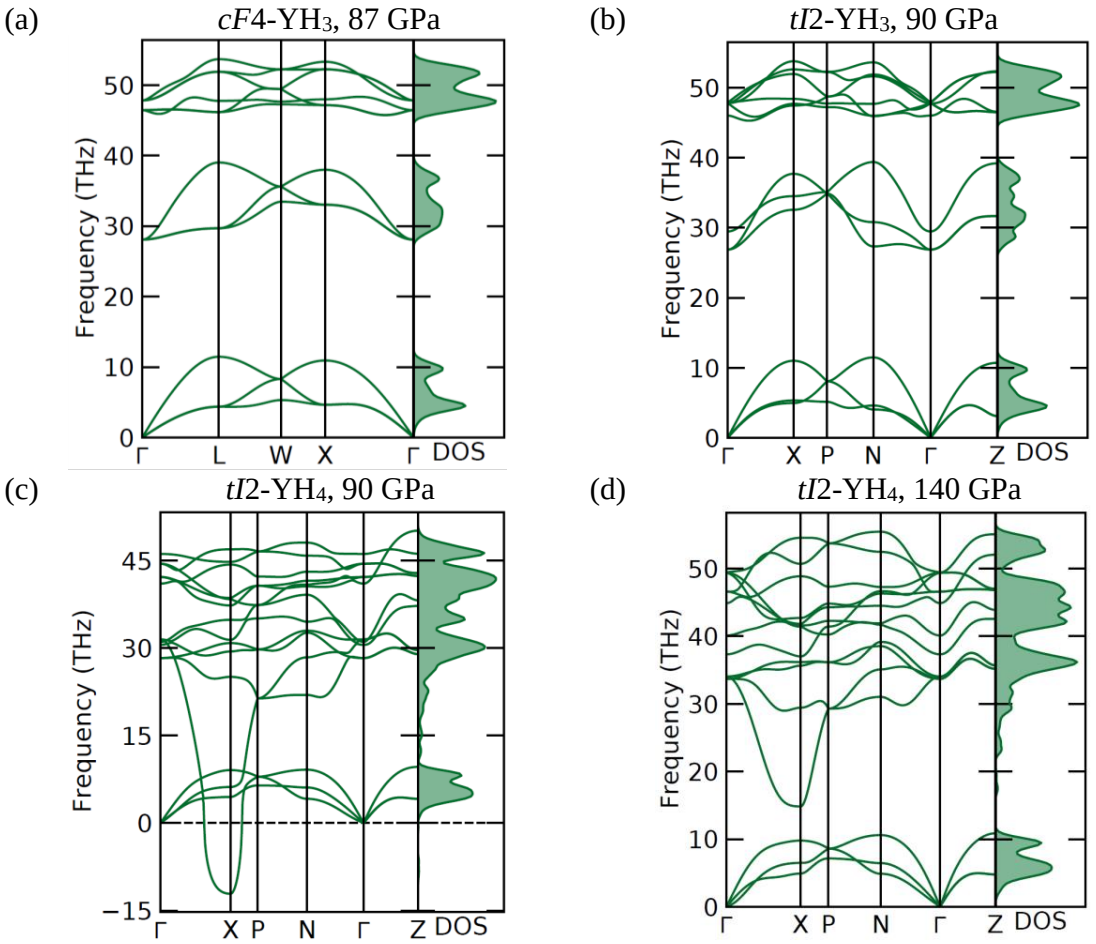

Fig. S6. Phonon dispersion curves calculated along high-symmetry directions in the Brillouin zone, and resulting phonon density of states: (a) for *cF*4-YH_3 at 87 GPa; (b) for *tI*2-YH_3 at 90 GPa (b); (c) for *tI*2-YH_4 at 90GPa and (d) for *tI*2-YH_4 at 140 GPa.

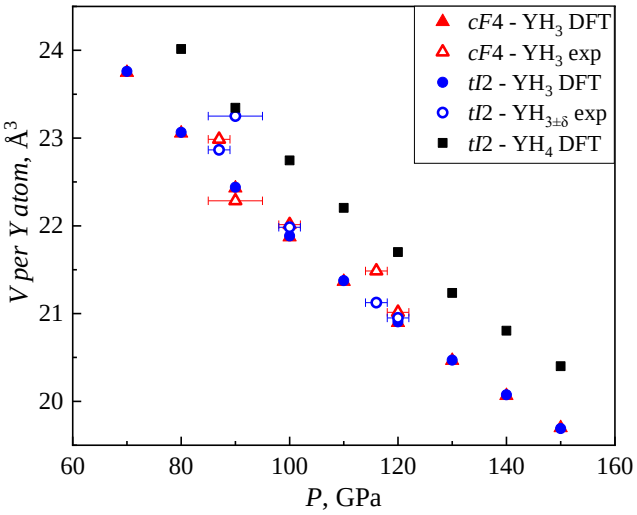

Fig. S7. The pressure dependence of the volume per yttrium atom for yttrium hydrides in a range of 70-150 GPa. The data for *cF*4-YH_3 and *tI*2-$YH_{3\pm\delta}$, are shown in red triangles and blue circles, respectively; open and solid symbols correspond to the experimental and DFT-calculated values, respectively. Black solid squares represent the DFT-calculated values for *tI*2-YH_4.

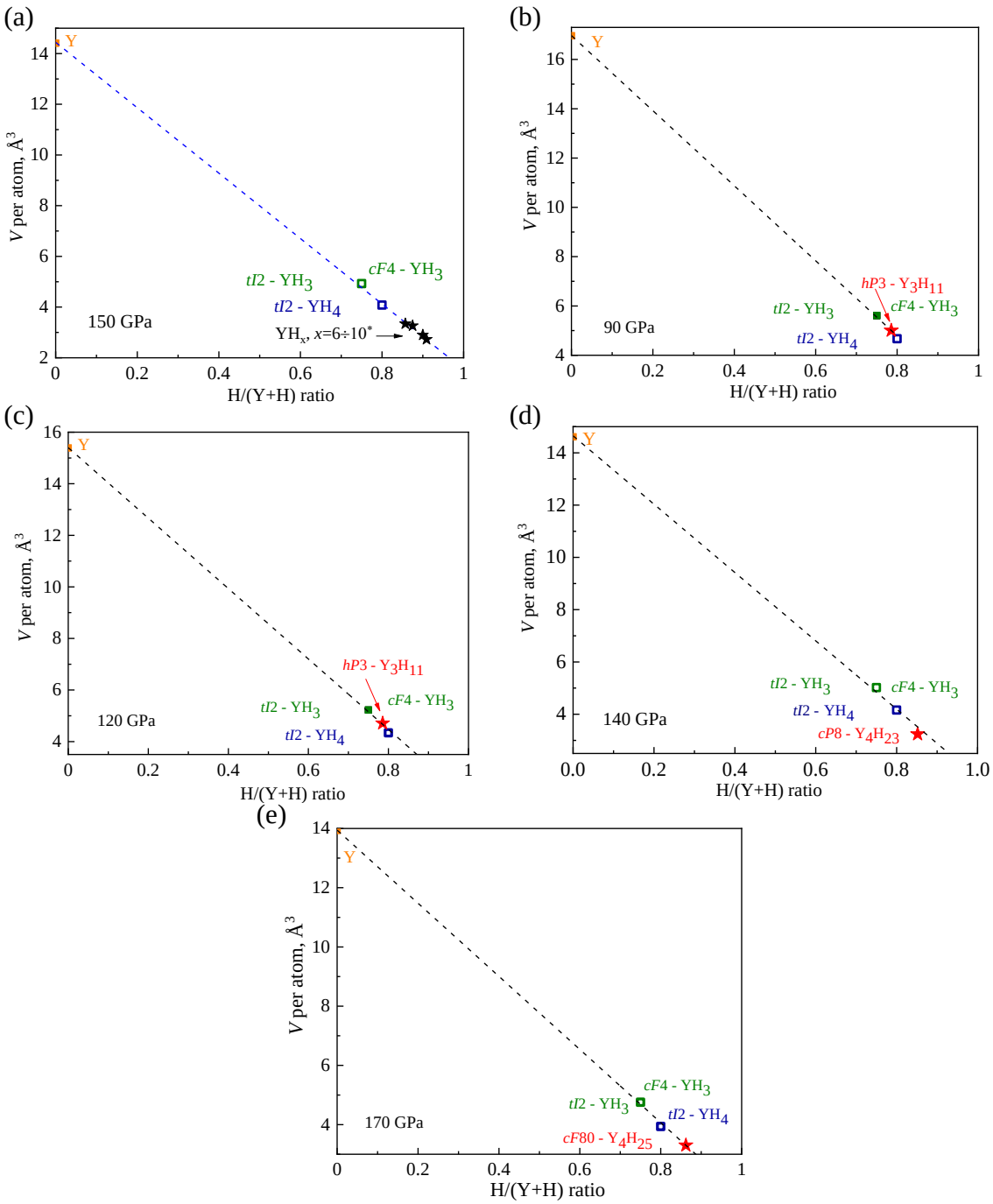

Fig. S8. The illustration of the "Retger's law" approximation for Y-H compounds. The relation between the volume per atom and the hydrogen content is given for (a) 150 GPa, (b) 90 GPa, (c) 120 GPa, (d) 140 GPa, and (e) 170 GPa. The open symbols represent the *P*-*V* data resulting from DFT calculations, solid symbols represent experimental values. The dotted line is the linear fit of the data for Y (*34*), YH_3 and YH_4. The data from (*8*, *7*, *24*) on predicted hydrides YH_x (x=6..10) at 150 GPa are marked as black stars; this data perfectly fit the common trend. The linear fit can be described with the following equations (V_{at} = *V* per atom; *r* = n/(n+m) for each Y_mH_n compound):
(a) $V_{at} = 14.44 - 12.90 \cdot r$; (b) $V_{at} = 16.97 - 15.22 \cdot r$; (c) $V_{at} = 15.39 - 13.66 \cdot r$;
(d) $V_{at} = 14.65 - 13.07 \cdot r$; (e) $V_{at} = 13.94 - 12.35 \cdot r$

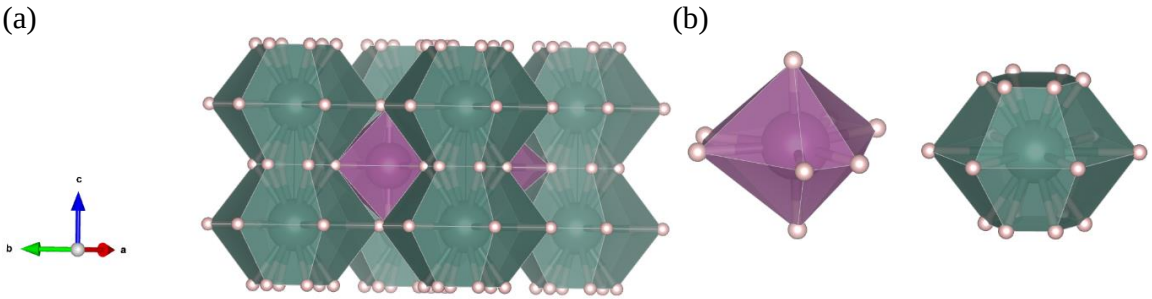

Fig. S9. A polyhedral model of the crystal structure of *hP*3-Y_3H_{11}. (a) A unit cell with the Y atoms shown as violet (Y1) and green (Y2), and hydrogen atoms as light pink balls. (b) Coordination environment of Y1 (violet) and Y2 (green) atoms.

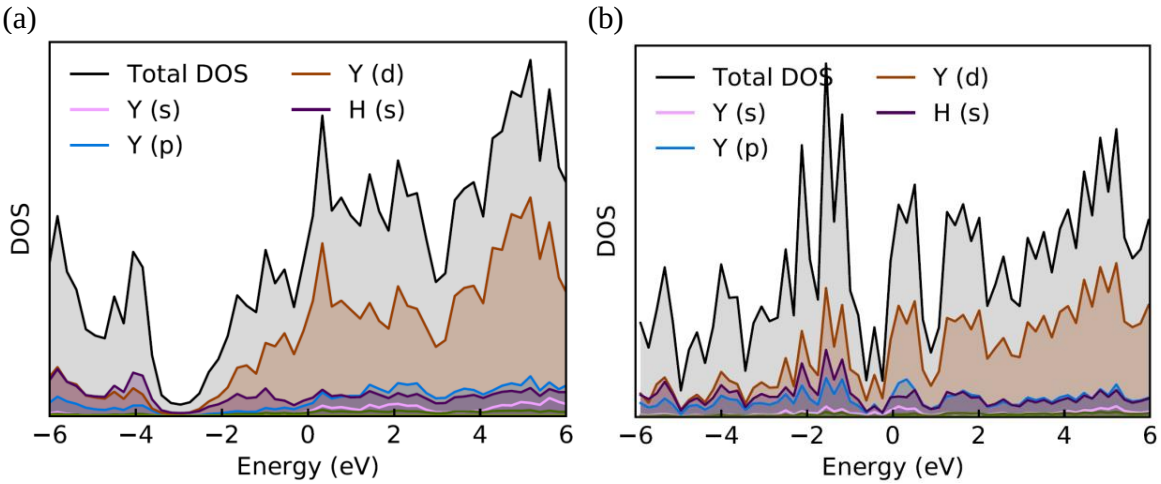

Fig. S10. Electronic density of states for novel high-pressure yttrium hydrides *cP*8-Y_4H_{23} and *cF*80-Y_4H_{25}. (a) The eDOS for *cP*8-Y_4H_{23} at the experimental pressure of 138 GPa. (b) The eDOS for *cF*80-Y_4H_{25} at the experimental pressure of 171 GPa. The Fermi energy level was set to 0 eV.

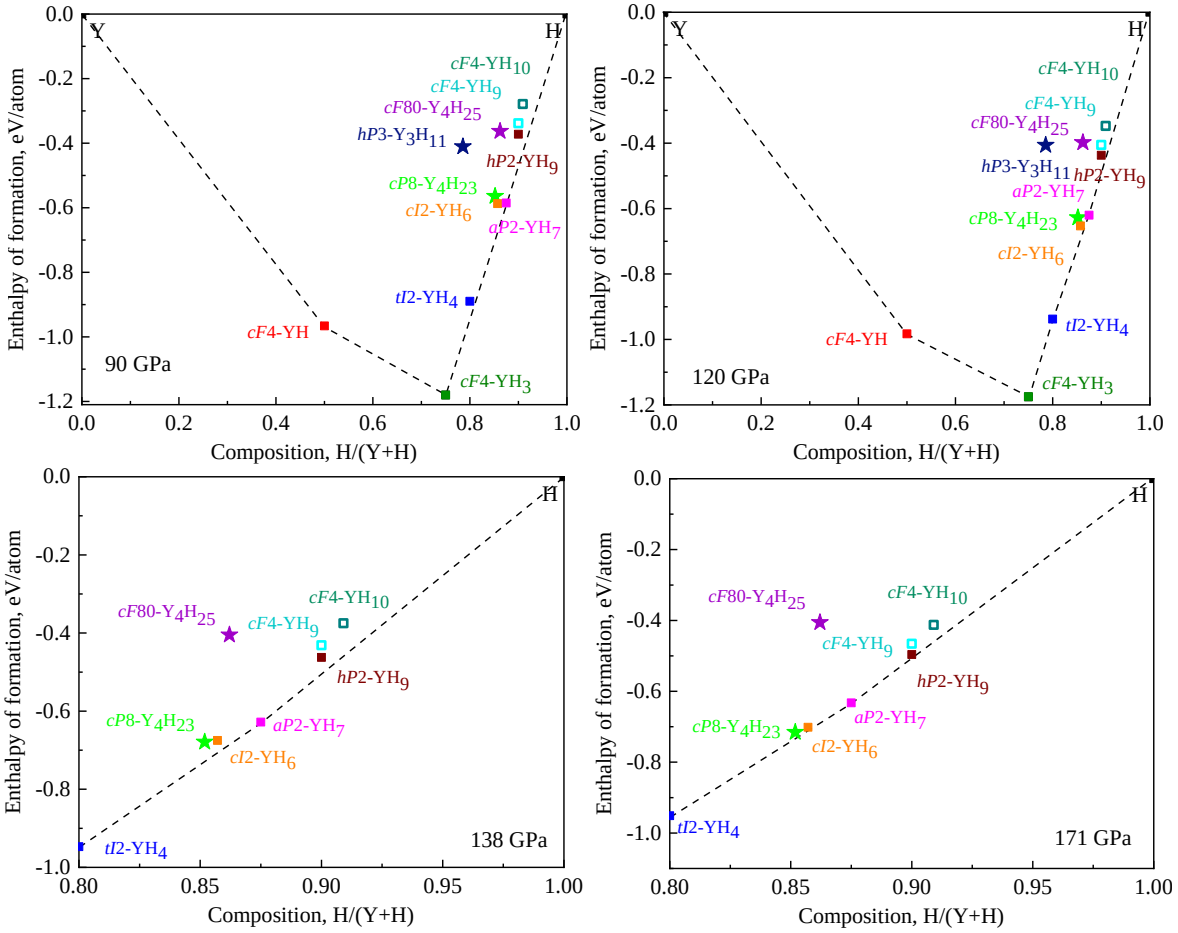

Fig. S11. The calculated convex hull for known binary yttrium hydrides at 90, 120, 138, and 171 GPa. The solid symbols represent phases which were observed experimentally, while open symbols are for predicted phases. The compounds which were synthesized in this work are marked with solid stars. The phases, which lie on the convex hull (black dashed line) are thermodynamically stable.

(a) (b)

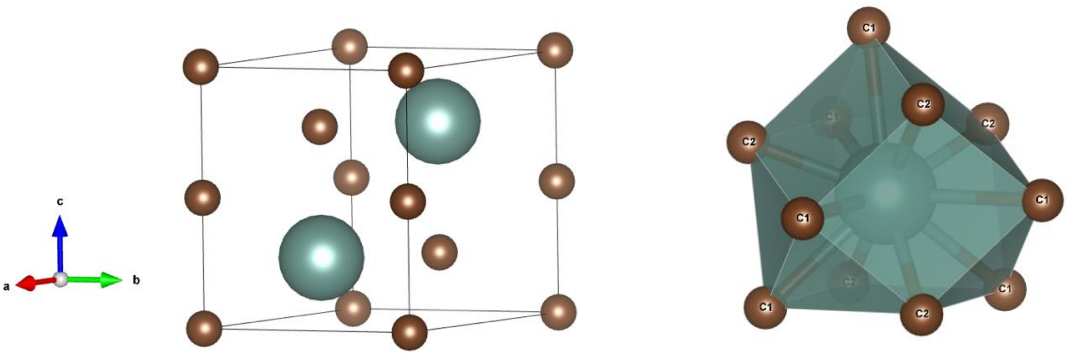

Fig. S12. Crystal structure of yttrium carbide $P6_3/mmc$ YC_2. (a) A unit cell of the structure with the Y atoms shown as green and carbon atoms as brown balls. (b) The $Y(C1)_6(C2)_5$ polyhedron.

Table S1: The details of the DAC experiments* and the lists of obtained phases.

	Reagents	*P* (GPa)	Products of the reaction
DAC1	Y in paraffin oil	87(2)	*tI*2-YH_3; *cF*4-YH_3; *hP*3-Y_3H_{11}; YC_2
		116(2)	*tI*2-YH_3; *cF*4-YH_3
DAC2	Y in paraffin oil	100(2)	*tI*2-YH_3; *cF*4-YH_3
DAC3	Y in paraffin oil	120(2)	*tI*2-YH_3; *cF*4-YH_3; YC_2
DAC4	Y in paraffin oil	138(2)	*cP*8-Y_4H_{23}; *hP*26-$Y_{13}H_{75}$; *tI*8-Y
		171(2)	*cF*80-Y_4H_{25}
DAC5	Y in NH_3BH_3	90(5)	*tI*2-YH_3; *cF*4-YH_3; *hP*3-Y_3H_{11}
		120(5)	*hP*3-Y_3H_{11}; *hP*2-Y_2H_9; *hP*3-Y-II

* The maximum temperature during laser-heating was the same within the error for all experiments (T = 3000(200) K)

Table S2: Crystal structure and refinement details of novel HP-HT *hP*3-Y-II yttrium allotrope, obtained in DAC5 at 120 GPa. The corresponding cif file can be accessed from the CCDC database using the identifier CSD 2295636.

Phase			*hP*3-Y-II (experiment)	*hP*3-Y-II (theory)
P, GPa			120(5)	86.9
Space group, Z			$P\bar{6}m2$, 3	$P\bar{6}m2$, 3
a, Å			2.773(4)	2.7494
c, Å			7.06(2)	7.1801
V, Å^3			47.0(2)	47.0
V, Å^3 / Y atom			15.667	15.667
R_{int}, %			3.66	-
Number of measured/independent reflections ($I \geq 3\sigma$)			82 / 50 (49)	-
Number of refined parameters			6	-
R_1, wR_2, % ($I \geq 3\sigma$)			5.7, 13.39	-
$\Delta\rho_{min}$, $\Delta\rho_{max}$, eÅ^{-3}			1.7, -2.1	-
Wyckoff site and fractional atomic coordinates (x; y; z):	Y1	1*f*	2/3; 1/3; 0.5	2/3; 1/3; 0.5
	Y2	2*h*	1/3; 2/3; 0.1957(8)	1/3; 2/3; 0.17258

Table S3: Crystal structure and refinement details of novel HP-HT *tI*8-Y yttrium allotrope, obtained in DAC4 at 138 GPa. The corresponding cif file can be accessed from the CCDC database using the identifier CSD 2295638.

Phase			*tI*8-Y (experiment)	*tI*8-Y(theory)
P, GPa			138(2)	95.3
Space group			*I*4/*mcm*, 8	*I*4/*mcm*, 8
a, Å			5.3001(10)	5.1116
c, Å			4.391(3)	4.7172
V, Å^3			123.35(8)	123.35
V, Å^3 / Y atom			15.4188	15.4188
R_{int}, %			8.70	-
Number of measured/independent reflections ($I \geq 3\sigma$)			309 / 106 (79)	-
Number of refined parameters			5	-
R_1, wR_2, % ($I \geq 3\sigma$)			4.55, 9.65	-
$\Delta\rho_{min}$, $\Delta\rho_{max}$, eÅ^{-3}			2.1, -2.6	-
Wyckoff site and fractional atomic coordinates (*x*; *y*; *z*):	Y1	8*h*	0.1703(1); 0.6703(1);0.5	0.1817; 0.6817;0.5

Table S4: Crystal structure and refinement details of *cF*4-YH_3 ($Fm\bar{3}m$) for all experimental pressure points at which it was observed.

DAC number	DAC1	DAC2	DAC1	DAC3	DAC5*
P, GPa	87(2)	100(2)	116(2)	120(2)	90(5)
a, Å	4.5133(18)	4.4488(9)	4.4129(17)	4.3872(13)	4.467(3)
V, Å^3	91.94(6)	88.05(3)	85.94(6)	84.44(4)	89.14(11)
V, Å^3 / Y atom	22.985	22.013	21.485	21.110	22.285
R_{int}, %	4.3	2.09	3.09	3.83	-
Number of measured/independent reflections ($I \geq 3\sigma$)	144 / 35 (35)	57 / 21 (21)	57 / 18 (18)	63 / 22 (22)	-
Number of refined parameters	2	2	2	2	-
R_1, wR_2, % ($I \geq 3\sigma$)	4.41, 10.1	4.76, 10.9	5.8, 14.1	4.43, 10.25	-
$\Delta\rho_{min}$, $\Delta\rho_{max}$, eÅ^{-3}	3.0, -1.1	2.5, -1.8	1.5, -2.5	1.1, -1.7	-

* The unit cell parameters and volumes were obtained from powder XRD data.

Table S5: Crystal structure and refinement details of *tI*2-YH_3 (*I*4/*mmm*) at all experimental pressures.

DAC number	DAC1	DAC2*	DAC1	DAC3	DAC5*
P, GPa	87(2)	100(2)	116(2)	120(2)	90(5)
a, Å	3.2013(16)	3.1479(5)	3.0888(11)	3.123(2)	3.2292(11)
c, Å	4.465(4)	4.4371(10)	4.4285(19)	4.301(3)	4.5022(17)
V, $Å^3$	45.75(6)	43.968(17)	42.25(3)	41.9(3)	46.95(3)
V, $Å^3$ / Y atom	22.875	21.984	21.125	20.95	23.25
R_{int}, %	3.84	-	1.3	2.4	-
Number of measured/independent reflections ($I \geq 3\sigma$)	142 / 54 (54)	-	105 / 59 (58)	100 / 42 (42)	-
Number of refined parameters	3	-	3	3	-
R_1, wR_2, % ($I \geq 3\sigma$)	3.1, 6.8	-	5.89, 15.04	4.22, 10.5	-
$\Delta\rho_{min}$, $\Delta\rho_{max}$, $eÅ^{-3}$	-3.1, 2.4	-	3.4, -3.3	2.5, -1.8	-

* The unit cell parameters and volumes were obtained from powder XRD data.

Table S6: The values of the Y-Y distances in novel yttrium hydrides and in yttrium allotropes known in the literature, shown at 90, 120, 138, and 171 GPa.

Phase	Pressure, GPa	Minimal Y-Y distance, Å	Y-Y distance in Y metal, Å
Y_3H_{11}	90	2.9578(2)	2.6334 ($R\bar{3}m$ – Y)
Y_2H_9	120	3.0870(12)	2.5395 (*Fddd* – Y)
$Y_{13}H_{75}$	138	2.8816(4)	2.5099 (*Fddd* – Y)
Y_4H_{23}	138	2.7908(5)	2.5099 (*Fddd* – Y)
Y_4H_{25}	171	2.8806(3)	2.4452 (*Fddd* – Y)

Table S7: Crystal structure and refinement details of novel yttrium hydride *hP*3-Y_3H_{11} (*P*6/*mmm*) at all experimental pressures. The corresponding cif file at 120 GPa can be accessed from the CCDC database using the identifier CSD 2295619.

DAC number	DAC1	DAC5	DAC5
P, GPa	87(2)	90(5)	120(5)
a, Å	5.123(3)	5.140(5)	4.978(3)
c, Å	3.083(3)	3.106(3)	3.0784(15)
V, Å^3	70.07(10)	71.06(12)	66.06(9)
V, Å^3 / Y atom	23.357	23.687	22.02
R_{int}, %	7.22	4.61	8.79
Number of measured/independent reflections ($I \geq 3\sigma$)	455 / 132 (78)	106 / 42 (21)	147 / 51 (22)
Number of refined parameters	5	5	5
R_1, wR_2, % ($I \geq 3\sigma$)	6.39, 17.1	8.60, 21.5	4.68, 14.45
$\Delta\rho_{min}$, $\Delta\rho_{max}$, eÅ^{-3}	3.8, -2.9	2.8, -2.5	1.4, -2.0

Table S8: The DFT-relaxed structure of a novel HP yttrium hydride *hP*3-Y_3H_{11} at 90 and 120 GPa.

Crystal phase			*hP*3-Y_3H_{11} (theory)	*hP*3-Y_3H_{11} (theory)
Space group, *Z*			*P*6/*mmm*, 1	*P*6/*mmm*, 1
a (Å)			4.99089	4.79494
c (Å)			3.30781	3.21793
V (Å^3)			71.06	66.06
Pressure *P* (GPa)			97.2	123.2
Wyckoff site and fractional atomic coordinates (*x*; *y*; *z*):	Y1	2*d*	2/3; 1/3; 0.5	2/3; 1/3; 0.5
	Y2	1*a*	0; 0; 0	0; 0; 0
	H1	6*k*	0.24050; 0; 0.5	0.23539; 0; 0.5
	H2	3*f*	2/3; 1/3; 0	0.5; 0; 0
	H3	2*c*	0.5; 0; 0	0; 0; 0.5

Table S9: Crystal structure and refinement details for the novel yttrium hydrides *cP*8-Y_4H_{23}, *hP*26-$Y_{13}H_{75}$, *cF*80-Y_4H_{25}, and *hP*2-Y_2H_9 at different experimental pressures. The corresponding cif file can be accessed from the CCDC database using the identifiers CSD 2295644, 2295626, 2295645, and 2295620, respectively.

Phase	*cP*8-Y_4H_{23}	*hP*26-$Y_{13}H_{75}$	*cF*80-Y_4H_{25}	*hP*2-Y_2H_9
DAC number	DAC4	DAC4	DAC4	DAC5
P, GPa	138(2)	138(2)	171(2)	120(5)
Space group	$Pm\bar{3}n$	$P6_3/mmc$	$F\bar{4}3m$	$P6_3/mmc$
a, Å	5.5815(8)	8.9730(13)	12.4201(14)	3.162(3)
c, Å	-	8.9085(8)	-	4.958(2)
V, Å^3	173.88(7)	621.17(19)	1915.9(4)	42.94(9)
V, Å^3 / Y atom	21.735	23.891	23.949	21.47
R_{int}, %	9.83	9.67	9.98	9.16
Number of measured/independent reflections ($I \geq 3\sigma$)	555 / 90 (67)	3505 / 974 (601)	1139 / 371 (210)	70 / 28 (20)
Number of refined parameters	4	17	15	3
R_1, wR_2, % ($I \geq 3\sigma$)	4.84, 10.81	4.34, 8.11	5.71, 12.43	8.24, 16.98
$\Delta\rho_{min}$, $\Delta\rho_{max}$, eÅ^{-3}	4.1, -2.5	3.0, -2.9	1.8, -1.9	2.0, -1.6

Table S10: Crystallographic data for a novel HP yttrium hydride *cP*8-Y_4H_{23} at 138 GPa in comparison to the corresponding DFT-relaxed structure.

Crystal phase			Y_4H_{23} (experiment)	Y_4H_{23} (theory)
Space group, *Z*			$Pm\bar{3}n$, 2	$Pm\bar{3}n$, 2
a (Å)			5.5815(8)	5.5815
V (Å^3)			173.88(7)	173.88
Pressure *P* (GPa)			138 (2)	147.2
Wyckoff site and fractional atomic coordinates (*x*; *y*; *z*):	Y1	6*d*	0.25; 0.5; 0	0.25; 0.5; 0
	Y2	2*a*	0; 0; 0	0; 0; 0
	H1*	6*c*	-	0.25; 0; 0.5
	H2*	16*i*	-	0.2010; 0.2010; 0.2010
	H3*	24*k*	-	0; 0.3103; 0.1492

* The hydrogen atoms were placed according to the structural data for isostructural hydrides M_4H_{23} (*M* = Ba, La, and Eu).

Table S11: Experimentally determined crystallographic data for the novel HP yttrium hydride *cF*80-Y_4H_{25} at 171 GPa in comparison to the corresponding DFT-relaxed structure.

Crystal phase			Y_4H_{25} (experiment)	Y_4H_{25} (theory)
Space group, *Z*			$F\bar{4}3m$, *Z* = 20	$F\bar{4}3m$, *Z* = 20
a (Å)			12.4201(11)	12.4201
V (Å^3)			1915.9(4)	1915.9
Pressure *P* (GPa)			171 (2)	168.6
Wyckoff site and fractional atomic coordinates (*x*; *y*; *z*):	Y1	24*f*	0.3130; 0; 0	0.3326; 0; 0
	Y2	16*e*	0.3368; 0.3368; 0.3368	0.3401; 0.3401; 0.3401
	Y3	24*g*	0.5616; 0.25; 0.25	0.5617; 0.25; 0.25
	Y4	16*e*	0.0943; 0.0943; 0.0943	0.1214; 0.1214; 0.1214
	H1	96*i*	-	0.6312; 0.0391; 0.7562
	H2	48*h*	-	0.6255; 0.1255; 0.2969
	H3	96*i*	-	0.7984; 0.0093; 0.0837
	H4	48*h*	-	0.6054; 0.1054; 0.2232
	H5	48*h*	-	0.6425; 0.1425; 0.0404
	H6	48*h*	-	0.8697; 0.1303; 0.0395
	H7	48*h*	-	0.5374; 0.0374; 0.3702
	H8	24*g*	-	0.25; 0.0952; 0.25
	H9	16*e*	-	0.7018; 0.2018; 0.2018
	H10	24*f*	-	0.0765; 0; 0
	H11	4*b*	-	0.5; 0; 0

Table S12: Experimentally determined crystallographic data for a novel HP yttrium carbide YC_2 at 120 GPa in comparison to the corresponding DFT-relaxed structure. The corresponding cif file can be accessed from the CCDC database using the identifier CSD 2295639.

Crystal phase			YC_2 (experiment)	YC_2 (theory)
Space group, Z			$P6_3/mmc$, 2	$P6_3/mmc$, 2
a (Å)			3.6000(17)	3.6000
c (Å)			4.439(8)	4.439
V (Å^3)			49.82(13)	49.82
Pressure P (GPa)			120 (2)	127.3
Wyckoff site and fractional atomic coordinates (x; y; z):	Y1	2c	1/3; 2/3; 1/4	1/3; 2/3; 1/4
	C1	2a	0; 0; 0	0; 0; 0
	C2	2d	1/3; 2/3; 3/4	1/3; 2/3; 3/4
Number of measured/independent reflections ($I \geq 3\sigma$)			129/ 36 (32)	-
R_{int}			0.0675	-
Final R indexes (all)			R_1 = 0.0506; wR_2 = 0.915	
Final R indexes ($I \geq 3\sigma$)			R_1 = 0.0396; wR_2 = 0.0869	-
$\Delta\rho_{min}$, $\Delta\rho_{max}$, eÅ^{-3}			-0.7, 0.5	
Number of refined parameters			4	-

Data S1. Crystallographic information file for *hP*3-Y-II.
Data from single-crystal X-ray diffraction experiments at 120 GPa for *hP*3-Y.

Data S2. Crystallographic information file for *tI*8-Y.
Data from single-crystal X-ray diffraction experiments at 138 GPa for *tI*8-Y.

Data S3. Crystallographic information file for Y_2H_9.
Data from single-crystal X-ray diffraction experiments at 120 GPa for Y_2H_9.

Data S4. Crystallographic information file for Y_3H_{11}.
Data from single-crystal X-ray diffraction experiments at 120 GPa for Y_3H_{11}.

Data S5. Crystallographic information file for Y_4H_{23}.
Data from single-crystal X-ray diffraction experiments at 138 GPa for Y_4H_{23}.

Data S6. Crystallographic information file for Y_4H_{25}.
Data from single-crystal X-ray diffraction experiments at 171 GPa for Y_4H_{25}.

Data S7. Crystallographic information file for $Y_{13}H_{75}$.
Data from single-crystal X-ray diffraction experiments at 138 GPa for $Y_{13}H_{75}$.

Data S8. Crystallographic information file for YC_2.
Data from single-crystal X-ray diffraction experiments at 120 GPa for YC_2.

4.3. Novel High-Pressure Yttrium Carbide γ-Y_4C_5 Containing [C_2] and Nonlinear [C_3] Units with Unusually Large Formal Charges.

This section contains the following manuscript and the related supplementary material:

"Novel High-Pressure Yttrium Carbide γ-Y_4C_5 Containing [C_2] and Nonlinear [C_3] Units with Unusually Large Formal Charges"

A. Aslandukova, A. Aslandukov, L. Yuan, D. Laniel, S. Khandarkhaeva, T. Fedotenko, G. Steinle-Neumann, K. Glazyrin, N. Dubrovinskaia & L. Dubrovinsky

Status: published in *Physical Review Letters*, 127, 135501

(2021)

Novel High-Pressure Yttrium Carbide γ-Y_4C_5 Containing $[C_2]$ and Nonlinear $[C_3]$ Units with Unusually Large Formal Charges

Alena Aslandukova,[1*] Andrey Aslandukov,[2] Liang Yuan,[1] Dominique Laniel,[2] Saiana Khandarkhaeva,[2] Timofey Fedotenko,[2] Gerd Steinle-Neumann,[1] Konstantin Glazyrin,[3] Natalia Dubrovinskaia,[2,4] and Leonid Dubrovinsky[1]
[1]*Bavarian Research Institute of Experimental Geochemistry and Geophysics, University of Bayreuth, 95440 Bayreuth, Germany*
[2]*Material Physics and Technology at Extreme Conditions, Laboratory of Crystallography, University of Bayreuth, 95440 Bayreuth, Germany*
[3]*Photon Science, Deutsches Elektronen-Synchrotron, Notkestrasse 85, 22607 Hamburg, Germany*
[4]*Department of Physics, Chemistry and Biology (IFM), Linköping University, SE-581 83 Linköping, Sweden*

(Received 19 May 2021; accepted 18 August 2021; published 22 September 2021)

Changes in the bonding of carbon under high pressure leads to unusual crystal chemistry and can dramatically alter the properties of transition metal carbides. In this work, the new orthorhombic polymorph of yttrium carbide, γ-Y_4C_5, was synthesized from yttrium and paraffin oil in a laser-heated diamond anvil cell at ~50 GPa. The structure of γ-Y_4C_5 was solved and refined using *in situ* synchrotron single-crystal x-ray diffraction. It includes two carbon groups: $[C_2]$ dimers and nonlinear $[C_3]$ trimers. Crystal chemical analysis and density functional theory calculations revealed unusually high noninteger charges ($[C_2]^{5.2-}$ and $[C_3]^{6.8-}$) and unique bond orders (<1.5). Our results extend the list of possible carbon states at extreme conditions.

DOI: 10.1103/PhysRevLett.127.135501

Introduction.—Metal carbides exhibit high melting points, high hardness, and metallic conductivity that make them attractive candidates for different technological applications in material science [1]. Carbon has the capability of forming various bond states affecting the structures and properties of transition metal carbides [2]. Most metal carbides are either substitutional or interstitial solid solutions, or they form binary compounds with simple crystal structures (e.g., of a rock salt type) [3]. However, more complex carbides with covalent C-C bonds are also known.

There is a large number of metal carbides containing $[C_2]$ dimers, for example, CaC_2, SrC_2, BaC_2, YC_2, LaC_2, La_2C_3, CeC_2, TbC_2, YbC_2, and LuC_2 [4–7]. The C-C bond length in these carbides depends on the charge of the cation and increases proportionally with the valence of the metal [8–10]. The crystal chemistry of carbides containing triatomic $[C_3]$ units is much more varied. The $[C_3]$ unit was suggested to be in Li_4C_3 [11] and is known to exist in Mg_2C_3, Me_4C_7 (Me = Y, Ho, Er, Tm, Lu), Sc_3C_4, and Ln_3C_4 (Ln = Ho − Lu) compounds [3,12–14]. The structures of Ln_3C_4 contain both $[C_3]$ and $[C_2]$ units, as well as isolated carbon atoms. Usually $[C_3]$ trimers are linear $[C=C=C]^{4-}$ groups with the C-C bond length of 1.34–1.35 Å (e.g., like in Mg_2C_3), which is close to that in gaseous allene (1.335 Å) [15]. However, the $[C_3]$ units in Sc_3C_4 and Ln_3C_4 structures are not linear. Hoffmann and Meyer [16] performed a fragment molecular orbital analysis to study the bonding characteristics of the $[C_3]$ units in Sc_3C_4 with the unusual bending (175.8°), the latter attributed to the packing arrangement. Later, more binary carbides with Me_4C_7 compositions containing similar $[C_3]$ units, but with the bending angles of 167.8°—168.3°, were found [3,12].

High pressure alters the bonding patterns in carbides, leading to new compounds with unusual structural units and interesting properties, and as such, compression might enable exploring the catenation of carbon. Namely, for the binary systems Mg-C [17], Ca-C [18], Y-C [19,20], and La–C [2], an *ab initio* structure search predicts the formation of unusual metal carbides with exotic $[C_4]$, $[C_5]$ units and $[C_6]$ rings, graphitic carbon sheets, and a number of structural transitions. Carbon polymerization under high pressure can drastically change the physical properties of carbides and can lead, for example, to superconductivity [21,22].

At ambient pressure, the yttrium carbides family includes a large variety of binary phases with different stoichiometry and crystal chemistry [3]: Y_2C with isolated carbon atoms; YC_2 and Y_2C_3 with $[C_2]$ units; Y_3C_4 with $[C_3]$ units; Y_4C_5 with both single carbon atoms and $[C_2]$ units; Y_4C_7 with single carbon atoms and $[C_3]$ units. For Y_4C_5, two modifications are known: low-temperature α-Y_4C_5 and high-temperature β-Y_4C_5 [23]. Whereas the crystal structure of α-Y_4C_5 was solved and refined [space group $Pbam$ (#55), $a = 6.5735(9)$, $b = 11.918(1)$, $c = 3.6692(5)$ Å] at ambient conditions [23], the structure of β-Y_4C_5 remains unknown. Under high pressure, only Y_2C_3 has been investigated [24–26]. Here, we report on the synthesis and characterization of a new high-pressure

modification of yttrium carbide, γ-Y_4C_5, with novel structure and very unusual crystal chemistry.

Results and discussion.—The γ-Y_4C_5 phase was first synthesized through a chemical reaction of yttrium with paraffin oil at ~44 GPa and ~2500 °C in the laser-heated diamond anvil cell (DAC1, Table S1 in the Supplemental Material [27]). The *in situ* synchrotron single-crystal x-ray diffraction enabled the crystal structure solution and refinement. The details of the sample preparation, data collection, structure determination, and refinement are described in the Supplemental Material [27]. To reproduce the synthesis of the γ-Y_4C_5 phase from the same precursors, two additional experiments were performed at ~46 GPa and ~2800 °C (DAC2), and at ~51 GPa and ~2500 °C (DAC3) [27]. In DAC2, only the known cubic Y_2C_3 phase [the Pu_2C_3-type structure, space group I-43d, $Z = 8$, $a = 7.745(4)$ Å] [27] was observed, which might be due to a different Y:C local ratio at the laser-heated spot. The γ-Y_4C_5 compound, which was also synthesized in DAC3, was gradually decompressed. At each pressure step of a few GPa, XRD data were collected to explore the behavior and the equation of state of γ-Y_4C_5. Reflections of the γ-Y_4C_5 phase were observed down to 16(2) GPa.

The γ-Y_4C_5 crystallizes in an orthorhombic structure (space group Cmce, $Z = 8$) with the unit cell parameters $a = 12.183(6)$, $b = 7.659(3)$, and $c = 8.858(2)$ Å at 44 GPa [Fig. 1(a)]. Full crystallographic information is provided in Table S2 [27]. Notable structural elements of the γ-Y_4C_5 are the diatomic [C_2] (dimers or dumbbells), which lie in the bc plane, and triatomic [C_3] units (trimers). If viewed along the b direction (see Fig. S1a [27]), the structure may be described as a series of layers of Y atoms stacked along the a direction. Every third layer includes the [C_2] dimers alternating with Y atoms in the rows along the b direction. The [C_2] dimers in the adjacent rows are mutually oriented in a "parquetlike" manner (see Fig. S1b [27]). The nonlinear [C_3] trimers fill the space between the adjacent Y layers, which do not include dimers. The trimers form rows along the b direction. In each row, the summits of the trimers point to the same direction (see Fig. S1c [27]). The direction differs in each of two adjacent rows. In the projection on the ac plane the trimers are turned with respect to each other and can be seen as crosses (see Fig. S1a [27]).

In the γ-Y_4C_5 structure, there are three crystallographically nonequivalent yttrium atoms with different coordination environment. The Y1 atoms possess the highest coordination number, CN = 10, with respect to the nearest carbon atoms, four of which belong to the two [C_2] units in a side-on orientation, four to the two [C_3] units, each giving two atoms, and two more carbon atoms come from the two end-on [C_3] units (Fig. S1d [27]). The Y2 atoms have a CN of 6 with the contribution of one [C_2] dimer in a side-on orientation, two more atoms- from two [C_2] dimers in end-on orientation, and two atoms from the two end-on [C_3] units (Fig. S1e [27]). The Y3 atoms are eight-fold coordinated (CN = 8) by two end-on [C_2] dumbbells and by three differently coordinated [C_3] units, as shown in Fig. S1f [27]. Such variation of yttrium coordination number in γ-Y_4C_5 is not unprecedented for yttrium carbides (see Table S3 [27] for the CN data for α-Y_4C_5, Y_4C_7, and Y_3C_4). However, C-C distances in [C_2] dimers [1.40(2) Å] and [C_3] trimers [1.43(1) Å] are unusual: they are significantly larger than expected for double-bonded carbon (~1.34 Å) and much shorter than for single-bonded (~1.54 Å) carbon atoms. They are not believed to be artifacts as the crystallographic data, including the C-C distance [1.32(1) Å, Table S4 [27]] obtained at ~46 GPa for the previously known cubic Y_2C_3 [21], are reasonable. Also, the significant bending of the triatomic carbon units (with the C3-C2-C3 angle of ~134°) in γ-Y_4C_5 calls for a more detailed analysis of the C-C bonds.

Upon decompression from 51 to 16 GPa, γ-Y_4C_5 expands quasi-isotropically (Fig. S2a [27]), and pressure-volume (P-V) data can be described by a second order Birch-Murnaghan equation of state (EOS) with the parameters $V_0 = 1016(8)$ Å^3 (the unit cell volume at ambient conditions) and $K_0 = 135(7)$ GPa (the bulk modulus) [Fig. 2(a)]. Unfortunately, the quality of the XRD data collected on decompression was insufficient to locate carbon atoms precisely, so that the changes in the C-C

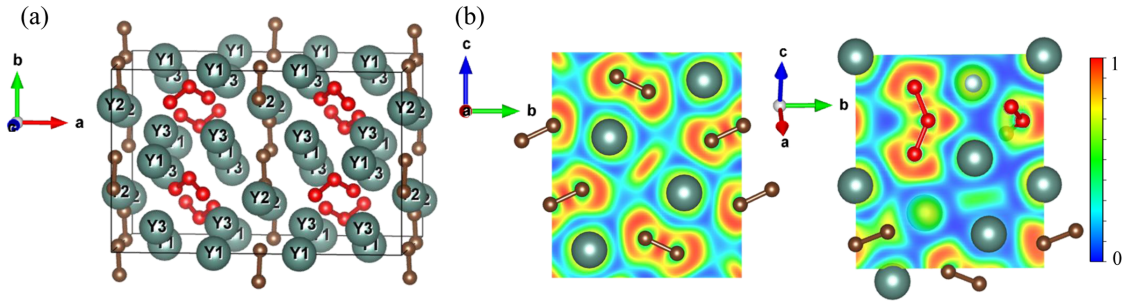

FIG. 1. Crystal structure of γ-Y_4C_5 at 44 GPa and corresponding 2D electron localization function (ELF) maps. (a) A unit cell of the structure with the Y atoms shown as gray and carbon atoms as brown and red balls, in dimers and trimers, respectively. (b) Cross sections of the calculated ELF shown in the planes containing the [C_2] (left) and [C_3] (right) units.

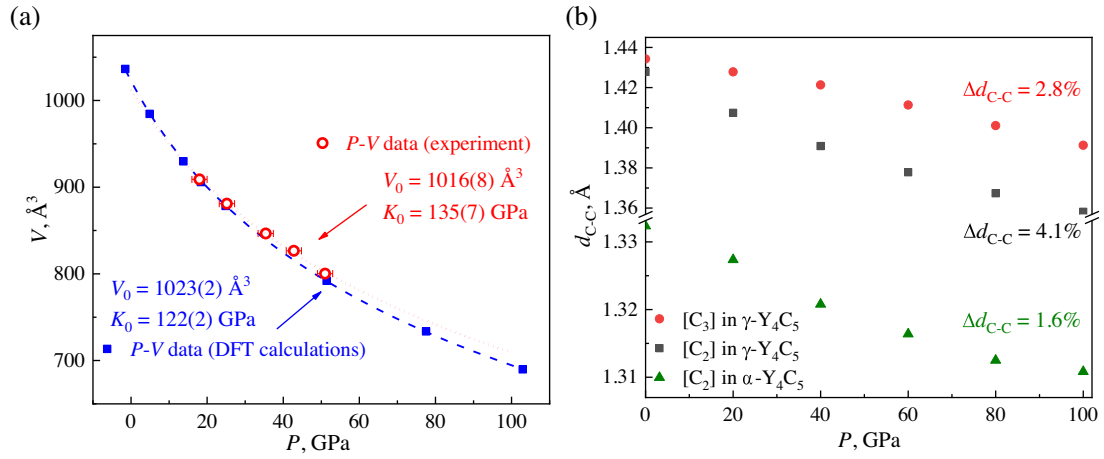

FIG. 2. Pressure dependence of the unit cell volume of γ-Y_4C_5 and the C-C distances ($d_{C\text{-}C}$) in the carbon units, for two Y_4C_5 polymorphs. (a) The P-V data for γ-Y_4C_5 obtained from XRD experiment and DFT calculations. The open red symbols represent experimental values of V in the decompression cycle for DAC3; the red dashed line shows the fit using the second order Birch-Murnaghan EOS. The blue solid symbols represent the P-V data resulted from DFT calculations; the blue dashed line is the corresponding second-order Birch-Murnaghan fit of the E-V data. (b) Pressure dependence of the calculated C-C distances in carbon units in α-Y_4C_5 and γ-Y_4C_5. The solid red circles, gray squares, and green triangles represent the C-C distances in the [C_3] and [C_2] units in γ-Y_4C_5, and the [C_2] units in α-Y_4C_5, respectively. The relative change in the C-C bond length ($\Delta d_{C\text{-}C} = (d_{C\text{-}C(0\ GPa)} - d_{C\text{-}C(100\ GPa)})/d_{C\text{-}C(0\ GPa)}$) is 2.8% and 4.1% for the [C_3] and [C_2] in γ-Y_4C_5, and 1.6% for the [C_2] in α-Y_4C_5.

distances in both dimers and trimers could not be traced. However, they were extracted from the relaxed structures obtained as a result of *ab initio* calculations using density functional theory (DFT).

The full relaxation of the structural model (at a volume corresponding to ~44 GPa) using DFT, as implemented in the plane wave VASP code [40], results in unit cell parameters and atomic coordinates which perfectly agree with the experiment (Table S1 [27]). The EOS parameters [$V_0 = 1024(1)$ Å^3 and $K_0 = 122(1)$ GPa] obtained from the computations based on energies from the optimization of the crystal structure of γ-Y_4C_5 over a wide volume range [Fig. 2(a)] are close to the experimental ones. The calculated bulk modulus of γ-Y_4C_5 is slightly larger than that of α-Y_4C_5 [$K_0 = 113(3)$ GPa], correlating well with the smaller volume per formula unit of γ-Y_4C_5 in comparison to α-Y_4C_5 (Fig. S3 [27]). According to the calculations, over the whole pressure range up to 100 GPa, the C-C distances in the [C_3] units remain longer than in the [C_2] dimers, but the C-C bonds in the dimers are almost 1.5 times more compressible than in the trimers [Fig. 2(b)]. It means that the dimers respond to compression by contraction, whereas the trimers partly adapt to the volume decrease through gradual bending. Indeed, in the pressure range from 0 to 100 GPa, the C3-C2-C3 bending angle changes from 139.6° to 133.5° (Fig. S2b [27]).

Harmonic phonon dispersion calculations using the Phonopy software [41] reveal that γ-Y_4C_5 is dynamically stable at its synthesis pressure of 44 GPa (Fig. S4 [27]), but is unstable at ambient conditions. The calculated electron density of states shows that high-pressure γ-Y_4C_5 is metallic and the main contributions at the Fermi level come from the Y $4d$ and C $2p$ states (Fig. S5 [27]). In order to understand the stability range of γ-Y_4C_5, its enthalpy is compared with that of the known α-Y_4C_5, revealing that for $P > 12$ GPa γ-Y_4C_5 is thermodynamically favorable (Fig. S6 [27]). To explore the thermodynamic stability of γ-Y_4C_5 in comparison to other yttrium carbides, a convex hull was constructed for the binary Y-C system at different pressures considering known carbides [3,23,42]. The formation enthalpies of the compounds ($Y + xC \rightarrow YC_x$) are calculated relative to the DFT total energies of the end-member elements Y and C as $\Delta H_{Formation} = (H_{YCx} - H_Y - x \cdot H_C)/(1 + x)$. The γ-Y_4C_5 lies on the convex hull and therefore is thermodynamically stable for $P > 20$ GPa (Figs. 3 and S7 [27]), at least to the highest P explored (100 GPa).

To further explore the nature of the chemical bonding in γ-Y_4C_5 at 44 GPa, the computed charge density was analyzed in terms of the electron localization function (ELF) [43], which revealed strong covalent bonding between carbon atoms within the [C_2] and [C_3] units, and ionic bonds between Y and C (Fig. S8 [27]). Charge density maps in the planes containing the [C_2] and [C_3] units [Fig. 1(b)] show slightly larger ELF values between carbon atoms in dimers than in trimers. Therefore, one can assume a slightly higher bond order in the dimer, which correlates with experimentally obtained bond lengths.

Bader charge analysis [44] for Y1, Y2, and Y3 atoms yields values of 1.52, 1.25, and 1.51, respectively, in agreement with Bader charges for other yttrium carbides [45]. Notably, the lowest charge of 1.25 corresponds to the

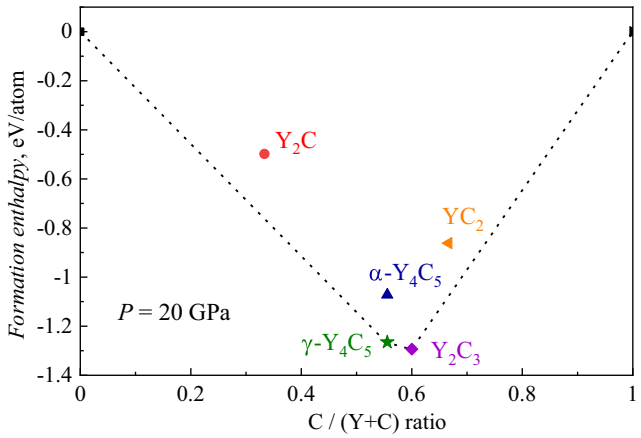

FIG. 3. The calculated convex hull in the Y-C binary-join for known yttrium carbides at 20 GPa. The phases γ-Y_4C_5 and Y_2C_3 lie on the convex hull (black dashed line) and are thus thermodynamically stable. Phases Y_2C, α-Y_4C_5, and YC_2 are off the convex hull and therefore unstable.

Y2 atom, with the smallest CN = 6, and, as a consequence, with the most limited Y to C charge transfer. The charges of carbon atoms C1, C2, C3, and C4 are −1.22, −0.78, −1.25, and −1.29, respectively, so that the edge carbon atoms in the trimer (C3) and in the dimer (C1 and C4) have similar charge states, while the charge for C2 at the center of the trimer is significantly smaller. According to our analysis of charge distribution in the ionic approximation based on a generalization of Pauling's concept of bond strength [46], made using CHARDI2015 [47], the carbon dimers and trimers have charges of −5.13 and −6.47, respectively. Full information on the charge distribution is summarized in Table S5 [27]. The obtained charge values for carbon units are unusually large, therefore to verify our results we performed charge calculations for Y_2C_3, YC_2, and α-Y_4C_5 yttrium carbides with known charge distribution (Table S6 [27]). Whereas the charges obtained for yttrium atoms in γ-Y_4C_5 and in Y_2C_3, YC_2, and α-Y_4C_5 compounds are almost the same and agree well with typical Bader charges for Y [45,48], the charges of carbon (and, as a consequence, of $[C_2]$ units) in γ-Y_4C_5 appear much larger (see Tables S5 and S6 [27]).

At ambient pressure, the low-temperature α-Y_4C_5 polymorph contains single carbon atoms and $[C_2]$ units, with a C-C bond length of 1.33 Å for $[C_2]$, which is equal to the double C-C bond in ethylene (∼1.335 Å) [15]. This corresponds to a $[C_2]^{4-}$ dimer charge state and the formula of α-Y_4C_5 can be written as $Y_4^{3+}[C_2]_2^{4-}C^{4-}$ that is in a good agreement with charges calculated by the CHARDI method (Table S6 [27]). It is worth noticing here that the chemistry of rare earth metal carbides gives evidence that simple rules of electron counting do not describe these materials very well, so that no conclusion about their electronic properties, e.g., metallicity or non-metallicity, can be drawn directly from such assignments.

For the $[C_2]$ and $[C_3]$ units in γ-Y_4C_5, the C-C distances are 1.40(2) and 1.43(1) Å, respectively. They are longer than expected for double-bonded (∼1.34 Å) and much shorter than for single-bonded (∼1.50 Å) carbon atoms. The length of the C-C bond of the order of 1.5—like in benzene—is equal to 1.39 Å at ambient pressure, slightly shorter than both C-C bond lengths in γ-Y_4C_5. This leads us to the conclusion that the C-C bond orders in the $[C_2]$ and $[C_3]$ units are noninteger and should be in the range of 1.0–1.5.

Assuming that the $[C_2]^{Q1-}$ and $[C_3]^{Q2-}$ units have integer formal charges Q, the formula of γ-Y_4C_5 might be represented as $Y_4^{3+}[C_2]^{5-}[C_3]^{6-} \cdot 1e$, where the extra valence electron is delocalized in the conduction band, and does not participate in the Y-C or C-C bonding. The presence of delocalized valence electrons has been demonstrated for other binary metal carbides, e.g., for $Sc_3C_4 = Sc_{30}^{3+}[C_2]_2^{2-}[C_3]_8^{4-}C_{12}^{4-} \cdot 6e$ [14]. In this simple concept of charges' assignment, the new nonlinear $[C_3]^{6-}$ is an anion with 18 electrons, thus it is isoelectronic with the ozone O_3 molecule and the $[CBC]^{7-}$ anion in the $La_9Br_6(CBC)_3$ compound [49,50], both of which are also bent. The bending angles are naturally different for $[CBC]^{7-}$ ($\angle$C-*B*-C = 148°), $[C_3]^{6-}$ ($\angle$C-C-C = 139.6°), and O_3 ($\angle$O-O-O = 116.8°). Although the formal charge scheme for γ-Y_4C_5 is nice and even provides a simple interpretation for the C-C-C bending, it is inconsistent with the C-C bond lengths, and we suggest that the "spare" electrons contribute to the C-C bonding, and that the charges of the $[C_2]$ and $[C_3]$ units in γ-Y_4C_5 are noninteger. A similar phenomenon has recently been reported for $Na_3(N_2)_4$, where $[N_2]$ dimers have noninteger charges of −0.75 [51]. According to the charge analysis (Table S5 [27]), the Q_1/Q_2 ratio for $[C_2]^{Q1-}$ and $[C_3]^{Q2-}$ are very similar, regardless of the chosen analysis method. Assuming that the yttrium cation possesses its common charge Y^{3+}, and using the average ratio $Q_1/Q_2 = 0.775$, we obtain the following noninteger charges for the dimers and trimers $[C_2]^{5.24-}$ and $[C_3]^{6.76-}$ in γ-Y_4C_5. The noninteger charges of the carbon units can be explained by the delocalization of the electrons donated by Y atoms on the partially filled antibonding π^* molecular orbitals of the $[C_2]$ and $[C_3]$ units. The electrons transfer from yttrium to the carbon dumbbells is higher than to the trimers due to the shorter average distance between Y and C atoms in dimers (2.31 Å) in contrast to trimer (2.55 Å). This is in a good agreement with the averaged charges of −2.62 and −2.25 per carbon atom in dimers and trimers, respectively. The bond order is defined as a half of the difference between the number of bonding and of antibonding electrons, so for carbon anions $[C_2]^{5.24-}$ and $[C_3]^{6.76-}$, the bond orders are 1.38 and 1.31, respectively (Fig. S9, [27]). The noninteger formal charges of dimers are known for dinitrogen anions in recently synthesized compounds [51] and they obey the linear dependency between N-N bond length and charge state of $[N_2]^{x-}$. Here we explored

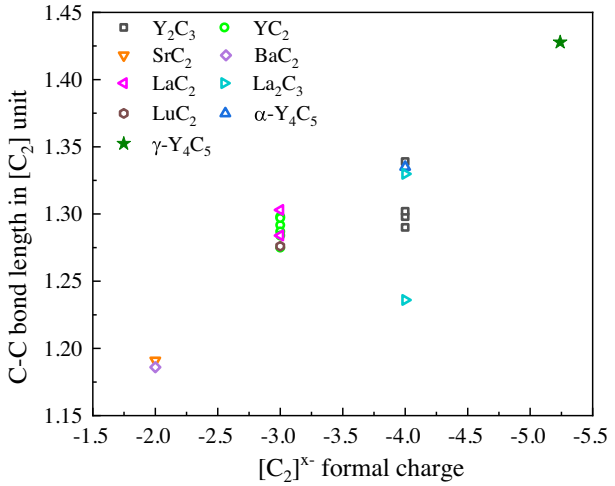

FIG. 4. Correlation between the C-C bond length and charges of the carbon dimers in binary metal carbides at 1 bar. For all presented carbides except γ-Y_4C_5, the C-C distances are those determined from experimental data [6,10,21,23,26,52–56], for γ-Y_4C_5 the value was obtained by DFT calculation from structure relaxation to 0 GPa.

the relationship between formal charges of dimers and the C-C interatomic distances for a number of metal carbides [6,10,23,52–56] and found an expected correlation between the two parameters: the C-C distance increases with an increase in the formal charge of the dimer (Fig. 4). Values predicted for γ-Y_4C_5 mainly match this trend, thus supporting our evaluation of the formal charge of $[C_2]$ as being high and non-integer.

Prior to this work, $[C_3]$ trimers have been considered as mainly linear $[C=C=C]^{4-}$ groups. Possible bending known so far does not exceed 15° (a bending angle of 167.8° was reported for Ho_4C_7) [12]—usually explained by denser packing arrangements in the structure. However, for γ-Y_4C_5, the C3-C2-C3 angle is 134.4(2)°, deviating from 180° by almost 50°, which cannot be explained by the packing arrangement alone. We suggest that the observed extreme bending is a result of pressure-induced charge transfer from Y d orbitals to antibonding states of $[C_3]$ units which leads to a decrease in the multiplicity of the C-C bonds and, as a result, the center C2 carbon atom cannot be considered as sp hybridized.

Conclusions.—The chemical reaction of yttrium and paraffin oil at pressures of ~50 GPa and temperatures of ~2500 °C led to the synthesis of a previously unknown polymorph of yttrium carbide, orthorhombic γ-Y_4C_5. The carbon atoms in the γ-Y_4C_5 crystal structure form $[C_2]$ dumbbells and nonlinear $[C_3]$ trimers with the unusual bending angle of 134.4(11)°. Density functional theory based calculations demonstrate the metallic nature of γ-Y_4C_5 and its dynamic stability at the synthesis pressures. They also indicate that above 12 GPa γ-Y_4C_5 is thermodynamically favorable relative to α-Y_4C_5. Noninteger charges of carbon units, $[C_2]^{5.24-}$ and $[C_3]^{6.76-}$, determined by charge distribution analysis, can be explained by the delocalization of the electrons donated by Y on the partially filled antibonding π^* molecular orbitals of the $[C_2]$ and $[C_3]$ units. The partial filling of the antibonding π^* molecular orbitals of the $[C_3]$ unit results in an unusual C-C bond order of 1.31 and a considerable bending of the $[C_3]$ units. In this work we have demonstrated that covalently bonded carbon species can accommodate very large non-integer formal charges.

The authors acknowledge the Deutsches Elektronen-Synchrotron (DESY, PETRA III) for provision of beamtime at the P02.2. D. L. thanks the Alexander von Humboldt Foundation for financial support. N. D. and L. D. thank the Federal Ministry of Education and Research, Germany (BMBF, Grant No. 05K19WC1) and the Deutsche Forschungsgemeinschaft (DFG projects DU 954–11/1, DU 393–9/2, and DU 393–13/1) for financial support. N. D. also thanks the Swedish Government Strategic Research Area in Materials Science on Functional Materials at Linköping University (Faculty Grant SFO-Mat-LiU No. 2009 00971).

*Corresponding author.
Alena.Aslandukova@uni-bayreuth.de

[1] A. T. Santhanam, in *The Chemistry of Transition Metal Carbides and Nitrides*, edited by S. T. Oyama (Springer, Netherlands, 1996), https://dx.doi.org/10.1007/978-94-009-1565-7_2.
[2] C. Su, J. Zhang, G. Liu, X. Wang, H. Wang, and Y. Ma, Phys. Chem. Chem. Phys. **18**, 14286 (2016).
[3] V. Babizhetskyy, B. Kotur, V. Levytskyy, and H. Michor, *Handbook on the Physics and Chemistry of Rare Earths*, 1st ed (Elsevier B.V., New York, 2017), Vol. 52.
[4] L. E. Toth, *Transition Metal Carbides and Nitrides*, 1st ed. (Academic Press, New York–London, 1971).
[5] F. H. Spedding, K. Gschneidner, and A. H. Daane, J. Am. Chem. Soc. **80**, 4499 (1958).
[6] T. Sakai and G. Y. Adachi, T. Yoshida, and J. Shiokawa, J. Chem. Phys. **75**, 3027 (1981).
[7] R. E. Rundle, N. C. Baenziger, A. S. Wilson, and R. A. McDonald, J. Am. Chem. Soc. **70**, 99 (1948).
[8] M. Atoji, K. Gschneidner, A. H. Daane, R. E. Rundle, and F. H. Spedding, J. Am. Chem. Soc. **80**, 1804 (1958).
[9] M. Atoji and R. C. Medrud, J. Chem. Phys. **31**, 332 (1959).
[10] M. Atoji, J. Chem. Phys. **35**, 1950 (1961).
[11] R. West, I. A. Carney, and I. C. Mineo, J. Am. Chem. Soc. **87**, 3788 (1965).
[12] H. Mattausch, T. Gulden, R. K. Kremer, J. Horakh, and A. Simon, Z. Naturforsch. B **49**, 1439 (1994).
[13] H. Fjellvág and P. Karen, Inorg. Chem. **31**, 3260 (1992).
[14] R. Pöttgen and W. Jeitschko, Inorg. Chem. **30**, 427 (1991).
[15] A. Almenningen, Acta Chem. Scand. **13**, 1699 (1959).
[16] R. Hoffmann and H. J. Meyer, J. Inorg. Gen. Chem. **607**, 57 (1992).

[17] T. A. Strobel, O. O. Kurakevych, D. Y. Kim, Y. Le Godec, W. Crichton, J. Guignard, N. Guignot, G. D. Cody, and A. R. Oganov, Inorg. Chem. **53**, 7020 (2014).
[18] Y. L. Li, S. N. Wang, A. R. Oganov, H. Gou, J. S. Smith, and T. A. Strobel, Nat. Commun. **6**, 6974 (2015).
[19] S. Roszak and K. Balasubramanian, J. Phys. Chem. **100**, 8254 (1996).
[20] X. Gao, Y. Jiang, R. Zhou, and J. Feng, J. Alloys Compd. **587**, 819 (2014).
[21] M. C. Krupka, A. L. Giorgi, N. H. Krikorian, and E. G. Szklarz, J. Less Common Met. **17**, 91 (1969).
[22] C. P. Poople, *Handbook of Superconductivity*, 1st ed. (Academic Press, San Diego, 2020).
[23] R. Czekalla, T. Hüfken, W. Jeitschko, R. D. Hoffmann, and R. Pöttgen, J. Solid State Chem. **132**, 294 (1997).
[24] G. Amano, S. Akutagawa, T. Muranaka, Y. Zenitani, and J. Akimitsu, J. Phys. Soc. Jpn. **73**, 530 (2004).
[25] S. Akutagawa and J. Akimitsu, Sci. Technol. Adv. Mater. **7**, 2 (2006).
[26] T. Nakane, T. Naka, H. Kito, T. Wada, A. Matsushita, H. Kumakura, and T. Mochiku, Physica (Amsterdam) **426–431C**, 492 (2005).
[27] See Supplemental Material at http://link.aps.org/supplemental/10.1103/PhysRevLett.127.135501 for experimental and theoretical calculations details, Tables S1–S6, Figs. S1–S8, and bibliography, which includes Refs. [28–39].
[28] I. Kantor, V. Prakapenka, A. Kantor, P. Dera, A. Kurnosov, S. Sinogeikin, N. Dubrovinskaia, and L. Dubrovinsky, Rev. Sci. Instrum. **83**, 125102 (2012).
[29] Rigaku Oxford Diffraction, CrysAlisPro Software system (2015).
[30] C. S. Zha, W. A. Bassett, and S. H. Shim, Rev. Sci. Instrum. **75**, 2409 (2004).
[31] S. Anzellini, A. Dewaele, F. Occelli, P. Loubeyre, and M. Mezouar, J. Appl. Phys. **115**, 043511 (2014).
[32] Y. Akahama and H. Kawamura, J. Appl. Phys. **100**, 043516 (2006).
[33] T. Fedotenko, L. Dubrovinsky, G. Aprilis, E. Koemets, A. Snigirev, I. Snigireva, A. Barannikov, P. Ershov, F. Cova, M. Hanfland, and N. Dubrovinskaia, Rev. Sci. Instrum. **90**, 104501 (2019).
[34] CrysAlisPro Data Collection, and Processing Software for Agilent X-Ray Diffractometers, Agilent Technol. Oxford (2014).
[35] V. Petrícek, M. Dušek, and L. Palatinus, Z. Krist. **229**, 345 (2014).
[36] K. Momma and F. Izumi, J. Appl. Crystallogr. **44**, 1272 (2011).
[37] J. Gonzalez-Platas, M. Alvaro, F. Nestola, and R. Angel, J. Appl. Crystallogr. **49**, 1377 (2016).
[38] J. P. Perdew, K. Burke, and M. Ernzerhof, Phys. Rev. Lett. **77**, 3865 (1996).
[39] G. Kresse and D. Joubert, Phys. Rev. B **59**, 1758 (1999).
[40] G. Kresse and J. Furthmüller, Phys. Rev. B **54**, 11169 (1996).
[41] A. Togo and I. Tanaka, Scr. Mater. **108**, 1 (2015).
[42] M. Atoji, R. C. Medrud, K. Gschneidner, A. H. Daane, R. E. Rundle, F. H. Spedding, K. Gschneidner, A. H. Daane, T. Sakai, G. Y. Adachi, T. Yoshida, J. Shiokawa, R. E. Rundle, N. C. Baenziger, A. S. Wilson, and R. A. McDonald, J. Chem. Phys. **80**, 99 (1958).
[43] A. Savin, A. D. Becke, J. Flad, R. Nesper, H. Preuss, and H. G. von Schnering, *Angew. Chem. Int. Ed. English* 30, 409 (1991).
[44] G. Henkelman, A. Arnaldsson, and H. Jónsson, Comput. Mater. Sci. **36**, 354 (2006).
[45] X. Feng, S. Lu, C. J. Pickard, H. Liu, S. A. T. Redfern, and Y. Ma, Commun. Chem. **1**, 85 (2018).
[46] L. Pauling, J. Am. Chem. Soc. **51**, 1010 (1929).
[47] M. Nespolo and B. Guillot, J. Appl. Crystallogr. **49**, 317 (2016).
[48] J. Chen, W. Cui, K. Gao, J. Hao, J. Shi, and Y. Li, Phys. Rev. Research **2**, 043435 (2020).
[49] H. Mattausch, A. Simon, C. Felser, and R. Dronskowski, Angew. Chem., Int. Ed. Engl. **35**, 1685 (1996).
[50] H. Mattausch and A. Simon, Angew. Chem., Int. Ed. Engl. **34**, 1633 (1995).
[51] M. Bykov, K. R. Tasca, I. G. Batyrev, D. Smith, K. Glazyrin, S. Chariton, M. Mahmood, and A. F. Goncharov, Inorg. Chem. **59**, 14819 (2020).
[52] V. Vohn, M. Knapp, U. Ruschewitz, V. Vohn, W. Kockelmann, and U. Ruschewitz, J. Solid State Chem. **151**, 111 (2000).
[53] M. Knapp and U. Ruschewitz, Chem. Eur. J. **7**, 874 (2001).
[54] V. Vohn, M. Knapp, and U. Ruschewitz, J. Solid State Chem. **151**, 111 (2000).
[55] Y. Yosida, J. Appl. Phys. **92**, 5494 (2002).
[56] M. Atoji and D. E. Williams, J. Chem. Phys. **35**, 1960 (1961).

Supplementary Materials

Novel high-pressure yttrium carbide, γ-Y_4C_5, containing [C_2] and non-linear [C_3] units with unusually large formal charges

Alena Aslandukova[1], Andrey Aslandukov[2], Liang Yuan[1], Dominique Laniel[2], Saiana Khandarkhaeva[2], Timofey Fedotenko[2], Gerd Steinle-Neumann[1], Konstantin Glazyrin[3], Natalia Dubrovinskaia[2,3], Leonid Dubrovinsky[1].

[1] Bavarian Research Institute of Experimental Geochemistry and Geophysics, University of Bayreuth, 95440 Bayreuth, Germany

[2] Material Physics and Technology at Extreme Conditions, Laboratory of Crystallography, University of Bayreuth, 95440 Bayreuth, Germany

[3] Photon Science, Deutsches Elektronen-Synchrotron, Notkestrasse 85, 22607 Hamburg, Germany

[4] Department of Physics, Chemistry and Biology (IFM), Linköping University, SE-581 83 Linköping, Sweden

Experimental method

Sample preparation.

The BX90-type large X-ray aperture diamond anvil cell (DAC) equipped with Boehler-Almax type diamonds (culet diameter is 250 mm) was used for single-crystal XRD studies [1,2]. Rhenium foil pre-indented to a thickness ~20 μm and a hole of ~100 μm in diameter drilled in the center of the indentation served as a sample chamber. A piece of pure metallic yttrium was placed in the sample chamber filled with paraffin oil. Pressure was determined using the equation of states (EOS) of Re [3,4], and additionally monitored by the Raman signal from the diamond anvils [5]. Samples were compressed up to 51 GPa and laser heated (LH) to ~ 2500(200)°C. LH of the samples was performed using *in house* laser heating setup [6], equipped with two YAG lasers (1064 nm central wavelength) and IsoPlane SCT 320 spectrometer with a 1024×2560 PI-MAX 4 camera for collection of thermal emission spectra from the heated spot. Temperatures were estimated by fitting of thermal emission spectra of the sample to the grey body approximation of Planck's radiation function over a given wavelength range (570-830 nm).

X-ray diffraction.

XRD measurements were performed at beamline P02.2 of Petra III (DESY, Hamburg, Germany) with the X-ray beam (λ = 0.2891 Å) focused down to 1.8 × 2 μm^2 by a Kirkpatrick−Baez mirror system, and XRD patterns were collected on a PerkinElmer 1621 XRD flat-panel detector. For single-crystal XRD measurements, samples are rotated around a vertical ω axis in a range ±35°. The XRD images were collected with an angular step Δω = 0.5° and an exposure time of 2s per

frame. The CrysAlisPro software package was used for analysis of the single-crystal XRD data (indexing, data integration, frame scaling, and absorption correction) [7]. A single crystal of $(Mg_{1.93},Fe_{0.06})(Si_{1.93},Al_{0.06})O_6$ orthoenstatite (*Pbca*, $a = 18.2391(3)$, $b = 8.8117(2)$, $c = 5.18320(10)$ Å), was used to calibrate instrument model of the CrysAlisPro software (sample-to-detector distance, the detector's origin, offsets of the goniometer angles and rotation of the X-ray beam and the detector around the instrument axis). The structure solution was performed with the *Jana2006* software [8]. Crystal structure visualization was made with the VESTA software [9]. The experimental EOS of the synthesized materials were obtained by fitting the pressure-volume data using the EoSFit7-GUI [10].

Computational method.

The properties of the systems were determined via the first-principles calculations using Kohn-Sham density functional theory (DFT) with the generalized gradient approximation (GGA) by Perdew–Burke–Ernzerhof (PBE) [11] for the exchange–correlation energy implemented within the projector-augmented wave (PAW) method [12] for describing the interaction between the core and the valence electrons (4*s*4*p*5*s*4*d* and 2*s*2*p* for Y and C, respectively) in the Vienna ab initio simulation package (VASP) [13]. We used the Monkhorst–Pack scheme with 4 × 6 × 6 *k*-points for Brillouin zone sampling and a energy cutoff for the plane wave expansion of 800 eV, with which total energies are converged to better than 2 meV/atom. Computations were performed for eight volumes that cover the pressure range of 0-100 GPa. Harmonic lattice dynamics calculations were performed with the Phonopy software using the finite displacement method [14].

Tables.

Table S1: Diamond anvil cell experiments.

	Reagents	Pressure range (GPa)	Temperatures (°C)
DAC1	pure metallic Y in paraffin oil	44(1)	2500(200)
DAC2	pure metallic Y in paraffin oil	46(1)	2000(200) – 3000(200)
DAC3	pure metallic Y in paraffin oil	0 – 51(1)	2500(200)

Table S2: Experimentally determined crystallographic data for the γ-Y_4C_5 phase at 44 GPa in comparison to the corresponding DFT-relaxed structure. The full crystallographic dataset was deposited to the CCDC under the deposition number 2083934.

Crystal phase			γ-Y_4C_5 (experiment)	γ-Y_4C_5 (theory)
Pressure (GPa)			44(1)	41
Space group, *Z*			*Cmce,* 8	*Cmce,* 8
a (Å)			12.183(6)	12.3311
b (Å)			7.659(3)	7.5829
c (Å)			8.858(2)	8.8394
V (Å^3)			826.54(5)	826.536
Wyckoff site and fractional atomic coordinates (*x*; *y*; *z*):	Y1	*8d*	(0.3525(1); 0.5; 0.5)	(0.3518; 0.5; 0.5)
	Y2	*8f*	(0.5; 0.7895(2); 0.6299(1))	(0.5; 0.8026; 0.6234)
	Y3	*16g*	(0.6451(1);0.6247(2);0.8548(1))	(0.6449; 0.6266; 0.8529)
	C1	*8f*	(0.5; 0.5015(16); 0.6768(14))	(0.5; 0.5077; 0.6750)
	C2	*8e*	(0.75; 0.3835(14); 0.75)	(0.75; 0.3835; 0.75)
	C3	*16g*	(0.6934(8);0.3114(12);0.8762(9))	(0.6935; 0.3123; 0.8762)
	C4	*8f*	(0.5; 0.3371(18); 0.6073(14))	(0.5; 0.3413; 0.6086)
C-C distance in [C_2] units (Å)			1.40(2)	1.392
C-C distance in [C_3] units (Å)			1.43(1)	1.422
Number of measured/independent reflections (I ≥ 3σ)			560 / 239 (221)	-
R_{int}			0.0267	-
Final R indexes (I ≥ 3σ)			R_1 = 0.0227; wR_2 = 0.0255	-
Final R indexes (all data)			R_1 = 0.0252; wR_2 = 0.0260	-
Number of refined parameters			33	-

Table S3. Crystallographic data for yttrium atomic coordinates, coordination numbers of Y and Y-C distances for the α-Y_4C_5, Y_4C_7 and Y_3C_4 at ambient pressure.

Composition	Y atom / wyckoff site	Fractional atomic coordinates (*x*; *y*; *z*)	CN of Y	Y-C distances in first coordination sphere, Å
α-Y_4C_5	Y0 / 4h	0.3922; 0.3045; 0.5	9	2.499 - 2.873
	Y1 / 4g	0.2455; 0.0434; 0	5	2.390 - 2.648
Y_4C_7	Y0 / 4e	0.0427; 0.1651; 0.1595	9	2.423 - 2.825
	Y1 / 4e	0.3247; 0.4374; 0.2091	7	2.478 – 2.878
Y_3C_4	Y0 / 16i	0.1006; 0.2883; 0.1466	7	2.357 - 2.859
	Y1 / 8h	0.0956; 0.7018; 0.50	7	2.498 - 2.775
	Y2 / 4e	0; 0; 0.3124	6	2.358 - 2.643
	Y3 / 2a	0; 0; 0	6	2.514 – 2.621

Table S4: Experimentally determined crystallographic data for the Y_2C_3 phase at 46 GPa.

Crystal phase			Y_2C_3 (experiment)
Pressure (GPa)			46
Space group, *Z*			*I*-43*d,* 8
a (Å)			7.745(2)
V (Å^3)			464.65(6)
Wyckoff site and fractional atomic coordinates (*x*; *y*; *z*):	Y	*16c*	(0.0516(2); 0.4484(2); 0.5516(2))
	C	*24d*	(0; 0.25; 0.790(3))
C-C distance in [C_2] units (Å)			1.32(1)
Number of measured/independent reflections (I ≥ 3σ)			654 / 230 (181)
R_{int}			0.0699
Final R indexes (I ≥ 3σ)			R_1 = 0.0674; wR_1 = 0.0629
Final R indexes (all data)			R_1 = 0.0949; wR_1 = 0.0697
Number of refined parameters			6

Table S5: Results of charge distribution analysis using Bader charge calculations based on the computed charge density and charge analysis in the ionic approximation (CHARDI2015) from the refined structure at 44 GPa (DAC1).

Atom	Bader charge analysis	CHARDI method
Y1	1.52	2.95
Y2	1.25	2.79
Y3	1.51	2.93
C1	-1.22	-2.55
C2	-0.78	-1.87
C3	-1.25	-2.30
C4	-1.29	-2.58

Charge analysis for carbon units in the γ-Y_4C_5					
Carbon unit	Bond length, Å	Bader charge analysis		CHARDI method	
		Q value	Q_1/ Q_2	*Q* value	Q_1/ Q_2
$[C_2]^{Q1-}$	1.40(2)	-2.51	0.76	-5.13	0.79
$[C_3]^{Q2-}$	1.43(1)	-3.28		-6.47	

Table S6. Results of charge distribution analysis using Bader charge calculations based on the computed charge density and charge analysis in the ionic approximation for the yttrium carbides Y_2C_3, YC_2 and α-Y_4C_5 at ambient pressure.

	Atom and Wyck. site	fractional atomic coordinates (*x*; *y*; *z*)	Bader charge analysis	Charge of [C_2]	CHARDI method	Charge of [C_2]
Y_2C_3	Y / 16c	0.0510; 0.0510; 0.0510	1.62	-2.16	2.96	-3.94
	C / 24d	0.2960; 0; 0.25	-1.08		-1.97	
YC_2	Y / 2a	0; 0; 0	1.85	-1.86	2.98	-2.98
	C / 4e	0; 0; 0.3951	-0.93		-1.49	
α-Y_4C_5	Y0 / 4h	0.3922; 0.3045; 0.5	1.67	-2.24	3.36	-3.91
	Y1 / 4g	0.2455; 0.0434; 0	1.65		2.64	
	C0 / 4g	0.0930; 0.3443; 0	-1.08		-1.99	
	C1 / 4g	0.1400; 0.2353; 0	-1.16		-1.92	
	C2 / 2b	0; 0; 0.5	-2.16		-4.19	

Figures.

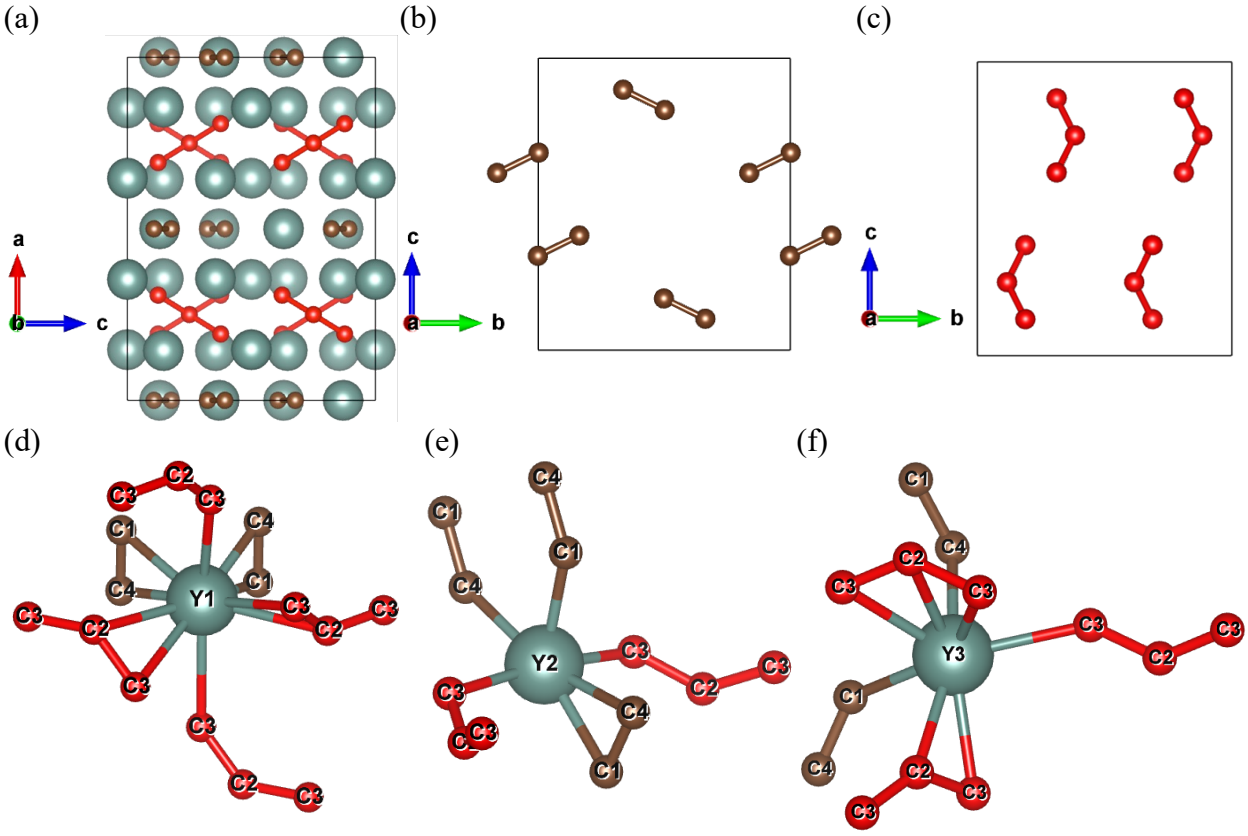

FIG. S1. Crystal structure of γ-Y_4C_5 at 44 GPa. (a) The unit cell viewed along the *b* direction; balls symbolize yttrium and carbon atoms: dark gray balls are Y atoms; carbon atoms if $[C_2]$ are shown in brown and of $[C_3]$- in red (b) Arrangement of $[C_2]$ units in the rows along the *b* direction (Y atoms in the raw are not shown); $[C_2]$ dimers in the adjacent rows are mutually oriented in a "parquet-like" manner. (c) Arrangement of $[C_3]$ units. (d) – (f) Coordination environment of Y1, Y2 and Y3 atoms.

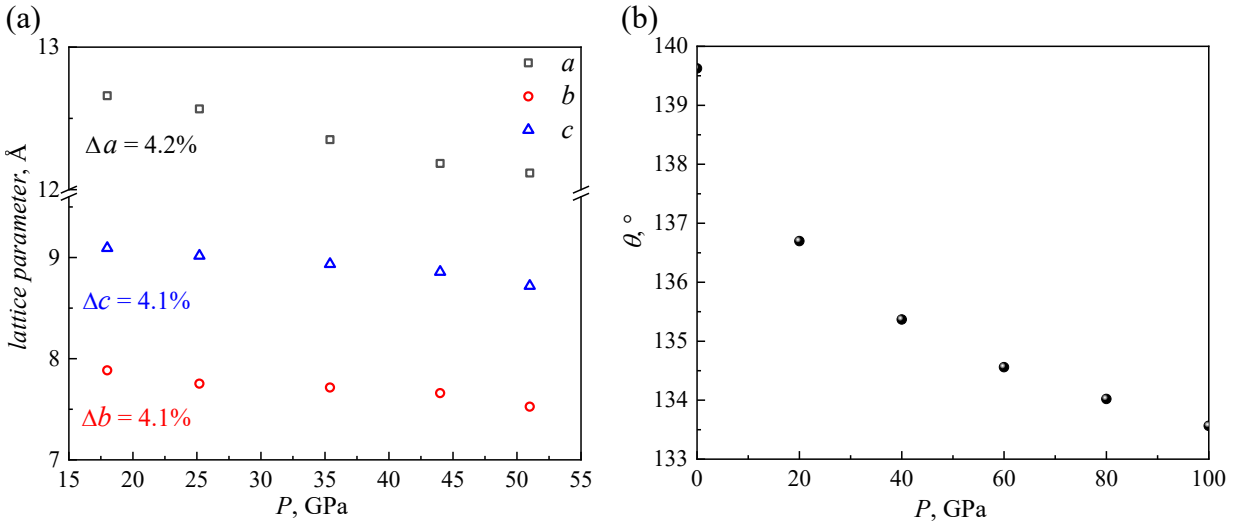

FIG. S2. Pressure dependence of the lattice parameters and calculated angle between atoms C3-C2-C3 for γ-Y_4C_5 phase. (a) Pressure-dependent experimental values of lattice parameters. The open gray, red and blue symbols represent a, b and c lattice parameters, respectively. The relative change in the length are the same (~ 4%) for each crystallographic direction. (b) Pressure dependence of the bending angle in $[C_3]$ carbon units calculated by DFT.

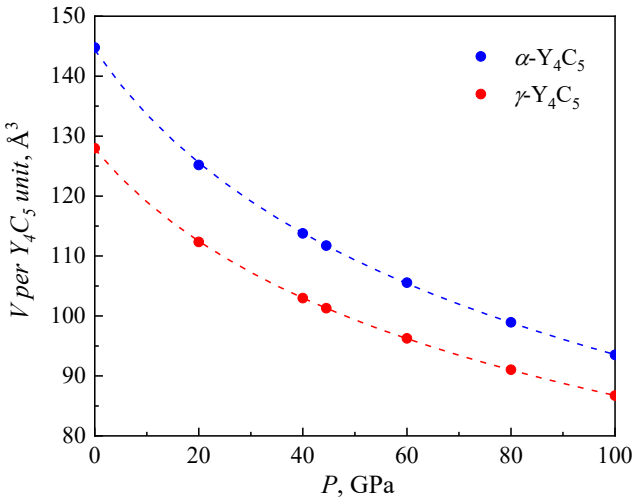

FIG. S3. Pressure-volume dependence for α-Y_4C_5 (blue) and γ-Y_4C_5 (red) from the DFT calculations using fixed pressures to construct the convex hull (Fig. S7). Dashed lines represent the second order Birch Murnaghan fit of the results.

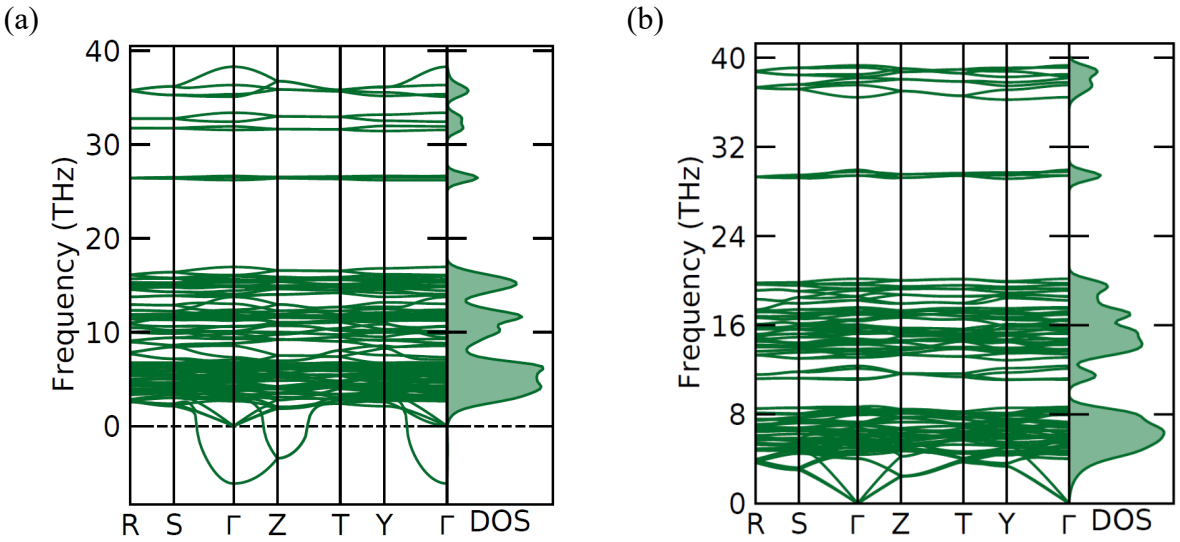

FIG. S4. Phonon dispersion curves along high-symmetry directions in the Brillouin zone and phonon density of states for γ-Y_4C_5 calculated at (a) 0 GPa and (b) 44 GPa.

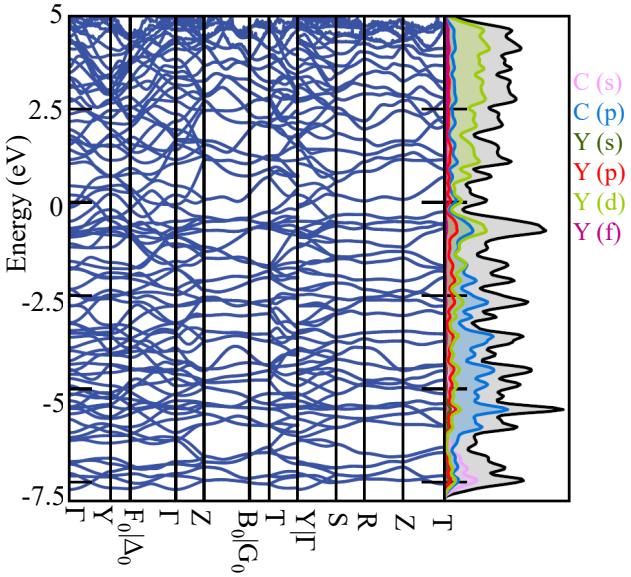

FIG. S5. The electronic band structure (left side) and electronic density of states (right side) of γ-Y_4C_5 calculated at 44 GPa along high-symmetry directions in the Brillouin zone.

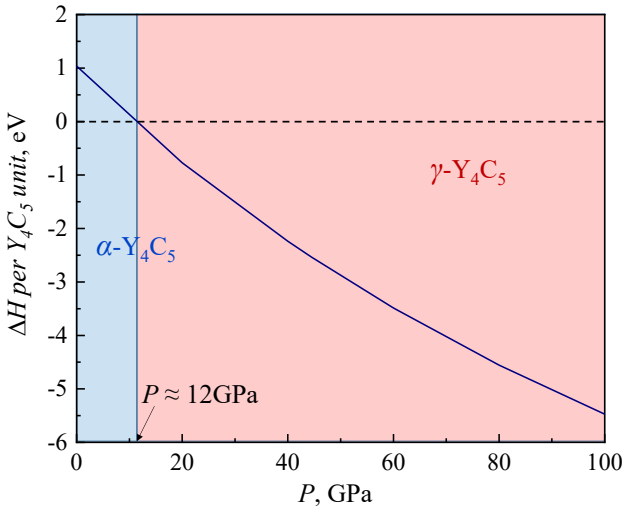

FIG. S6. Calculated difference in enthalpy per formula unit between α-Y_4C_5 and γ-Y_4C_5 phases ($\Delta H = H(\alpha\text{-}Y_4C_5)/Z - H(\gamma\text{-}Y_4C_5)/Z$) as a function of pressure.

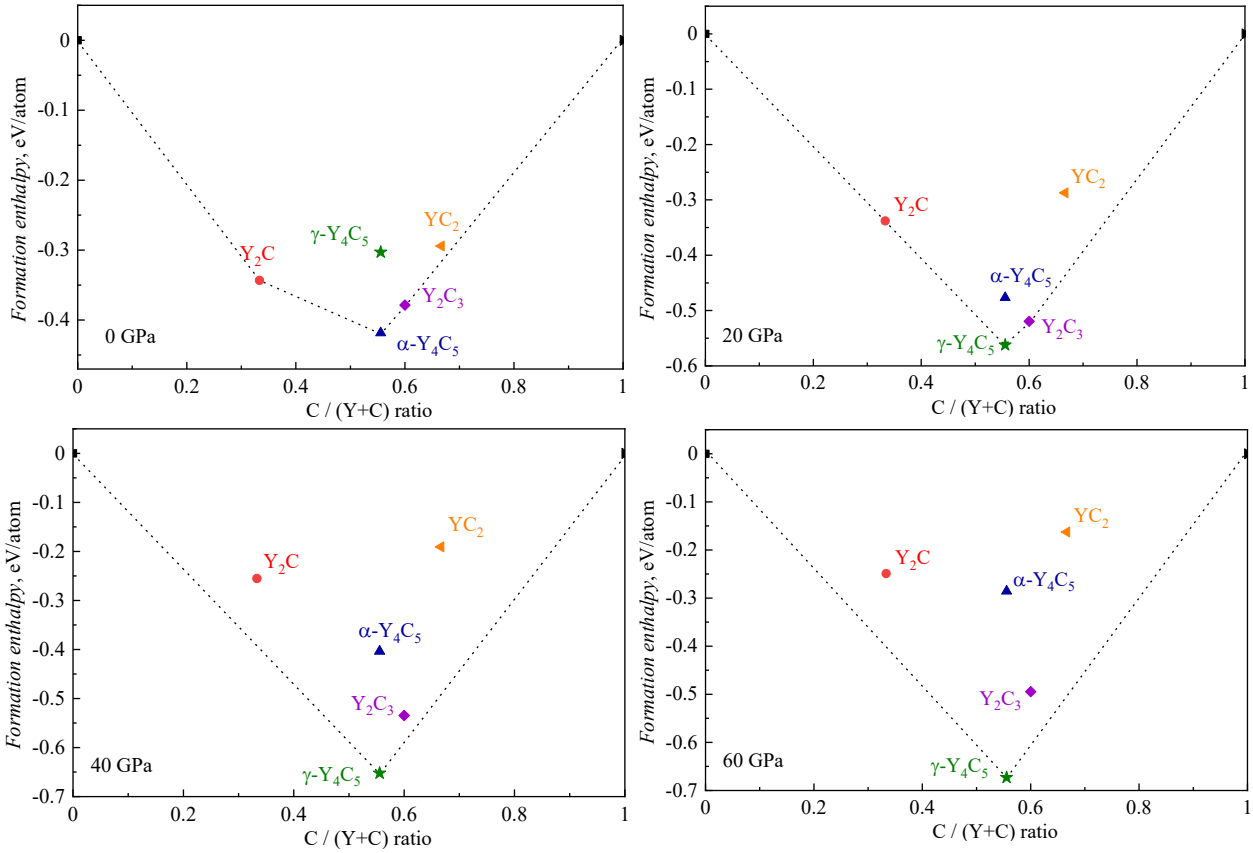

Fig. S7. Calculated convex hull in the Y-C binary for known yttrium carbides at 0 GPa, 20 GPa, 40 GPa and 60 GPa. Phases that lie on the convex hull (black dashed line) are thermodynamically stable (there are no other lower energy phases into which they can decompose). Phases that are off the convex hull are unstable.

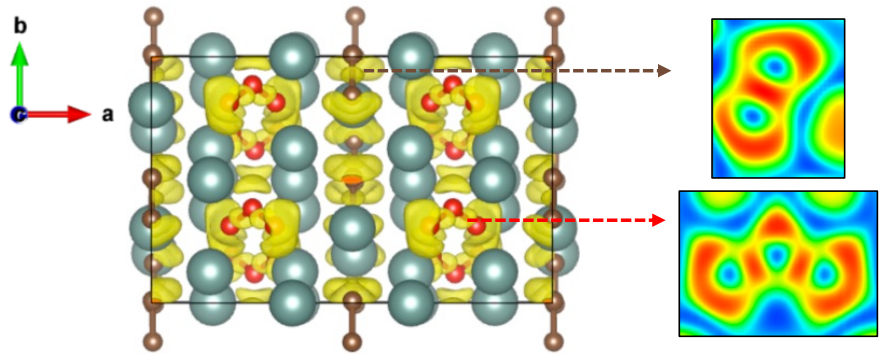

FIG. S8. (a) Calculated electron localization function (ELF) with an isosurface value of 0.8 superimposed over the crystal structure of γ-Y_4C_5 at 44 GPa and 2D ELF shown for the cross-sections of the [C2] and [C3] carbon units.

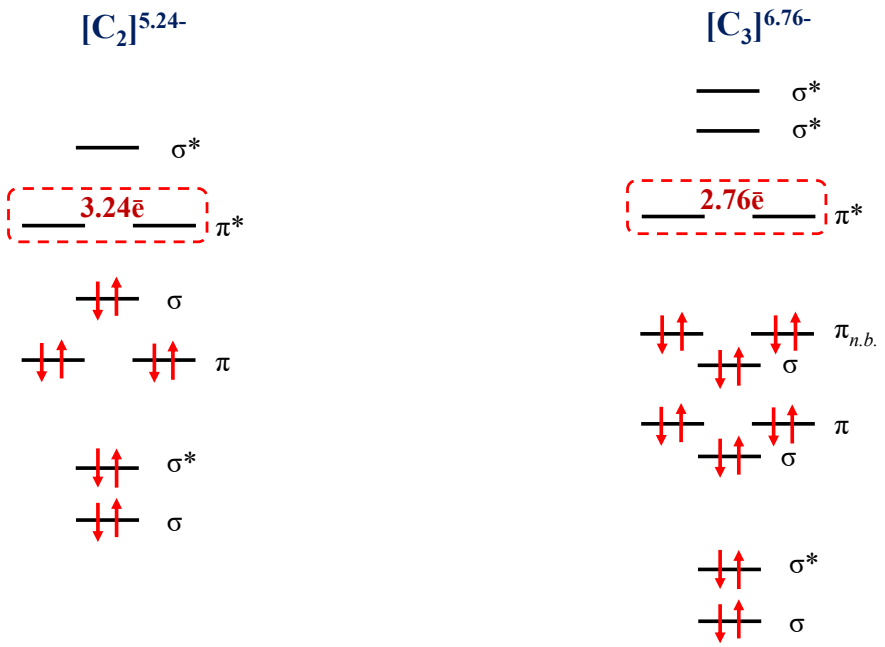

Fig. S9. Qualitative molecular orbital diagrams with intermediate average occupancy for carbon anions $[C_2]^{5.24-}$ and $[C_3]^{6.76-}$.

References

[1] I. Kantor, V. Prakapenka, A. Kantor, P. Dera, A. Kurnosov, S. Sinogeikin, N. Dubrovinskaia, and L. Dubrovinsky, Rev. Sci. Instrum. **83**, 125102 (2012).
[2] Rigaku Oxford Diffraction, CrysAlisPro Software system (2015).
[3] C. S. Zha, W. A. Bassett, and S. H. Shim, Rev. Sci. Instrum. **75**, 2409 (2004).
[4] S. Anzellini, A. Dewaele, F. Occelli, P. Loubeyre, and M. Mezouar, J. Appl. Phys. **115**, 043511 (2014).
[5] Y. Akahama and H. Kawamura, J. Appl. Phys. **100**, 043516 (2006).
[6] T. Fedotenko, L. Dubrovinsky, G. Aprilis, E. Koemets, A. Snigirev, I. Snigireva, A. Barannikov, P. Ershov, F. Cova, M. Hanfland, and N. Dubrovinskaia, Rev. Sci. Instrum. **90**, 104501 (2019).
[7] CrysAlisPro Data Collection and Processing Software for Agilent X-Ray Diffractometers, Agilent Technol. Oxford (2014).
[8] V. Petrícek, M. Dušek, and L. Palatinus, Zeitschrift Fur Krist. **229**, 345 (2014).
[9] K. Momma and F. Izumi, J. Appl. Crystallogr. **44**, 1272 (2011).
[10] J. Gonzalez-Platas, M. Alvaro, F. Nestola, and R. Angel, J. Appl. Crystallogr. **49**, 1377 (2016).
[11] J. P. Perdew, K. Burke, and M. Ernzerhof, Phys. Rev. Lett. **77**, 3865 (1996).
[12] D. Joubert, Phys. Rev. B - Condens. Matter Mater. Phys. **59**, 1758 (1999).
[13] G. Kresse and J. Furthmüller, Phys. Rev. B. B. **54**, 11169 (1996).
[14] A. Togo and I. Tanaka, Scr. Mater. **108**, 1 (2015).

4.4. High-pressure yttrium borate o*C*20-YBO_3 and orthocarbonate *hR*39-$Y_3(CO_4)_2$ synthesized at megabar pressures.

This section contains the following manuscript and the related supplementary material:

"High-pressure yttrium borate o*C*20-YBO_3 and orthocarbonate *hR*39-$Y_3(CO_4)_2$ synthesized at megabar pressures"

A. Aslandukova, A. Aslandukov, Y. Yin, M. Bykov, A. Pakhomova, N. Dubrovinskaia & L. Dubrovinsky

Status: to be submitted to *Angewandte Chemie*.

High-pressure yttrium borate o*C*20-YBO_3 and orthocarbonate *hR*39-$Y_3(CO_4)_2$ synthesized at megabar pressures

Alena Aslandukova[1,2], Andrey Aslandukov[1,2], Yuqing Yin[3], Maxim Bykov[4], Anna Pakhomova[5], Natalia Dubrovinskaia[2,3], Leonid Dubrovinsky[1]

[1] Bavarian Research Institute of Experimental Geochemistry and Geophysics (BGI), University of Bayreuth, 95440 Bayreuth, Germany
[2] Material Physics and Technology at Extreme Conditions, Laboratory of Crystallography, University of Bayreuth, 95440 Bayreuth, Germany
[3] Department of Physics, Chemistry and Biology (IFM), Linköping University, SE-581 83, Linköping, Sweden
[4] Institute of Inorganic Chemistry, University of Cologne, 50939 Cologne, Germany
[5] European Synchrotron Radiation Facility, 38000 Grenoble, France

Abstract

Two novel ternary compounds, yttrium borate *oC*20-YBO_3 and orthocarbonate *hR*39-$Y_3(CO_4)_2$, were synthesized at two pressures of ~ 90 and 120 GPa and temperatures of ~3500K in the laser-heated diamond anvil cell. Their crystal structures were solved and refined using *in situ* high-pressure synchrotron single-crystal X-ray diffraction. The crystal structure of *oC*20-YBO_3 features a unique previously unobserved isolated infinite zig-zag unbranched chains of corner-sharing BO_4 tetrahedra. The *hR*39-$Y_3(CO_4)_2$ is comprised of isolated $[CO_4]^{4-}$ orthocarbonate anions and represents the first rare-earth orthocarbonate. Density functional theory (DFT) calculations support these discoveries and provide further insight into the stability and physical properties of the synthesized compounds. Our results enrich borate and carbonate chemistry.

Introduction

Metal borates and carbonates are important inorganic solids, that have been studied extensively both from geoscience and material science perspectives [1–3]. Rare-earth borates are known as multifunctional optical materials. Yttrium borates are known as host matrices for luminescence lanthanide ions[4,5]. There are a few reported yttrium anhydrous borates synthesized at ambient pressure, YBO_3[6–8] and Y_3BO_6 [9] containing isolated $[B_3O_9]^{6-}$ or $[BO_3]^{3-}$ anions. Several more borates $Y(BO_2)_3$ [10], α-$Y_2B_4O_9$ [11], β-$Y_2B_4O_9$ [12] and YB_7O_{12} [13] were obtained since 2017 under moderate pressure up to 12.3 GPa. These high-pressure phases possess different anionic motifs: bands of BO_4 tetrahedra as well as planar BO_3-groups in β-$Y_2B_4O_9$, ribbons of BO_4 tetrahedra in $Y(BO_2)_3$, and 3D frameworks of BO_4 tetrahedra in α-$Y_2B_4O_9$ and YB_7O_{12}.

Rare-earth carbonates at ambient conditions are usually present as carbonate crystallohydrates, oxo- or hydroxy-carbonates. Yttrium carbonate $Y_2(CO_3)_3 \cdot nH_2O$ in a form of crystallohydrate with different water content (including minerals like tengerite-(Y) (n=2-3)[14–16] and yuchuanite-(Y) (n=1)[17]), oxycarbonate $Y_2O_2CO_3$[18], and hydroxycarbonate $YOHCO_3$[16,19] are known at ambient pressure containing only planar trigonal $[CO_3]^{2-}$. It is well-established, that high pressure promotes the stabilization of more complex anions such as pyrocarbonate $[C_2O_5]^{4-}$ anion[20,21] and sp^3-carbonate anions built of CO_4 tetrahedra — isolated[22–24] or connected to other tetrahedra by corner-sharing forming rings[25–27], finite [22,28] or infinite chains[29]. However, high-pressure rare-earth carbonates are not yet known.

Here, we report crystal structures of a novel high-pressure modification of yttrium borate *oC*20-YBO_3 with unique unbranched chains of the corner-sharing $[BO_4]$ tetrahedra and first rare-earth orthocarbonate *hR*39-$Y_3(CO_4)_2$. They were serendipitously obtained simultaneously in a laser-heated diamond cell at 120 and 90 GPa during the exploration of high-pressure yttrium hydrides. Their crystal structures were solved and refined based on synchrotron single-crystal X-ray diffraction. DFT calculations give further insight into the stability and physical properties of discovered compounds.

The novel yttrium borate o*C*20-YBO_3 and orthocarbonate *hR*39-$Y_3(CO_4)_2$ were obtained as minor byproducts during the high-pressure synthesis of the yttrium hydrides in one out of five laser-heated DACs (namely DAC#5) reported in [30]. This DAC was loaded with the yttrium (Y) pieces in between two layers of ammonia borane (NH_3BH_3), which was used as a hydrogen-rich source, as well as a pressure-transmitting media. The details of the sample preparation, data collection, structure determination, and refinement are described in the Supplemental Material. The presence of oxygen in the reaction products is apparently related to oxygen contamination of yttrium pieces since yttrium loading was done in air, and therefore the partial oxidizing of yttrium pieces was possible. The carbon originates from the diamond anvils, well known to be able to act as a carbon source and participate in chemical reactions[30–35]. Below YBO_3 is first discussed, and then $Y_3(CO_4)_2$.

The novel high-pressure polymorph of YBO_3 was observed at ~ 120 GPa and 90 GPa after laser-heating to ~ 3500 K through a chemical reaction of partially oxidized yttrium with ammonia borane. The *in-situ* synchrotron single-crystal X-ray diffraction enabled the crystal structure solution and refinement (crystallographic information is provided in Table S1). YBO_3 crystallizes in the orthorhombic space group $C222_1$ (#20, $Z = 4$, Pearson symbol *oC*20) with the unit cell parameters $a = 5.594(13)$ Å, $b = 7.225(3)$ Å, and $c = 3.3428(13)$ Å (unit cell volume is 135.1(3) $Å^3$) at 120(2) GPa (Fig. 1). Yttrium and boron atoms occupy Wyckoff positions 4*b* and 4*a*, respectively, while oxygen atoms are located at two distinct 8*c* and 4*b* Wyckoff sites. Yttrium polyhedra YO_{10} can be considered as distorted bicapped square prisms, with the Y-O distances ranging between 2.07(4) and 2.441(14) Å (Fig. 1c). In this structure, BO_4 tetrahedra connected via common vertices, form a complex quasi 1D anionic network – infinite zig-zag unbranched boron-oxygen chains $[-O-B(O_2)-]^{3-}$ along the *c* axis (Fig. 1b). The boron bond with bridging oxygen O2 is slightly elongated in comparison to non-bridging oxygen O1 (Fig. 1d). Considering higher pressure, the B-O bond length (1.34(7) and 1.44(6) Å) and ∠O-B-O angles (109(7)° and 111(4)°) in *oC*20-YBO_3 at 120 GPa are in good agreement with those in other compounds with corner-connected BO_4 tetrahedra, *i.e.* YB_7O_{12} at 10 GPa (1.397(2)-1.562(2) Å, 100.2(7)°-119.8(8)°) or *β*-MgB_4O_7 at 1 bar (1.434(4)-1.569(6) Å, 106.6(2)°-111.4(4)°) [13,36].

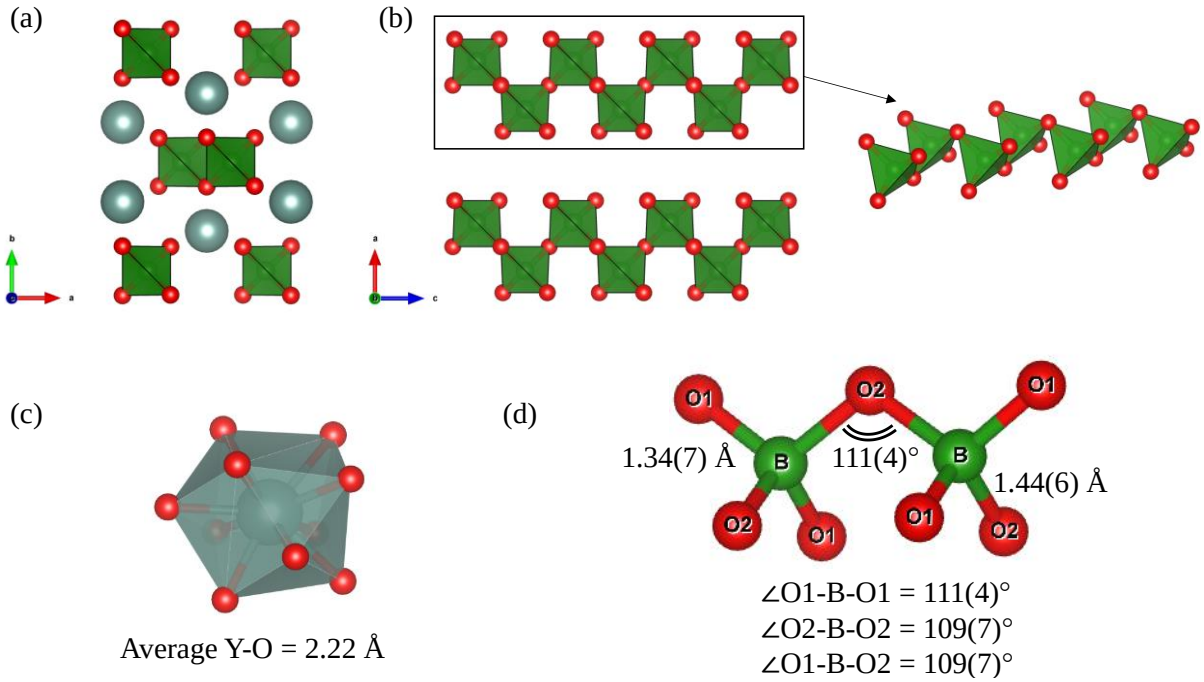

Fig. 1. Crystal structure of *oC*20-YBO_3. A unit cell of the structure with the Y, B, and O atoms shown as gray, green, and red balls, respectively, (a) along *c*-direction and (b) along *b*-direction with the illustration of the unique zig-zag unbranched boron-oxygen chains. (c) The coordination environment of the Y atoms. (d) The illustration of the boron coordination environment in BO_4 tetrahedra connected via common vertices.

The structure motif of unbranched chains, solely built up by one BO_4 tetrahedron as a fundamental building block, is not unknown to borate chemistry but very scarce. In anhydrous borates, $[BO_3]_\infty$ chains solely built up by corner-linked $[BO_4]$ tetrahedra were observed only in $Ln_2GeB_2O_8$ (RE = Nd, Sm−Tb)[37], and $LnMBO_5$ (Ln = La, Pr; M = As, Ge) series[38]. However, infinite chains of corner-sharing $[BO_4]$ tetrahedra in structures of $Ln_2GeB_2O_8$ and $LnMBO_5$ are not isolated but further bridged by $[MO_4]$ (M = As, Ge) tetrahedra via corner-sharing to form 2D anionic layered frameworks, in which the $[BO_4]$ and $[MO_4]$ (M = As, Ge) tetrahedra are in an alternated arrangement (Fig. S1a-b). Among hydrogen-containing borates, there is one known mineral vimsite, $Ca[B_2O_2(OH)_4]$, which consists of highly protonated BO_4 chains[39]. In $Ca[B_2O_2(OH)_4]$, the chains form sheets, which are connected by H-bonds, and Ca^{2+} cations only reside between these layers(Fig. S1c). Whereas the chains in here-discovered *oC*20-YBO_3 are not linked and are surrounded by Y^{3+} cations (Fig. 1). Therefore, anionic unbranched $[BO_3]_\infty$ chains of corner-sharing $[BO_4]$ tetrahedra found in YBO_3 is a unique structure motif, that enrich state-of-art borate chemistry.

Interestingly, the isostructural to *oC*20-YBO_3 pyroxene-type $CaCO_3$-I structure was predicted to be the most stable polymorph for $CaCO_3$ above 137 GPa[40]. The Y and C atoms are located at the same sites as Ca and C in the structure of $CaCO_3$-I. The same phases were predicted for $MgCO_3$ and $SrCO_3$ compounds. The $CaCO_3$-I phase is denser than any other

polymorph[41], which is considered the primary factor contributing to its stabilization under high pressure[40]. We observed similar characteristics for YBO_3: according to DFT calculations, the *oC*20-YBO_3 polymorph is ~14% times denser at 90 GPa than the monoclinic *mC*60- and orthorhombic *oC*60-YBO_3 polymorphs [6–8].

The full relaxation of the structural model (with the fixed unit cell volume obtained from the experiment at ~ 120 GPa and 90 GPa) results in the unit cell parameters, atomic coordinates, and pressure value, that are in very good agreement with the experimental data (Table S1). The pressure dependence of the unit cell volume for *oC*20-YBO_3, obtained from the computations over a wide pressure range 1 bar – 150 GPa, can be described by a third-order Birch-Murnaghan equation of state with the following parameters: bulk modulus K_0 = 175.4(5) GPa, V_0 = 191.84(5) Å^3, and the pressure derivative of the bulk modulus K_0' = 4.07(1) (Fig. S2). The calculated bulk modulus of *oC*20-YBO_3 is the same within the error bar as that of known *mC*60-YBO_3 (K_0 = 163(13) GPa – experimentally obtained value by[8]) and *oC*60-YBO_3 (175.13 GPa – calculated value from[42]) modifications.

Harmonic phonon dispersion calculations using the Phonopy software[43] reveal that novel YBO_3 is dynamically stable at synthesis pressures (Fig. 2a), but unstable at ambient conditions, i.e. there are imaginary frequencies at 0 GPa (Fig. S3a). To explore the thermodynamic stability of *oC*20-YBO_3 the calculated enthalpy as a function of pressure was compared with the enthalpy of known modification of yttrium borate – *mC*60-YBO_3[7] (structure from 114335-ICSD was adapted) and *oC*60-YBO_3[6] (structure from 44162-ICSD was adapted). In agreement with our observations, the *oC*20-YBO_3 is thermodynamically favorable over *mC*60-YBO_3 and *oC*60-YBO_3 above ~23 and 19 GPa, respectively (Fig. S4).

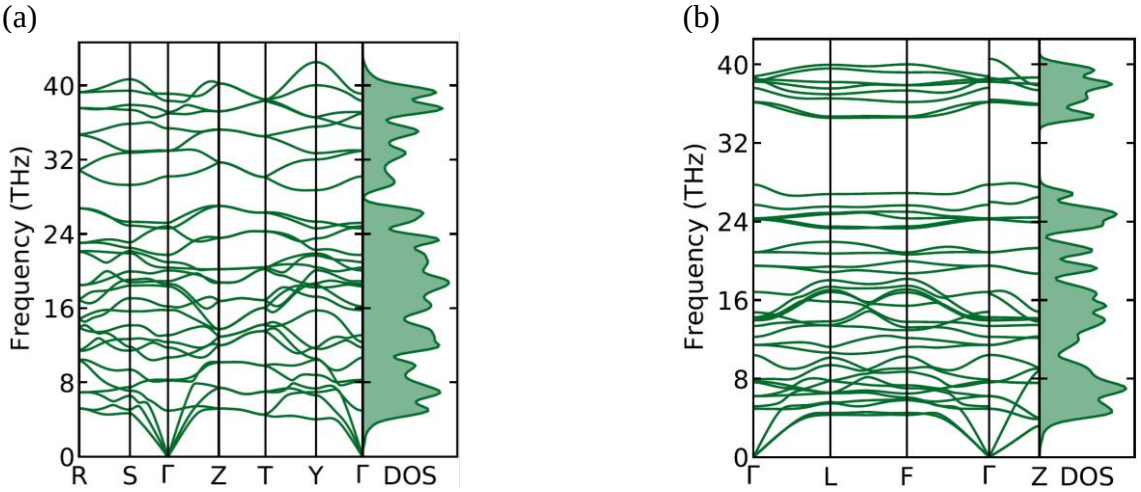

Fig. 2. Phonon dispersion curves along high-symmetry directions in the Brillouin zone and phonon density of states for (a) for *oC*20-YBO_3 calculated at 125.9 GPa (corresponding to the experimental volume of ~135.1(3) Å^3); (b) for *hR*39-$Y_3(CO_4)_2$ calculated at 112.5 GPa (corresponding to the experimental volume of ~ 283.7(2) Å^3).

To further explore the nature of chemical bonding in *oC*20-YBO_3, we analyzed the computed charge density in terms of the electron localization function[44] which revealed strong covalent bonding between boron and oxygen atoms, and ionic bonds between Y and O (Fig. 3a). Charge density map in the *ac* plane containing the infinite zig-zag boron-oxygen chains is shown in Figure 3b.

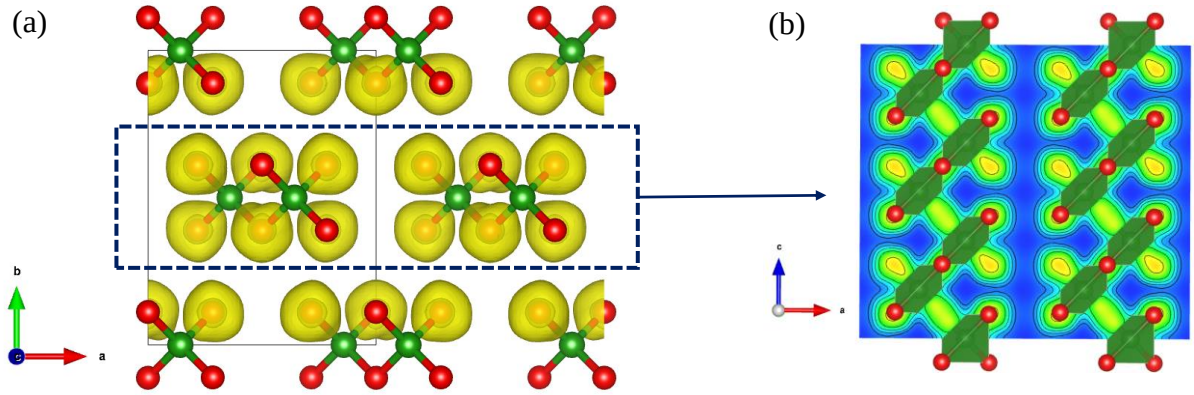

Fig. 3. Calculated (a) electron localization function with an isosurface value of 0.8 superimposed over the crystal structure of *oC*20-YBO_3 at 125.9 GPa (corresponding to the experimental volume of ~135.1(3) $Å^3$) and (b) its cross-sections in the plane (010).

The high-pressure yttrium orthocarbonate *hR*39-$Y_3(CO_4)_2$ was obtained in the same DAC with o*C*20-YBO_3 at ~ 120 GPa and 90 GPa after laser-heating to ~ 3500 K through a chemical reaction of partially oxidized yttrium with carbon from diamond anvils. It crystallizes with the palmierite structure type (space group $R\bar{3}m$, #166, $Z = 3$) with the unit cell parameters a = 4.4114(15) Å, and c = 16.832(5) Å (unit cell volume is 283.7(2) $Å^3$) at 120(2) GPa (Fig. 3). Details of the single-crystal structure refinement and crystallographic information is provided in Table S2. Yttrium atoms occupy two 3*a* (Y1) and 6*c* (Y2) Wyckoff positions, oxygen atoms are located at 6*c* and 18*h* sites, while carbon atoms are located at one 6*c* Wyckoff site, similarly to Ca, O, and P atoms, respectively, in the γ-form of the $Ca_3(PO_4)_2$ structure[45] (Fig. S5). Y1 is bonded in a 12-coordinate geometry to twelve O^{2-} atoms (Fig.4), with the Y-O distances ranging between 2.178(12) and 2.5478(11) Å. In the second yttrium site, Y2 is surrounded by ten oxygen atoms (Fig. 4b) with a spread of Y-O bond distances ranging from 2.06(3) - 2.237(10) Å. The key structural feature of orthocarbonates and their main difference from carbonates is the CO_4 tetrahedron anion, which contains carbon in the sp^3-hybridized state. The C–O bond lengths within the tetrahedron in *hR*39-$Y_3(CO_4)_2$ vary from 1.322(15) to 1.41(4) Å at 120 GPa, which is in good agreement with known orthocarbonates[23,28,46,47]. Bond angles vary in the range 108.1(1) – 110.8(2)° at 120 GPa (Fig. 4e), thus, the deviation from the angles of the ideal tetrahedron does not exceed 2°. In this structure, an anionic subsystem can be considered as layers of isolated CO_4 tetrahedral units (Fig. 4c-d). The $Y1O_{12}$ and $Y2O_{10}$

polyhedra share common faces and form a sandwich-like stacking of $Y2O_{10}$ - $Y1O_{12}$ - $Y2O_{10}$, which ends with a corner coordinated CO_4 polyhedron (Fig. 4b), spaced by empty octahedral sites – "voids". The voids are located at a high symmetry point – 3*a* Wyckoff site (Fig. 4d).

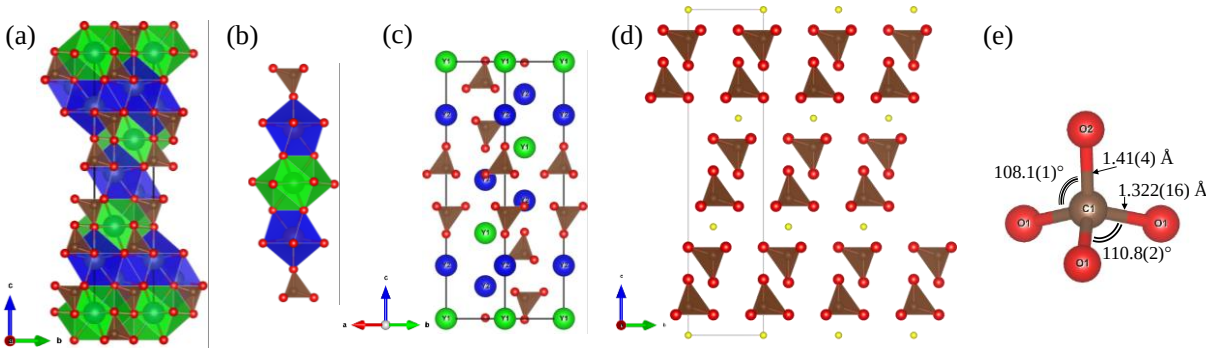

Fig. 4. Crystal structure of *hR*39-$Y_3(CO_4)_2$. (a) A unit cell of the structure with the Y1, Y2, C, and O atoms shown as green, blue, brown, and red balls, respectively, along a-direction. (b) The illustration of the linkage scheme of polyhedral cations and surrounded oxygen atoms. A unit cell along a-direction, showing the CO_4 polyhedron – (c) all atoms are shown and (d) yttrium atoms are not shown; voids are shown as yellow balls. The coordination environment of the C atoms in isolated CO_4 tetrahedra.

For the palmierite structure (which is a cation-deficient derivative of the 9*R*-hexagonal perovskite polytype $A_3B_2O_9$) the proton and oxide ion conductivity is known, due to high proton mobility in ordered voids[48]. Assuming all yttrium to be Y^{3+} the charge distribution for the *hR*39-$Y_3(CO_4)_2$ can be represented as $Y^{3+}{}_3[CO_4]_2^{4-}\cdot 1e$, where one extra valence electron per formula unit is needed to achieve electroneutrality (*Z*=3, therefore, in total it is 3 electrones per unit cell). There are three voids per unit cell, which suggests that each additional electron might be localized in each of these voids (Fig. 4d). Therefore, instead of assuming proton mobility, one might consider electron mobility. However, this hypothesis is beyond the scope of this work and needs to be validated by theorists.

In order to gain a deeper insight into the stability and pressure-volume behavior $Y_3(CO_4)_2$, we performed theoretical calculations based on the density functional theory. The full relaxation of the structural model of *hR*39-$Y_3(CO_4)_2$ at an experimental pressure of 120 GPa results in the unit cell parameters and atomic coordinates that agree well with the experimental data (Table S2). Harmonic phonon dispersion calculations along the high-symmetry directions of the Brillouin zone show that *hR*39-$Y_3(CO_4)_2$ is dynamically stable at the experimental volume of ~ 283.7(2) $Å^3$ (corresponds to theoretical pressure of ~113 GPa) (Fig. 2b), but unstable at ambient conditions (Fig. S3b). The pressure dependence of the theoretical values of the unit cell volume of $Y_3(CO_4)_2$ can be described by the third-order Birch-Murnaghan equation of state with the parameters V_0 = 389.05(6) $Å^3$, K_0 = 184.6(3) GPa and K' = 4.14(1) (Fig. S6).

To summarize, a novel polymorph of yttrium borate o*C*20-YBO_3 and first orthocarbonate *hR*39-$Y_3(CO_4)_2$ were obtained at pressures of ~ 90 and 120 GPa and temperatures of ~3500K in the LHDAC. Their structures were solved and refined in situ using HP synchrotron SCXRD. In o*C*20-YBO_3, BO_4 tetrahedra are connected via common vertices, forming the unique isolated quasi 1D anionic network – infinite zig-zag unbranched boron-oxygen chains. Our results extend the list of possible B-O networks in borates. The *hR*39-$Y_3(CO_4)_2$ is the first rare-earth orthocarbonate. Moreover, considering the electroneutrality of $Y_3(CO_4)_2$ and assuming all yttrium to be Y^{3+}, the charge distribution for the $Y_3(CO_4)_2$ can be represented as $Y_3^{3+}[CO_4]_2^{4-}\cdot 1e$. Density functional theory-based calculations demonstrate dynamic and thermodynamic stability of obtained compounds at synthesis pressures.

References

[1] M. Mutailipu, K. R. Poeppelmeier, S. Pan, *Chem Rev* **2021**, *121*, 1130–1202.

[2] C. Chen, T. Sasaki, R. Li, Y. Wu, Z. Lin, Y. Mori, Z. Hu, J. Wang, S. Uda, M. Yoshimura, Y. Kaneda, *Nonlinear Optical Borate Crystals*, Wiley, **2012**.

[3] B. N. Orcutt, I. Daniel, R. Dasgupta, Eds. , *Deep Carbon*, Cambridge University Press, **2019**.

[4] I. P. Kostova, T. A. Eftimov, K. Hristova, S. Nachkova, S. Tsoneva, A. Peltekov, *Crystals (Basel)* **2024**, *14*, 575.

[5] E. A. Tkachenko, R. Mahiou, G. Chadeyron, D. Boyer, P. P. Fedorov, S. V. Kuznetsov, *Russian Journal of Inorganic Chemistry* **2007**, *52*, 829–834.

[6] K. C. Mishra, B. G. Deboer, P. C. Schmidt, I. Osterloh, M. Stephan, V. Eyert, K. H. Johnson, *Berichte der Bunsengesellschaft für physikalische Chemie* **1998**, *102*, 1772–1782.

[7] J. Lin, D. Sheptyakov, Y. Wang, P. Allenspach, *Chemistry of Materials* **2004**, *16*, 2418–2424.

[8] R. Turnbull, D. Errandonea, J. Á. Sans, V. P. Cuenca-Gotor, R. I. Vilaplana, J. Ibáñez, C. Popescu, A. Szczeszak, S. Lis, F. J. Manjón, *J Alloys Compd* **2021**, *866*, 158962.

[9] J. H. Lin, S. Zhou, L. Q. Yang, G. Q. Yao, M. Z. Su, L. P. You, *J Solid State Chem* **1997**, *134*, 158–163.

[10] M. K. Schmitt, H. Huppertz, *Zeitschrift für Naturforschung B* **2017**, *72*, 983–988.

[11] M. K. Schmitt, H. Huppertz, *Zeitschrift für Naturforschung B* **2017**, *72*, 977–982.

[12] Fuchs, Schröder, Heymann, Jüstel, Huppertz, *Inorganics (Basel)* **2019**, *7*, 136.

[13] B. Fuchs, M. K. Schmitt, K. Wurst, H. Huppertz, *Eur J Inorg Chem* **2019**, *2019*, 271–276.

[14] R. Miyawaki, J. Kuriyama, I. Nakai, *American Mineralogist* **1993**, *78*, 425–432.

[15] L. Spiridigliozzi, M. Bortolotti, G. Accardo, A. Vergara, D. Frattini, C. Ferone, R. Cioffi, G. Dell'Agli, *Journal of Rare Earths* **2022**, *40*, 1281–1290.

[16] Y. Zhang, M. Gao, K. Han, Z. Fang, X. Yin, Z. Xu, *J Alloys Compd* **2009**, *474*, 598–604.

[17] W. Yao, P. Liu, G. Li, N. Sun, W. Yang, C. Jiang, W. Du, C. Zhang, W. Song, N. J. Cook, J. Mao, *American Mineralogist* **2024**, *109*, 599–605.
[18] N. Imanaka, T. Masui, Y. Mayama, K. Koyabu, *J Solid State Chem* **2005**, *178*, 3601–3603.
[19] G. W. Beall, W. O. Milligan, S. Mroczkowski, *Acta Crystallogr B* **1976**, *32*, 3143–3144.
[20] D. Spahr, J. König, L. Bayarjargal, V. Milman, A. Perlov, H.-P. Liermann, B. Winkler, *J Am Chem Soc* **2022**, *144*, 2899–2904.
[21] D. Spahr, J. König, L. Bayarjargal, R. Luchitskaia, V. Milman, A. Perlov, H.-P. Liermann, B. Winkler, *Inorg Chem* **2022**, *61*, 9855–9859.
[22] V. Cerantola, E. Bykova, I. Kupenko, M. Merlini, L. Ismailova, C. McCammon, M. Bykov, A. I. Chumakov, S. Petitgirard, I. Kantor, V. Svitlyk, J. Jacobs, M. Hanfland, M. Mezouar, C. Prescher, R. Rüffer, V. B. Prakapenka, L. Dubrovinsky, *Nat Commun* **2017**, *8*, 15960.
[23] D. Laniel, J. Binck, B. Winkler, S. Vogel, T. Fedotenko, S. Chariton, V. Prakapenka, V. Milman, W. Schnick, L. Dubrovinsky, N. Dubrovinskaia, *Acta Crystallogr B Struct Sci Cryst Eng Mater* **2021**, *77*, 131–137.
[24] J. Binck, D. Laniel, L. Bayarjargal, S. Khandarkhaeva, T. Fedotenko, A. Aslandukov, K. Glazyrin, V. Milman, S. Chariton, V. B. Prakapenka, N. Dubrovinskaia, L. Dubrovinsky, B. Winkler, *American Mineralogist* **2022**, *107*, 336–342.
[25] J. Binck, L. Bayarjargal, S. S. Lobanov, W. Morgenroth, R. Luchitskaia, C. J. Pickard, V. Milman, K. Refson, D. B. Jochym, P. Byrne, B. Winkler, *Phys Rev Mater* **2020**, *4*, 055001.
[26] S. Chariton, M. Bykov, E. Bykova, E. Koemets, T. Fedotenko, B. Winkler, M. Hanfland, V. B. Prakapenka, E. Greenberg, C. McCammon, L. Dubrovinsky, *Acta Crystallogr E Crystallogr Commun* **2020**, *76*, 715–719.
[27] M. Merlini, V. Cerantola, G. D. Gatta, M. Gemmi, M. Hanfland, I. Kupenko, P. Lotti, H. Müller, L. Zhang, *American Mineralogist* **2017**, *102*, 1763–1766.
[28] M. Merlini, M. Hanfland, A. Salamat, S. Petitgirard, H. Müller, *American Mineralogist* **2015**, *100*, 2001–2004.
[29] S. S. Lobanov, X. Dong, N. S. Martirosyan, A. I. Samtsevich, V. Stevanovic, P. N. Gavryushkin, K. D. Litasov, E. Greenberg, V. B. Prakapenka, A. R. Oganov, A. F. Goncharov, *Phys Rev B* **2017**, *96*, 104101.
[30] A. Aslandukova, A. Aslandukov, D. Laniel, Y. Yin, F. I. Akbar, M. Bykov, T. Fedotenko, K. Glazyrin, A. Pakhomova, G. Garbarino, E. L. Bright, J. Wright, M. Hanfland, S. Chariton, V. Prakapenka, N. Dubrovinskaia, L. Dubrovinsky, *Sci Adv* **2024**, *10*, DOI 10.1126/sciadv.adl5416.
[31] Y. Yin, F. I. Akbar, E. Bykova, A. Aslandukova, D. Laniel, A. Aslandukov, M. Bykov, M. Hanfland, G. Garbarino, Z. Jia, L. Dubrovinsky, N. Dubrovinskaia, *Commun Chem* **2022**, *5*, 122.
[32] F. I. Akbar, A. Aslandukova, A. Aslandukov, Y. Yin, F. Trybel, S. Khandarkhaeva, T. Fedotenko, D. Laniel, M. Bykov, E. Bykova, N. Dubrovinskaia, L. Dubrovinsky, *Front Chem* **2023**, *11*, DOI 10.3389/fchem.2023.1210081.
[33] F. I. Akbar, A. Aslandukova, Y. Yin, A. Aslandukov, D. Laniel, E. Bykova, M. Bykov, E. L. Bright, J. Wright, D. Comboni, M. Hanfland, N. Dubrovinskaia, L. Dubrovinsky, *Carbon N Y* **2024**, *228*, 119374.
[34] A. Aslandukov, P. L. Jurzick, M. Bykov, A. Aslandukova, A. Chanyshev, D. Laniel, Y. Yin, F. I. Akbar, S. Khandarkhaeva, T. Fedotenko, K. Glazyrin, S. Chariton, V. Prakapenka, F. Wilhelm, A. Rogalev, D. Comboni, M. Hanfland, N. Dubrovinskaia, L. Dubrovinsky, *Angewandte Chemie International Edition* **2023**, *62*, DOI 10.1002/anie.202311516.

[35] D. Laniel, F. Trybel, B. Winkler, F. Knoop, T. Fedotenko, S. Khandarkhaeva, A. Aslandukova, T. Meier, S. Chariton, K. Glazyrin, V. Milman, V. Prakapenka, I. A. Abrikosov, L. Dubrovinsky, N. Dubrovinskaia, *Nat Commun* **2022**, *13*, 6987.
[36] L. C. Pasqualini, H. Huppertz, *Zeitschrift für Naturforschung B* **2023**, *78*, 285–291.
[37] J.-H. Zhang, P.-X. Li, J.-G. Mao, *Dalton Transactions* **2010**, *39*, 5301.
[38] E. L. Belokoneva, W. I. F. David, J. B. Forsyth, K. S. Knight, *Journal of Physics: Condensed Matter* **1998**, *10*, 9975–9989.
[39] M. A. Simonov, Yu. K. Egorov Tismenko, N. V. Belov, *Kristallografiya* **1976**, *21*, 592–594.
[40] A. R. Oganov, C. W. Glass, S. Ono, *Earth Planet Sci Lett* **2006**, *241*, 95–103.
[41] S. Ono, T. Kikegawa, Y. Ohishi, *American Mineralogist* **2007**, *92*, 1246–1249.
[42] mp-29205: YBO_3. data from https://legacy.materialsproject.org/materials/mp-29205/.
[43] A. Togo, I. Tanaka, *Scr Mater* **2015**, *108*, 1–5.
[44] A. Savin, A. D. Becke, J. Flad, R. Nesper, H. Preuss, H. G. von Schnering, *Angewandte Chemie International Edition in English* **1991**, *30*, 409–412.
[45] R. M. Thompson, X. Xie, S. Zhai, R. T. Downs, H. Yang, *American Mineralogist* **2013**, *98*, 1585–1592.
[46] D. N. Sagatova, N. E. Sagatov, P. N. Gavryushkin, M. V. Banaev, K. D. Litasov, *Cryst Growth Des* **2021**, *21*, 6744–6751.
[47] D. Sagatova, A. Shatskiy, N. Sagatov, P. N. Gavryushkin, K. D. Litasov, *Lithos* **2020**, *370–371*, 105637.
[48] S. Fop, J. A. Dawson, D. N. Tawse, M. G. Skellern, J. M. S. Skakle, A. C. Mclaughlin, *Chemistry of Materials* **2022**, *34*, 8190–8197.

High-pressure yttrium borate o*C*20-YBO_3 and orthocarbonate *hR*39-$Y_3(CO_4)_2$ synthesized at megabar pressures

Supporting Information

EXPERIMENTAL METHODS

Sample preparation

The BX90-type large X-ray aperture diamond anvil cell (DAC) equipped with Boehler-Almax type diamonds (culet diameter is 120 μm) was used for single-crystal XRD studies [1,2]. Rhenium foil pre-indented to a thickness of ~20 μm and a hole of ~60 μm in diameter drilled in the center of the indentation served as a sample chamber. A piece of yttrium was placed in the sample chamber filled with NH_3BH_3. Pressure was determined using the equation of states of Re [3,4], and additionally monitored by the Raman signal from the diamond anvils [5]. A sample were compressed up to 90 GPa and laser heated (LH) to ~ 3000(200)K, for the second experemental point the pressure was increased to 120 GPa and samples was re-heated to 3000(200)K. LH of the samples was performed using an *in house* laser heating setup[6], equipped with two YAG lasers (1064 nm central wavelength).

X-ray diffraction measurements and data analysis procedure

XRD measurements were performed at the ID27 beamline (ESRF, Grenoble, France) with an X-ray beam (λ = 0.3738 Å) focused to a size of 1.5 × 1.5 μm^2, and the XRD patterns were collected on an Eiger2X CdTe 9M hybrid photon-counting pixel detector. For SCXRD measurements, samples were rotated around a vertical ω axis in a range of ±36°. The XRD images were collected with an angular step $\Delta\omega = 0.5°$. The CrysAlis^{Pro} software package [7] was used for the analysis of the single-crystal XRD data (indexing, data integration, frame scaling, and absorption correction). A single crystal of $(Mg_{1.93},Fe_{0.06})(Si_{1.93},Al_{0.06})O_6$ orthoenstatite (*Pbca*, *a* = 18.2391(3), *b* = 8.8117(2), *c* = 5.18320(10) Å), was used to calibrate instrument model of the CrysAlis^{Pro} software. The DAFi program[8] was used for the search of reflection's groups belonging to the individual single-crystal domains. Using the OLEX2 software package[9] the structures were solved with the ShelXT structure solution program[10] using intrinsic phasing and refined with the ShelXL[11] refinement package using least-squares minimization. Crystal structure visualizations were made with the VESTA software[12]. The

EoS of the synthesized materials were obtained by fitting the calculated pressure-volume data using the EoSFit7-GUI [13].

COMPUTATIONAL DETAILS

The first-principles calculations were done using the framework of density functional theory (DFT) as implemented in the Vienna Ab initio Simulation Package (VASP) [14]. To expand the electronic wave function in plane waves we used the Projector-Augmented-Wave (PAW) method [15,16]. The Generalized Gradient Approximation (GGA) functional was used for calculating the exchange-correlation energies, as proposed by Perdew–Burke–Ernzerhof (PBE) [17]. The PAW potentials with following valence electrons of 4*s*4*p*5*s*4*d* for Y, 2*s*2*p* for C, O, and B were used. The Monkhorst-Pack [18] k-point grid and an energy cutoff for the plane wave expansion were selected based on convergence tests with a threshold of 2 meV per atom for energy. The phonon frequencies and phonon band structure calculations were performed in the harmonic approximation with non-analytical term correction with the help of PHONOPY software55 using the finite displacement method for 2x2x3 (for YBO_3) and 2x2x2 (for $Y_3(CO_4)_2$) supercells (made for the primitive cell (PPOSCAR)) with respectively adjusted *k*-points. Equation of state (EoS) and static enthalpy calculations were performed via variable-cell structural relaxations between 1 bar and 160 GPa. In our calculations, temperature, configurational entropy, and the entropy contribution due to lattice vibrations were neglected.

Tables

Table S1: Experimentally determined crystallographic data for a novel yttrium boride *oC*20-YBO_3 at 120(5) and 90(5) GPa in comparison to the corresponding DFT-relaxed structure. The full crystallographic dataset was deposited to the CCDC under deposition number 2279789.

			experiment	theory
$P_{experiment}$ = 120(5) GPa				
Space group, *Z*			$C222_1$, 4	$C222_1$, 4
a (Å)			5.594(13)	5.60978
b (Å)			7.225(3)	7.2405
c (Å)			3.3428(13)	3.32626
V (Å^3)			135.1(3)	135.1
Pressure *P* (GPa)			120(5)	125.9
N_m / N_i ($I \geq 3\sigma$)*			160 / 109 (79)	-
R_{int}; $I/\sigma(I)$			0.0475; 12.7	-
Final *R* indexes (all)			R_1 = 0.082; wR_2 = 0.105	-
Final *R* indexes ($I \geq 3\sigma$)			R_1 = 0.051; wR_2 = 0.095	-
$\Delta\rho_{min}$, $\Delta\rho_{max}$, eÅ^{-3}			-1.3, 1.8	-
N_P*; N_i / N_P			14; 7.79	-
Wyckoff site and fractional atomic coordinates (*x*; *y*; *z*):	Y1	4*b*	0; 0.6833(3); 0.25	0; 0.68285; 0.25
	B1	4*a*	0.150(18); 0; 0	0.14175; 0;0
	O1	4*b*	0; 0.1133(16); 0.25	0; 0.1118; 0.25
	O2	8*c*	0.215(4); 0.3895(11); 0.270(13)	0.21612; 0.38948;0.26204
$P_{experiment}$ = 90(5) GPa				
Space group, *Z*			$C222_1$, 4	$C222_1$, 4
a (Å)			5.659(13)	5.79741
b (Å)			7.528(4)	7.51703
c (Å)			3.4490(13)	3.37157
V (Å^3)			146.9(3)	146.9
Pressure *P* (GPa)			90(5)	81
N_m / N_i ($I \geq 3\sigma$)*			141/95 (68)	-
R_{int}; $I/\sigma(I)$			0.033; 20.4	-
Final *R* indexes (all)			R_1 = 0.110; wR_2 = 0.202	-
Final *R* indexes ($I \geq 3\sigma$)			R_1 = 0.086; wR_2 = 0.186	-
$\Delta\rho_{min}$, $\Delta\rho_{max}$, eÅ^{-3}			-1.7; 1.9	-
N_P*; N_i / N_P			14; 6.79	-
Wyckoff site and fractional atomic coordinates (*x*; *y*; *z*):	Y1	4*b*	0; 0.6838(5); 0.25	0; 0.68658; 0.25
	B1	4*a*	0.135(18); 0; 0	0.14362; 0; 0
	O1	4*b*	0; 0.116(4); 0.25	0; 0.10782; 0.25
	O2	8*c*	0.202(9); 0.392(3); 0.217(14)	0.21653; 0.3889; 0.26834

* N_m - number of measured reflections and N_i - number of independent reflections; N_P - number of refined parameters;

Table S2: Experimentally determined crystallographic data for a novel yttrium orthocarbonate *hR*39-$Y_3(CO_4)_2$ at 120(5) and 90(5) GPa in comparison to the corresponding DFT-relaxed structure. The full crystallographic dataset was deposited to the CCDC under deposition number 2279788.

			experiment	theory
$P_{experiment}$ = 120(5) GPa				
Space group, Z			$R\bar{3}m$, 3	$R\bar{3}m$, 3
a (Å)			4.4114(15)	4.3883
c (Å)			16.832(5)	17.0095
V (Å^3)			283.67(16)	283.67
Pressure P (GPa)			120(5)	112.6
N_m / N_i ($I \geq 3\sigma$)			250/136 (91)	-
R_{int}; $I/\sigma(I)$			0.069; 10.2	-
Final R indexes (all)			R_1 = 0.087; wR_2 = 0.114	-
Final R indexes ($I \geq 3\sigma$)			R_1 = 0.059; wR_2 = 0.107	-
$\Delta\rho_{min}$, $\Delta\rho_{max}$, eÅ^{-3}			-1.5; 1.9	-
N_P*; N_i / N_P			17; 8.0	-
Wyckoff site and fractional atomic coordinates (x; y; z):	Y1	3*a*	0; 0; 0	0; 0; 0
	Y2	6*c*	0; 0; 0.20707(12)	0; 0; 0.20873
	C1	6*c*	0; 0; 0.4143(17)	0; 0; 0.40815
	O1	6*c*	0; 0; 0.329676(19)	0; 0; 0.32979
	O2	18*h*	0.4971(2); 0.5025(3); 0.2289(11)	0.49676; 0.50324; 0.2313
$P_{experiment}$ = 90(5) GPa				
Space group, Z			$R\bar{3}m$, 3	$R\bar{3}m$, 3
a (Å)			4.534(8)	4.5025
c (Å)			17.114(12)	17.3545
V (Å^3)			304.7(11)	304.7
Pressure P (GPa)			90(5)	78.1
N_m / N_i ($I \geq 3\sigma$)			175/105 (85)	-
R_{int}; $I/\sigma(I)$			0.0241; 41.1	-
Final R indexes (all)			R_1 = 0.077; wR_2 = 0.103	-
Final R indexes ($I \geq 3\sigma$)			R_1 = 0.064; wR_2 = 0.099	-
$\Delta\rho_{min}$, $\Delta\rho_{max}$, eÅ^{-3}			-1.2; 1.8	-
N_P*; N_i / N_P			17; 6.18	-
Wyckoff site and fractional atomic coordinates (x; y; z):	Y1	3*a*	0; 0; 0	0; 0; 0
	Y2	6*c*	0; 0; 0.2072(1)	0; 0; 0.20897
	C1	6*c*	0; 0; 0.4128(14)	0; 0; 0.40796
	O1	6*c*	0; 0; 0.3286(4)	0; 0; 0.33031
	O2	18*h*	0.499(4); 0.499(4); 0.2296(15)	0.49543; 0.50457; 0.23189

Figures

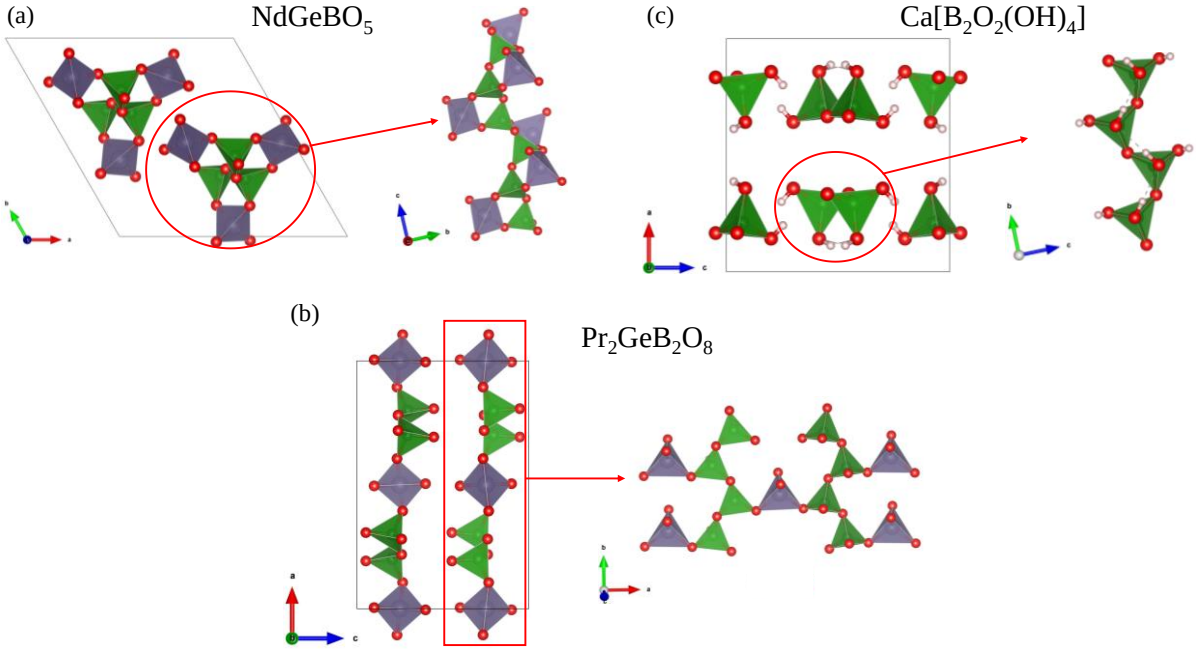

Fig. S1. A unit cell of the crystal structure of (a) $NdGeBO_5$ along *b* direction (structure from 168970-ICSD), (b) $Pr_2GeB_2O_8$ along *c* direction (structure from 86742-ICSD), and (c) $Ca[B_2O_2(OH)_4]$ along *b* direction (structure from 44162-ICSD). The left part of each figure shows the illustration of the infinite anionic chains. The Ge, B, O, and H atoms are shown as gray, green, red, and white balls, respectively. Pr, Nd, and Ca atoms are not shown.

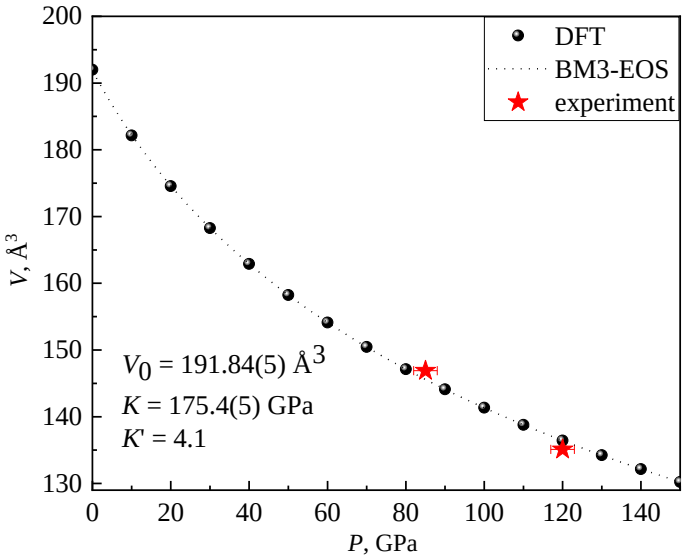

Fig. S2. The pressure dependence of the o*C*20-YBO_3 unit cell volume. Red solid stars represent experimental data, while black solid circles – values from DFT calculations. The black dashed line shows the fit of the calculated *P*-*V* data using the third-order Birch-Murnaghan equation of state (V_0 = 191.84(5) Å^3, K_0 = 175.4(5) GPa and K' = 4.1(1)).

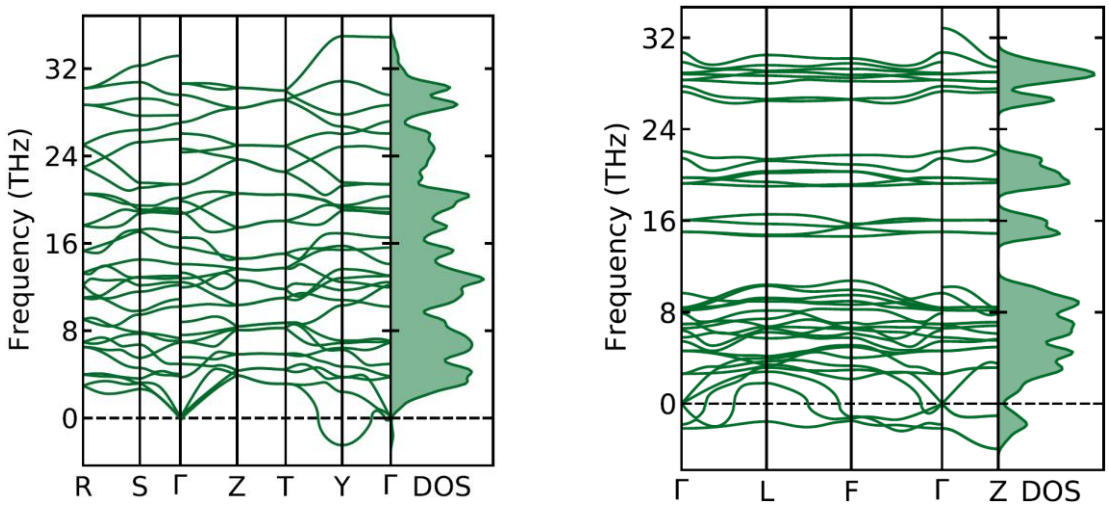

Fig. S3. Phonon dispersion curves along high-symmetry directions in the Brillouin zone and phonon density of states for *oC*20-YBO_3 (a) and $R\bar{3}m$ – $Y_3(CO_4)_2$ (b), calculated at 1 bar.

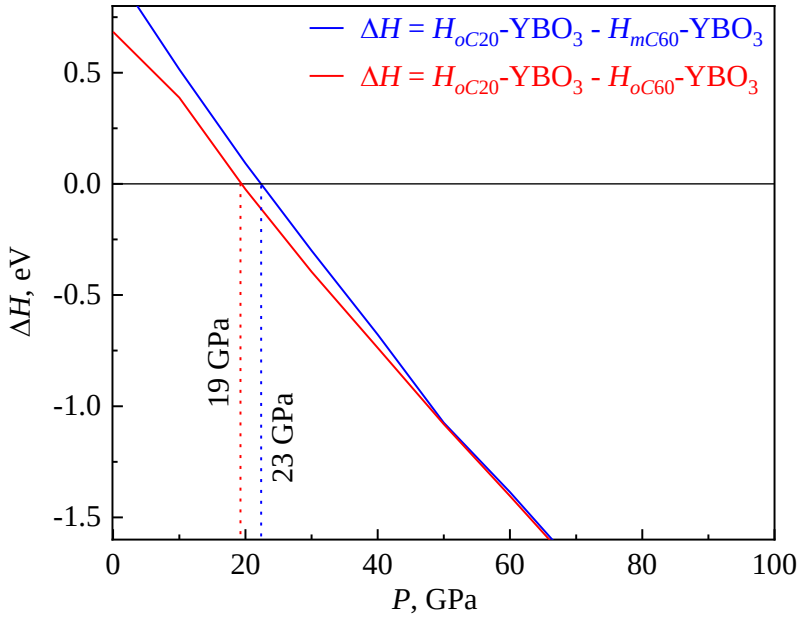

Fig. S4. Results of DFT calculated enthalpy difference between novel *oC*20-YBO_3 and known monoclinic *mC*60- and hexagonal *oC*60-YBO_3 polymorphs: $\Delta H = H_{oC16\text{-}YBr3} - H_{hR24\text{-}YBr3}$.

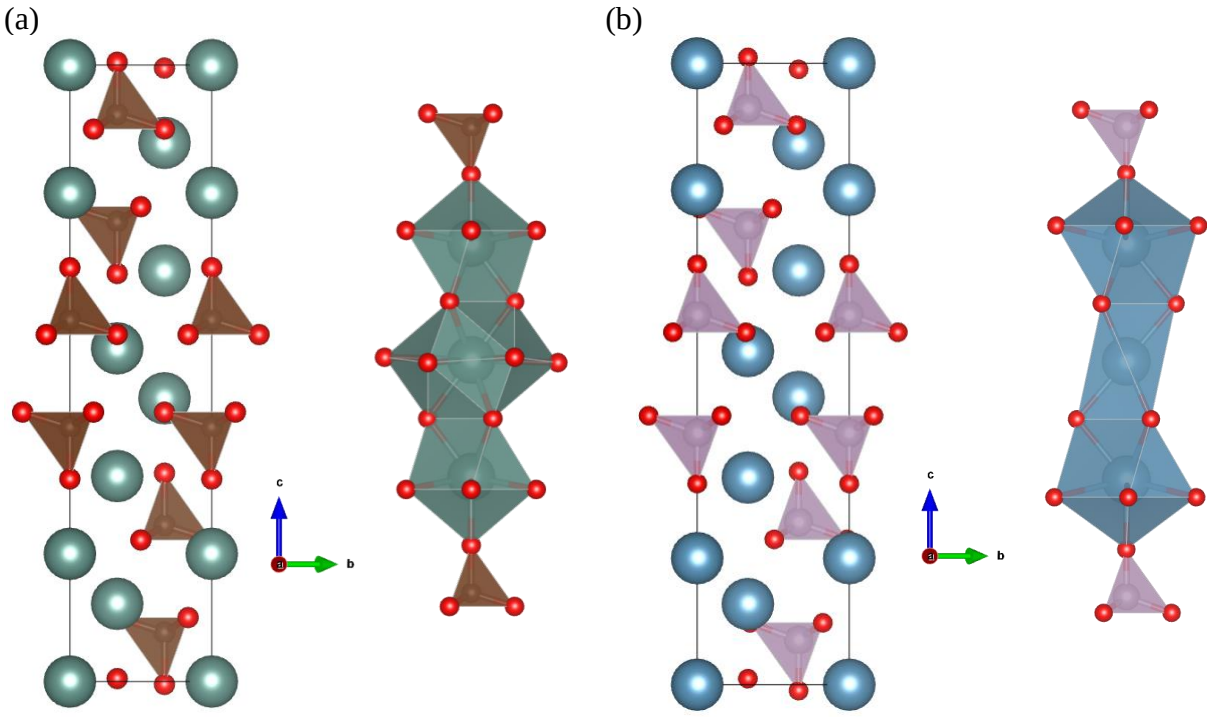

Fig. S5. Crystal structure of $Y_3(CO_4)_2$ and $Ca_3(PO_4)_2$. (a) A unit cell of the structure of $Y_3(CO_4)_2$ with the Y, C, and O atoms shown as green, brown, and red balls, respectively, along *a*-direction. (b) A unit cell of the structure of $Ca_3(PO_4)_2$ with the Ca, P, and O atoms shown as blue, violet, and red balls, respectively, along *a*-direction. The right part of both figures shows an illustration of the forming "pinwheels"-fragment made of (a) Y and CO_4 polyhedra, and (b) Ca and PO_4 polyhedra.

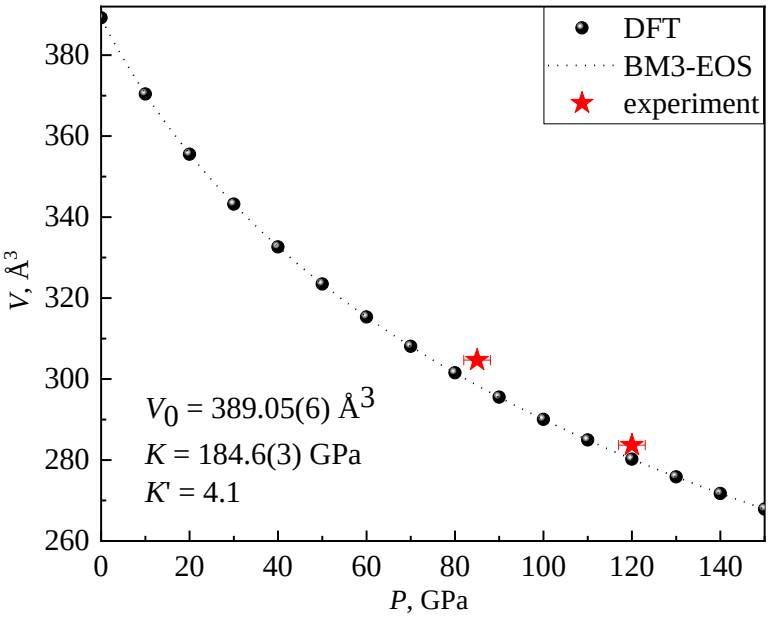

Fig. S6. The pressure dependence of the $Y_3(CO_4)_2$ unit cell volume. Red solid stars represent experimental data, while black solid circles – values from DFT calculations. The black dashed line shows the fit of the calculated *P*-*V* data using the third-order Birch-Murnaghan equation of state (V_0 = 389.05(6) Å^3, K_0 = 184.6(3) GPa and K' = 4.1(1)).

REFERENCES

[1] I. Kantor, V. Prakapenka, A. Kantor, P. Dera, A. Kurnosov, S. Sinogeikin, N. Dubrovinskaia, L. Dubrovinsky, Review of Scientific Instruments 2012, 83, 125102.

[2] Rigaku Oxford Diffraction, CrysAlisPro Software system (2015). DOI 10.1063/1.2372734.

[3] C. S. Zha, W. A. Bassett, S. H. Shim, Review of Scientific Instruments 2004, 75, 2409–2418.

[4] S. Anzellini, A. Dewaele, F. Occelli, P. Loubeyre, M. Mezouar, J Appl Phys 2014, 115, 043511.

[5] Y. Akahama, H. Kawamura, J Appl Phys 2006, 100, 043516.

[6] T. Fedotenko, L. Dubrovinsky, G. Aprilis, E. Koemets, A. Snigirev, I. Snigireva, A. Barannikov, P. Ershov, F. Cova, M. Hanfland, N. Dubrovinskaia, Review of Scientific Instruments 2019, 90, 104501.

[7] CrysAlisPro Data Collection and Processing Software for Agilent X-ray Diffractometers 2014, 1–53.

[8] A. Aslandukov, M. Aslandukov, N. Dubrovinskaia, L. Dubrovinsky., J. Appl. Crystallogr. 2022, 55, 1.

[9] O. V. Dolomanov, L. J. Bourhis, R. J. Gildea, J. A. K. Howard, H. Puschmann, Journal of Applied Crystallography 2009, 42, 339–341.

[10] V. Petrícek, M. Dušek, L. Palatinus, Zeitschrift fur Kristallographie 2014, 229, 345–352.

[11] G. M. Sheldrick, Acta Crystallographica Section C Structural Chemistry 2015, 71, 3–8.

[12] K. Momma, F. Izumi, Journal of Applied Crystallography 2011, 44, 1272–1276.

[13] J. Gonzalez-Platas, M. Alvaro, F. Nestola, R. Angel, Journal of Applied Crystallography 2016, 49, 1377–1382.

[14] G. Kresse, J. Furthmüller, Comput Mater Sci 1996, 6, 15–50.

[15] P. E. Blöchl, Phys Rev B 1994, 50, 17953–17979.

[16] G. Kresse, D. Joubert, Phys Rev B 1999, 59, 1758–1775.

[17] J. P. Perdew, K. Burke, M. Ernzerhof, Phys Rev Lett 1996, 77, 3865–3868.

[18] Hendrik J. Monkhorst and James D. Pack, Phys Rev B 1976, 13, 5188–5192.

[19] A. Togo, I. Tanaka, Scr Mater 2015, 108, 1–5.

List of publications.

As the first author (chronological order):

1) **Aslandukova, A.**, Aslandukov A., Yin Y., Bykov M., A. Pakhomova A., Dubrovinskaia N., Dubrovinsky L. High-pressure yttrium borate o*C*20-YBO_3 and orthocarbonate *hR*39-$Y_3(CO_4)_2$ synthesized at megabar pressures. ***Inorg. Chem.*** **10**, 5098-5104 (2025).
DOI: 10.1021/acs.inorgchem.4c05308

2) **Aslandukova, A.**, Aslandukov A., Akbar F. I., Yin Y., Trybel F., Pakhomova A., Chariton S., Prakapenka V., Dubrovinskaia N., Dubrovinsky L. High-pressure *oC*16-YBr_3 polymorph recoverable to ambient conditions: from 3D framework to layered material, ***Inorg. Chem.*** (2024).
DOI: 10.1021/acs.inorgchem.4c00813

3) **Aslandukova, A.**, Aslandukov A., Laniel D., Yin Y., Akbar F. I., Bykov M., Fedotenko T., Glazyrin K., Pakhomova A., Garbarino G., Bright E. L., Wright J., Hanfland M., Chariton S., Prakapenka V., Dubrovinskaia N., Dubrovinsky L. Diverse high-pressure chemistry in Y–NH_3BH_3 and Y–paraffin oil systems, ***Science Advances*** **10**, 1-8 (2024). DOI: 10.1126/sciadv.adl5416.

4) **Aslandukova, A.**, Aslandukov, A., Laniel, D., Khandarkhaeva, S., Steinle-Neumann, G., Fedotenko, T., Ovsyannikov, S. V., Yin, Y., Akbar, F. I., Glazyrin, K., Hanfland, M Dubrovinskaia, N., Dubrovinsky, L. High-pressure *hP*3 yttrium allotrope with $CaHg_2$-type structure as a prototype of the *hP*3 rare-earth hydride series, ***Phys. Rev. B*** **107**, 014103(8) (2023).
DOI: 10.1103/PhysRevB.107.014103.

5) **Aslandukova, A.**, Aslandukov, A., Yuan, L., Laniel, D., Khandarkhaeva, S., Fedotenko, T., Steinle-Neumann, G., Glazyrin, K., Dubrovinskaia, N., & Dubrovinsky, L. Novel High-Pressure Yttrium Carbide γ-Y_4C_5 Containing [C_2] and Nonlinear [C_3] Units with Unusually Large Formal Charges, ***Phys Rev Lett*** **127**, 135501(6) (2021).
DOI: 10.1103/PhysRevLett.127.135501

6) **Aslandukova, A.**, Sobolev, A.V., Silkin, I.G., Morozov, I.V., Glazkova, I.S., & Presniakov, I.A. (2020). *Probe ^{57}Fe Mössbauer diagnostic of magnetic phase transition in phosphide MnP*, ***JETP*** 130, 864–872
DOI: 10.1134/S1063776120050027

Others (chronological order):

7) Aslandukov, A., Liang, A., Ehn, A., Trybel, F., Yin, Y., **Aslandukova, A.**, Akbar, F. I., Ranieri, U., Spender, J., Howie, R. T., Bright, E. L., Wright, J., Hanfland, M., Garbarino, G., Mezouar, M., Fedotenko, T., Abrikosov, I. A., Dubrovinskaia, N., Dubrovinsky, L., Laniel, D. (2024). *Synthesis of $LaCN_3$, $TbCN_3$, $CeCN_5$, and $TbCN_5$ Polycarbonitrides at Megabar Pressures.* ***Journal of the American Chemical Society***, 146(26), 18161–18171. DOI:10.1021/jacs.4c06068.

8) Yin, Y., Dubrovinsky, L., Aslandukov, A., Aslandukova, A., Akbar, F. I., Zhou, W., Hanfland, M., Abrikosov, I. A., & Dubrovinskaia, N. (2024). *High-Pressure Synthesis of the Iodide Carbonate $Na_5(CO_3)_2I$*. ***Solids***, 5(2), 333–340.
DOI:10.3390/solids5020022.

9) Akbar, F. I., **Aslandukova, A.**, Yin, Y., Aslandukov, A., Laniel, D., Bykova, E., Bykov, M., Bright, E. L., Wright, J., Comboni, D., Hanfland, M., Dubrovinskaia, N., Dubrovinsky, L.

(2024). *High-pressure dysprosium carbides containing carbon dimers, trimers, chains, and ribbons.* **Carbon**, 228, 119374.
DOI: 10.1016/j.carbon.2024.119374.

10) Khandarkhaeva, S., Fedotenko, T., **Aslandukova, A.**, Akbar, F. I., Bykov, M., Laniel, D., Aslandukov, A., Ruschewitz, U., Tobeck, C., Winkler, B., Chariton, S., Prakapenka, V., Glazyrin, K., Giacobbe, C., Bright, E. L., Belov, M., Dubrovinskaia, N., Dubrovinsky, L. (2024). *Extending carbon chemistry at high-pressure by synthesis of CaC_2 and Ca_3C_7 with deprotonated polyacene- and para-poly(indenoindene)-like nanoribbons*. ***Nature Communications***, 15(1), 2855.
DOI: 10.1038/s41467-024-47138-2.

11) Aslandukov, A., **Aslandukova, A.**, Laniel, D., Khandarkhaeva, S., Yin, Y., Akbar, F. I., Chariton, S., Prakapenka, V., Bright, E. L., Giacobbe, C., Wright, J., Comboni, D., Hanfland, M., Dubrovinskaia, N., Dubrovinsky, L. (2024). *Stabilization of N_6 and N_8 anionic units and 2D polynitrogen layers in high-pressure scandium polynitrides.* ***Nature Communications***, 15(1), 2244.
DOI:10.1038/s41467-024-46313-9.

12) Aslandukov, A., Jurzick, P. L., Bykov, M., **Aslandukova, A.**, Chanyshev, A., Laniel, D., Yin, Y., Akbar, F. I., Khandarkhaeva, S., Fedotenko, T., Glazyrin, K., Chariton, S., Prakapenka, V., Wilhelm, F., Rogalev, A., Comboni, D., Hanfland, M., Dubrovinskaia, N., & Dubrovinsky, L. (2023). *Stabilization Of The CN_3^{5-} Anion In Recoverable High-pressure $Ln_3O_2(CN_3)$ (Ln=La, Eu, Gd, Tb, Ho, Yb) Oxoguanidinates*. ***Angewandte Chemie International Edition***, 62(47).
DOI: 10.1002/anie.202311516.

13) Yin Y., Aslandukov A., M. Bykov, D. Laniel, **Aslandukova A.,** A. Pakhomova, T. Fedotenko, W. Zhou, F.I. Akbar, M. Hanfland, K. Glazyrin, C. Giacobbe, E.L. Bright, G. Garbarino, Z. Jia, N. Dubrovinskaia, L. Dubrovinsky (2023), *Polytypism of Incommensurately Modulated Structures of Crystalline Bromine upon Molecular Dissociation under High Pressure*, ***Physical Review Letters***, under review.

14) K.Glazyrin, Aslandukov A., **Aslandukova A.,** T. Fedotenko, S. Khandarkhaeva, D. Laniel, M. Bykov, L. Dubrovinsky. (2023) *High-pressure reactions between the pnictogens: the rediscovery of BiN*. ***Frontiers in Chemistry***, 11, 1257942.
DOI: 10.3389/fchem.2023.1257942

15) Akbar, F. I., **Aslandukova, A.**, Aslandukov, A., Yin, Y., Trybel, F., Khandarkhaeva, S., Fedotenko, T., Laniel, D., Bykov, M., Bykova, E., Dubrovinskaia, N., & Dubrovinsky, L. (2023). *High-pressure synthesis of dysprosium carbides.* ***Frontiers in Chemistry***, 11.
DOI: 10.3389/fchem.2023.1210081

16) Yin, Y., **Aslandukova, A.,** Jena, N., Trybel, F., Abrikosov, I. A., Winkler, B., Khandarkhaeva, S., Fedotenko, T., Bykova, E., Laniel, D., Bykov, M., Aslandukov, A., Akbar, F. I., Glazyrin, K., Garbarino, G., Giacobbe, C., Bright, E. L., Jia, Z., Dubrovinsky, L., & Dubrovinskaia, N. (2023). *Unraveling the Bonding Complexity of Polyhalogen Anions: High-Pressure Synthesis of Unpredicted Sodium Chlorides Na_2Cl_3 and Na_4Cl_5 and Bromide Na_4Br_5.* ***JACS Au***, 3(6), 1634–1641.
DOI: 10.1021/jacsau.3c00090

17) Gorelova, L., Vereshchagin, O., Aslandukov, A., **Aslandukova, A.,** Spiridonova, D., Krzhizhanovskaya, M., Kasatkin, A., & Dubrovinsky, L. (2023). *Hydroxylherderite ($Ca_2Be_2P_2O_8(OH)_2$) stability under extreme conditions (up to 750°C/100 GPa).* ***Journal of the American Ceramic Society***, 106(4), 2622–2634.

DOI: 10.1111/jace.18923

18) Aslandukov, A., Trybel, F., **Aslandukova, A.,** Laniel, D., Fedotenko, T., Khandarkhaeva, S., Aprilis, G., Giacobbe, C., Lawrence Bright, E., Abrikosov, I. A., Dubrovinsky, L., & Dubrovinskaia, N. (2022). *Anionic N18 Macrocycles and a Polynitrogen Double Helix in Novel Yttrium Polynitrides YN_6 and Y_2N_{11} at 100 GPa.* ***Angewandte Chemie,*** 134(34).
DOI: 10.1002/ange.202207469

19) Yin, Y., Akbar, F. I., Bykova, E., **Aslandukova, A.,** Laniel, D., Aslandukov, A., Bykov, M., Hanfland, M., Garbarino, G., Jia, Z., Dubrovinsky, L., & Dubrovinskaia, N. (2022). *Synthesis of rare-earth metal compounds through enhanced reactivity of alkali halides at high pressures.* ***Communications Chemistry***, 5(1), 122.
DOI: 10.1038/s42004-022-00736-x

20) Hsieh, W., Marzotto, E., Ishii, T., Dubrovinsky, L., **Aslandukova, A. A.,** Criniti, G., Tsao, Y., Lin, C., Tsuchiya, J., & Ohtani, E. (2022). *Low Thermal Conductivity of Hydrous Phase D Leads to a Self-Preservation Effect Within a Subducting Slab.* ***Journal of Geophysical Research: Solid Earth***, 127(6).
DOI: 10.1029/2022JB024556.

21) Kiseeva, E. S., Korolev, N., Koemets, I., Zedgenizov, D. A., Unitt, R., McCammon, C., **Aslandukova, A.,** Khandarkhaeva, S., Fedotenko, T., Glazyrin, K., Bessas, D., Aprilis, G., Chumakov, A. I., Kagi, H., & Dubrovinsky, L. (2022). *Subduction-related oxidation of the sublithospheric mantle evidenced by ferropericlase and magnesiowüstite diamond inclusions.* ***Nature Communications***, 13(1), 7517.
DOI: 10.1038/s41467-022-35110-x

22) Britvin, S. N., Vlasenko, N. S., Aslandukov, A., **Aslandukova, A.,** Dubrovinsky, L., Gorelova, L. A., Krzhizhanovskaya, M. G., Vereshchagin, O. S., Bocharov, V. N., Shelukhina, Y. S., Lozhkin, M. S., Zaitsev, A. N., & Nestola, F. (2022). *Natural cubic perovskite, $Ca(Ti,Si,Cr)O_{3-\delta}$, a versatile potential host for rock-forming and less-common elements up to Earth's mantle pressure.* ***American Mineralogist***, 107(10), 1936–1945.
DOI: 10.2138/am-2022-8186

23) Bykova, E., Johansson, E., Bykov, M., Chariton, S., Fei, H., Ovsyannikov, S. V., **Aslandukova, A.,** Gabel, S., Holz, H., Merle, B., Alling, B., Abrikosov, I. A., Smith, J. S., Prakapenka, V. B., Katsura, T., Dubrovinskaia, N., Goncharov, A. F., & Dubrovinsky, L. (2022*). Novel Class of Rhenium Borides Based on Hexagonal Boron Networks Interconnected by Short B2 Dumbbells.* ***Chemistry of Materials***, 34(18), 8138–8152.
DOI: 10.1021/acs.chemmater.2c00520

24) Laniel, D., Fedotenko, T., Winkler, B., **Aslandukova, A.,** Aslandukov, A., Aprilis, G., Chariton, S., Milman, V., Prakapenka, V., Dubrovinsky, L., & Dubrovinskaia, N. (2022). *A reentrant phase transition and a novel polymorph revealed in high-pressure investigations of CF_4 up to 46.5 GPa.* ***The Journal of Chemical Physics***, 156(4), 044503.
DOI: 10.1063/5.0079402

25) Laniel, D., Trybel, F., Winkler, B., Knoop, F., Fedotenko, T., Khandarkhaeva, S., **Aslandukova, A.,** Meier, T., Chariton, S., Glazyrin, K., Milman, V., Prakapenka, V., Abrikosov, I. A., Dubrovinsky, L., & Dubrovinskaia, N. (2022). *High-pressure synthesis of seven lanthanum hydrides with a significant variability of hydrogen content.* ***Nature Communications,*** 13(1), 6987.
DOI: 10.1038/s41467-022-34755-y

26) Meier, T., Trybel, F., Khandarkhaeva, S., Laniel, D., Ishii, T., **Aslandukova, A.,** Dubrovinskaia, N., & Dubrovinsky, L. (2022). *Structural independence of hydrogen-bond symmetrisation dynamics at extreme pressure conditions.* ***Nature Communications***, 13(1), 3042.
DOI: 10.1038/s41467-022-30662-4

27) Laniel, D., Winkler, B., Fedotenko, T., **Aslandukova, A.,** Aslandukov, A., Vogel, S., Meier, T., Bykov, M., Chariton, S., Glazyrin, K., Milman, V., Prakapenka, V., Schnick, W., Dubrovinsky, L., & Dubrovinskaia, N. (2022). *High-pressure $Na_3(N_2)_4$, $Ca_3(N_2)_4$, $Sr_3(N_2)_4$, and $Ba(N_2)_3$ featuring nitrogen dimers with noninteger charges and anion-driven metallicity.* ***Physical Review Materials***, 6(2), 023402.
DOI: 10.1103/PhysRevMaterials.6.023402

28) Aslandukov, A., **Aslandukova, A.,** Laniel, D., Koemets, I., Fedotenko, T., Yuan, L., Steinle-Neumann, G., Glazyrin, K., Hanfland, M., Dubrovinsky, L., & Dubrovinskaia, N. (2021). *High-Pressure Yttrium Nitride, Y_5N_{14}, Featuring Three Distinct Types of Nitrogen Dimers.* ***The Journal of Physical Chemistry C***, 125(32), 18077–18084.
DOI: 10.1021/acs.jpcc.1c06210

29) Bykova, E., Bykov, M., Chariton, S., Prakapenka, V. B., Glazyrin, K., Aslandukov, A., **Aslandukova, A.,** Criniti, G., Kurnosov, A., & Goncharov, A. F. (2021). *Structure and composition of C-S-H compounds up to 143 GPa.* ***Physical Review B***, 103(14), L140105.
DOI: 10.1103/PhysRevB.103.L140105

30) Laniel, D., **Aslandukova, A. A.,** Aslandukov, A. N., Fedotenko, T., Chariton, S., Glazyrin, K., Prakapenka, V. B., Dubrovinsky, L. S., & Dubrovinskaia, N. (2021). *High-Pressure Synthesis of the β-Zn_3N_2 Nitride and the α-ZnN_4 and β-ZnN_4 Polynitrogen Compounds.* ***Inorganic Chemistry***, 60(19).
DOI: 10.1021/acs.inorgchem.1c01532

31) Meier, T., **Aslandukova, A.,** Trybel, F., Laniel, D., Ishii, T., Khandarkhaeva, S., Dubrovinskaia, N., & Dubrovinsky, L. (2021). *In situ high-pressure nuclear magnetic resonance crystallography in one and two dimensions.* ***Matter and Radiation at Extremes***, 6(6).
DOI: 10.1063/5.0065879

32) Ovsyannikov, S. V., **Aslandukova, A. A.,** Aslandukov, A., Chariton, S., Tsirlin, A. A., Korobeynikov, I. V., Morozova, N. V., Fedotenko, T., Khandarkhaeva, S., & Dubrovinsky, L. (2021*). Structural Stability and Properties of Marokite-Type γ-Mn_3O_4.* ***Inorganic Chemistry***, 60(17), 13440–13452.
DOI: 10.1021/acs.inorgchem.1c01782

33) Ovsyannikov, S. V., Tsirlin, A. A., Korobeynikov, I. V., Morozova, N. V., **Aslandukova, A.** A., Steinle-Neumann, G., Chariton, S., Khandarkhaeva, S., Glazyrin, K., Wilhelm, F., Rogalev, A., & Dubrovinsky, L. (2021). *Synthesis of Ilmenite-type ε-Mn_2O_3 and Its Properties.* ***Inorganic Chemistry***, 60(17), 13348.
DOI: 10.1021/acs.inorgchem.1c01666

34) Nawa, K., Avdeev, M., Berdonosov, P., Sobolev, A., Presniakov, I., **Aslandukova, A.,** Kozlyakova, E., Vasiliev, A., Shchetinin, I., & Sato, T. J. (2021). *Magnetic structure study of the sawtooth chain antiferromagnet $Fe_2Se_2O_7$.* ***Scientific Reports***, 11(1), 24049.
DOI: 10.1038/s41598-021-03058-5

35) Sobolev, A. V., **Aslandukova, A. A.,** Kozlyakova, E. S., Kuznetsova, E. S., Akhrorov, A. Yu., Berdonosov, P. S., Glazkova, I. S., Volkova, O. S., Vasiliev, A. N., & Presniakov, I. A.

(2020). *Magnetic hyperfine interactions in a sawtooth chain iron oxoselenite $Fe_2O(SeO_3)_2$: Experimental and theoretical Investigation.* ***Journal of Alloys and Compounds***, 822, 153549. DOI: 10.1016/j.jallcom.2019.153549

36) Sobolev, A. V., Glazkova, I. S., **Akulenko, A. A.,** Sergueev, I., Chumakov, A. I., Yi, W., Belik, A. A., & Presniakov, I. A. (2019). *^{61}Ni Nuclear Forward Scattering Study of Magnetic Hyperfine Interactions in Double Perovskites A_2NiMnO_6 (A = Sc, In, Tl).* ***The Journal of Physical Chemistry C***, 123(38).
DOI: 10.1021/acs.jpcc.9b06621

37) Sobolev, A. V., **Akulenko, A. A.,** Glazkova, I. S., Zvereva, E. A., Ovanesyan, N. S., Markina, M. M., & Presniakov, I. A. (2019). *Spin ordering and hyperfine interactions in langasite-like ferrite $Ba_3SbFe_3Si_2O_{14}$: ^{57}Fe Mössbauer reinvestigation and ESR measurements.* ***Journal of Alloys and Compounds***, 797, 432–442.
DOI: 10.1016/j.jallcom.2019.05.020

38) Sobolev, A. V., **Akulenko, A. A.,** Glazkova, I. S., Belik, A. A., Furubayashi, T., Shvanskaya, L. V., Dimitrova, O. V., & Presniakov, I. A. (2018). *Magnetic Hyperfine Interactions in the Mixed-Valence Compound $Fe_7(PO_4)_6$ from Mössbauer Experiments.* ***The Journal of Physical Chemistry C***, 122(34).
DOI: 10.1021/acs.jpcc.8b05516

39) Sobolev, A. V., **Akulenko, A. A.,** Glazkova, I. S., Pankratov, D. A., & Presniakov, I. A. (2018). *Modulated magnetic structure of Fe_3PO_7 as seen by ^{57}Fe Mössbauer spectroscopy*. ***Physical Review B***, 97(10), 104415.
DOI: 10.1103/PhysRevB.97.104415

40) Sobolev, A., Rusakov, V., Moskvin, A., Gapochka, A., Belik, A., Glazkova, I., **Akulenko, A.,** Demazeau, G., & Presniakov, I. (2017). *^{57}Fe Mössbauer study of unusual magnetic structure of multiferroic 3R-$AgFeO_2$.* ***Journal of Physics: Condensed Matter***, 29(27), 275803.
DOI: 10.1088/1361-648X/aa70ae

(Eidesstattliche) Versicherungen und Erklärungen

(§ 9 Satz 2 Nr. 3 PromO BayNAT)

Hiermit versichere ich eidesstattlich, dass ich die Arbeit selbstständig verfasst und keine anderen als die von mir angegebenen Quellen und Hilfsmittel benutzt habe (vgl. Art. 97 Abs. 1 Satz 8 BayHIG).

(§ 9 Satz 2 Nr. 3 PromO BayNAT)

Hiermit erkläre ich, dass ich die Dissertation nicht bereits zur Erlangung eines akademischen Grades eingereicht habe und dass ich nicht bereits diese oder eine gleichartige Doktorprüfung endgültig nicht bestanden habe.

(§ 9 Satz 2 Nr. 4 PromO BayNAT)

Hiermit erkläre ich, dass ich Hilfe von gewerblichen Promotionsberatern bzw. -vermittlern oder ähnlichen Dienstleistern weder bisher in Anspruch genommen habe noch künftig in Anspruch nehmen werde.

(§ 9 Satz 2 Nr. 7 PromO BayNAT)

Hiermit erkläre ich mein Einverständnis, dass die elektronische Fassung meiner Dissertation unter Wahrung meiner Urheberrechte und des Datenschutzes einer gesonderten Überprüfung unterzogen werden kann.

(§ 9 Satz 2 Nr. 8 PromO BayNAT)

Hiermit erkläre ich mein Einverständnis, dass bei Verdacht wissenschaftlichen Fehlverhaltens Ermittlungen durch universitätsinterne Organe der wissenschaftlichen Selbstkontrolle stattfinden können.

…….
Ort, Datum, Unterschrift